Immobilisation of Caesium from Crystalline Silicotitanate by Hot Isostatic Pressing

by

Tzu-Yu Chen

Supervisor: Dr Joseph A. Hriljac

A thesis submitted to The University of Birmingham for the degree of Doctor of Philosophy

The School of Chemistry
College of Engineering and Physical Sciences
University of Birmingham
Oct 2012

UNIVERSITY OF BIRMINGHAM

University of Birmingham Research Archive

e-theses repository

Abstract

The main aim of this project was to develop a durable ceramic wasteform by HIPing Cs-exchanged crystalline silicotitanate (CST) used for nuclear waste clean-up. The sodium form (Na-CST) and niobium substituted sodium form (Na-Nb/CST) CST were hydrothermally synthesised and characterised. The synthesised CSTs and a commercial CST containing material, IONSIV®, were subjected to ion exchange studies and then the crystal phases present after HIPing were investigated. Cs-IONSIV® was thermally decomposed and converted to two major Cs-containing phases, $Cs_2TiNb_6O_{18}$ and $Cs_2ZrSi_6O_{15}$, and a series of other phases. Additionally the effect of metal addition on phase formation under HIP conditions was explored. The microstructure and phase assemblage of HIPed Cs-IONSIV® samples as a function of Cs content were examined using XRD, XRF, SEM and TEM/EDX.

To understand the Cs bonding environment in these Cs-containing phases, structural characterisation was undertaken using Rietveld analysis of synchrotron X-ray powder diffraction data and neutron diffraction data. The potential of these phases for hosting Cs^+ and its decay product Ba^{2+} was also studied.

This thesis is also concerned with determining the aqueous durability of these HIPed samples by carrying out MCC-1 and PCT-B leach tests. These show very low Cs leach rates and the promise of safe long-term immobilisation of Cs from CSTs as well as suggesting these phases are more leach resistant than hollandite - the material targeted for Cs sequestration in Synroc.

I

Acknowledgements

First and foremost I would like to acknowledge my supervisor Dr. Joe Hriljac for his invaluable support, guidance and patience throughout this PhD. I would also like to thank Prof. Neil Hyatt and Dr. Ewan Maddrell for their advice and encouragement. This thesis would have never been possible without their input. The additional sponsorship from School of Chemistry, University of Birmingham and NNL was greatly appreciated.

Thanks go to the members of the 5th floor Chemistry, past and present, for their help and always making it an enjoyable place to work. A massive thank you must be expressed to Ben, Cathryn, Ivan, Yasmin and Ying, for those days panicking together and supporting each other, Tom M and Alex for helping me fit in and improving my English (in a slightly painful way), Victoria and Tom C for sharing their precious synchrotron beam time with me, Dr. Jackie Deans and Annabelle for the technical support and the big smiles and my friends Yina and Su, from Mat & Met, for the help and company since the very beginning of our PhDs.

Special mention to the following people who have helped with the acquisition of results included in this thesis. Mr. Mike Glynn, Univ. Birmingham, for running the HIP and being an entertaining and supportive friend. Dr. Martin Stennett and Dr. Amy Gandy, Univ. Sheffield, for their help with TEM microstructure analyses, Mr. Paul Stanley and Dr. Ming Chu, Univ. Birmingham, for the SEM and TEM support, Mr. Steve Baker, Univ. Birmingham, for the ICP analyses and Dr. Ron Smith, ISIS, for the neutron diffraction data collection.

Most of all I would like to thank my parents and my beloved family for their unconditional support and encouragement. Without them I would never been able to gain this incredible experience of studying abroad, making lifelong friends and having the chance to make them proud of me. Thank you!

Abbreviations

CST	Crystalline Silicotitanate
Na-CST	Sodium Crystalline Silicotitanate, $Na_2Ti_2O_3SiO_4 \cdot 2H_2O$
Na-Nb/CST	Niobium Substituted Crystalline Silicotitanate
PXRD	Powder X-ray Diffraction
XRD	X-ray Diffraction
GSAS	General Structural Analysis System
BVS	Bond Valence Sum
SEM	Scanning Electron Microscopy
EDX	Electron Dispersive X-ray
TEM	Transmission Electron Microscopy
XRF	X-ray Fluorescence
TGA	Thermogravimetric Analysis
DTA	Differential Thermal Analysis
MS	Mass Spectrum
HIP	Hot Isostatic Pressing
ASTM	American Society for Testing and Materials
MCC	Materials Characterisation Centre
PCT	Product Consistency Test

Table of Contents

Chapter 3 Synthesis and Characterisation of Crystalline Silicotitanate..58

Chapter 4 Immobilisation of Cs from Crystalline Silicotitanate by Hot Isostatic Pressing 101

Chapter 5 Properties, Structure Determination and Ba Substitution of Cs-Containing Phases as Potential Ceramic Wasteforms

Chapter 1   Introduction

1.1 Background

Nuclear power supplies ~ 14% of electricity around the world today.[1] Since nuclear power is recognised as the only large-scale CO_2 emission free power source, the use of nuclear power has been continuously promoted. Despite the public debate concerning safety of nuclear power, especially driven by the recent Fukushima disaster, several countries have restricted or halted nuclear development, for example, Switzerland and Germany. Although many nuclear plants are being decommissioned, the large amount of radioactive waste world-wide is still substantial and requires further treatment. In contrast, a number of countries, such as China, India and the UK, have announced a significant expansion of nuclear power to meet the increasing energy demand.

Like many other sources of power generation, nuclear power introduces waste. Huge quantities of radioactive waste generated in the past few decades cannot be treated as normal hazardous wastes due to the harmful radioactivity. According to its heat generating capacity and activity content, radioactive wastes are generally classified into several categories including very low level waste (VLLW), low level waste (LLW), intermediate level waste (ILW) and high level waste (HLW).

The majority of radioactivity is in the HLW. Sources of HLW include the reprocessing of spent nuclear fuel. After a fuel assembly has been used in the reactor core for power generation, the fission products held inside the cladding of the fuel must be disposed of in a

safe fashion.[2] In addition, corrosion products, activated products that are carried by the reactor coolant system, filter cartridges and demineraliser resins must be treated as radioactive waste. Minor nuclear fuel components and transmutation products comprising α-emitters and process contaminants are also included in HLW.[3] Another source of HLW arises from the production of plutonium metal and tritium for defence weapon application.

Typically aqueous HLW streams are treated on the basis of "concentration" by evaporation and stored as aqueous nitric acid solutions in stainless steel tanks. Alternatively, the solution may be neutralised by addition of an alkali.[4] The radiochemical composition of fission products changes significantly over time due to the decay of the short-lived radionuclides, and the fraction of long-lived isotopes, such as ^{135}Cs (half-life of 3×10^6 years), ^{137}Cs (half-life of 30.1 years), ^{90}Sr (half-life of 28.78 years) and ^{129}I (half-life of 1.57×10^7 years), constantly increases. Safe, efficient and constant upgrading process technologies are required in order to minimise the toxicity and reduce the volume of the radioactive waste prior to final disposal or storage. Thus, separation of radionuclides from nuclear wastes will be an important issue prior to permanent disposal. Once the radionuclides are removed, the residual waste can then be treated as LLW which requires less restrict regulations than HLW.

Treatment of liquid radioactive waste usually involves several steps, such as filtration, precipitation, sorption, ion exchange, evaporation, scrubbing, solvent extraction and/or membrane separation. Of these, radioactive decontamination using an inorganic ion exchanger has received more and more attention and been considered as an efficient way from the viewpoint of an industrial application. It is also believed that inorganic ion exchangers exhibit greater selectivity than organic resins because of the highly crystalline framework structure.

The radioactive nuclides of interest, particularly ^{137}Cs in this work, are present in the waste solutions at trace concentrations along with other mixed interfering elements. Hence separation of Cs from the waste solution is difficult. Up until now, there is no demonstrated process that can be used for easy, efficient and economic separation of the Cs from highly basic waste solutions containing complex salts. Of the options available, an ion exchange process displays many advantages for achieving efficient separation:

- It is versatile in both continuous flow (ion exchanger columns) and batch processing tank systems.

- It is a flexible and efficient process, and decontamination factors of many orders of magnitudes can be achieved.

- The equipment for the ion exchange process is simple and mature for either stationary (plant) or mobile waste management systems.

- No hazardous organic solvents are introduced into the waste stream during the process.

Extensive research and development has been done on the application of ion exchange for the separation of Cs. Both organic and inorganic sorbents can be used[5], however inorganic ion exchangers often show greater resistant to radiation damage, chemical oxidation and thermal degradation over organic ion exchangers. It is also believed that inorganic ion exchangers exhibit greater selectivity because of the highly crystalline framework structure. Hence, it is more feasible to dispose nuclear waste by loading on inorganic ion exchangers.

1.2 Inorganic Ion Exchangers

Many investigations have been carried out using zeolites[6-10] in large-scale processes to treat wastes owing to their ease of use. Natural zeolite materials such as clinoptilolite[11-17],

chabazite[18-20] and mordenite[21-23] have been extensively studied for applications in nuclear waste treatment. Their ion exchange properties have been extensively studied, and the regular structures are well suited for many modelling purposes.[8] A better capacity and selectivity can be achieved by varying the Si/Al ratio in the composition. However, their use is limited to a fairly narrow pH value because of the dissolution of Si and Al from the framework at extreme pH conditions. The development of novel inorganic materials as ion exchangers for the separation of Cs is therefore an active area.

Synthetic zeolites, phosphates[24-26], heteropolyacid salts of molybdemum and tungsten[27], silicotitanates and transition metal hexacyanoferrates[28-30] have all received enormous attention in recent years and have shown improved ion exchange properties in regard to selective separation and recovery of Cs from highly radioactive solutions.

Ammonium molybdophosphate (AMP), $(NH_4)_3PMo_{12}O_{40}$, is one of the most investigated ion exchangers. The ion exchange properties of AMP for Cs were firstly discovered by Smit et al.[31, 32] AMP showed about a 100 times higher distribution coefficient value (K_d) for Cs and a large value of separation factor for Cs^+/Na^+ ion pair at 6000 or greater than the organic resin Dewex-50 (NH_4^+ form)[32]. Due to the important features such as the high selectivity, rapid sorption rate of Cs over the organic resin, great radiation resistance and relatively low cost, AMP has been enormously investigated and applied for Cs separation. However, some technical limits exist due to its narrow working pH range.

CsTreat[®] is a transition metal hexacyanoferrate [$K_2CoFe(CN)_6$] product commercialised by Fortum Engineering Ltd. CsTreat[®] has a great processing capacity, high Cs selectivity and works in a wide operational pH range (pH 1 to 13)[33], therefore it has been utilised in industrial scale for radioactive Cs separation at several nuclear power plants in many

countries, such as Russia, Finland and the United States.[34, 35] CsTreat® is effective for the treatment of many types of nuclear wastes, however the performance of Cs uptake is markedly affected by the presence of high concentrations of potassium and ammonium ions.[33, 35] Additionally, CsTreat® can only work at operating temperature below 80 °C, the application is therefore limited.

Another promising material for Cs removal is crystalline silicotitanate (referred to as CST in the following) developed by Sandia National Laboratory (SNL) and Texas A&M University. It was first developed based on the successful use of amorphous hydrous titanium oxide (HTO) in the 1960s as an ion exchanger for most cationic radionuclides, such as Sr and Pu. However, HTO exhibits very poor affinity for Cs. As a result, a new ion exchanger named TAM-5 was prepared by Anthony et al.[36] in the early 1990s. Crystals of CST with the ideal composition of $Na_2Ti_2O_3SiO_4 \cdot 2H_2O$ (referred to **Na-CST** in the following) are tetragonal, and the typical crystal sizes are 0.1 to 0.4 μ m. The uniform channels, which are ideally suited for extraction of Cs ions, were found in the framework structure.[37, 38]
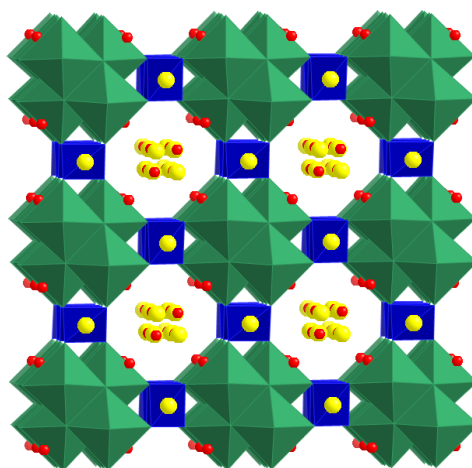
Figure 1.1 Schematic diagram illustrates the structure of $Na_2Ti_2O_3SiO_4 \cdot 2H_2O$. Blue tetrahedra represent SiO_4, green octahedra represent TiO_6, and red and yellow spheres represent O and Na atoms, respectively.

A hydrothermal synthesis to produce highly crystalline Na-CST was reported by Poojary et al.[39] and the structure solutions of a variety of cation exchanged forms were carried out. The structure information reported for the synthetic Na form is very similar to that of a natural sitinakite reported by Sokolova et al.[40]. The composition of the natural material suggests that Nb can substitute for Ti in the structure and it was indeed demonstrated by Anthony et al.[38] that niobium substituted CST has significantly better Cs^+ selectivity at high pH.

The CST product with niobium substitution was subsequently commercialised by University Oil Products (UOP) and given the name IONSIV® IE-910 for the powdered form and IONSIV® IE-911 for the engineered form. The IONSIV® IE-911, which combines the powdered form of CST with $Zr(OH)_4$ as binder to increase column performance, is widely applied in fixed bed columns for continuous treatment systems. More literature survey regarding CST and IONSIV® will be described in Chapter 3.

Table 1-1 summarises some properties of the mostly widely used inorganic ion exchangers. CST is considered the most promising material due to its great selectivity of Cs over a broad pH range in the presence of interfering salts. However, the spent ion exchanger still poses some hazards and needs to be further treated before geological disposal. For example, Cs cations are tightly bound inside the structure of the ion exchanger, but once the structural properties are damaged due to exposure to radiation or heat the risks of Cs leaching to the environment will rapidly increase. Furthermore, large space is needed for storing the low density spent ion exchanger, an efficient volume reduction is preferred. Safe and efficient solutions for immobilisation of spent ion exchanger before final disposal have therefore been sought.

Table 1-1 Brief comparison of natural or synthetic materials applied for ion exchange process

Materials	Characteristics
Zeolite Clinoptilolite	• Cavities and tunnels of 4-7 Å in the framework structure separate ions by size. • Different selectivity and capacity can be obtained by varying the Si/Al ratio. • The use is limited to a fairly narrow pH range due to Si and Al dissolution at extreme pH ranges.
Ammonium molybdophosphate (AMP) $(NH_4)_3PMo_{12}O_{40}$	• Poor selectivity in highly alkaline and high Na^+ solution. • Limited working pH range due to Mo dissolution at pH > 6.
Hexacyanoferrate $K_2CoFe(CN)_6$ (CsTreat®)	• Broad working range pH 1-13. • Good efficiency in the presence of Na^+, Ca^{2+} and Mg^{2+}. • Hexacyanoferrates of Ni-, Zn- and Cu- form have been studied for use in nuclear waste treatment.
Crystalline silicotitanate (CST)	• Efficient in a broad pH range and high salt containing waste solutions. • Better Cs^+ affinity in alkaline solution can be achieved by adding Nb^{5+}.

1.3 General Immobilisation Options

Various radioactive waste disposal concepts, including deep-seabed disposal, disposal in the polar ice sheets, and rocketing waste into space etc., have been investigated. With respect to technical practicality, safety, cost and environment compact, geological disposal seems to be the most appropriate solution.[41] So far, tonnes of immobilised HLW in glass wasteforms are in interim storage at vitrification plants waiting for final disposal. In most countries the HLW is eventually destined to be put underground in geological disposal facilities (GDF) called "repositories".[1, 41-44] Although there is currently no final disposal repository in the

world, the first operational spent fuel repository is likely to be in Finland sometime in the next decade.

HLW requires long-tem storage for 10^3-10^5 years depending on composition and activity. The inorganic wastes must be conditioned to durable wasteforms. Immobilisation may be accomplished either by dissolution of the waste elements on an atomic scale into a host lattice, or encapsulation of the waste within an inert matrix.[4, 45] To be a feasible wasteform, a monolithic form is usually desired due to the smaller surface area than powder form, thus the release rate is reduced when the wasteform contacts with water. In addition, it must meet many other requirements, including high chemical durability and radiation resistance under repository conditions (200-400 °C underground, i.e. hydrothermal conditions), high thermal conductivity to dispel heat from radioactive decay, high waste loading in order to minimise the overall volume, strong mechanical integrity, compatibility with the geological environment and so on.[3]

Of course no wasteform can satisfy all the above requirements. Many different types of matrices (amorphous, crystallised or composites) have been studied over a long period of time to seek a suitable wasteform and understand the behaviour of a potential host that immobilises a specific waste. Several candidates, such as glasses, ceramics and cements, are considered for immobilising HLW, as listed in Table 1-2.

Table 1-2 Selected candidates considered for HLW immobilisation

System	Host	Example
Glasses	Silicate	Aluminosilicate, Borosilicate
	Phosphate	Sodium aluminum phosphate, Iron-lead phosphate
	Other glasses	Rare earth oxide glasses, Sintered glasses
Ceramics	*Single-phase*	
	Alumina	Aluminosilicate, Zeolites
	Titanite	$CaTiSiO_5$
	Zircon	$ZrSiO_4$
	Zirconolite	$CaZrTi_2O_7$
	Pollucite	$CsAl_2SiO_6$
	Perovskite	$CaTiO_3$
	Pyrochlore	$Ln_2Ti_2O_7$ (Ln = rare earth elements)
	Hollandite	$BaAl_2Ti_6O_{16}$
	Multi-phases	
	Synroc	Zirconolite + Hollandite + Perovskite
Glass-ceramics	Celsian based barium aluminosilicates glass	$BaAl_2Si_2O_8$
	Fresnoite based barium titanium silicates glass	$BaTiSi_2O_8$
	Synroc based glass	Zirconolite
Cements	Silicate based	
	Phosphate based	
Other wasteforms	Composite materials	Glass-bonded sodalite, Silicotitanate, Phosphate
	Porous crystalline matrix	Gubka
	Bitumen	

1.3.1 Glass Wasteforms

Although many different types of materials have been investigated as possible candidates for immobilisation of HLW, glass is the generally accepted wasteform due to its random network to accommodate ions with widely variable charges and radii.[4, 46] It is also simple to produce and highly resistant to radiation. The great chemical resistance of glasses also allows them to remain stable in corrosive environments for many years. As a result, many industrial-scale vitrification plants have been in operation to immobilise HLW into glass wasteforms. HLW is dissolved to form a homogeneous and glassy product that can be cast into suitable forms. Under suitable condition, up to 25-30 wt.% of HLW can be incorporated into a glass.[4] The choice of glass composition highly depends on several factors, for example, the stability of HLW and operating glass formation temperature. Some loss of volatile elements is observed due to the high melting temperature of glass, thus temperature may be regarded as a limit for vitrification of Cs-bearing waste.[47] Undesired crystallisation might occur during annealing the glass or storage, therefore cause the glass to crack.

Silicate and Borosilicate Glasses

The use of glass as the host of HLW was firstly investigated in Canada in the early 1950s using a natural silicate, nepheline syenite, as raw material.[3, 4] Silicate glasses have long been the preferred wasteform since then because of the ease in modification to optimise the properties. The melting temperature of silicate glass was around 1350 °C, however appreciable Cs and Ru losses were noticed due to the volatilisation at high temperature.[3, 46] Therefore, boric oxide was added in order to modify the properties and reduce the processing temperature. The base borosilicate glass is a Na_2O-SiO_2-B_2O_3 system, and LiO_2 may be added to further reduce the processing temperature.[48] The mechanical property, thermal/radiation

stability, chemical durability, corrosion behaviour and devitrification of borosilicate glasses have been well characterised and understood.

There are also some limits of borosilicate glasses. Some components, such as platinoids (Ru, Pd and Rh), high oxidation state cations (e.g. Mo^{6+}, S^{6+} and Cr^{6+}) and refractory oxides (e.g. Al_2O_3 and Cr_2O_3), are poorly dissolved in silicate glasses, therefore it results in a low weight loading.[4, 49, 50] Beyond the solubility limit, the excess is segregated as a separate phase and therefore results in higher leach rates of radionuclides. For example, in molybdate- and chromate-containing waste vitrification, an immiscible liquid alkaline and alkaline-earth molybdate complex, commonly known as "yellow phase," may form.[3, 51]

Phosphate Glasses

Phosphate-based glasses were initially developed in the early 1960s. Unlike silicate glass where the network containing random arrangement of interconnecting tetrahedra, the characteristic bonding in phosphate glasses is via long chains of cross-linked PO_4 tetrahedra, which is more similar to organic polymers. Hence the feature leads to many different properties to silicate glass family.[4, 52] Phosphate glasses show a number of advantages over silicate glasses, including lower melting temperature (< 1000 °C), lower melt viscosities and greater solubility of sulphates and metal oxides.

However, phosphate glasses generally exhibit less chemical durability in aqueous environments and poorer thermal stability than borosilicate glasses. In addition, phosphate melts are highly corrosive and this factor limits the melting lifetime. Due to these reasons, interests in phosphate glasses rapidly declined. There are, however, still a large number of

researchers working on modifications of sodium aluminophosphate, iron aluminophosphate and zinc phosphate to achieve improved thermal or chemical durability.[53, 54]

A new family of glasses, lead-iron phosphates (LIP), was proposed for HLW immobilisation with high Fe content. These glasses show good thermal stability, and the melt was less corrosive than the earlier phosphate compositions. This glass can be prepared at around 800 °C and is very resistant to devitrification. It was also found that this glass exhibited excellent chemical durability due to its characteristic bonding feature. This glass consists of poly-phosphate chains cross-linked by octahedrally coordinated Fe^{3+} ions, and the coordination number of Pb^{2+} is 8 or 9. This strong network blocks the percolation of Pb and hydronium ions so that the chemical durability is highly increased.[3] By optimising the Fe_2O_3 and PbO content or adding CaO to iron phosphate, a better chemical durability can be achieved.[4, 55]

Other Glasses

There are also many other kinds of glasses that have been studied for immobilisation of HLW, for example, chalcogenide element-based glasses and halide-based glasses. "Löffler", the commercial lanthanide borosilicate, has been suggested as a potential host for the immobilisation of U, Pu and Am.[56] Sintered glasses, which are produced by sintering of HLW components into a glass matrix, have much lower processing temperature than borosilicate glass fabrication thus reducing evaporation losses of volatile radionuclides, particularly Cs, Ru, Mo and Tc. It was also confirmed that "hot pressing" was essential to prepare sintered glass wasteforms of compact density (> 95% of theoretical density).[49]

1.3.2 Ceramic Wasteforms

HLW can be directly immobilised into crystalline ceramic wasteforms. The basic idea underpinning ceramic wasteforms is to use durable analogues of minerals that have been preserved in natural conditions over geological times as immobilising matrices.[50] A number of candidates including single-phase or multi-phase ceramics have been developed and show potential as good hosts for immobilising radioactive nuclides. A brief description of the selected crystalline ceramic wasteforms for immobilisation of rare earth elements and actinides is given below.

Titanate ceramics have been the most widely studied wasteforms for HLW immobilisation. The most well known materials are the synthetic rock (**Synroc**) family, an assemblage of geologically stable titanate minerals developed by Rinwood et al. in the 1970s.[57-59] Synroc, which mainly comprises of perovskite ($CaTiO_3$), zirconolite ($CaZrTi_2O_7$), Ba-hollandite ($BaAl_2Ti_6O_{16}$), has been developed and used to treat a wide range of fission products, actinides and process chemicals by incorporating them and the other waste constituents as dilute solid solutions within the individual crystal lattice of the various ceramic phases. HLW could therefore be immobilised for long periods when Synroc is buried in a suitable geological environment.

Natural **perovskite** has a formula of $CaTiO_3$. In the perovskite structure, the large cations (e.g. Ca^{2+}) are located in 12 coordinated positions between groups of eight TiO_6 octahedra which are linked by sharing corners to form a three-dimensional framework, as shown in Figure 1.2.

13
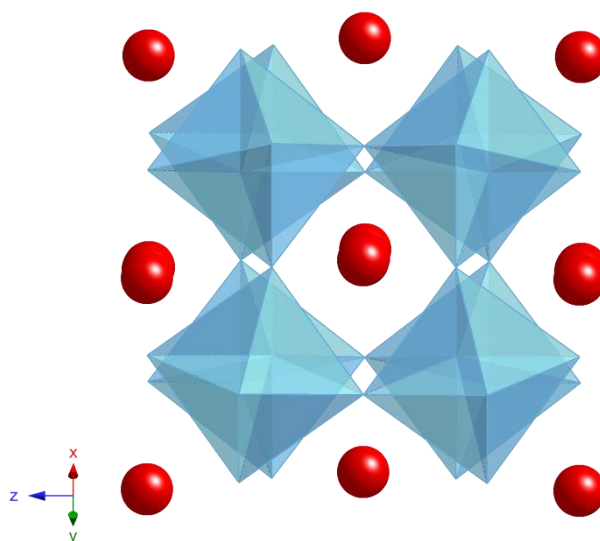
Figure 1.2 Crystal structure of perovskite

The ideal ABO_3 perovskite structure can be formed only for a rather restricted size-range for A and B cations. The A cations have to be sufficiently large to form a close packed array with oxygen anions whilst the B ions must fit within the octahedral holes of the A-O close-packed array to maintain high symmetry. If the requirements are not met, the simple perovskite lattice may become distorted and result in a smaller coordination number of the A cations.

This mineral structure is capable of taking an extremely wide range of other elements into stable solid solutions. Ca^{2+} can be replaced by Sr^{2+}, Ba^{2+} and all the rare earth elements via a simple substitution, whilst Ti^{4+} sites can be replaced by Pu^{4+}, Th^{4+}, U^{4+}, Ru^{4+}, Fe^{3+} and Al^{3+} etc. Perovskite naturally occurs in alkaline mafic and ultramafic rocks, where it is known to have remained stable in geological environments for periods exceeding 1000 million years.[60]

Pyrochlore has the general formula of $A_2B_2O_6Y$ where the A sites are occupied with 8-coordinated large cations (Na, Ca, actinides), the B sites with 6-coordinated low radius and

higher-valence cations (Nb, Ta, Ti, Zr) and Y sites with additional ions or remain vacant. Pyrochlore is an anion-deficient derivative of the fluorite structure (AX_2). Fluorite itself has a face-centred (space group *Fm*3*m*) structure composed of edge-sharing cubic sites with each cation coordinated to eight anions. Pyrochlore is derived from fluorite by removing 1/8 of the anions in an ordered fashion, such that half of the cubic polyhedra are missing two opposed vertices. Thus the cell edge was doubled, and the space group is changed to *Fd*3*m*.[61]
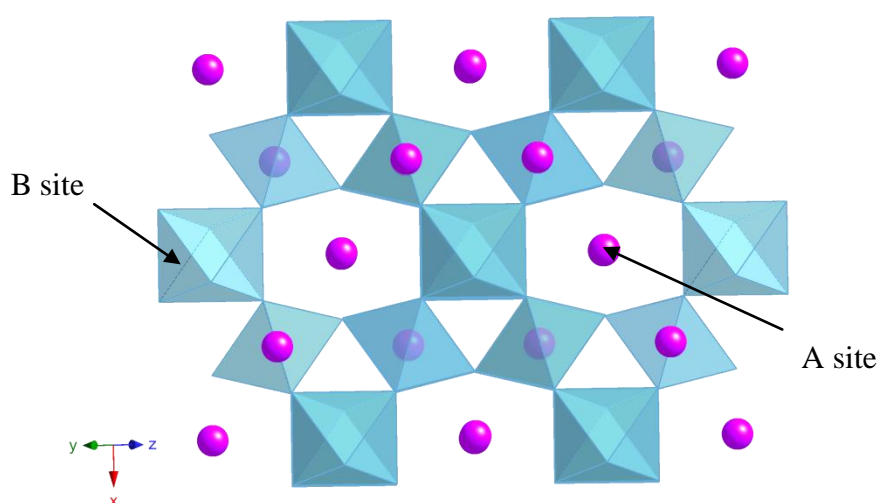
Figure 1.3 Crystal structure of pyrochlore

In ternary metal oxide systems, pyrochlores ($A_2B_2O_7$) are of greatest interest in nuclear waste management because of their ability to incorporate trivalent lanthanides and tri- and tetra-valent actinides.[62, 63] Actinides (3+, 4+ and 5+) are predicted to form the pyrochlore structure by substitutions on both the A- and B-sites $A^{III}_2B^{(IV,V)}_2O_7$. Those with higher valence states (e.g. Np^{6+} and Pu^{6+}) can be incorporated into ideal or defect pyrochlores at the B-site. Recent interest has focused on titanate pyrochlore due to its great chemical durability. However, owing to the radiation damage from the alpha-decay of actinides, a radiation-induced transition from the crystalline-to-aperiodic state occurs in these compositions.[62]

Zirconolite, with the generic formula $Ca^{2+}Zr^{4+}_xTi^{4+}_{(3-x)}O_7$ (where $0.8 < x < 1.35$) but ideally $CaZrTi_2O_7$, has a complex monoclinic symmetry. Zirconolite is an anion-deficient fluorite-derivative structure closely related to pyrochlore. Alternating layers comprising (Ca, Zr) polyhedra are stacked with layers consisting of Ti polyhedra; stacking occurs parallel with the crystal plane [001][64], as shown in Figure 1.4.

The end-member of titanate-based zirconolite is $CaZrTi_2O_7$ (2M polytype), in which Ca and Zr have 8- and 7-fold coordination, respectively. Different polytypes (e.g. 3T, 3O, 4M) arise through solid solutions towards lanthanide and actinide-bearing end-members[65, 66]. It is suitable for accommodating the tri- and tetra-valent actinides by substitution at the Ca site and Zr site, respectively, along with Al as charge compensator. Various ionic substitutions ensure chemical flexibility within the zirconolite. Both natural and synthetic zirconolites show great chemical durability, radiation stability and corrosion resistance.
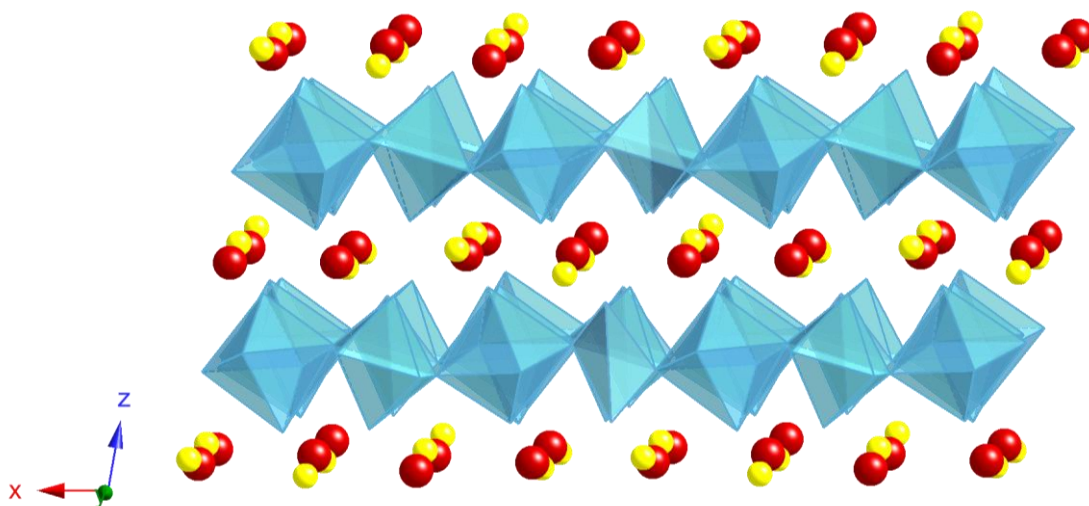
Figure 1.4 Crystalline structure of zirconolite 2M $CaZrTi_2O_7$. The layers formed by polyhedra of Ca (red) and Zr (yellow) ions alternate with layers of TiO_6 octahedra (blue).

Hollandite has a general formula of $A_xB_yC_{8-y}O_{16}$ where x ≤ 2, and is one of the major Synroc phases incorporating Cs and corrosion products. The A sites are occupied by large mono- or divalent cations (e.g. Na^+, Cs^+, Sr^{2+} and Ba^{2+}), and B and C sites are occupied by various cations with a charge of +2 to +5. In the hollandite structure, the small cations are octahedrally coordinated and each of these octahedra shares two edges to form paired chains running parallel to the *c* axis.[67] The double strings of octahedra, in turn, share corners to form a three-dimensional framework. Many large cations are situated in the tunnels and tightly "locked-up". Figure 1.5 shows the typical hollandite structure in $BaAl_2Ti_6O_{16}$, the most abundant mineral in Synroc A. Cs^+ can be incorporated into the tunnels where Ba^{2+} resides.
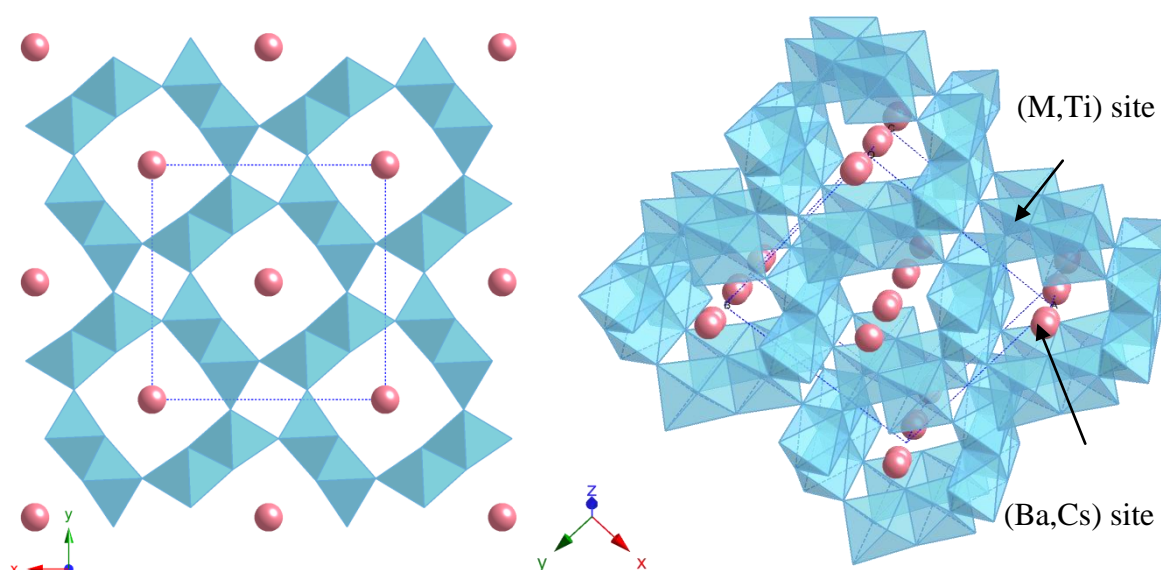
Figure 1.5 The hollandite structure in $BaAl_2Ti_6O_{16}$ viewed from (a) *c* axis (b) [111]

Hollandite shows excellent leach resistance due to its structure. Many hollandite phases, such as $Cs_2Al_2Ti_6O_{16}$, $BaAl_2Ti_6O_{16}$, $SrAl_2Ti_6O_{16}$, $Na_2Al_2Ti_6O_{16}$ and $K_2Al_2Ti_6O_{16}$, have been synthesised.[58] These phases have demonstrated a considerable flexibility of ionic

substitutions. It was also found that when a small amount of Cs^+ and K^+ enter the structure in solid solution replacing Ba^{2+}, the mono-valence cations are securely locked within the tunnels due to the relatively high bonding energy. Thus, the alkali metals are extremely immobile. This feature is particularly important when hollandite is considered as the potential candidate to host Cs in radioactive waste.

Since hollandite is a natural Ba containing phase, when Cs radioactively decays to Ba, its decay product can be nicely incorporated in the structure. Many studies throughout the years have also demonstrated that hollandite has good thermal conductivity[68] as well as good electron irradiation resistance.[69] Although hollandite hosts fission and corrosion products, which undergo β-γ irradiation, in a multi-phase ceramic system it will also experience irradiation from α-particles emitted in adjacent actinide-containing phases. It was reported by Weber[70] that about 2-2.5% of expansion in the unit cell volume and a structural transformation from tetragonal to a lower symmetry monoclinic structure occurred when hollandite was irradiated by α-particles from external $^{238}PuO_2$ and heavy-ions. The anisotropy of the unit cell expansion caused an increase in the size of the channels along the *c*-axis, which could significantly affect the ability of the barium hollandite structure to retain Cs cations in an aqueous environment.[71] The phenomena of radiation-induced volume expansion have been discovered for both the pyrochlore and zirconolite structures,[72] which also consist of TiO_6 octahedral networks.

1.3.3 Glass-ceramic Composite Wasteforms

Although many ceramic phases have demonstrated superior chemical durability to borosilicate glasses due to the structural advantages, the technology involving in the manufacture of ceramic phases is more complicated than that of glass production. Therefore,

producing glass composite materials (GCMs) offers a cheaper and easier way than ceramic preparation and also poses a better chemical durability than glasses.

GCMs can be fabricated in many different ways including the classic glass ceramic route. Glass ceramics are polycrystalline materials manufactured when glasses of suitable compositions undergo a controlled crystallisation by a specific heat treatment. They can be classified into two groups: spontaneously crystallised GCMs and induced crystalline GCMs.[3]

Spontaneously crystallised GCMs generally have coarse microstructure with large anisotropic crystal growing inwards from the surfaces of the glass, and their mechanical strengths are usually poor.

Induced crystallised GCMs are produced by introducing nucleating agents within the bulk of the glass. A large number of internal heterogeneities are provided and the major crystalline phase can form and grow. In this route, mechanically strong and fine-grained polycrystalline glass-ceramic materials can be obtained.[73]

To be a successful wasteform, glass-ceramics must be composed of durable glassy and crystalline phases. The long lived radionuclides (such as actinide species) are preferentially trapped in the more durable crystalline phase surrounded by a vitreous envelope which is used to accommodate the short lived radionuclides. The overall performance of the wasteform generally depends on the stability of the least durable component. It is important that the crystalline phases formed on devitrification do not contain too high a concentration of the glass-forming constituents, otherwise the remaining glassy phases may be unstable and exhibit poor leach resistance.[4]

Many glass-ceramic systems have been proposed for immobilisation of HLW, including barium aluminosilicate glass-ceramics, calcium magnesium silicate glass-ceramics, calcium titanium silicate glass-ceramics and phosphate glass-ceramics.[3, 46] Numerous studies have been performed on glass-ceramics containing Synroc phases, mainly zirconolite. Actinides, rare earth elements and some Sr are incorporated into zirconolite, and Cs and the remaining Sr into the vitreous phase. Basically the leach rates of actinides and rare earths are comparable to those in HLW glasses, but Cs leach rate is higher in about 2-3 orders of magnitudes. However, the problem of Cs leaching seems absent when glass-ceramics are used to immobilise separated actinides.

1.3.4 Cements

Major advantages of cement wasteforms include very simple production and relatively low cost of cementation technology. In addition, processing can be performed at low temperatures. However, cement wasteforms are mainly used to immobilise LLW and mixed waste rather than HLW. Cements contain high concentration of water and high levels of radioactivity will lead to radiolysis of the cement and hydrogen gas is then produced as a consequence of the breakdown of water or hydroxyl groups.[4] Many inactive constituents of waste streams can prevent the cement from hardening adequately. The microporous nature of cement and its alkaline character can lead to the precipitation of alkaline-insoluble waste species. These species are subsequently likely to be leached out of the cement by leachants of different pH.[3] The low chemical and radiation resistance of the cement wasteform has limited the use of cement for immobilisation of HLW.

1.3.5 Other Wasteforms

There are also various recently developed composite materials for HLW immobilisation, such as "Gubka"[74, 75] (or "sponge" in Russian), a open-cell porous crystalline matrix manufactured from hollow glass crystalline microspheres (cenospheres) recovered from fly ash, and bitumen wasteform, which is produced by simply mixing molten bitumen with processed liquid waste.[76-78] Their thermal/radiation/chemical stabilities have been studied for the candidates of HLW hosts.

1.4 Processing of Wasteforms

Processing of glasses, ceramics, or glass-ceramics wasteforms can be achieved in many different ways. A brief description of processing methods is given below.

1.4.1 Melting and Vitrification

Melting and vitrification is the most common method used for glass production.[4, 79, 80] Vitrification of radioactive wastes has been well-established and applied in industrial-scale plants. For simple pot vitrification, HLW is firstly evaporated to remove liquid and then mixed with glass frit at suitable proportions. The mixture is then fed and melted into a platinum crucible. In a modified pot vitrification processing, calcination of the HLW takes place prior to the vitrification stage. In a further modification of processing, a ceramic melter is employed. Volatilisation losses can thus be controlled to a minimum and fewer furnaces are contaminated.[3, 4, 78]

1.4.2 Powder Processing and Sintering

Conventional power methods involve preparing precursor materials by mechanical grinding and mixing. Sintering is generally considered as a physical process involving transport of matter by atomic diffusion or viscous flow in the case of glass production.[4] By carrying out powder processing and sintering, dense bodies at temperature far below the normal melting point of the main components can be achieved.[3, 4]

1.4.3 Sol-gel Processing

Compared with the traditional powder processing, wet chemistry routes, such as sol-gel method, have been shown to be a superior and efficient way in achieving homogeneous end products. Various glasses, ceramics and glass-ceramics can be successfully obtained using sol-gel processing. The sol-gel method can be conducted at low temperatures, which enables materials containing volatile elements to be prepared.[4]

1.4.4 Microwave Processing

Microwave processing has only been used in the last 20 years to produce ceramic products.[4, 78] Numerous materials including glasses, ceramics and composites have been successfully processed via microwave heating. Microwave processing provides rapid and uniform heat treatment throughout the body. Reduced time and temperature as well as a better control in microstructure can be achieved.

1.4.5 Hot Pressing

Hot pressing is the process of applying heat and pressure at the same time to the materials. In uniaxial hot pressing, pressure is applied to a sample contained in a mould via a punch, whilst in hot isostatic pressing (HIPing) the high pressure (usually inert gas) is applied in all directions to a sample contained in a can.[81] After hot pressing, internal pores and defects within a solid body collapse and weld up, as a consequence, a homogeneous material with a uniformed grain size and a nearly 100% density is achieved at lower temperature.[82, 83] Encapsulated powder and sintered components are densified and consolidated to give improved mechanical properties and a reduction in the scatter band of properties.[78, 82]

As HIPing applies pressure and heat to a sealed sample, notably no volatile radioactive discharge should take place in the consolidation step at high temperature, therefore HIPing shows great potential for the processing of HLW under flexible processing conditions. Due to the closed system, less secondary waste and off-gas emissions are generated. However, at HIPing conditions, the possible interactions between the wasteform and the container may in turn result in some detrimental effects on the quality of the wasteform.[66, 84, 85] As a result, the behaviours between wasteforms and have to be further investigated.

1.5 Scope of the Study

As Cs is one of the most troublesome species in HLW, an efficient way to separate Cs from wastes using inorganic ion exchangers has been employed. Among those ion exchangers, crystalline silicotitanate is one of the most promising materials for extracting Cs due to its excellent selectivity and wide working pH range in the presence of interfering ions. IONSIV®

IE-911, commercial Nb-substituted CST with $Zr(OH)_4$ as binder, has been applied in industry, however, the immobilisation of spent CST remains problematic.

Immobilisation of Cs by solid state sintering, vitrification and cementation has been studied previously. Nevertheless, solid state sintering requires relatively high temperatures, which can cause phase transformation or crystallisation and yield ceramics with considerable open porosity thereby reducing the chemical durability of the material, and further leading to Cs leaching.[86] Therefore, a more efficient method for densification and stabilisation of spent ion exchangers was required. Recently, HIPing has been proposed and exhibits the promise for immobilisation of HLW because a minimal enclosed porosity for the ceramic wasteform will be obtained.

The aim of this study is to develop an understanding on a potential ceramic wasteform manufactured by HIPing Cs-loaded IONSIV® IE-911 and CSTs, and also to access the feasibility of the wasteform in terms of long-tem behaviour. In this work, the methodology of synthesis/formation of the wasteform by HIPing as well as the subsequent physico-chemical characterisation will be discussed. From the particle viewpoint, two standard leach test methods, MCC-1 and PCT-B, were carried out to investigate the chemical durability of the wasteforms.

Chapter 2   Experimental

2.1 Synthesis

Throughout this project, three different synthesis routes were adopted for manufacturing materials. Crystalline silicotitanate ($Na_2Ti_2SiO_7 \cdot 2H_2O$, Na-CST) and partially niobium substituted CST (Na-Nb/CST) were both prepared hydrothermally using stainless steel autoclaves lined with a Teflon^{TM} reaction vessel. Powder samples of $Cs_2TiNb_6O_{18}$ were prepared using both solid state and sol-gel synthesis methods. $Cs_2ZrSi_6O_{15}$ and $Cs_2ZrSi_3O_9$ syntheses were carried out via sol-gel synthesis route.

2.1.1 Hydrothermal Synthesis

Hydrothermal synthesis involves heating aqueous solutions to high temperature (T > 25 °C) and autogenous water pressure (P > 100 kPa) to crystallise ceramic materials directly from solution. Crystals of good quality can be formed through hydrothermal synthesis, which involves H_2O as solvent. A highly pure and fine-grained powder with controlled morphology can be prepared by hydrothermal route.[87] For hydrothermal synthesis, starting materials with accurately known composition, good homogeneity and high purity are required. Syntheses are usually carried out at autogenous pressure, which corresponds to the saturated vapour pressure of the solution at the specified temperature and composition of the hydrothermal solution[88] Telfon^{TM} offers unique inertness and high temperature/pressure usefulness, which can often withstand pressures of up to 150 bar and temperatures of up to 270 °C, therefore it is an obvious choice as the material of construction for the liner.

Both Na-CST and Na-Nb/CST samples were synthesised hydrothermally using high pressure autoclaves. During the hydrothermal synthesis of CSTs, high alkalinity is critical for the formation of the correct structure. Hydrothermal experiments were generally carried out using acid digestion vessels (Parr, model 4749-23 mL capacity, 4744-45 mL capacity or 4748-125 mL capacity) with matched Teflon^{TM} liners. Detailed synthesis methodology is described in the following chapter.

2.1.2 Solid State Reactions

Solid state reaction is probably the oldest and still most commonly used synthetic method in solid state chemistry. It is a direct reaction of a mixture of solid starting materials with desired composition fired at high temperature. Solids do not usually react together at room temperature, therefore high temperature (often 1000-1500 °C) sintering is necessarily required for reaction to occur. This method is easy and the final product can be obtained directly, but sometimes a very high temperature is required to provide sufficient thermal energy for reactions. Also periodic grinding/sintering procedure is usually required because grain growth of both reactant and product phases may occur during heating, causing a reduction in the surface area of the mixture. Grinding maintains a high surface area and brings fresh surface into contact.

For synthesising a ceramic containing a volatile element, such as Cs, a solid state reaction is achievable but may not be ideal. A sol-gel method was therefore used to synthesise materials of Cs-rich materials, such as $Cs_2TiNb_6O_{18}$, $Cs_2ZrSi_6O_{15}$ and $Cs_2ZrSi_3O_9$.

2.1.3 Sol-gel Method

The sol-gel method has been extensively used in the field of materials science for its advantages such as the ease of forming a variety of structures, products of high purity and homogeneity, and low processing temperature. Broadly speaking, sol-gel is the synthesis of ceramic materials by preparing a sol, gelation of the sol, removal of the solvent and then a firing at a suitable temperature.[89]

A sol is the colloidal suspension of metal oxides particles precipitated from a molecular precursor, which is usually metal alkoxide, in the solution. An organic solvent, such as ethanol, is usually used in sol-gel synthesis to increase the homogeneity of the solution. The sol is then destabilised and gelation involving hydrolysis-condensation reactions of alkoxides is initiated by aggregation, forming a rigid network: a gel. At gelation, the chemical reactions may not be completed; therefore aging is usually required to reinforce the network. The gel is porous after drying and it allows a lower firing temperature and/or shorter heating duration to be used than that in solid state reactions. The lower firing temperature of sol-gel derived materials can also be important in compositions which undergo undesired phase transitions or have volatile components.

The sol-gel method is considered a better route for synthesising Cs-rich phases due to the high volatility of Cs. In addition, it is better than solid state reactions for the desired Cs-Zr-Si phase synthesis because the reactants used in solid state reactions, such as ZrO_2 and SiO_2, barely react even at high temperatures. The sol-gel method used in this study is based on the procedure reported by Balmer et al.[90]. Starting materials and compositions are modified for synthesising different Cs-phases.

2.2 Crystallography and Diffraction

2.2.1 Fundamentals of Crystallography

Crystals are solids where the atoms possess a regular arrangement with respect to each other. Ideally, the arrangement is repeating and the smallest repeating unit, containing all necessary symmetry, is called the unit cell. Unit cells can be stacked to generate a lattice via translations and show the full symmetry of the crystal structure. The lengths of the unit cell edges are written as *a*, *b* and *c*, and the angles between the unit cell edges are written as α, β and γ. Those collected values for a crystal structure are termed the unit cell or lattice parameters. By having one or more relationships between these lattice parameters, seven crystal systems - triclinic, monoclinic, orthorhombic, tetragonal, trigonal, hexagonal and cubic - are derived in three dimensions.

By combining one of the seven crystal systems with one of the lattice centerings, such as primitive (*P*), body-centred (*I*) or face-centred (*F*), a total of 14 lattice types are generated, also known as the Bravais lattices (shown in Figure 2.1). The Bravais lattices describe the geometrical arrangement of the lattice points and therefore the translational symmetry of the crystal. Each Bravais lattice refers to a distinct lattice type.

With the addition of atoms to the unit cell, there are supplementary symmetry elements that need to be considered in three dimensions. They are point symmetry elements (centres of symmetry, mirror planes and inversion axes) to describe the symmetry of the three dimensional motif, and also translational symmetry elements (glide planes and screw axes) to describe all the possible patterns which arise by combining motifs of different symmetries with their appropriate lattices. A combination of the 14 Bravais lattices with the 32

crystallographic point groups, gives 230 three-dimensional repeating crystallographic patterns classified as space groups.
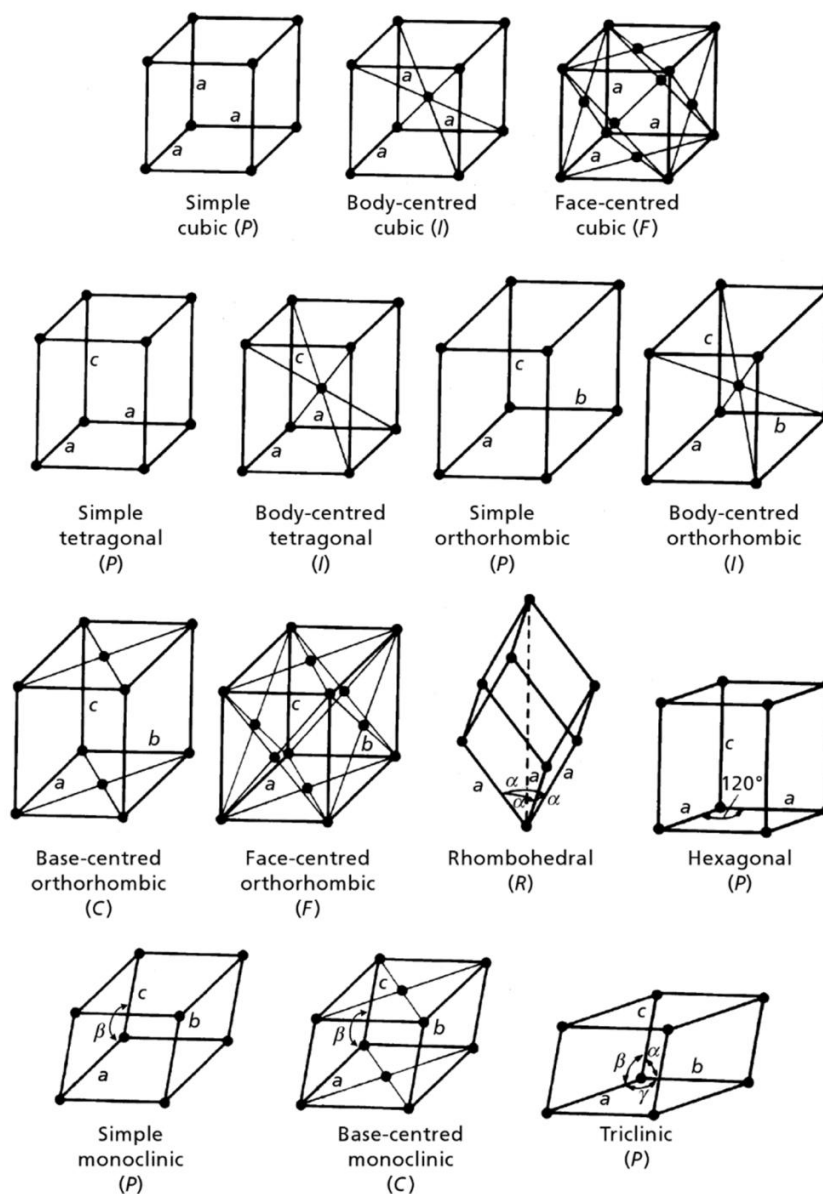
Figure 2.1 Fourteen Bravais lattice. Adopted from reference [91].

Any three-dimensional crystal unit cell must have an internal symmetry that corresponds to one of the 230 crystallographic space groups. Crystals could always be described as a series of lattice planes. Each plane is given a set of three integers, the reciprocals of the fractional

intercepts which the plane makes with the crystallographic axes, referred to as Miller indices and labelled as (*hkl*) for the plane. Some of the planes will be equivalent to others depends on the symmetry, for example, (100), (010) and (001) planes in cubic system. A family of those equivalent lattice planes are parallel to each other and separated by a fixed translation distance (defined as d_{hkl}) in a direction perpendicular to the plane.

2.2.2 Diffraction

When X-rays or neutrons encounter a crystal with a set of parallel lattice planes at an angle θ, they are scattered with an angle of reflection also equal to θ. The diffracted beams are found to occur when the reflections from planes of atoms interfere constructively, giving the path length difference ($\overline{AB}+\overline{BC}$) equal to an integer number of wavelengths, as illustrated in Figure 2.2. It means that the two reflected beams are in phase and satisfy Bragg's law:

$$n \cdot \lambda = 2d_{hkl} \cdot \sin\theta$$

Equation 2-1 Bragg's law

Lattice planes where the constructive interferences occur produce a peak in the intensity of the reflected beams detected for each value of 2θ. The condition for maximum intensity created by a set of reflections at a characteristic d_{hkl} (or θ_{hkl}) allows us to characterise the crystal structure.
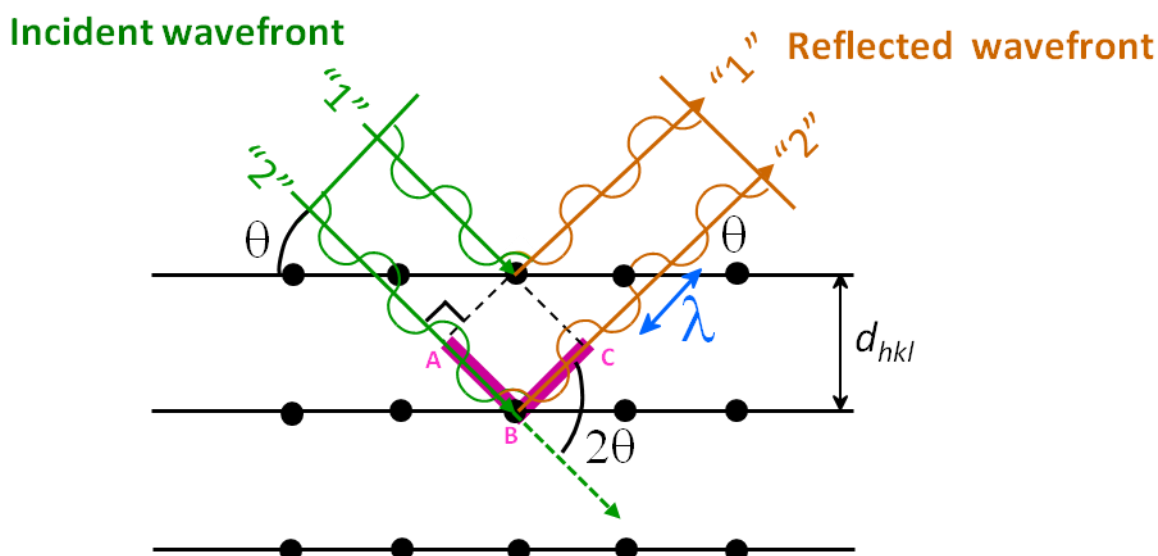
Figure 2.2 Schematic representation of Bragg's Law

2.3 X-ray Diffraction

X-ray crystallography has been of major importance in material science. X-rays have the wavelengths equivalent to the interatomic distances and hence they will interact with a solid specimen when they pass through it. Therefore X-ray diffraction provides the ideal means to understand structures of the materials on an atomic scale. It thus establishes relationships between the crystal structure and the physical/chemical properties of the material.

2.3.1 Generation of the X-rays

X-ray sources

In a conventional X-ray instrumentation, the X-ray beam is generated within an "X-ray tube". The X-ray tube consists of a tungsten filament (cathode) and a water-cooled material

(anode) in vacuum environment. A large voltage difference (usually ~ 40 kV) generated between the filament and target accelerates the electrons in the direction towards the target material, as shown in Figure 2.3. Some of the accelerated electrons hit the target material and ionise the electrons from the inner shell of the metal target, leaving vacancies in the orbitals. Electrons with higher energy therefore jump from outer shell and fill the vacancies. Upon relaxation, these transitions within the atoms lead to the emission of radiation of characteristic wavelengths. Only a small proportion of their energy is radiated in the form of X-rays, the majority ends up in the form of heat. The radiation is dependent on the target material and is consequently called "characteristic radiation". For example, if an electron within the target material drops from the *L* shell to a *K* shell, K_α radiation emits. K_β irradiates when electron drops from *M* to *K* shell. For copper, the most common target material, K_α has an average wavelength of 1.5418 Å, and K_β 1.3922 Å.

The other way of X-ray generation is from Bremsstrahlung. The abrupt acceleration of the electrons when in contact with the metal target results in energy loss and is in turn converted into electromagnetic photons called Bremsstrahlung, also known as white radiation. X-ray radiation generated via deceleration has a continuous spectrum.

X-rays that are generated from both transitions to the *K* shell and the Bremsstrahlung contribute to the spectrum showing discrete wavelength radiation characteristic of the metal target as well as a continuous background spectrum. Once generated, the X-rays leave the tube through beryllium windows. Be is essentially invisible to X-rays due to the low atomic number. The use of Be windows allows the X-rays to emit whilst maintaining the vacuum inside the X-ray tube.
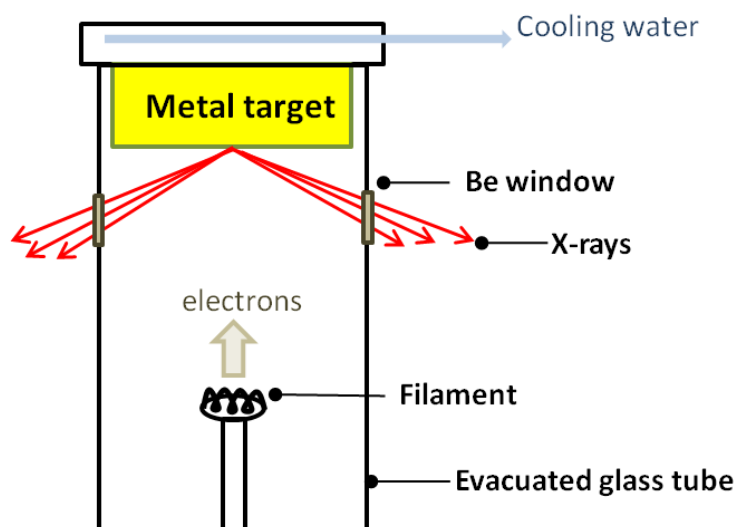
Figure 2.3 Schematic representation of an X-ray tube

Filter and monochromator

A single intense wavelength of radiation is required for X-ray diffraction. For every target material, there exists a chemical element whose absorption edge falls just between the K_α and K_β of the target material. Therefore, the element can function as a filter. Normally, a Zr-filter is used for Mo-target material, and a Ni-filter is used for Cu-target material. However, a loss in intensity is inevitable.

Alternatively, single crystal monochromators which are set at specific angles and typically made from silicon, quartz or germanium, are used to remove unwanted wavelength and produce monochromatic radiation. When a white beam hits a crystal, the desired wavelength of diffracted radiation which satisfies Bragg's law can be selected.

Detectors

The most common detectors to measure the intensities of X-rays are scintillation counters. It is a phosphor which can convert X-ray photons to light. The emitted light photons, which are proportional to the number of X-rays, are converted to voltage pulses by a photo multiplier tube. To shorten the data collection time, position sensitive detectors (PSD) are commonly used. PSD simultaneously measures diffracted intensity at all angles, resulting in rapid collection of diffraction patterns.

2.3.2 Powder Diffraction

Powders can be regarded as a polycrystalline mass with a large number of crystallites in random orientations. One or more crystallites will be oriented so that their (*hkl*) planes follow Bragg's law. Each of the crystallites diffracts X-ray beam independently, and the diffracted beams which have the same *d*-spacing are distributed over cones (so called Debye-Scherrer cones), as shown in Figure 2.4. These cones are recorded by detectors such as proportional or scintillation counters in modern X-ray techniques, giving a series of peaks.[92] The combination of the unique set of angles (θ) at which a powder reflects X-rays and the corresponding intensities, yields a fingerprint which can be used to identify the crystal structure. A powder diffraction pattern contains several elements, such as background, peak shape, peak position and peak intensity, showing the information of structure. The amount of information which can be extracted from a powder diffraction pattern is summarised in Table 2-1.
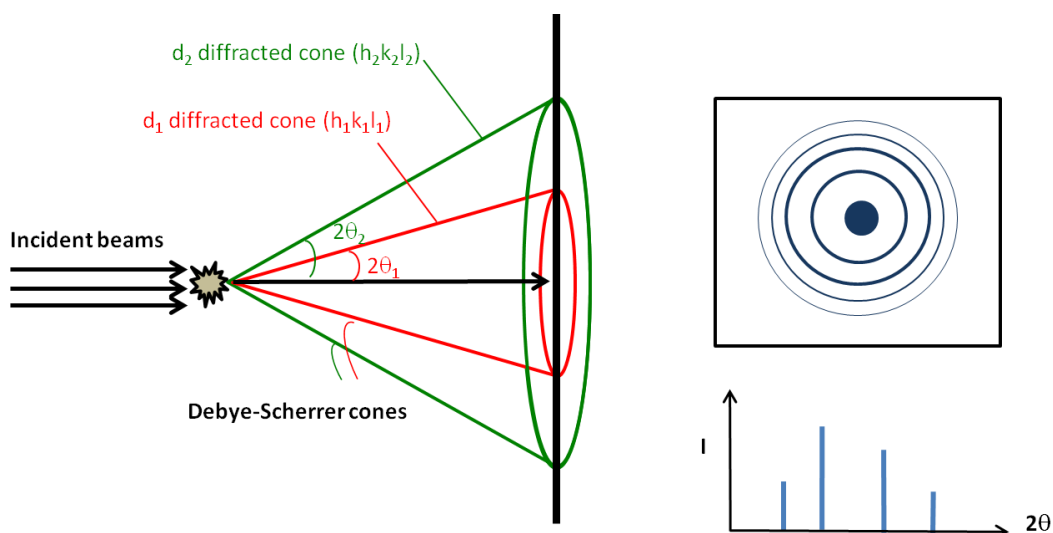
Figure 2.4 Schematic diagram of the generation of Debye-Scherrer cones

Table 2-1 Information content of a powder pattern

Feature	Information obtained
Background	• Amorphous fraction • Incoherent scattering • Absorption • Contribution from sample holder or sample preparation
Peak positions (2θ values)	• Lattice parameters • Space group • Symmetry • Zero point • Sample height • Wavelength
Non-indexable lines	• Presence of a crystalline impurity
Peak intensities	• Atomic positions • Preferred orientation • Occupancies (disorder) • Thermal vibrations • Phase fractions
Width of peaks (FWHM)	• Crystallite size • Crystallinity • Strain • Stress • Instrument functions
Peak shapes (other than widths)	• Stacking faults • Layer defects

2.3.3 Laboratory Diffractometers

With a fixed wavelength, laboratory powder X-ray diffraction data are collected using either transmission or reflection geometry (shown in Figure 2.5) as a function of increasing angle (θ). Basically, if the crystallites in the powder sample are randomly oriented, these two methods will yield the same data. In comparison, transmission mode is best for samples with low absorption. Furthermore, air sensitive samples or suspensions can be filled in capillaries and analysed in transmission mode. In reflection mode a flat sample surface is required and it is best for analysing strongly absorbing samples. For in-situ investigations, such as variable temperature studies, reflection mode is more easily adapted.
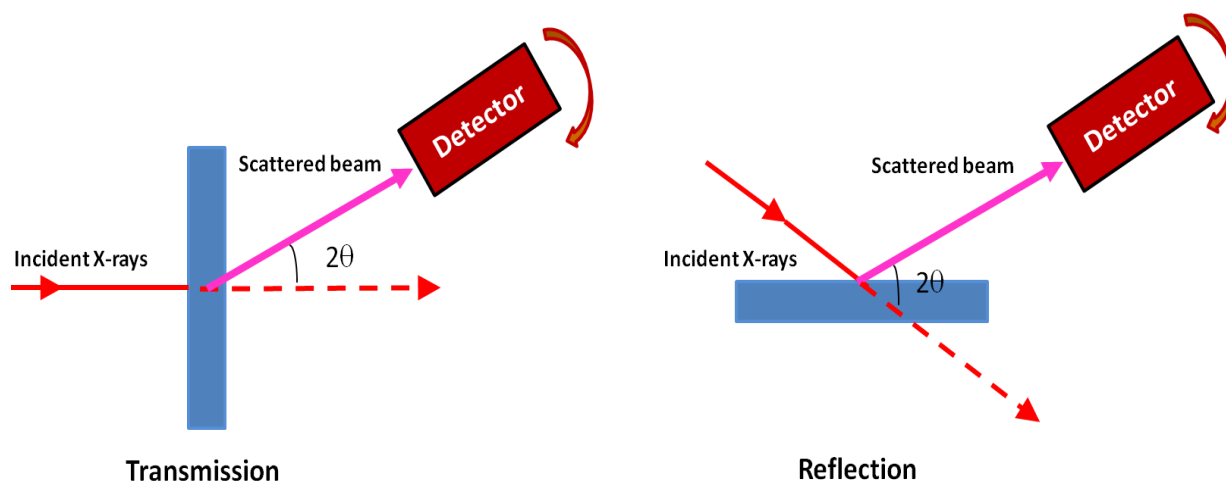
Figure 2.5 Diffractometer geometries

In this work, most of the powder diffraction data were measured using a Bruker D8 diffractometer in transmission mode. A copper X-ray source was monochromated using a germanium crystal monochromator to give Cu $K_{\alpha1}$ radiation at a wavelength of 1.5406 Å. Samples were prepared by grinding in a pestle and mortar and mounting onto Scotch™ "Magic Tape". The magic tape gives very little scattering compared to the crystalline samples.

The samples were rotated throughout data collection and a diffraction pattern was produced electronically.

Variable temperature studies were carried out on a Bruker D8 diffractometer (reflection mode) equipped with a MRI heating stage. Desired temperatures were programmed and 10 mins of dead time for equilibrating the temperature was setup between every analysis. This diffractometer is also equipped with a germanium crystal monochromator to produce Cu $K_{\alpha 1}$ radiation at a wavelength of 1.5406 Å.

2.3.4 Synchrotron X-ray Diffraction

When electrons are accelerated at relativistic velocities in circular orbits, as velocities approach the speed of light they emit electromagnetic radiation in the X-ray region, so called synchrotron X-rays. The light is channelled down beamlines to experimental workstations where it is used for research. Synchrotron X-rays have played an important role in materials science due to features such as high intensity, excellent vertical collimation and a range of wavelengths. High resolution, combined with high signal to noise and high X-ray photon flux rate, provides improved accuracy in structure solution, phase identification, quantitative analysis and rapid data acquisition.

Synchrotron data were collected at station I11, Diamond Light Source, UK. Samples were firmly packed into glass capillaries (0.5 mm in diameter) and sealed. The sealed capillaries were fixed onto magnetic holders and pre-aligned before mounting onto a sample spinner, thus reducing any preferred orientation effects. The exact wavelength of the radiation used was determined from silicon standards, but was typically set at ca. 0.83 Å.

2.4 Neutron Diffraction

Neutrons penetrate considerable distances into a solid and only interact with the massive nucleus. Neutrons are diffracted following Bragg's law, and the intensities of diffracted beams can be calculated in a similar way to that used for X-ray beams. However, neutron diffraction has several characteristic differences with X-ray diffraction. Unlike X-rays, which are scattered entirely by electrons of atoms, neutrons scatter from the materials by interacting with the atomic nuclei in the sample. The scattering length differs from isotope to isotope rather than linearly with the atomic number, therefore neutron diffraction studies offer several advantages over X-rays. Firstly, it is easier to determine the location of light elements in the presence of heavier atoms. The intensity of X-ray scattering from lighter atoms is relatively low and can be concealed by that from heavier elements. Therefore, neutron diffraction provides a more precise determination for light elements. Secondly, neutron has an intrinsic magnetic moment and it interacts strongly with atoms and ions in the crystals which also have magnetic moments. As a result, neutrons are an important tool in investigating magnetic ordering in some materials.

Additionally, it also enables to distinguish certain neighbouring elements in the periodic table. Neighbouring elements have similar number of electrons and are difficult to distinguish using X-ray methods, however, some of the neighbouring elements exhibit substantially different neutron scattering and can be examined in neutron diffraction.

Furthermore, it is of importance to study structural disorder using neutron diffraction. For some cases, different elements simultaneously occupy one position resulting in a mixed occupancy. Untangling the ordering of these cations using X-rays can only be achieved indirectly by the analysis of bond lengths, but these are not definitive since bond lengths are

affected by factors other than the specific site occupancy. Neutron diffraction allows the direct determination of their site occupancies and order-disorder distributions.[93]

Typically, neutrons are produced in two different ways. The first one is reactor source, the fission of radioactive nuclei that leads to a chain reaction moderated by heavy water producing a continuous beam of high velocity neutrons. The energy (wavelength) of neutrons is controlled by the temperature of the moderating medium.

The other neutron source is produced by spallation, a process in which a heavy metal target is bombarded with high energy protons generating a pulsed neutron beam. The target breaks down with the emission of multiple neutrons. In this work, GEM, the neutron diffractometer at ISIS, uses spallation source.[94] The geometry of GEM is also shown in Figure 2.6.
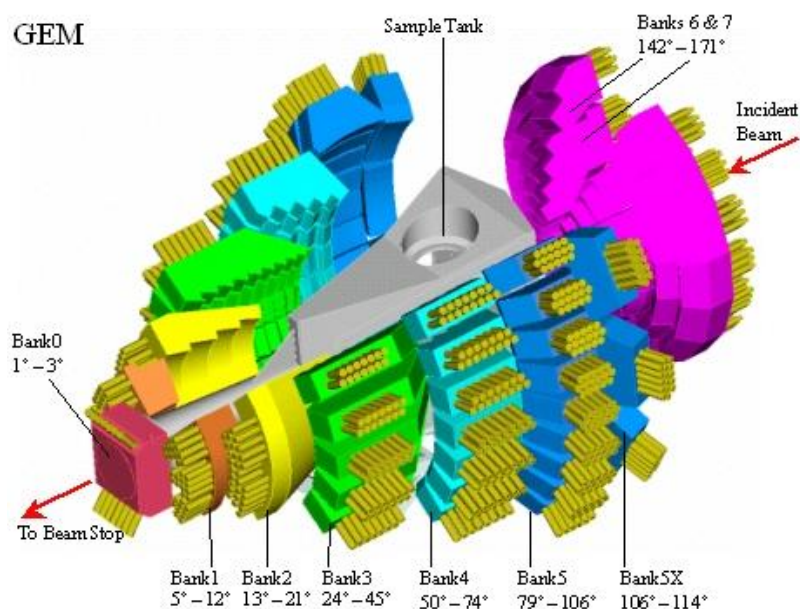
Figure 2.6 Schematic diagram illustrating the layout of the general materials powder diffractometer (GEM) at ISIS.[95]

Neutrons produced by spallation are commonly utilised in time of flight (TOF) techniques. TOF experiments use diffraction from a range of wavelengths of the neutrons and detectors at fixed angles (θ), and a known distance from the sample. The geometry of TOF technique is illustrated in Figure 2.7. The time of flight (*t*) of a measured Bragg reflection is related to its *d*-spacing, and an approximate value can be calculated combining Bragg's Law with the de Broglie relationship and the associated knowledge of the total flight of length (*L*) and scattering angle, 2θ, of a detector (Equation 2-2) to yield the expression (Equation 2-3).

$$\lambda = \frac{h}{mv} = \frac{h}{m}\frac{t}{L}$$

Equation 2-2

$$t = \left(\frac{2m}{h}\right) L \times sin\theta_d \times d_{hkl}$$

Equation 2-3

where *h* is Planck's constant, m is the neutron mass, *t* is the total time of flight, *L* is the total flight path from moderator to sample to detector, d_{hkl} is the lattice *d*-spacing for reflection *(hkl)*, and θ_d is half the Bragg scattering angle ($2\theta_d$).

Thus, the intensity of diffracted neutrons is then recorded as a function of the time of flight, as the Equation 2-4. (The unit of t_{hkl} is in ms, *L* in m and d_{hkl} in Å)

$$t_{hkl} = 505.56 \times L \times sin\theta_d \times d_{hkl}$$

Equation 2-4
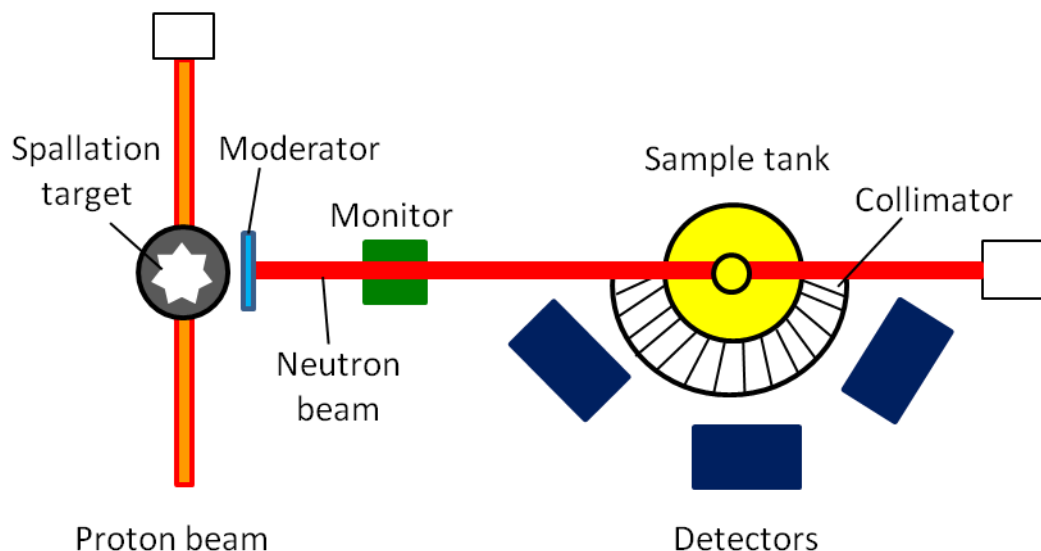
Figure 2.7 Geometry of time of flight (TOF) neutron diffraction

For this work, neutron diffraction was used to complement XRPD of $Cs_2TiNb_6O_{18}$ and to give further structural information to determine Ti/Nb cation disorder. The technique is extremely sensitive to the presence of Ti because of the negative neutron scattering length of Ti (-3.438 fm) compared with the positive scattering length of Nb (7.054 fm) present in the material.[96]

2.5 Rietveld Refinement

The Rietveld method[97-99] is a "whole-pattern-fitting" strategy to refine powder diffraction data to obtain an accurate crystal structure. The basic concept is the calculation of the entire powder pattern using a variety of different refineable parameters. To start a Rietveld refinement, a crystallographic model containing lattice parameters, space group and atomic positions, as well as instrument parameters, such as wavelength, is required. The model is

then refined by varying a number of parameters and the difference between calculated and experimental data is minimised using least square methods, illustrated as Equation 2-5.

$$S_y = \sum_j w_i(y_i - y_{ci})^2$$

Equation 2-5 Residual

Where S_y is the residual, w_i is weighting factor and equal to $1/y_i$, y_i is the observed intensity at the ith step, and y_{ci} is the calculated intensity at the ith step.

The calculated intensity can be expressed as Equation 2-6.

$$y_{ci} = S \sum_j L_{(hkl)} |F_{(hkl)}|^2 \phi_i(2\theta_i - 2\theta_k)P_{(hkl)}A + y_{bi}$$

Equation 2-6 Intensities

where **S** is the scale factor,

$L_{(hkl)}$ is Lorentz, polarization and multiplicity factors,

Φ_ι is the reflection profile function,

$2\theta_i$ is 2θ position of the ith profile point in the diffraction pattern,

$2\theta_k$ is the calculated 2θ position of the kth reflection,

$P_{(hkl)}$ is the preferred orientation function,

A is the absorption factor,

$F_{(hkl)}$ is the structure factor, and

y_{bi} is background intensity represents the miller indices *(hkl)* for a Bragg reflection at the ith step.

Many different statistical agreement factors have been used for judging the quality of a Rietveld refinement. The most common ones are so called weighted profile R-factor (R_{wp}) which is defined by Equation 2-7,

$$R_{wp} = \sqrt{\frac{\sum w_i(y_i - y_{ci})^2}{\sum w_i(y_i)^2}}$$

Equation 2-7 R_{wp}

R-pattern (R_p) which is defined by Equation 2-8,

$$R_p = \frac{\sum|y_i - y_{ci}|}{\sum y_i}$$

Equation 2-8 R_p

and R-expected (R_e) which is defined as Equation 2-9.

$$R_e = \sqrt{\frac{(N - P - C)}{\sum w_i(y_i)^2}}$$

Equation 2-9 R_e

Where w_i is weighting factor,

y_i is the observed intensity,

y_{ci} is the calculated intensity,

N is the number of observables,

P is the number of refined parameters, and

C is the number of constrains used.

43

Combining R_{wp} and R_e gives the "goodness of fit" value, χ^2, which is ideally equal to one in a perfect refinement; however, in reality this is not possibly achieved. Apart from those numerical indicators, the quality of fitting can also be assessed by inspecting the calculated atomic bond distances, angles and fractional occupancies.

A large number of Rietveld programs are available, such as General Structure Analysis System (GSAS), Fullprof, and the commercially available Topas. These programs have similar capabilities with individual strengths. All Rietveld refinements in this work were performed using the EXPGUI GSAS[100] software suite.

2.6 Bond Valence Sum

Once a satisfactory refinement has been achieved, a valence sum calculation can be carried out for validating the determined structures, geometry and properties of a compound. The valence of a bond (s) relates empirically with the bond lengths (R) and nature of the atoms around it. Given the length of a particular bond, the bond valence is calculated based on the relationship shown in Equation 2-10.[101]

$$s = e^{\frac{(R_0 - R)}{b}}$$

Equation 2-10 Valence of a bond

where R_0 and b are bond valence parameters corresponding to the pair of ions forming the bond. Bond valence parameters are mostly taken from a table[102, 103] which covers the most commonly encountered bonds, chiefly bonds to oxygen. The value of b is found to lie between 0.3 and 0.6 Å but because of the limited range of experimental bond lengths its

precise value is not easy to determine. For this reason a value of 0.37 Å is frequently assumed.[104]

The bond valence is equal to three different quantities: the number of electrons each atom contributes to the bond, the number of electron pairs that form the bond and the electrostatic flux linking each core to the bonding electron pair.[101] The sum of these bonds (bond valence sum, BVS), as expressed in Equation 2-11, should be equal to the formal oxidation state of the cation or anion respectively. Thus, BVS theory can then be used to check if the structure is chemically valid. Theoretical bond valence calculation is easy to perform, however, it can only be used where electronic or steric effects are absent. Structural determination should be carefully examined if any poor agreement between bond valence sum and the atomic valence is noticed. Agreement may originate from the use of an incorrect space group, or some missing bonds or atoms.[105]

$$V_j = \sum_i S_{ij}$$

Equation 2-11 Valence sum

2.7 Electron Microscopy

Electron microscopy has greater resolving powder than optical microscopy and has been widely used for examining the microstructure of materials. Quantitative analysis can be also achieved simultaneously. The use of electron microscopy with quantitative analysis for characterisation has shown its importance in materials science.

2.7.1 SEM/EDX

Scanning electron microscopy (SEM) has been widely applied for observations of specimen surfaces and microstructures. When the electron beam, also called electron probe, strikes a specimen, interactions between the incident electrons and the constituent elements in the specimen produce various signals emitted from the surface, as shown in Figure 2.8. Those signals are used to convey different types of information about the specimen.
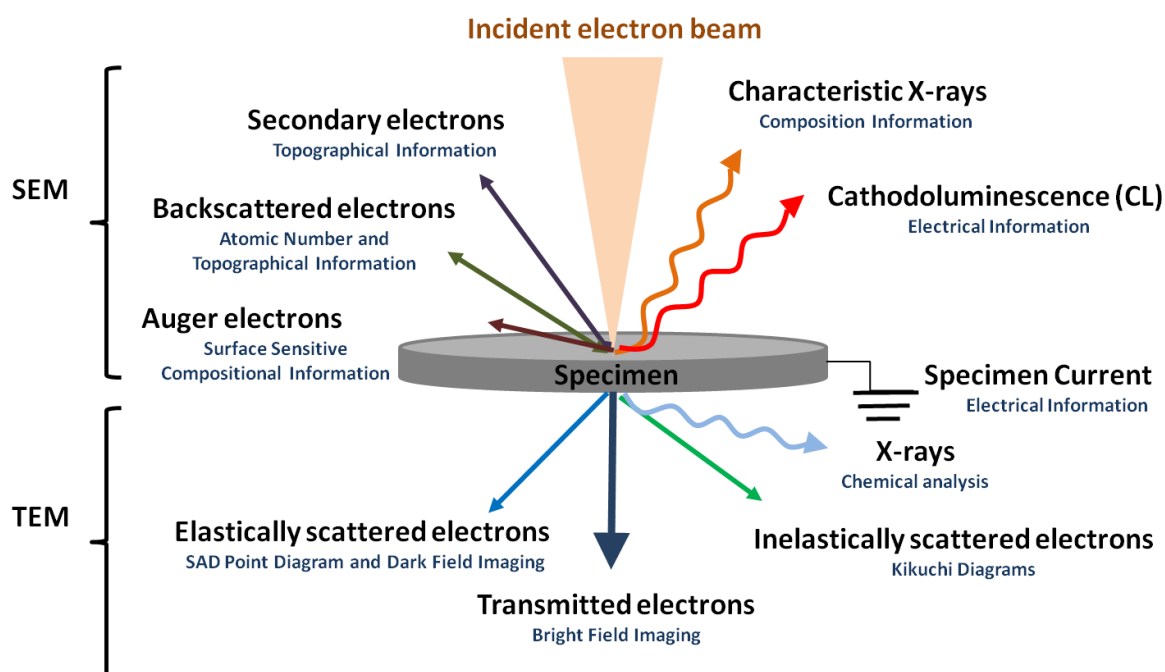
Figure 2.8 Emission of various signals when a specimen is irradiated by incident electron beam

The topography of the surface, i.e. surface texture and roughness, can be observed by two dimensional scanning of the electron beam over the surface and acquisition of an image using secondary electron signals. Secondary electrons are produced from the emission of the loosely bound electrons of the constituent atoms in the specimen. Since the energy of secondary

electrons is very small, only those generated at the top surface of the specimen are emitted and received by the detector, as shown in Figure 2.9, meaning this detection is very surface sensitive. In addition, the signal is also sensitive to the incident angle of the probe. When the specimen surface is perpendicular to the beam, the amount of electrons emitted from secondary electron diffusion area is smaller than that when the surface is titled, as seen in Figure 2.10. The difference of the incident angle of roughness results in the difference in the brightness in the secondary image.
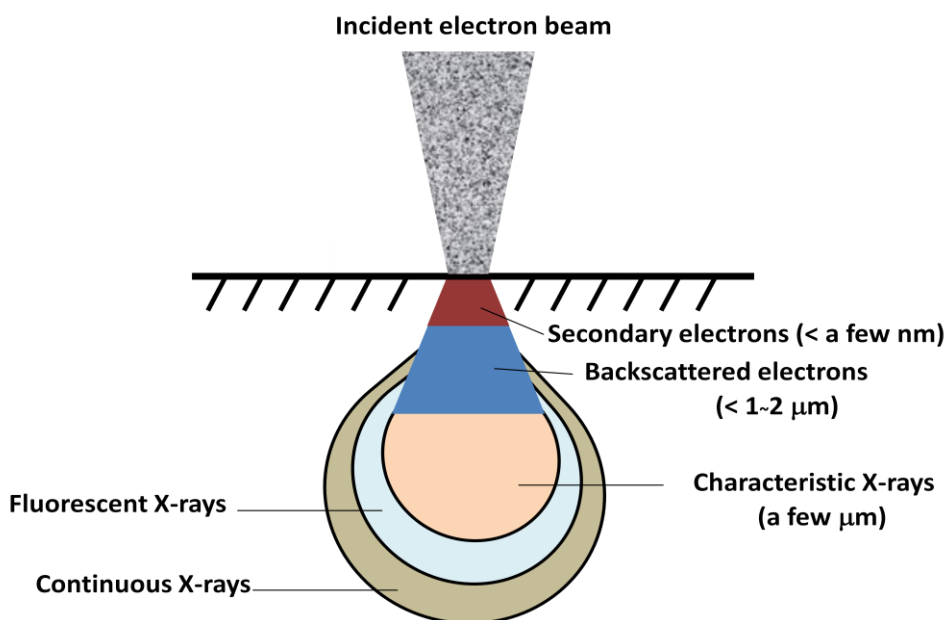
Figure 2.9 Schematic diagram of interaction region with different electron
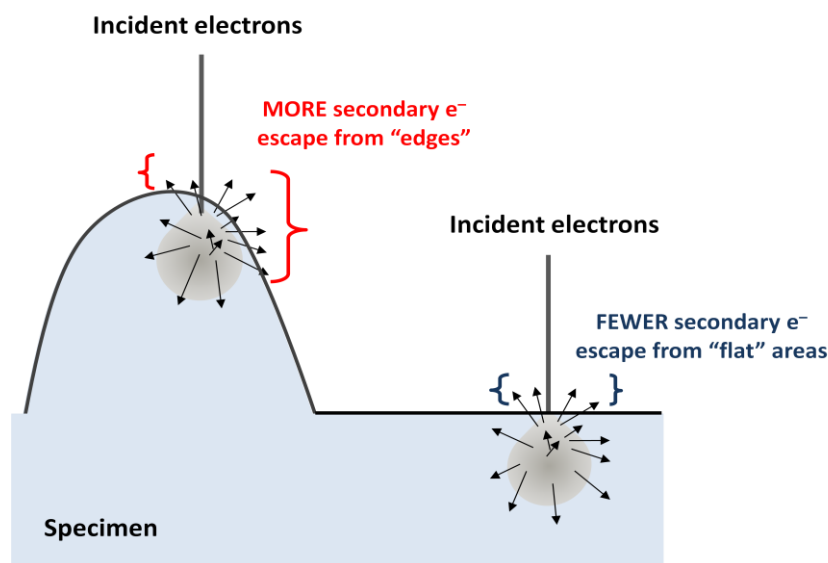
Figure 2.10 Relation between the incident angle of the electron beam and the secondary electron yield

In order to gain a better resolution in a SEM image, a conductive sample is required therefore coating is usually applied to increase the generation of secondary electrons. Carbon coating was selected in this study because of its low cost, good conductivity, and most importantly, low X-ray absorbance due to its low atomic number. Other coating materials such as Au, Pt, Au-Pd and Al are available according to the purposes.

The other image system can be obtained using backscattering electrons (BSE, also called reflection electrons). BSE are those produced by the elastic interactions between the specimen and incident beam. Backscattering electrons have higher energy than secondary electrons, therefore information from a relatively deep region is contained, as shown in Figure 2.9.

BSE are sensitive to the composition of the specimen. The constituent atoms with larger atomic number have a higher probability of producing BSE because of their greater cross-sectional area. Thus, an area that consists of heavy elements appears bright contrast in the

BSE image. This feature is suitable for observing the element distribution or compositional differences.

Furthermore, surface irregularity is also a factor contributing the brightness in a BSE image. As shown in Figure 2.11, the intensity of BSE becomes higher in the direction of specimen reflection, resulting in the higher brightness in BSE image. Therefore, a polished specimen is required to eliminate the error caused by surface roughness.[106]
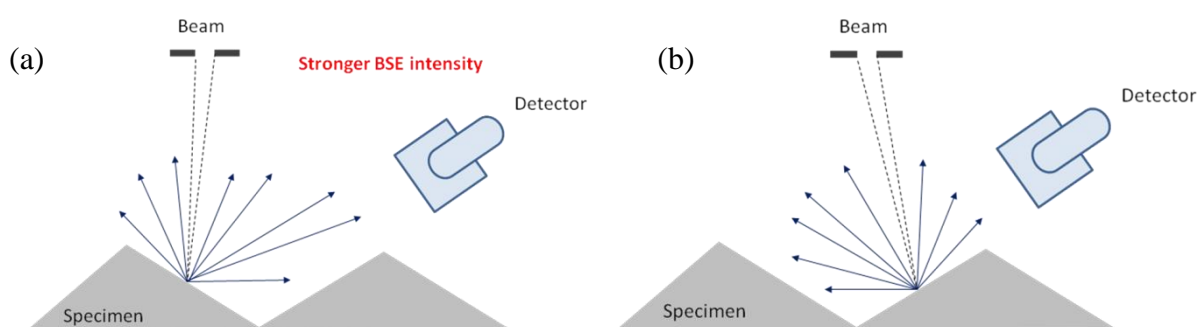
Figure 2.11 Relation between the electron beam incident angle and the BSE intensity. Surface (a) shows brighter than surface (b) in BSE mode.

The other reason to prepare a flat sample is to gain a more accurate elemental analysis using energy dispersive X-ray detector (EDX). Characteristic X-rays are also one of the signals generated as a consequence of electron bombardment. Each element has a characteristic spectrum, and an energy/wavelength dispersive spectrometer detects X-rays as a function of the intensity and energy. As a result, EDX analysis can provide the elemental information and a semi-quantitative estimation in weight concentration. A wide range of elements from B to U can be analysed in-situ in SEM.

However, the X-ray generation area has a certain size and this is of the order of microns in normal operation conditions. This means an actual analysis area becomes fairly wide when an observation on a sub-micrometer particle is performed. Although reducing accelerating voltage decreases the analysis area, there is a limit in choosing a suitable accelerating voltage because accelerating voltage must be higher than that of the characteristic X-ray to be excited. The best policy is to prepare a thin film with a thickness of ~ 100 nm for EDX analysis.

When a quantitative analysis is carried out, the weight fraction of a certain element in an unknown specimen can be obtained by comparing the X-ray intensities of the certain element between the standard and unknown specimens. However, X-rays that generated in the specimen may be absorbed in the specimen or excite the X-rays from other elements before they are emitted in vacuum. Thus, quantitative correction is needed. To do the correction in the present EDX, a specimen with homogeneous elemental distribution and flat surface as well as the perpendicular electron beam to the specimen is required. Otherwise a quantitative analysis result might have appreciable errors.[107]

2.7.2 TEM

As shown in Figure 2.8, TEM utilises three different interactions between electron beam and specimen, transmitted beam (unscattered electrons), diffracted beam (elastically scattered electrons) and inelastically scattered electrons, for characterising the microstructure or crystallography of a material. By selecting the different types of electrons and adjusting the apertures, different types of images are obtained in TEM. Some analysis systems in the TEM used or attempted to use in the study are summarised.

Bright field imaging

When a high energy electron beam enters through a thin specimen without any interaction inside the sample, these transmitted electrons are inversely proportional to the specimen thickness. In the mass-thickness contrast mechanism, regions where electrons are scattered will appear dark in the image. Thicker areas (or regions with a higher atomic number) of the sample scatter more electrons than thinner (or regions with a lower atomic number). Therefore fewer electrons from the thick area are transmitted onto the screen, so the region appears darker in a bright field image.

Diffraction

TEM uses the elastically scattered electrons to show the diffraction patterns originating from the sample, illustrating the crystallographic information of the material. For example, distinguished dots in diffraction patterns indicate monocrystal materials, centred circles indicate polycrystalline materials and diffused circles indicate amorphous materials. All electrons are scattered following Bragg's law (Equation 2-1).

All incident electrons have the same energy/wavelength and enter the specimen, those are scattered by the same atomic spacing (a plane) will be scattered by the same angle. These scattered electrons can be collated to form a spot pattern. In the modern TEMs the users are able to tilt the specimen holders in order to obtain specific diffraction conditions. The apertures placed above the specimen also allow the user to choose the electrons that would otherwise be diffracted in a certain direction from entering the specimen. This diffraction pattern can then produce the information regarding the orientation, atomic arrangements and phases present in the examined area.

Elemental composition

The energy dispersive X-ray detector (EDX) in TEM works in the same manner as in SEM. Analysis in the TEM can be performed on very small areas due to very small interaction volume ($\sim 10^{-8}$ μm^3 for a FEG TEM) compared to that in SEM (~ 1 μm^3 from a 0.1 μm probe size) and the chemical analysis of interests with less bulk materials around can be acquired. A higher spatial resolution can be achieved in TEM due to a very weak beam broadening resulting from a small beam diameter ($\sim$ nm).

2.8 X-ray Fluorescence Spectroscopy (XRF)

XRF is one of the widely used qualitative and quantitative techniques for elemental analysis. The XRF principle is illustrated in Figure 2.12. When a specimen is subject to a primary X-ray beam, the X-rays react with the sample and excite an inner shell electron. During the relaxation process, an electron with higher energy moves and fills the vacancy created by the ejection and the excess energy releases in the form of fluorescent X-rays.

The spectrum of fluorescence reveals a number of characteristic peaks which are proportional to the concentration of the various elements in the sample, providing the elemental composition in a straightforward way. Fluorescence can be analysed using two systems, WDXRF (wavelength dispersive) which physically separates the X-rays according to their wavelengths or EDXRF (energy dispersive) which directly measures the different energies of the emitted X-rays from the sample. In WDXRF system, a parallel beam of X-rays selected by collimators is directed to a crystal, which diffracts the X-rays in different directions according to their wavelengths (energies). A better working resolution, improved sensitivity and detection limits can be achieved in WDXRF system. In this work,

measurements were carried out on a Bruker S8 high end wavelength dispersive X-ray fluorescence (WDXRF) spectrometer. Spectra plus software was used for the data analysis.
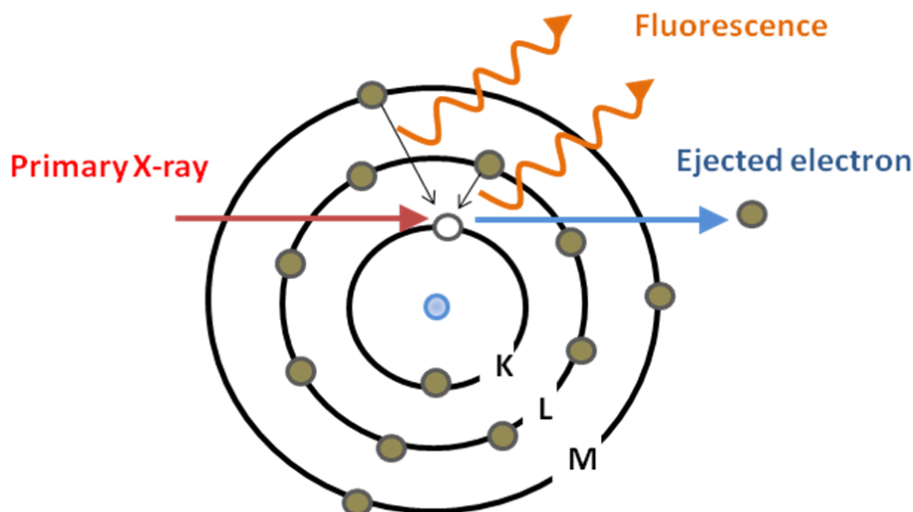
Figure 2.12 Generation of XRF by photoelectric effect

Various types of sample can be run in XRF. The simplest way to prepare a specimen is to press the powder into a pellet with or without binder. The binder must be stable under X-ray irradiation conditions, have low absorption and not introduce inter-element interferences. Wax is proven useful and successful as a binding material in XRF sample preparation. However, factors such as inhomogeneity and coarse particle size produce noticeable systematic errors in XRF analysis. To eliminate these effects, a better sample preparation is required.

Fused beads can be obtained by a dissolution or decomposition of material at high-temperatures in the presence of a fluxing compound as a solvent. Because of the good homogeneity through vitrification, reducing the size effect as well as the matrix effect, accurate and reproducible results are expected for XRF analysis. Lithium tetraborate is used in this study as it has the highest melting point (about 920 °C) among the common fluxes. The

temperature was set on 1050 °C to minimise flux and sample volatilisation. Non-wetting agents, usually halogen compounds (e.g. NH_4I, KI, LiI, LiBr and NaI), are added in order to make the melt more easily to remove from the platinum crucible. In this work, all the analyses were obtained using fused bead preparation due to its better accuracy.

2.9 TGA/DTA/MS

TGA/DTA is a powerful thermoanalytical technique to characterise materials with respect to their thermal behaviours. The basic principle in TGA is to measure the mass change of a material as a function of temperature (time) in a controlled atmosphere. It is ideally used to assess moisture and volatile content, composition of multi-component systems, thermal stability, oxidation/reduction, reaction kinetics, degradation characteristics etc.

Many thermal changes in materials do not involve a change of mass, therefore DTA can record the temperature difference between a reactive sample and reference as a function of time. A peak is displayed when an endothermic even occurs, and a dip shown in the DTA curve when an exothermic event is recorded. Usually the reference is a thermally inert material, typically Al_2O_3.

A mass spectrometer can be combined with the thermal analysis instrument to the apparatus for detection and identification of any gases evolved from the sample (evolved gas analysis - EGA) in exact time correlation with the other thermal analysis signals. Quadrupole Mass Spectrometer (QMS) converts the gas into positive charged ions and the different ions are detected according to their *M*/*Z* ratio. TGA-MS system is especially useful if the characterisation of decomposition products is of importance. In this work, all the experiments were undertaken on a NETZSCH STA 449F1 Jupiter (TGA) and NETZSCH 403 C (QMS).

2.10 Hot Isostatic Pressing

Hot isostatic pressing (HIPing) was invented in 1955 for a diffusing bonding of nuclear fuel element assemblies and has since been extensively studied for manufacturing and engineering applications.[108] In the past few decades, HIPing has been applied for treating high-level radioactive wastes due to its advantages, such as no radioactive volatile emissions in the closed processing system, less secondary waste and flexible processing conditions in the high temperature consolidation step. An encapsulated and densified wasteform can be generated from the HIP process.

The material is usually encapsulated in an evacuated metal, ceramic or glass container. Care must be taken in the design of the capsule. Ceramic moulds are used sometimes but costs are relative prohibitive. Glass capsules are used mainly for ceramic applications.[109] Various metal materials are selected as cans, such as stainless steel, aluminium or copper, depending on the purposes and applications. In this work, mild steel was chosen as the can material for its low reducing environment, ease to source, good weldability and deformable property at the high temperature and pressure under HIPing conditions.

Sample filling is sometimes performed in an inert atmosphere or in vacuum if required. The capsule filled with powder is usually vibrated to improve the fill density which should at least reach 68% of theoretical density to facilitate uniform shrinkage.[109] After filling, the capsule is evacuated and sealed. Air and moisture which may lead to oxide formation and hindering of the sintering process are thus removed.[109] Failure to achieve a good seal may result in the gas entering the can during pressurisation and causing a noticeable internal porosity in the final product.

Presently, typical HIP units operate to a temperature of 500-2000 °C and a pressure from vacuum to 200 MPa, and generally consist of a pressure vessel, a furnace, a gas system, a power supply, instrumentation and controls and auxiliary systems. The sequence of hot isostatic pressing is given below (summarised from the reference[82]).

(1) ***Preparation*****:** Components are placed within furnace furniture and separated suitably for expansion effects or batch control. Some support jigs may be provided for certain complex samples.

(2) ***Loading:*** Individual trays are assembled into supporting furniture and the completed charge is lowered into the pressure vessel. The pressure vessel is closed.

(3) ***Purging:*** The pressure vessel is evacuated and purged with the pressurising gas.

(4) ***Equalisation*****:** High purity argon is admitted to the vessel from the storage system until the vessel pressure has risen to the storage pressure.

(5) ***Compression*****:** Gas is pumped via a compressor from the storage system to the vessel until the required pressure is reached. Heating may take place while this is occurring and this contributes to the pressurisation.

(6) ***Heating*****:** The required HIPing temperature is achieved and sustained for required duration depends on the application.

(7) ***Cooling*****:** At the end of the sustain period, the furnace is allowed to cool. The inevitably reduces the pressure but some excess pressure is extremely important for cooling purposes. Natural cooling is usually at 5-10 °C min^{-1}, but jet cooling can be applied for different purposes.

(8) ***Charge removal*****:** The charge is removed from the pressure vessel.
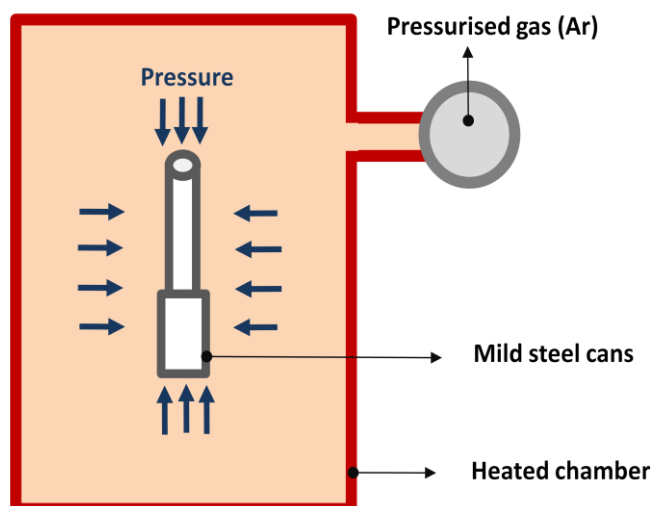
Figure 2.13 Schematic diagram of hot isostatic pressing

After HIPing, a nearly 100% dense monolithic sample is achieved. Normally, metal capsules can be removed by chemical pickling, mechanical machining or electron discharging machining (EDM). For characterisations, ceramic sample were sectioned by a diamond saw or a cutting machine with Al_2O_3 blade. Mild steel capsules were easily and quickly removed by immersing in diluted (20%) nitric acid. Silicotitanate is stable in acid environment and its chemical properties will not be affected by the can removal process.

Chapter 3   Synthesis and Characterisation of Crystalline Silicotitanate

3.1 Introduction

Crystalline silicotitanate (CST) with the sitinakite topology and composition $Na_2Ti_2O_4SiO_3 \cdot 2H_2O$ has been used as an inorganic ion exchanger for removing radionuclides from nuclear waste. CST exhibits great selectivity for both Cs and Sr,[36] and its structure[39, 110-112] (as shown in Figure 1.1) and ion exchange property[113-119] have been widely investigated. With the unique tunnel structure whose size is close to that of the Cs ion, CST exhibits great selectivity for Cs even in the presence of competing ions such as Na^+ and Ca^{2+}.[120-122] As illustrated in Figure 3.1, CST works in a wide pH range and its maximum Cs binding ability was observed over the pH range 2-6.[36]
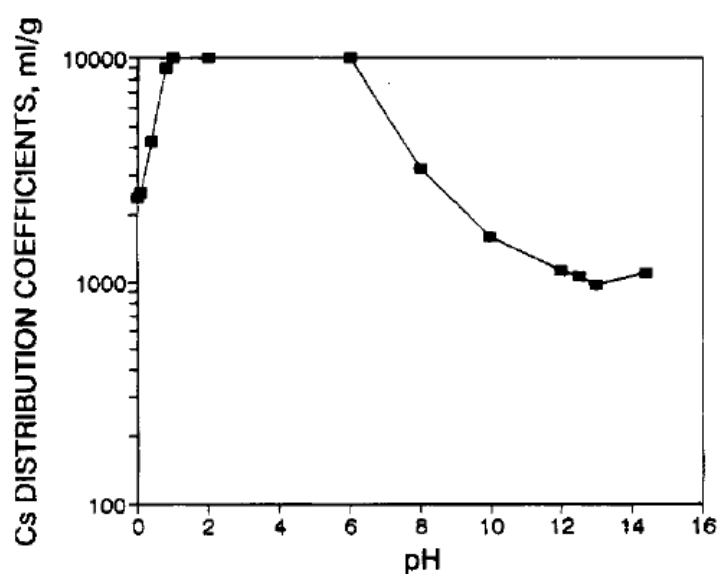
Figure 3.1 Caesium distribution coefficients of Na-CST (TAM-5) in 5.7 M $NaNO_3$ solution as a function of pH.[38]

There has been an ongoing research into studying and modifying the framework of CST to accommodate more Cs into the structure. Early work by Poojary et al.[110] investigated the structural studies of Na-CST as well as a number of alkali metal ion exchanged phases. The structure of Na-CST consists of clusters of four TiO_4 cubane like clusters that are linked by silicate groups which result to form a tunnel framework in the *c* direction. Half of the Na^+ ions are situated in the framework coordinated by silicate oxygen atoms and water molecules, the remaining Na^+ ions are present in the cavity, but there is insufficient room for them. Instead, some of them are replaced by protons, and the actual formula is $Na_{1.64}H_{0.36}Ti_2O_3(SiO_4)\cdot1.8H_2O$. Treatment of Na-CST with acid converts it to $H_2Ti_2O_3SiO_4\cdot1.5H_2O$ and creates more cavities within the walls of tunnels as secondary exchange sites.

The mechanism of Cs^+ exchange into the CST framework has been investigated. Celestian et al. investigated the structures of Na-CST as well as the Cs-exchanged CST and elucidated that Cs^+ exchange proceeds via a two-step process mediated by conformational changes in the framework.[117, 123, 124] The changes in water position in response to the initial introduction of Cs^+ leads to the structural transition, and this new geometric arrangement is required to provide the most stable bonding environment for the hydration of Cs site, as illustrated in Figure 3.2. Ultimately, the hydrogen layer on the silicotitanate framework is repelled resulting in the occupancy of the most favourable site. The rearrangement in CST conformation unlocks the preferred Cs site and the overall capacity and selectivity for ion exchange are thus increased.[117]

Upon Cs+ exchange, H₂O is forced to rotate close to the framework [lever 1 (green arrow)], and as a result, initiates lever 2 (orange arrow).

The hydroxyl bends away from the approaching H₂O.
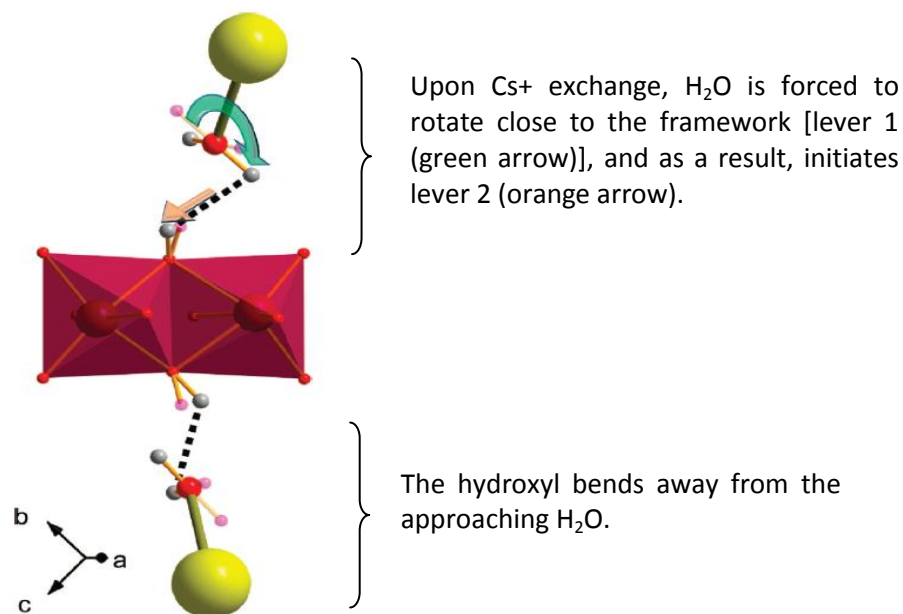
Figure 3.2 Illustration of the two step mechanism involving interactions of Cs2 with H_2O (Ow2) and hydroxyl, adapted from reference[117]. Colour codes: Cs^+ (yellow), O^{2-} (red) and Ti^{4+} (purple). Transparent pink atoms are the H^+ positions in the H-CST form and gray atoms are the H^+ positions in the (Cs, H)-CST form. The dashed line is the final H-H distance.

Although applications in nuclear waste treatment using pure CST have been widely studied, the modern trend is to partially replace the Ti with Nb[111, 123, 125, 126] or Ge[127] in the framework or modify CST with different cations[128] in the structure to achieve a better selectivity or capacity for Cs removal. Partially (25%) Nb-substituted CST (referred to **Na-Nb/CST** in this work) was extensively studied for achieving a better Cs uptake. The substitution of Nb^{5+} for Ti^{4+} reduces the required amount of Na^+ for charge neutralisation in the structure. As a consequence, it facilitates the uptake of hydrated Cs complexes into the less crowded tunnels, as shown in Figure 3.3 (b). Compared with Na-CST, it was found that the selectivity of Na-Nb/CST for Cs uptake was greatly improved, but it was less selective for Sr at high pH value.[126]
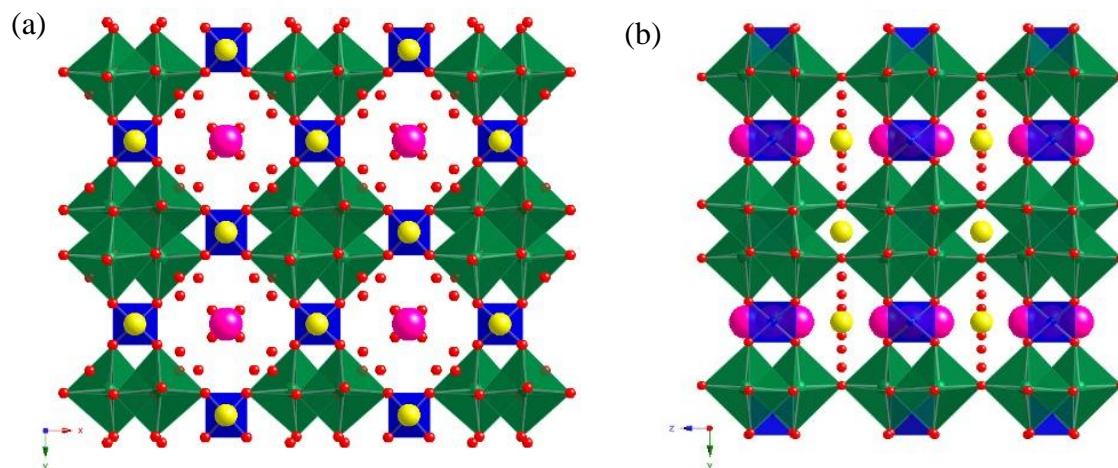
Figure 3.3 A polyhedral representation of the crystal structure of Cs exchanged Na-Nb/CST with the sitinakite topology along (a) [001] and (b) [100]. The pink and yellow spheres represent Cs and Na cations, respectively.

Ion exchanger IONSIV® IE-911, a CST containing product that was commercially developed and manufactured by UOP, has shown to be highly effective for removing Cs from solutions over a broad pH range and also revealed remarkable performance in both ion exchange columns and batch tank systems.[129-131] Furthermore, it was generally believed that pretreatment of IONSIV® IE-911 affected the rate of equilibrium and also increased the ability of Cs removal. Therefore, a pretreatment step recommended by UOP that recirculates the sorbent IONSIV® with 2 M HNO$_3$ was usually applied. It was also recommended to pretreat the sorbent with NaOH prior to use if IONSIV® IE-911 is to be applied in alkaline waste streams.

However, Mann and Todd[131] found from tests applying the acid pretreatment that the Zr(OH)$_4$ binder in IONSIV® IE-911 appears to dissolve in nitric acid and the acidic waste matrix used in these tests. The changes in the physical configuration of the sorbent could possibly cause a reduced number of exchange sites. In addition, the generation of fine particles, which may carry some caesium with them, can result in a deleterious effect on

caesium sorption. Therefore, pretreating IONSIV® IE-911 with acid solution before the ion exchange process is not necessary.

Ion exchanged properties of IONSIV® IE-911 can be affected by several factors. Fondeur et al. investigated the effect of heat, caustic pretreatment, and organic constituents (e.g. tri-*n*-butyl phosphate, dibutylphosphate, butanol and paraffin) as well as some trace components (carbonate, oxalate and peroxide) on the kinetics and extent of caesium adsorption of IONSIV® IE-911 in a simulated waste solution.[132, 133] It was discovered that heating IONSIV® IE-911 at 100 °C for 72 hours significantly degraded its Cs removal performance by a 40.7% reduction in capacity and a 43% reduction in sorption rate. In addition, it was found that IONSIV® IE-911 pretreated with caustic for 72 hours had a slower approach to equilibrium Cs distribution in batch contact tests than the untreated IONSIV® IE-911 samples.

The Cs loading on IONSIV® IE-911 varies proportionally with the amount of carbonate in solution due to a higher ionic strength of the solution, which decreases the activity coefficient of competitors. It was also found that oxalate and organic chemicals had no effect on Cs loading. Peroxide at a 0.13 M concentration lowered the Cs loading on IONSIV® IE-911 because of the destruction of the silicotitanate framework.

The effect of temperature on Cs removal was also examined by Mann and Todd[131]. Results from batch tests which were performed at 25 °C and 50 °C using IONSIV® with tank waste simulant indicated a decrease in ^{137}Cs K_d of approximately 40% when increasing the temperature from 25 °C to 50 °C. A similar temperature effect of decreased Cs K_d values with increasing temperatures for alkaline solutions was also examined by Taylor and Mattus[134]. A significant decrease in Cs K_d at 120 °C was observed when batch equilibrium experiments were performed with varied temperatures from 30-120 °C.

To sum up, the effects of operating factors, such as temperature, humidity and pH value, on ion exchange capacity and selectivity have been widely studied. CST has shown a great ability to ion exchange even under extreme conditions. For long term storage, however, the stability of Cs-exchanged CST in a long time scale is of most importance. In this chapter, Na-CST and Na-Nb/CST were synthesised by an optimised hydrothermal synthesis, and the chemical, structural and thermal properties of Na-CST and Na-Nb/CST were studied and compared to those of IONSIV®.

3.2 Experimental

3.2.1 Synthesis

In this work, two different hydrothermal synthesis routes using titanium tetraisoproxide (TTIP) and titanium tetrachloride ($TiCl_4$) as starting materials were adopted to synthesise Na-CST. Na-Nb/CST was obtained hydrothermally by partially (25%) substituting Ti with Nb using Nb_2O_5 or $Nb(OEt)_5$ as Nb sources. A 2-step treatment was then required to remove an impurity.

3.2.1.1 Synthesis of Na-CST

Na-CST of ideal composition $Na_2Ti_2O_4SiO_3 \cdot 2H_2O$ was synthesised hydrothermally under highly alkaline media. The Na-CST was synthesised according to two procedures using TTIP and $TiCl_4$ as titanium sources.

Method A. (This synthesis procedure is based on the hydrothermal reaction reported by Poojary et al.[39]) 4.56 g of titanium tetraisopropoxide (97%, Aldrich) was mixed with 3.33 g

of tetraethylorthosilicate (99.8%, Aldrich). 26 mL of 6.32 M NaOH solution was then added into the mixture under vigorous stirring. A white paste formed and was stirred for one hour until homogeneous. The mixture was transferred to two 45 mL Teflon^{TM}-lined vessels using extra 15 mL of deionised water. 0.1 g of seed crystal was added to the solution to increase the crystallinity and purity. Each bomb was filled no more than 60% full. The Teflon^{TM} liners were sealed in the stainless steel vessels and heated at 170 °C for 8 days. After the vessels were cooled down to room temperature, the product was obtained by filtration. The solid was washed first by DI-water until the pH value dropped below 8, and then rinsed with pure ethanol. The product was dried at 65 °C overnight. The yield was ~ 90% based on Ti (Si is in excess).

Method B. (This synthesis procedure is based on the hydrothermal reaction reported by Tripathi et al.[126]) The other starting gel was prepared by first adding 6.66 mL of $TiCl_4$ to 23.34 mL of deionised water in a plastic bottle A under vigorous stirring. To the mixture, 40 mL of H_2O_2 (30%) was added, followed by 150 mL of deionised water and 40 mL of 10 M NaOH solution. The solution was stirred for an additional 20 minutes after the colour turned to light green. To the other bottle B was added 200 mL of 1 M NaOH and 10.75 g of Ludox colloidal silica buffered by sodium (AS-40). The contents of bottles A and B were then combined and the solution was adjusted by 1 M NaOH until a pH value of 12.5-13 was achieved. The gel was immediately transferred to the bombs with capacity of 23 mL and 125 mL, filling to 60% full of the Teflon^{TM} liner. The bombs were sealed in stainless steel autoclaves and treated hydrothermally in a 210 °C oven for 10 days. The resulting product was filtrated, rinsed with first deionised water and then ethanol, and dried at 65 °C overnight. The yield was ~ 93% based on Ti (Si is in excess).

3.2.1.2 Synthesis of Na-Nb/CST

25% Nb substituted CST was synthesised by modifying the hydrothermal reaction described previously by Poojary et al.[39, 126], where 3.43 g of titanium tetraisopropoxide, 3.33 g of tetraethyl orthosilicate, and either 1.292 g of $Nb(OEt)_5$ or 0.54 g of Nb_2O_5 was added to 50 mL of 3.3 M NaOH solution. To this mixture was added a small amount of pure Na-Nb/CST (~ 0.1 g) as seed to increase the crystallinity. The mixture was stirred for one hour and then transferred to a 125 mL Teflon^{TM} lined autoclave and placed in a 200 °C oven for 3 days. The resulting product was filtrated, rinsed with first deionised water and then ethanol, and dried at 65 °C overnight.

3.2.1.3 Impurity Removal

Natisite (Na_2TiSiO_5) was possibly found as an impurity in the major CST products. A 2-step treatment was applied to remove the byproduct. The solid was exposed to a 1 M aqueous HCl wash for three hours at room temperature to decompose the byproduct. The resulting solid was then stirred in 1 M NaOH solution for three hours at 40 °C to dissolve the amorphous materials.

3.2.2 Characterisation

3.2.2.1 XRD

Powder X-ray diffraction patterns were collected on a Bruker D8 Advance diffractometer operating in transmission mode using Cu $K_{\alpha 1}$ radiation (λ= 1.5406 Å) in the range of 2θ from 5° to 80° at a step size of 0.0197° with a LynxEye Si-strip detector.

3.2.2.2 SEM/EDX

Secondary electron imaging (SEI) with an EDX system was used to determine the morphology and chemical composition of the samples. To prepare the sample for morphology observation, loose powder was spread on a conductive carbon film and coated with carbon for EDX analysis. All the investigations were carried out using a Philips XL30 ESEM-FEG with an Oxford Inca 300 EDX system operating at 10 kV.

3.2.2.3 XRF

Fused borate glass beads were prepared for the quantitative determination in CST samples using XRF. Before making fused beads, samples were first pre-oxidised in air at 800 °C for 12 hrs to assure that all the elements were converted into oxides. 0.35 g of sample was mixed with 3.5 g of lithium tetraborate, and the mixture was placed in a platinum/gold crucible and heated at 1050 °C for 7 mins. A non-wetting agent, ammonium iodide (NH_4I), was added and the sample was then returned to heat for another 7 mins. The bubbles in the fusion were removed by swirling the crucible if needed and the crucible was returned into the furnace for an additional 2 mins. After cooling, the beads were removed from the crucible and analysed by XRF (Bruker S8 Tiger WDXRF).

3.2.2.4 TGA

Thermogravimetric analysis and differential thermal analysis (TGA/DTA) experiments with mass spectral analysis were preformed on a NETZSCH STA 449FA instrument. Samples (30-40 mg) were heated to 900-1000 °C at a heating rate of 10 °C/min under a nitrogen atmosphere. Water content was also examined using TGA with mass spectrum monitoring molecule mass of 18 amu.

3.2.2.5 Variable Temperature XRD

High temperature XRD was used to examine the phase transition of the material. The sample was placed in an Al_2O_3 sample holder, and heated up from room temperature (25 °C) to 900-1000 °C with data collected every 20 °C. The XRD patterns were recorded on a Bruker D8 Advance diffractometer in reflection mode with an MRI heating stage, operating at 40 kV and 40 mA. Powder samples were ground before analysis. Data were collected from 8° to 70° (10° to 80° for IONSIV® samples) with a step size of 0.0197° with a LynxEye Si-strip detector.

3.2.2.6 Rietveld Refinement

Synchrotron data sets for the samples of Na-CST and Na-Nb/CST packed into capillaries were collected for Rietveld refinement. The General Structure Analysis System (GSAS) program was used to analyse the synchrotron data. The calibrated wavelength for the beam was 0.827435 Å. Atomic positions for the framework atoms reported in the literature[126] were used as the starting model for both Na-CST and Na-Nb/CST.

3.2.3 Ion Exchange

A pretreatment step recommended by UOP for using IONSIV® in acidic media is to recirculate the sorbent with HNO_3. However, this step has been shown unnecessary[131, 135] and was not applied to IONSIV® in this work. For Na-CST and Na-Nb/CST, the pretreatment was adopted to activate the samples for higher Cs capacity. These were soaked in 1 M of aqueous HNO_3 for 3 hours, and then filtered, washed with water and dried in air.

Cs-exchanged CSTs were then prepared by impregnating materials (Na-CST, Na-Nb/CST and IONSIV®) with aqueous $CsNO_3$ solutions at various Cs loadings (2, 4, 6, 8, 10 and 12 wt.%, ie. Cs/(Cs + initial mass of CSTs) = 0.02, 0.04, ….0.12) at room temperature for 3 days. Samples were washed with DI-water and recovered by filtration and then dried at 60 °C. Due to the difficulties in acquiring enough pure Na-CST, only 3 Cs loadings (2, 6 and 12 wt.%) were performed for the following HIP study.

3.3 Na-CST

3.3.1 Synthesis and Optimisation

Na-CST is tetragonal, $a = 7.8082$ Å, $c = 11.9735$ Å, space group $P4_2/mcm$. For the synthesis using TIPT, a pure CST product can sometimes be directly obtained via hydrothermal synthesis. The XRD pattern of Na-CST is shown in Figure 3.4.
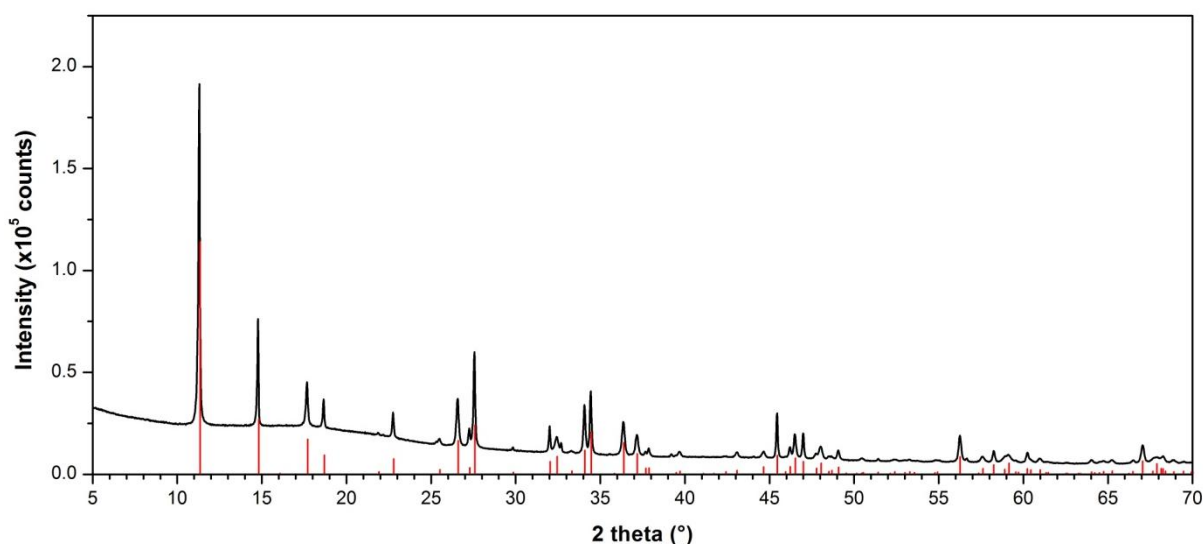
Figure 3.4 XRD pattern of Na-CST. The red lines are the indexed peaks from the ICDD PDF 01-082-1271 ($Na_{1.64}H_{0.36}Ti_2O_3SiO_4 \cdot 1.84H_2O$)

However, natisite (Na_2TiSiO_5, as shown in Figure 3.5(a)) is sometimes found as a byproduct in the sample. From the XRD pattern shown in the Figure 3.5 (a), a great amount of impurity in the form of natisite, whose crystal structure and chemical formula were reported previously in the literature[37, 136], was found. To remove the impurity, a 2-step treatment was usually applied as describe previously. The byproduct was successfully removed after the purification process. However, it was noticed that the treatment also led to a decrease in crystallinity in some cases. It is estimated that the condition applied for purification causes the damage in the structure. The optimised concentrations of acid and base were suggested to be no higher than 1 M.
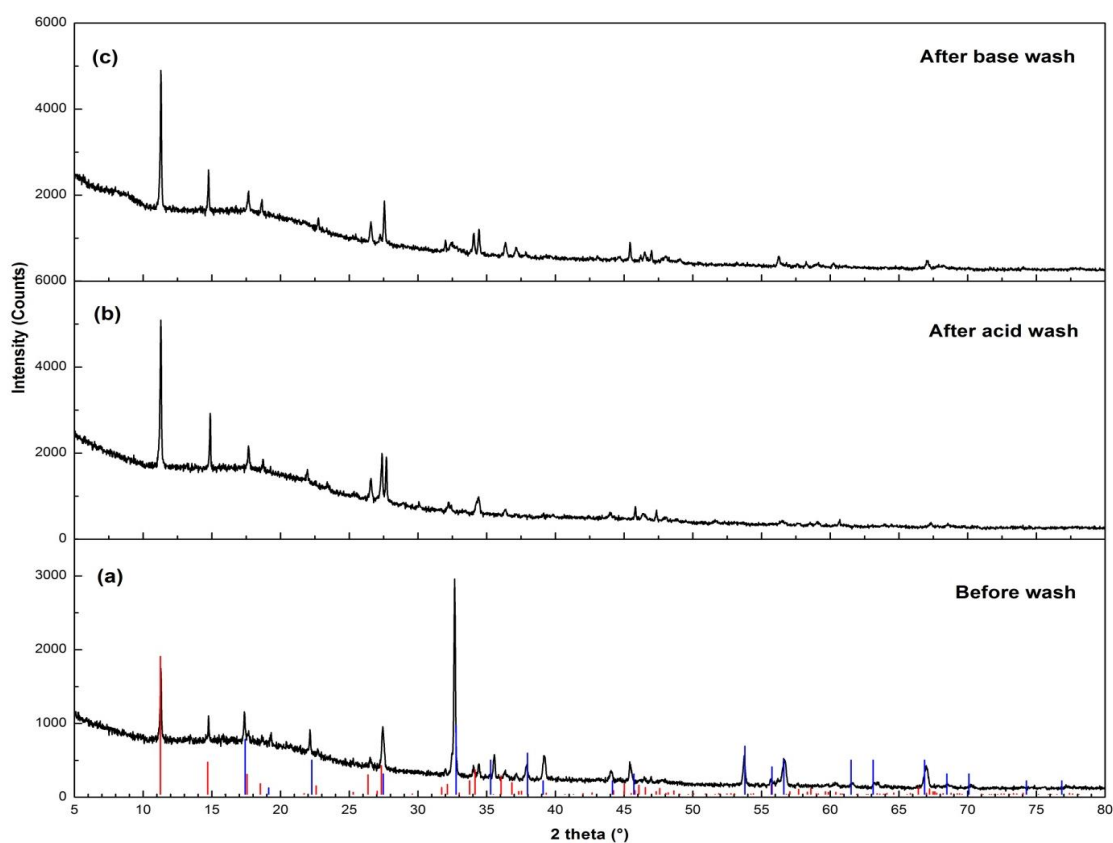
Figure 3.5 The XRD patterns of Na-CST after the 2-step treatment (a: before wash; b: after 1 M HCl wash for 3 hours; c: after 1 M NaOH wash at 40 °C for 3 hours). The red and blue lines are the indexed peaks from the ICDD PDF 01-082-1271 ($Na_{1.64}H_{0.36}Ti_2O_3SiO_4 \cdot 1.84H_2O$) and 00-029-1279 (Natisite), respectively.

In the case of using $TiCl_4$ as precursor, although higher temperature (210 °C) and longer time (10 days) were required for crystallisation, it was found more likely to obtain a pure product. However, relatively poor crystallinity was observed, as seen in the Figure 3.6. It is well known that the addition of good quality seeds is of great help for the formation of highly crystalline product. Improved crystallinity can be achieved by adding pure CST as seed material during synthesis.

The hydrothermal synthesis route for Na-CST using TTIP is considered the better one, because a more crystalline product can be achieved even if a further treatment is sometimes required. All the Na-CST used for study in this work was obtained hydrothermally using TTIP.
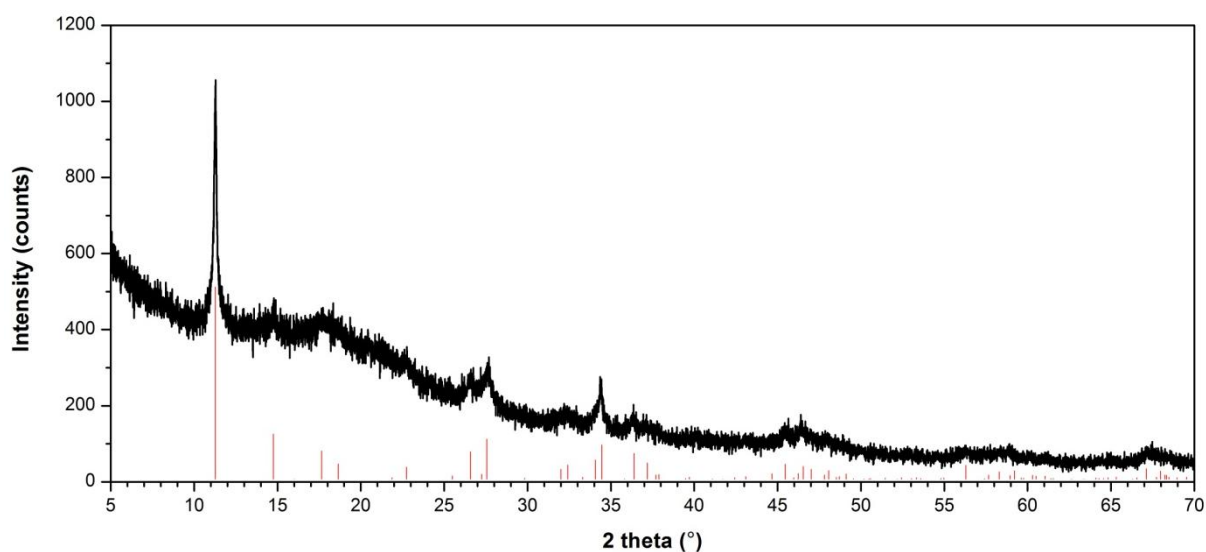
Figure 3.6 XRD pattern of Na-CST using $TiCl_4$ as starting material. The red lines are the indexed peaks from the ICDD PDF 01-082-1271 ($Na_{1.64}H_{0.36}Ti_2O_3SiO_4 \cdot 1.84H_2O$)

3.3.2 Morphology and Elemental Composition

Figure 3.7 and Figure 3.8 show the morphology of Na-CST. The sample was prepared by mixing several batches of Na-CST and spreading the mixed Na-CST on the carbon film for SEM observations. Na-CST exhibits well-defined crystals with cubic morphology of size 1 μm^3. However, some agglomerated particles, suggesting impurities or poor crystalline CST crystals, were also found in the sample. The differences in the crystallinity and particle size mostly resulted from the non-homogeneity from different batch syntheses. EDX results are in Table 3-1.
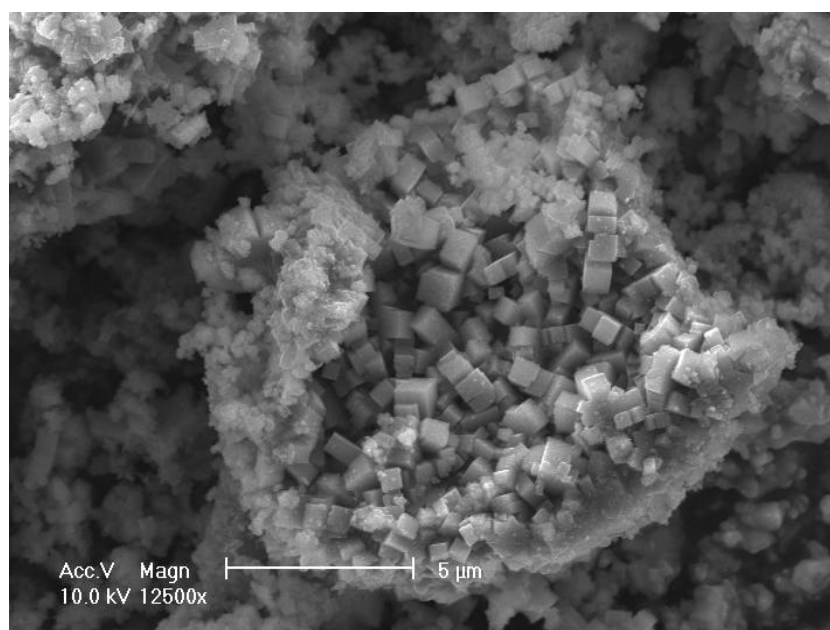
Figure 3.7 SEM/SEI image of Na-CST at the magnification of ×12,500
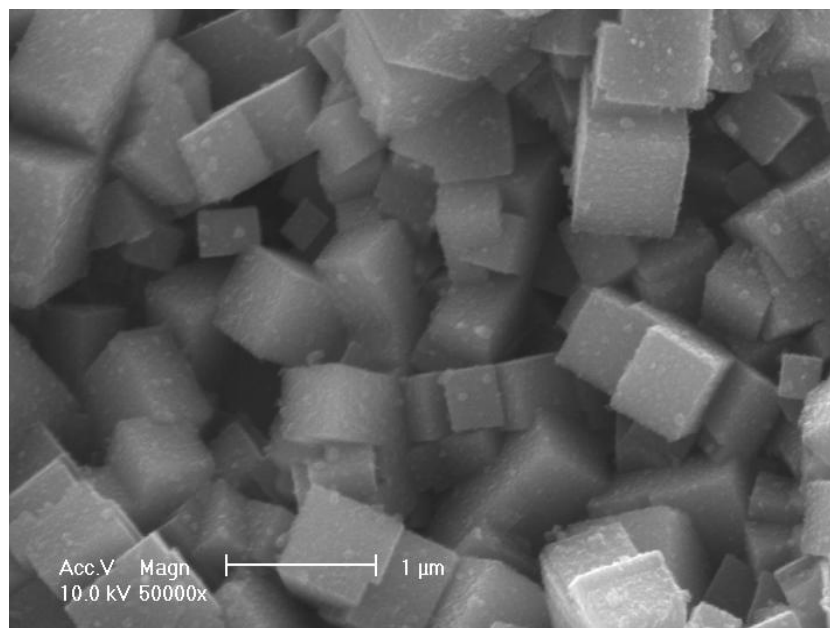
Figure 3.8 SEM/SEI image of Na-CST at the magnification of ×50k showing the uniform cubic morphology of size 1 μm in length

EDX analysis was performed in randomly selected area in Figure 3.8, and the average elemental composition of Na-CST is shown in Table 3-1. The Na/Si ratio is 1.57 which is lower than the ideal value of 2, suggesting that the sample may contain partially H-form CST that arises from hydrolysis during washing, which cannot be distinguished in the XRD pattern.

Table 3-1 Average elemental composition acquired from EDX analysis of Na-CST

Element	Weight %	Atomic %	Molar ratio (expected)	Molar ratio (normalised to Si)
Na K	13.92	13.34	2	1.57
Si K	9.84	7.74	1	1
Ti K	28.34	13.11	2	1.69

The elemental composition of Na-CST acquired using XRF is shown in Table 3-2. The molar ratios have been normalised to Si, which makes the assumption that most of the Si is incorporated within the silicotitanate. XRF results show that Na/Si and Ti/Si ratios are both greater than the ideal value 2, and this is not consistent with that obtained from EDX. Instead of the detection in a local area, XRF determines the bulk material so that the elemental information obtained also includes any impurity or amorphous substance which was not removed by the 2-step treatment. Hence, the high Na content is estimated to be from the remaining NaOH, and the high Ti/Si ratio is attributed to an impurity in the form of Ti phase or the incorporated Ti outside the framework. Although the EDX analysis is generally considered a semi-quantitative method and exhibits a poorer accuracy compared with XRF, the EDX result is still of value. A desired area in a well-defined crystal can be selected for analysis with the help of microscope; therefore, the unwanted information from any impurity can be avoided.

Table 3-2 XRF result of Na-CST (Fused bead)

Element	Weight %	Atomic %	Molar ratio (expected)	Molar ratio (normalised to Si)
Na K	17.00	17.65	2	2.31
Si K	8.99	7.64	1	1
Ti K	33.80	16.85	2	2.21

3.3.3 Structure Determination

Rietveld refinement of synchrotron data confirmed that Na-CST crystallises in the tetragonal structure with space group $P4_2/mcm$, and the unit cell dimensions are $a = 7.8040(1)$ Å and $c = 11.9729(1)$ Å. The experimental composition for Na-CST obtained from refinement

is $H_{0.6}Na_{1.40}Ti_2SiO_7 \cdot 1.6H_2O$, rather than the ideal formula of $Na_2Ti_2SiO_7 \cdot 2H_2O$. (See Appendix 1for the detailed refinement results)
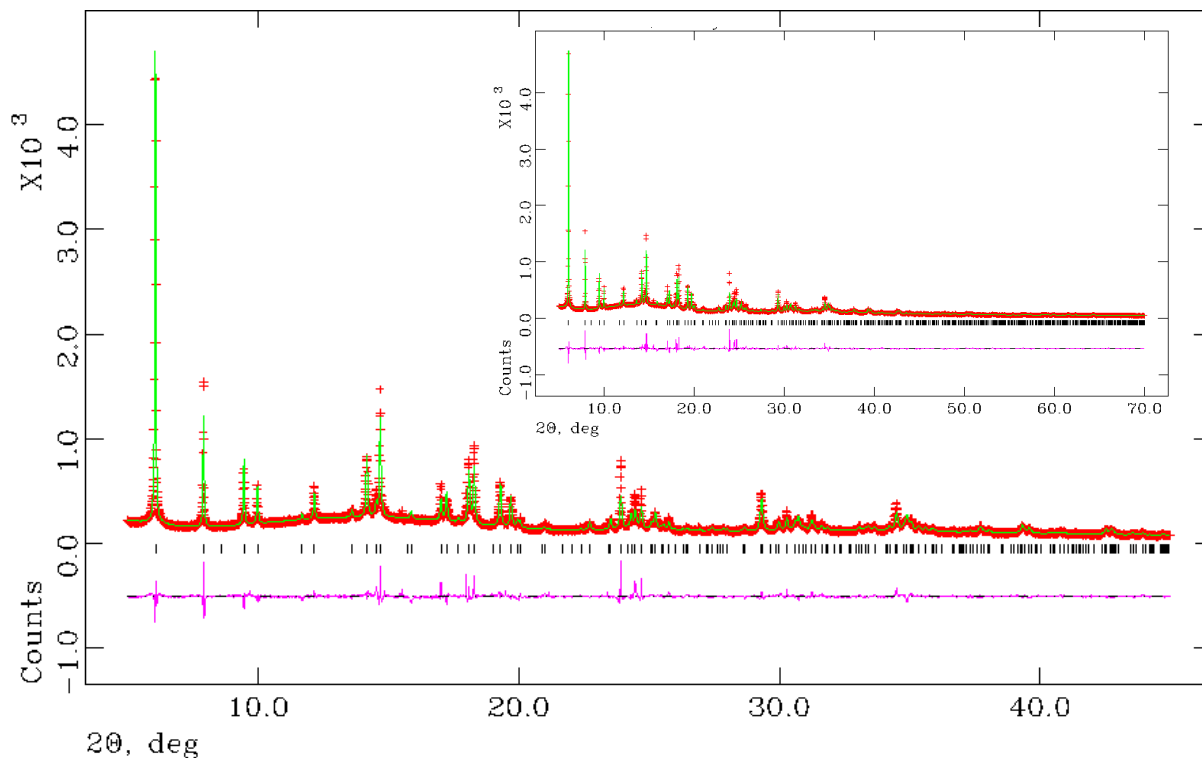
Figure 3.9 Observed (+) and calculated (−) profiles for the Rietveld refinement for Na-CST. The bottom curve is the difference plot on the same intensity scale. (χ^2 = 5.502, R_{wp} = 6.65%, R_p = 4.52%). Tick marks represent calculated peak positions.

3.3.4 Thermal Behaviour and Phase Transition

Thermogravimetric analysis (TGA) provides a useful means of characterising and quantifying the moisture content in materials and determining the temperatures at which decomposition, crystallisation and melting occur. TGA/DTA with mass spectrum and XRD analyses at variable temperatures were used to investigate the weight loss and thermal

properties of the materials. Na-CST was heated from room temperature (25 °C) to 1000 °C without any isothermal process. In Figure 3.10 is displayed the plot of weight loss, DTA curve, and mass spectrum of 18 amu as a function of temperature. Dehydration occurred between 250 °C and finished about 400 °C, and a total weight loss of 11.7% was found. The DTA curve exhibited two significant exothermic stages correspond to solid-solid phase transitions, the first one appeared between 610 °C and 675 °C, and the other one appeared between 775 °C to 850 °C.
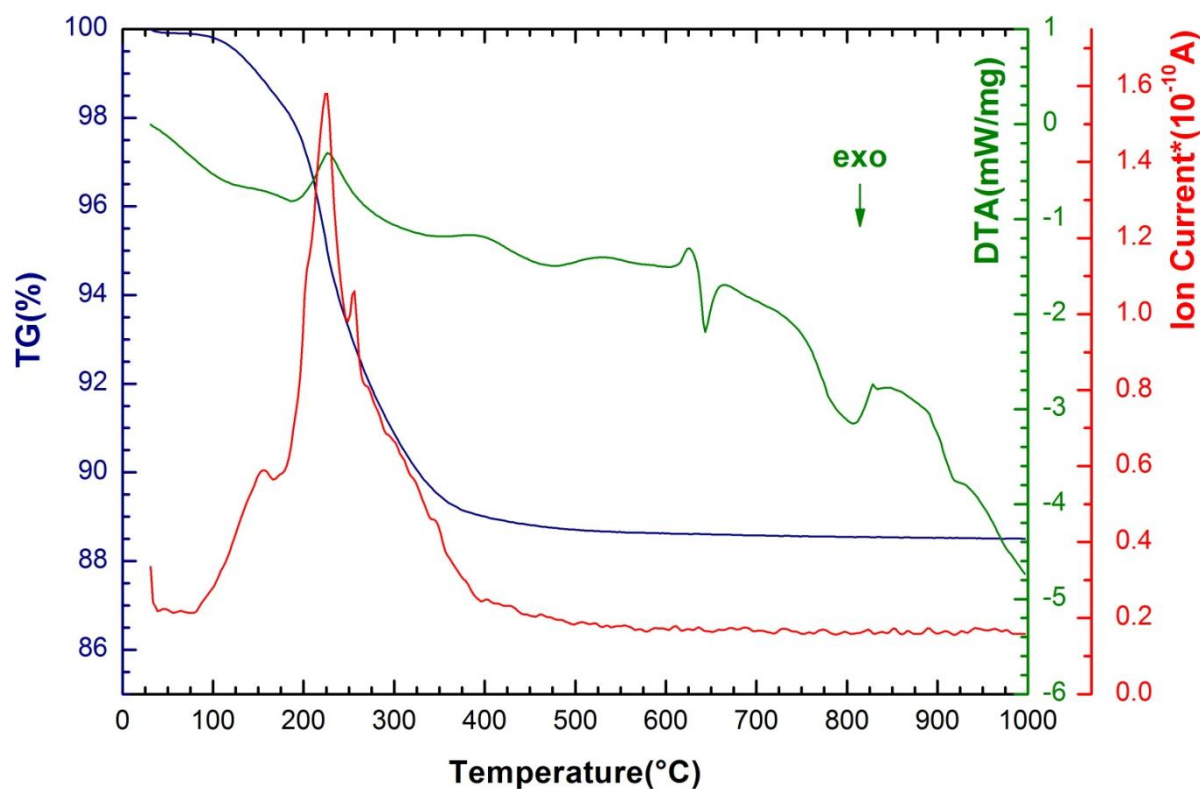
Figure 3.10 TGA/DTA/MS analysis of Na-CST
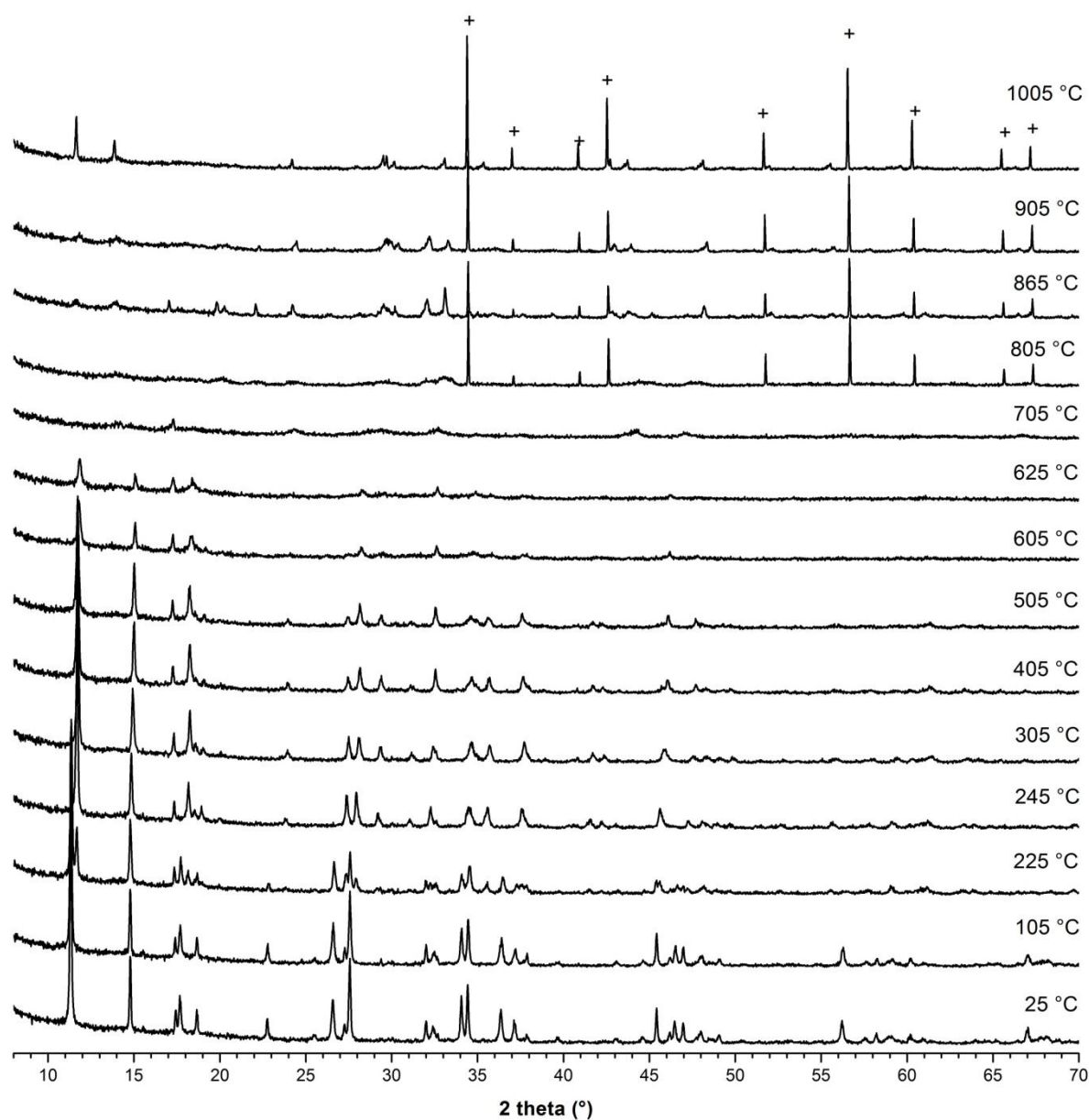
Figure 3.11 XRD patterns of Na-CST at variable temperature

The thermal behaviour observed from XRD patterns of Na-CST at high temperatures agrees with that from the DTA measurement. As illustrated in Figure 3.11, with increasing temperature, Na-CST retained good crystallinity until 605 °C, only a slight peak shift was observed due to dehydration after heating to 245 °C. Above 605 °C, the crystallinity

decreased and a nearly amorphous material was detected at 705 °C. This is in accord with the exothermic stage between 600-700 °C in the DTA trace shown in Figure 3.10. At the higher temperature of 845 °C, the sample re-crystallised. In addition, peaks from the aluminium sample holder (marked with +) were detected and are attributed to a great sample shrinkage that occurred during the heating treatment.

By studying the thermal behaviour of Na-CST, a better understanding of its ability to act as a durable Cs host will be achieved. From the TGA and variable temperature XRD results, the defined Na-CST structure is completely destroyed above 700 °C, indicating that an unsuccessful Cs retention may take place due to the structure damage. As Na-CST has been considered a promising candidate for nuclear waste treatment, the use of Na-CST at higher temperature or for further applications which require a heating process is not recommended.

3.3.5 Ion Exchange

To estimate the Cs level in Na-CSTs after ion exchange, samples were prepared and analysed using SEM/EDX. Several regions were selected to acquire elemental composition using EDX. Table 3-3 shows that there is only a small Cs content in all of the three Na-CSTs. Furthermore, the expected increase in Cs content with attempted Cs loadings was not achieved. It is suggested that the conditions for Cs ion exchange of Na-CST were not optimised.

Table 3-3 Elemental compositions (mole percentage) of non-activated Cs-exchanged Na-CSTs acquired using EDX.

Element	2 wt.% (N=5)		6 wt.% (N=5)		12 wt.% (N=5)	
	Average	Esd	Average	Esd	Average	Esd
O K	68.50	2.42	65.52	2.36	71.29	0.84
Na K	11.25	1.67	12.04	2.26	9.55	0.71
Si K	7.67	0.40	8.51	0.74	7.39	0.18
Ti K	12.18	0.75	13.07	1.92	10.91	0.44
Cs L	0.40	0.11	0.85	0.17	0.86	0.19

Due to the limited space in the CST structure, not all channel sites can be exchanged, resulting in the maximum exchanged composition of $Cs_{0.4}H_{1.6}Ti_2SiO_7 \cdot H_2O$ or $Cs_{0.5}H_{1.5}Ti_2SiO_7 \cdot H_2O$, according to the references [37] and [110], respectively. To increase the Cs capacity of Na-CST, pretreating with acid before ion exchange is considered a means to free the tunnels by replacing Na^+ with smaller protons. Thus, more possible sites can be created for Cs incorporation.[110]

XRF determination of 12 wt.% Cs-exchanged Na-CST after acid pretreatment (Referred to as **Na-CST-activated** in the following) has shown that a great amount of Cs (6.83 wt.%, 1.30 at.%) was detected in the sample. This demonstrated that the ion exchange ability in Na-CST has been improved by activating Na-CST with acid. However, a large amount of Na remains in the sample indicating that Na-CST has not been completely converted into the hydrogen form. To further improve the effect of acid activation, prolonging the duration of acid treatment, repeating the treatment, and breaking down the particle size of CSTs for higher surface area are suggested.

Table 3-4 Elemental composition of 12 wt.% Cs-exchanged Na-CST-activated using XRF

(Fused bead)

Element	Weight %	Atomic %	Molar ratio (expected)	Molar ratio (normalised to Si)
O	40.00	63.08	7	5.71
Na/H	5.34	5.86	1.6 (H)	0.53 (Na)
Si	12.30	11.05	1	1
Ti	35.50	18.71	2	1.69
Cs	6.83	1.30	0.4	0.12

3.4 Na-Nb/CST

25% Na-Nb/CST with an ideal formula of $Na_{1.5}(Ti_{0.75}Nb_{0.25})_2O_3SiO_4 \cdot 2H_2O$ was the target by hydrothermal synthesis. Modification of the framework by introducing the heteroatom Nb^{5+} to partially replace Ti^{4+} affects the ion exchange properties without changing the structure. Investigation of the effects of Nb substitution on the structure is of great help in understanding the ion exchange properties.

3.4.1 Synthesis and Optimisation

In the synthesis of Na-Nb/CST, Nb_2O_5 and $Nb(OEt)_5$ were used as Nb sources. It was evidenced that using $Nb(OEt)_5$ as a starting material is more favourable to form products of good crystallinity because the more homogeneous gel was formed prior to hydrothermal reaction. Figure 3.12 and Figure 3.13 display the XRD patterns of 25% Na-Nb/CST using Nb_2O_5 and $Nb(OEt)_5$ as precursors in the synthesis, respectively, and as well as the patterns of Na-Nb/CSTs after the 2-step treatment for removing an impurity.

The existence of impurities, identified as Nb_2O_5 and natisite, is more likely in the Na-Nb/CST synthesis using Nb_2O_5 due to the poor homogeneity of the crude gel. It was reported that the natisite impurity can be removed by further treatment. The procedure, the same one used in Na-CST, is considered an effective method to remove the byproduct. However, Nb_2O_5, originating from the unreacted starting material, was not removed through this treatment.
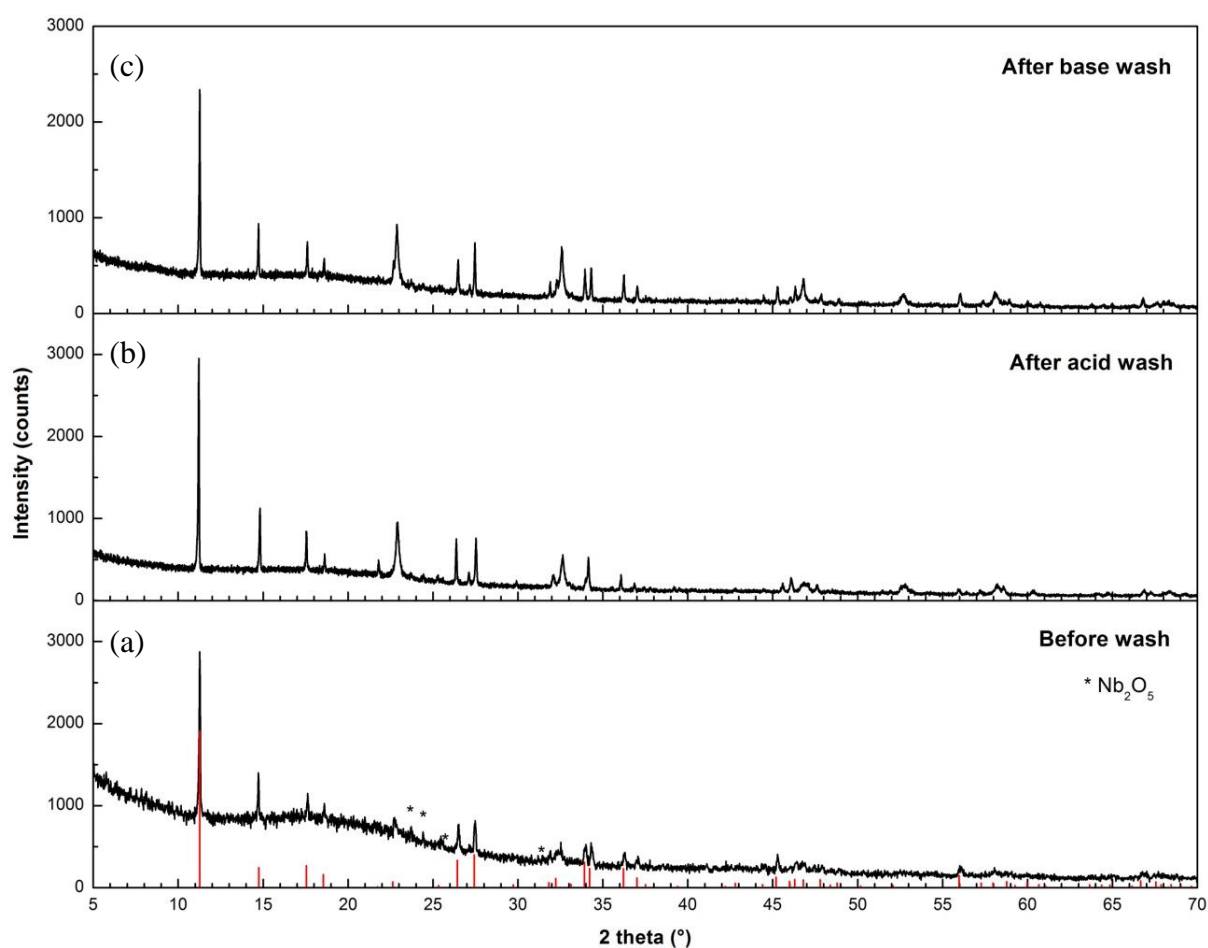
Figure 3.12 The XRD patterns of Na-Nb/CST synthesised using Nb_2O_5 after the 2-step treatment (a: before wash; b: after 1 M HCl wash for 3 hours; c: after 1 M NaOH wash at 40 °C for 3 hours) The red lines are the indexed peaks from the ICDD PDF 01-072-7604 ($H_{0.5}Na$ $(Nb_{0.5}Ti_{1.5})O_3SiO_4 \cdot 2H_2O$).

In the synthesis of Na-Nb/CST using Nb(OEt)$_5$, a better purity was achieved (see Figure 3.13 a). Nevertheless, a small amount of natisite impurity still remained in the product even after a 2-step treatment was applied. The purification process can be repeated if necessary but a noticeable loss in crystallinity was observed. Vigorous conditions, such as acid/base concentration higher than 1 M or base wash at higher temperature (over 50 °C), will result in an amorphous material.
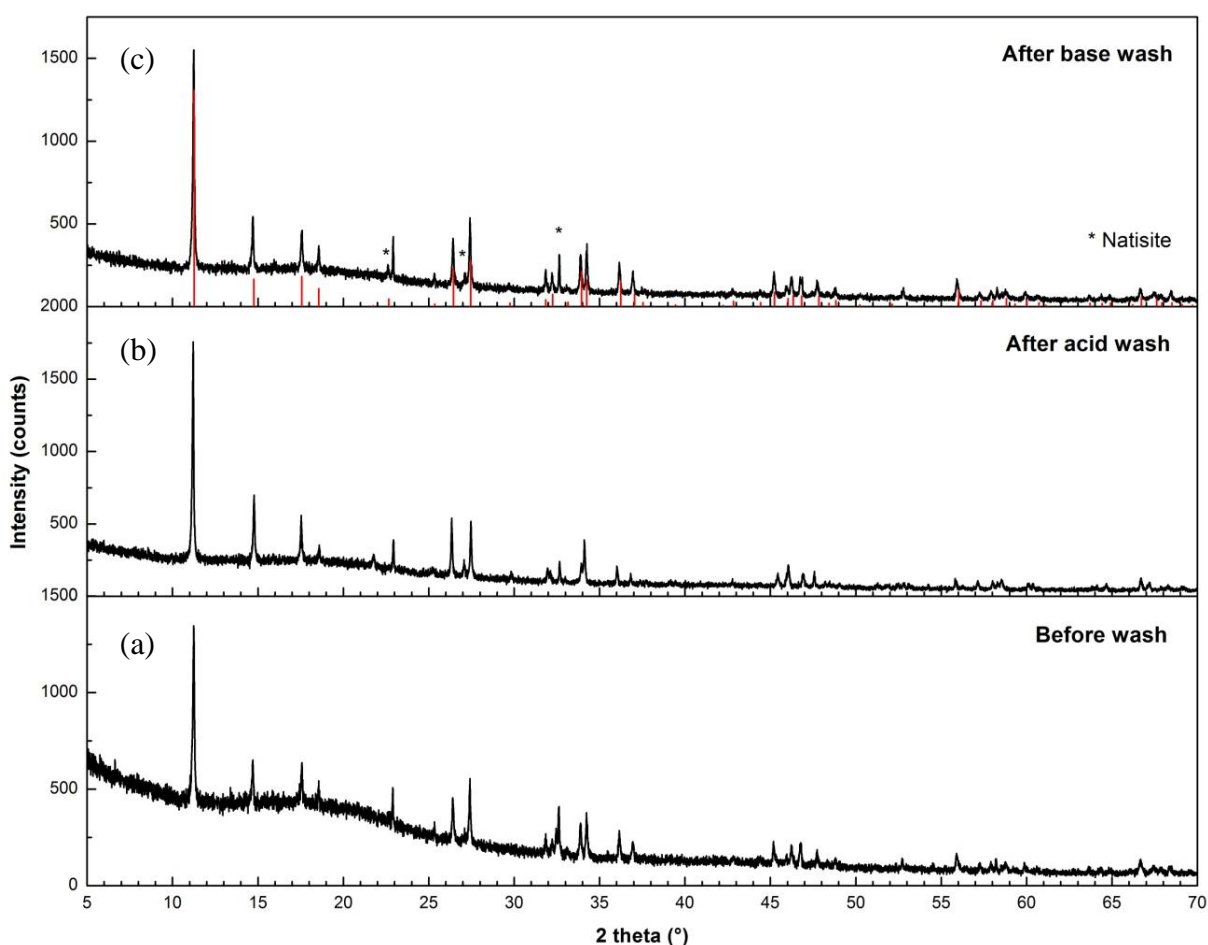
Figure 3.13 The XRD patterns of Na-Nb/CST synthesised using Nb(OEt)$_5$ after the 2-step treatment (a: before wash; b: after 1 M HCl wash for 3 hours; c: after 1 M NaOH wash at 40 °C for 3 hours) The red lines are the indexed peaks from the ICDD PDF 01-072-7604 (H$_{0.5}$Na (Nb$_{0.5}$Ti$_{1.5}$)O$_3$SiO$_4$ ·2H$_2$O).

3.4.2 Morphology and Elemental Composition

As shown as in Figure 3.14 and Figure 3.15, Na-Nb/CST crystals with cubic morphology were generally larger than those of Na-CST. The well-defined cubic particles, characteristic of this compound, indicate the great crystallinity of the products. The particles are in the range from 0.5 to 2 μm in length due to the differences in batch syntheses. To better estimate the proportion of Nb incorporated into the framework, only crystallites with cubic morphology were analysed using EDX. From the EDX results shown in Table 3-5, the (Nb+Ti)/Si ratio is slightly smaller than two, and the Na content is very close to 1.75, proving that the elemental composition of Na-Nb/CST corresponds to the desired one. However, only 13.68% of Nb substitution was detected from the selected crystallite, suggesting that some Nb was not completely introduced into the CST phase. It supports the XRD result that unreacted Nb_2O_5 is present as a minor impurity in CST product, resulting in Nb deficiency in Na-Nb/CST structure.
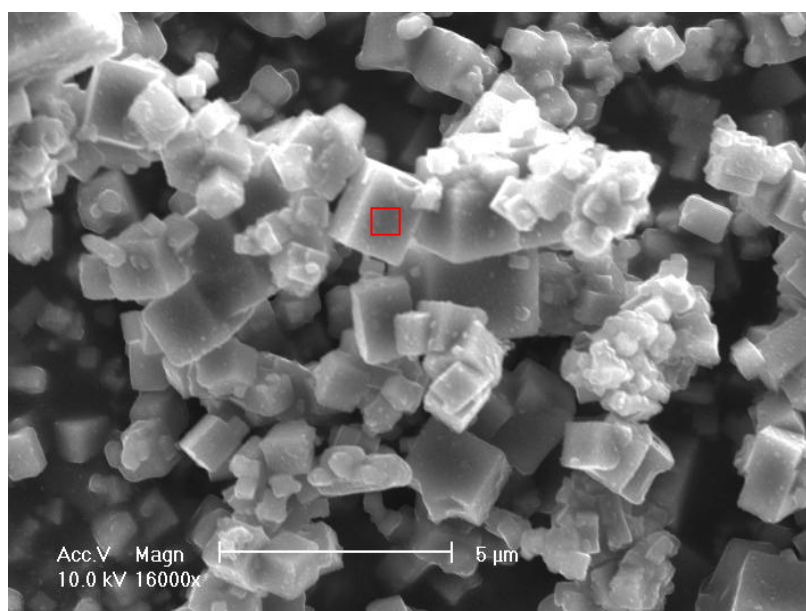
Figure 3.14 SEM/SEI image of Na-Nb/CST at the magnification of ×16k
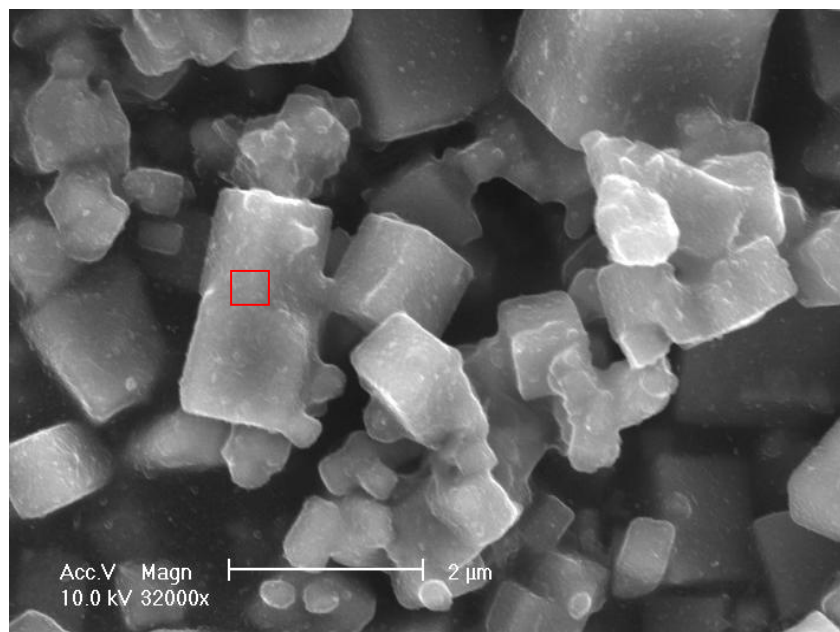
Figure 3.15 SEM/SEI image of Na-Nb/CST at the magnification of $\times$ 32k

Table 3-5 Average EDX result of Na-Nb/CST acquired from the selected areas marked in

Figure 3.14 and Figure 3.15

Element	Weight %	Atomic %	Molar ratio (expected)	Molar ratio (normalised to Si)
Ti K	23.85	11.31	1.75	1.64
Nb L	7.37	1.81	0.25	0.26
Na K	12.54	12.38	1.50	1.80
Si K	8.51	6.88	1	1

The XRF result provides the elemental composition from the bulk. A large Na content shows that the base was not completely washed out from the purification process. Much larger Nb/Si and Ti/Si ratios indicate the presence of impurities in the forms of Nb and Ti phases in bulk materials. The Nb/(Ti+Nb) ratio is 27.74%, which is close to the desired substitution of 25%.

Table 3-6 XRF result of Na-Nb/CST (Fused bead)

Element	Weight %	Atomic %	Molar ratio (expected)	Molar ratio (normalised to Si)
Ti K	23.73	13.02	1.75	1.98
Nb L	17.77	5.03	0.25	0.76
Na K	13.8	15.77	1.50	2.40
Si K	7.02	6.57	1	1

3.4.3 Structure Determination

The structural solution was carried out using Rietveld refinement. Na-Nb/CST crystallises in the tetragonal space group $P4_2/mcm$ with $a = 7.8251(1)$ Å and $c = 12.0001(2)$ Å, the same structure with Na-CST. The starting model reported by Poojary et al.[110] was adapted for Na-Nb/CST refinement.

A formula of $H_{0.08}Na_{1.74}Ti_{1.82}Nb_{0.18}SiO_7 \cdot 1.76H_2O$ was determined from the Rietveld refinement. More information including unit cell parameters, occupancies and atomic positions are shown in the Appendix 2. A small amount of an impurity indexed from the PDF database as Nb_2O_5, unreacted starting material, resulted in extra observed peaks in the pattern. However, a two phase refinement was not successful because of the difficulty in refining Nb_2O_5 due to the very low symmetry of the structure. Instead of fitting a Nb_2O_5 model, the region from 12.28° to 13.39° 2θ was excluded to reduce the effect of the Nb_2O_5 impurity on the refinement.
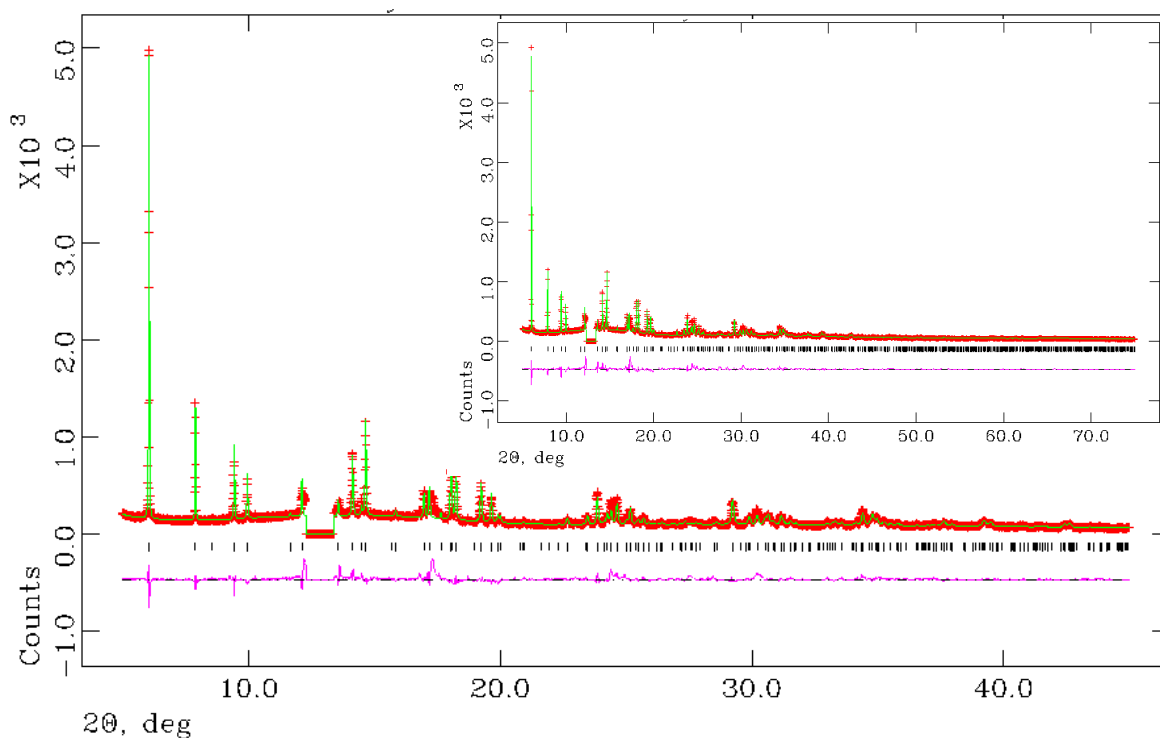
Figure 3.16 Observed (+) and calculated (−) profiles for the Rietveld refinement for Na-Nb/CST. The bottom curve is the difference plot on the same intensity scale. (χ^2= 9.599, R_{wp}= 9.74%, R_p= 6.66%). Tick marks represent calculated peak positions.

3.4.4 Thermal Behaviour and Phase Transition

TGA/DTA with mass spectrum analysis and XRD analysis at variable temperature were carried out to evaluate weight loss and thermal properties of the materials. As-synthesised Na-Nb/CST was heated from room temperature (25 °C) to 1000 °C without any isothermal process. Figure 3.17 displays the TGA/DTA results at a heating rate of 10 °C /min.

The moisture content for Na-Nb/CST is about 8.4% from the TG curve. Dehydration, which occurs below 400 °C, causes the majority of weight loss. From the mass spectrum of 18 amu, there are two stages of water loss firstly occurring at 150 °C for surface water and then

at 250 °C for crystallisation water. In addition, the exothermic stage in the range of 575 to 675 °C indicates a phase change.
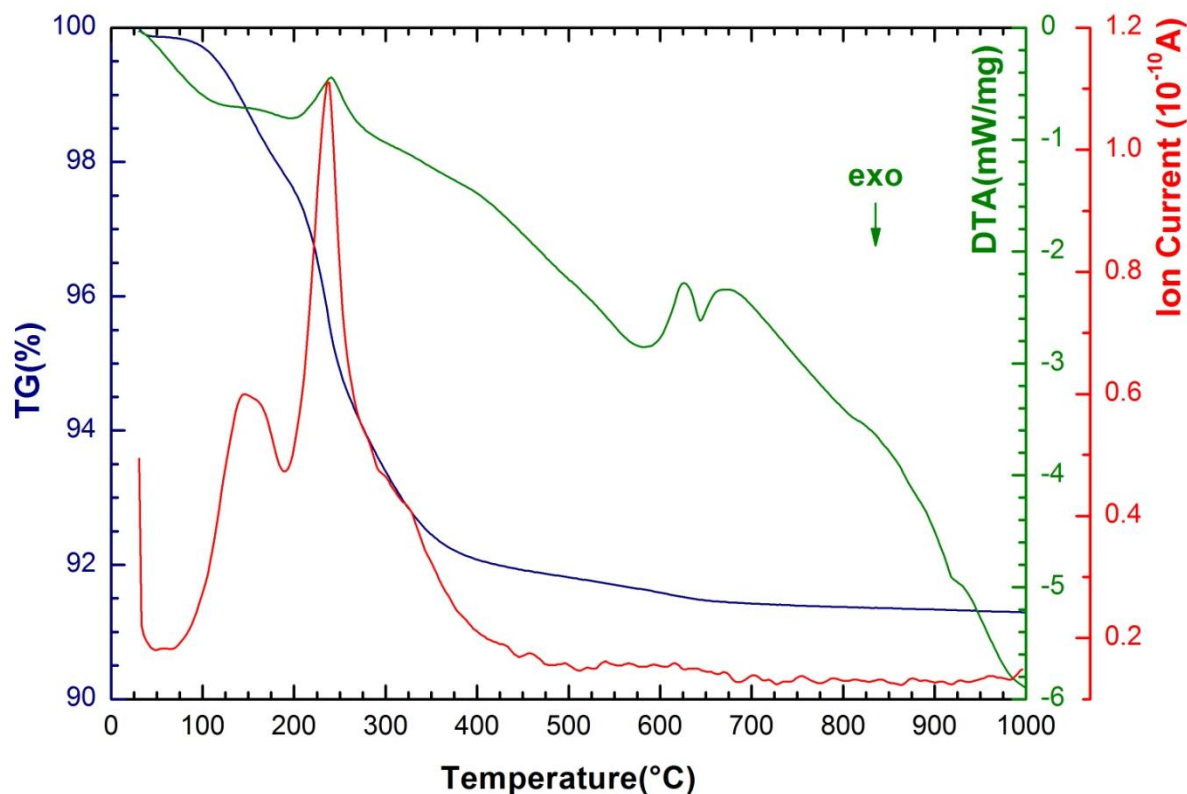
Figure 3.17 TGA/DTA/MS analysis of Na-Nb/CST. Blue-TG curve, green-DTA curve and red-MS curve of 18 amu.

The Na-Nb/CST used for TGA/DTA/MS and variable temperature XRD study was not entirely pure. A small amount of sodium niobate ($NaNbO_3$, marked with *) was observed in this batch synthesis. However, the impurity was too small to contribute to the observed thermal behaviour so was not evident in the DTA measurement. The exothermal stage observed around 900-950 °C indicates the transition of CST from crystalline to amorphous state based on the joint TGA/DTA/MS measurements with variable temperature XRD results. In addition, $NaNbO_3$ became the dominant phase when CST became amorphous at higher temperature, as shown in the XRD patterns of Na-Nb/CST above 700 °C. Furthermore, XRD

patterns show that CST recrystallises above 960 °C, however, this stage is not obviously detected in DTA result.
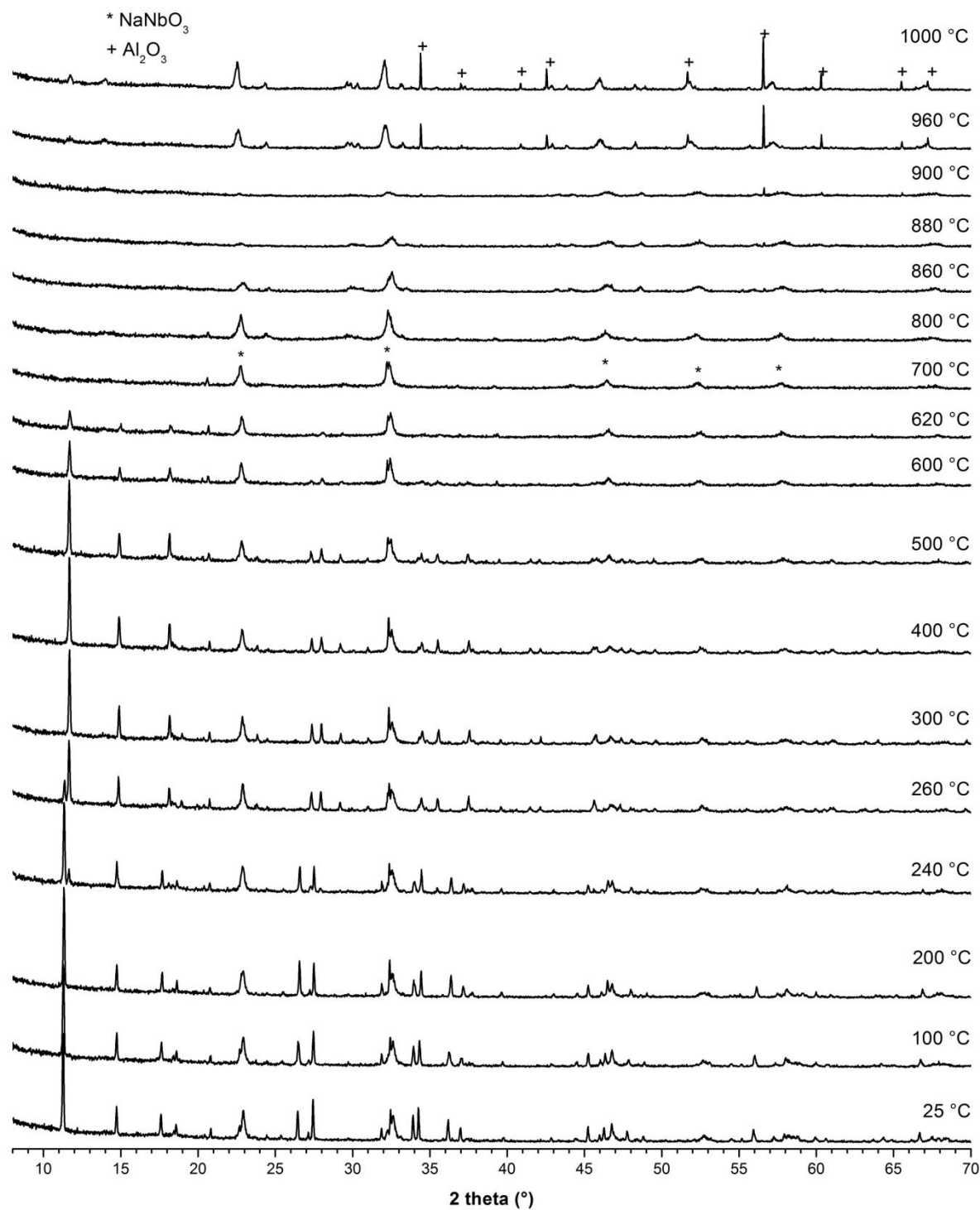
Figure 3.18 XRD patterns of Na-Nb/CST at variable temperature

3.4.5 Ion Exchange

Quantitative analysis using EDX of Na-Nb/CST samples after ion exchange with different Cs loadings was conducted to evaluate the Cs level. Several regions were selected randomly and analysed. Table 3-7 shows the EDX results in terms of atomic percentage. Only a small amount of Cs has been detected. A higher capacity of Cs was expected in Na-Nb/CST due to the structural advantage that more Cs can be accommodated into the less crowded tunnels because less Na^+ was required for charge balance (as described in Chapter 3). However, this was not observed and there was a failure in improving the Cs exchange ability of Na-Nb/CST.

Table 3-7 EDX results of elemental composition (atomic percentage) in non-activated Na-Nb/CST

| | 2 wt.% (N=5) | | 4 wt.% (N=5) | | 6 wt.% (N=5) | | 8 wt.% (N=5) | | 10 wt.% (N=7) | | 12 wt.% (N=9) | |
	Average	Esd	Average	Esd	Average	Esd	Average	Esd	Average	Esd	Average	Esd
O K	69.50	2.25	69.61	3.84	69.23	2.45	70.68	0.76	66.28	5.09	66.62	3.74
Na K	9.68	0.30	10.37	0.91	10.76	1.02	10.27	0.82	11.52	0.92	10.43	1.06
Si K	7.13	0.58	6.81	0.65	6.85	0.39	6.88	0.40	6.98	1.18	7.20	0.86
Ti K	11.50	1.47	11.02	2.38	10.76	2.09	9.72	1.14	12.34	2.41	13.14	2.31
Nb L	1.80	0.21	1.91	0.24	1.98	0.55	2.05	0.65	2.20	0.59	2.17	1.15
Cs L	0.39	0.13	0.28	0.14	0.43	0.21	0.40	0.16	0.68	0.25	0.44	0.18

The same acid pretreatment used for Na-CST was also applied to acid activate Na-Nb/CST before ion exchange. From the XRF results shown in Table 3-8, a higher Cs content than that in activated Na-CST was found. It indicates that, as expected from previously published work, Na-Nb/CST possesses a better potential to incorporate Cs and the activation procedure has improved the ion exchange capability.

Table 3-8 XRF results of HIPed 12 wt.% Cs-exchanged Na-Nb/CST-activated (Fused bead)

Element	Weight %	Atomic %
O	35.80	65.35
Na	1.51	1.92
Si	8.32	8.65
Ti	27.15	16.56
Nb	16.18	5.09
Cs	11.05	2.43

3.5 IONSIV®

IONSIV® IE-911 is a mixture of Na-Nb/CST with 30 mol% of Nb substitution, and 20 wt. % of amorphous $Zr(OH)_4$ as a binder added to increase the column performance. Figure 3.19 shows the XRD pattern of IONSIV®, indicating pure CST.
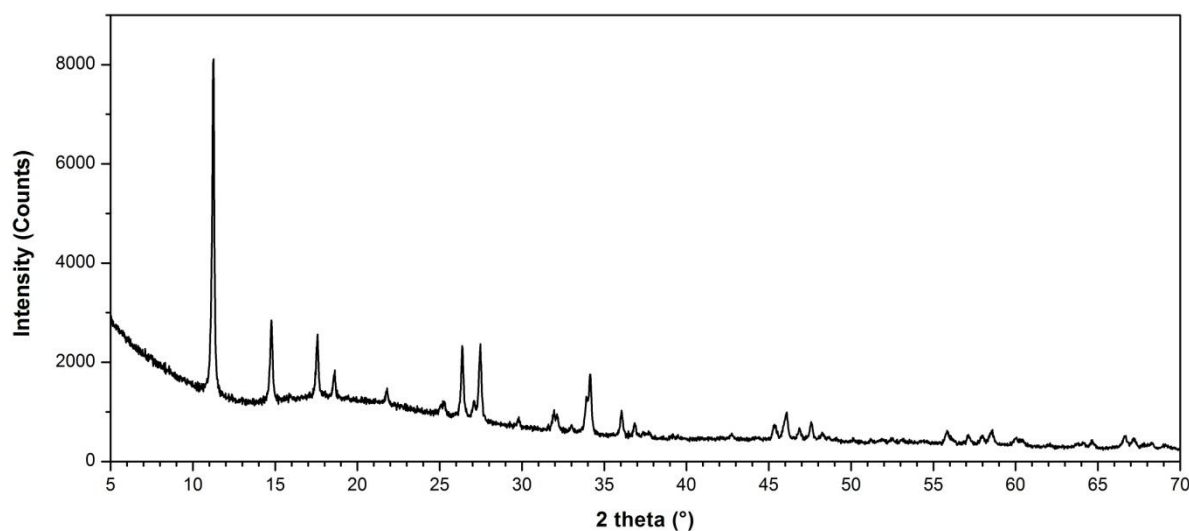
Figure 3.19 XRD pattern of IONSIV® IE-911

3.5.1 Morphology and Elemental Composition

Figure 3.20 shows the morphology of IONSIV® under SEM observation. The bead is sized ~ 600 μm in diameter and with a rough surface. To further investigate the morphology and elemental composition, the bead was ground and reexamined. It was observed that IONSIV® consists of uniform and spherical particles, as shown in Figure 3.20 (b). The size of a single grain is ranged 70-120 nm, measured from Figure 3.21. As it is composed of such small particles, IONSIV® exhibits a remarkably high surface area which results in good ion exchange ability.
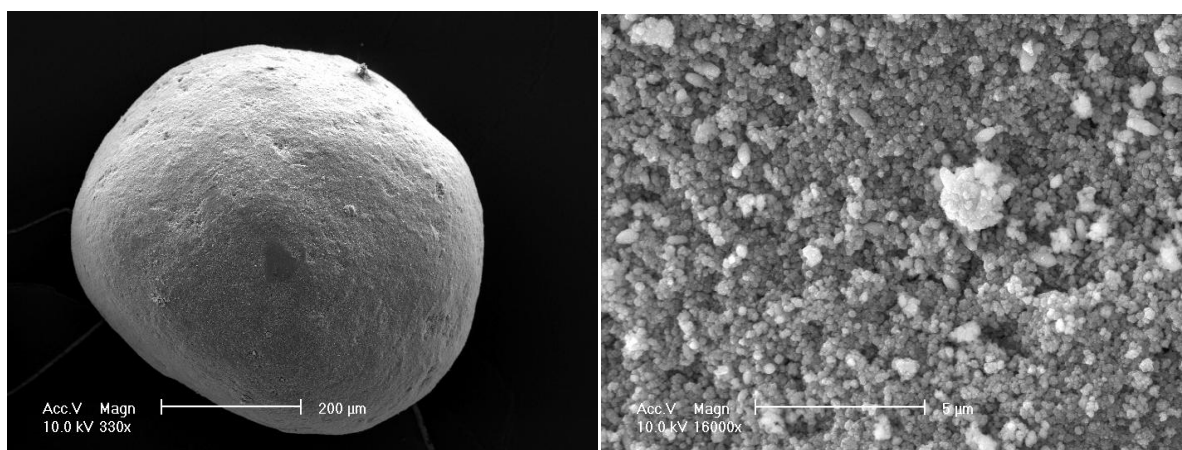
Figure 3.20 SEM/SEI micrograph of (a) IONSIV® bead (×330) (b) ground IONSIV® (×16k)
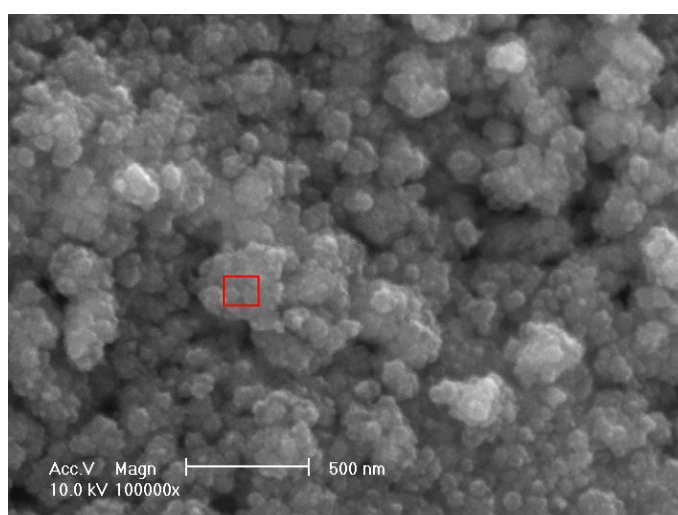
Figure 3.21 SEM/SE image of ground IONSIV® at the magnification of ×100k

The elemental composition of IONSIV® obtained using EDX in the selected area shown in Figure 3.21 and that using XRF are shown in Table 3-9 and Table 3-10, respectively. The Nb/(Nb+Ti) ratios are 29.70% and 26.92% from EDX and XRF results, respectively, suggesting that Nb substitution is close to 30 mol% which was reported officially. In addition, IONSIV® is claimed to be an acid form CST, therefore the small amount of Na detected from

both EDX and XRF is as expected. As IONSIV® is a highly pure product, the difference in elemental composition between bulk material and a selected grain is not significant.

Table 3-9 EDX results of IONSIV® IE-911

Element	Weight %	Atomic %	Molar ratio (normalised to Si)
Na K	0.98	1.06	0.16
Si K	7.58	6.76	1
Ti K	18.38	9.61	1.42
Zr L	9.55	2.62	0.39
Nb L	15.05	4.06	0.60

Table 3-10 XRF results of IONSIV® IE-911 (fused bead)

Element	Weight %	Atomic %	Molar ratio (normalised to Si)
Na K	2.39	3.13	0.36
Si K	8.02	8.60	1
Ti K	20.76	13.06	1.52
Zr K	13.49	4.46	0.52
Nb K	14.92	4.84	0.56

3.5.2 Thermal Behaviour and Phase Transition

TGA/DTA/MS and variable temperature XRD were used to investigate the thermal behaviour and phase transitions of IONSIV® at high temperature. IONSIV® was heated from room temperature to 900 °C under nitrogen atmosphere in the TGA, and in air in XRD. Combined TGA/DTA/MS and variable temperature XRD results are shown in Figure 3.22

and Figure 3.23. A decrease in crystallinity occurred above 225 °C and a completely

amorphous material was observed at 400 °C with a measured 14.4% of total water loss.

IONSIV® recrystallises to $ZrTiO_4$, marked with • in Figure 3.23, at temperature higher

than 775 °C, corresponding to the exothermic phenomenon observed in the DTA trace. Peaks

of Al_2O_3, marked with + in Figure 3.23, are from the sample holder and are detected due to

sample shrinkage after heating. During the heating process, IONSIV® undergoes a series of

changes, from CST to amorphous material, and then to form $ZrTiO_4$. It is clear that the binder

$ZrOH_4$ reacts with CST at high temperature. However, the destruction of the CST structure

when heat is applied also indicates the potential failure of Cs retention and would likely result

in a deleterious effect in terms of long-term and safety storage. Further studies of the effects

of Cs ions' presence and the binder on thermal properties and phase transitions of CST will be

discussed in Chapter 4.
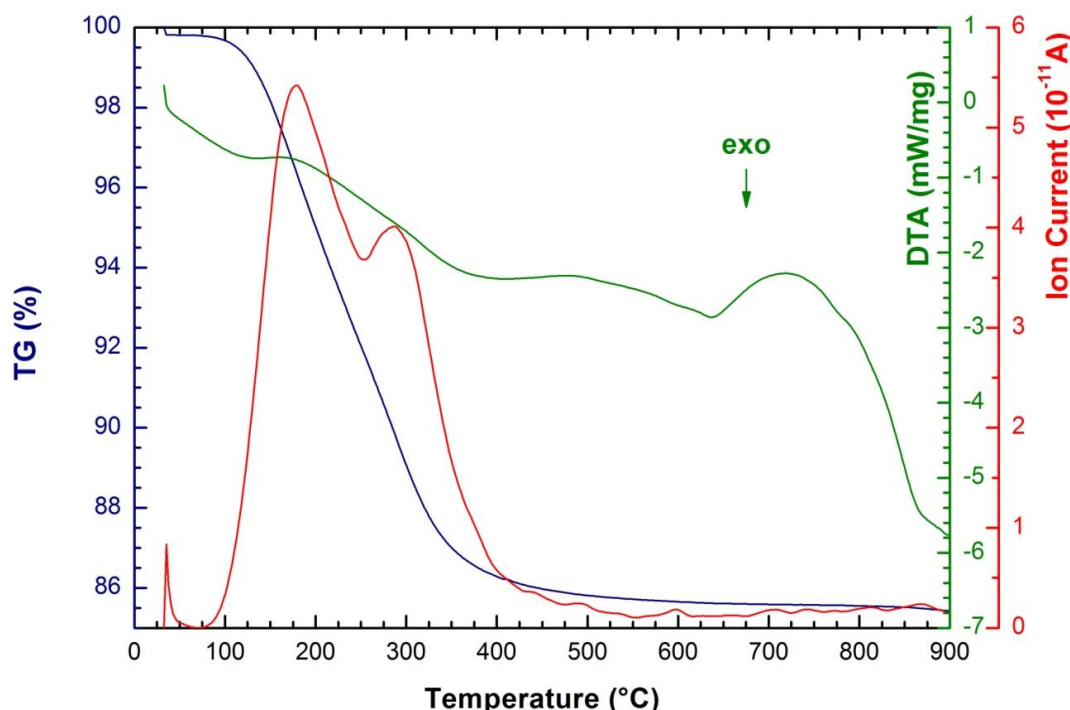
Figure 3.22 TGA/DTA/MS analysis of IONSIV®. Blue-TG curve, green-DTA curve and red-MS curve of 18 amu.
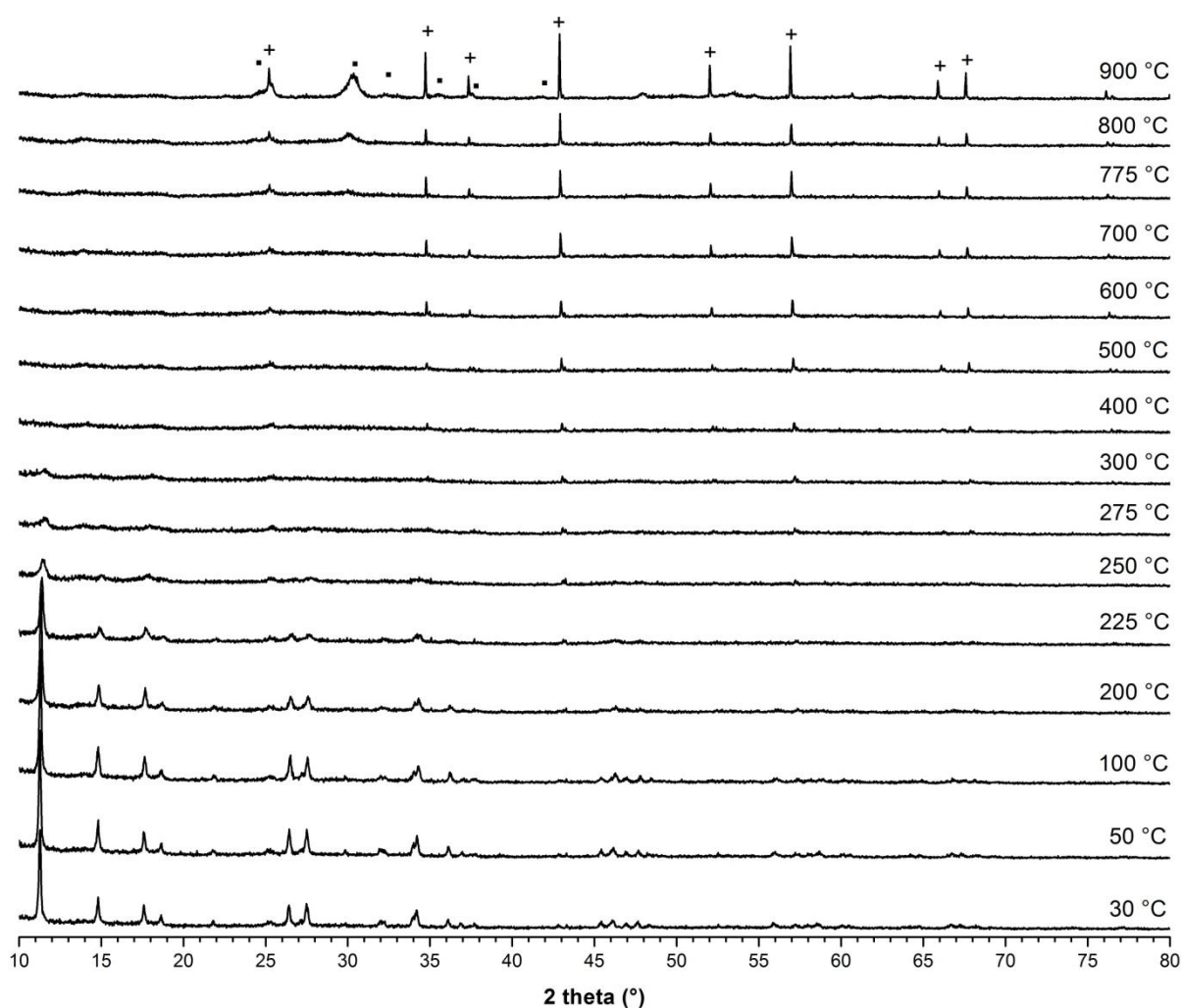
Figure 3.23 XRD patterns of IONSIV® at variable temperature

3.5.3 Ion Exchange

The ion exchange properties of IONSIV® were investigated by impregnating IONSIV® with $CsNO_3$ at different Cs loadings. As mentioned in the introduction of this chapter, pretreating IONSIV® with acid/base may cause negative effects on Cs uptake. Therefore, all the IONSIV® samples tested in ion exchange studies were used without any pretreatment.

After ion exchange experiments, IONSIV® samples were washed with DI water, dried, and fused into beads for XRF analyses. From the XRF results (Table 3-11), the Cs content increases with increasing Cs loading and the Na content reduces with the increasing Cs loading, proving the ion exchange process was carried out successfully and Na sites were replaced by Cs ions.

In addition, the chemical compositions of other elements, such as Zr, Si, Ti and Nb, remained nearly constant suggesting the crystal structure of CST is stable after the ion exchange process. The trend of each element exchanged into the samples as a function of Cs loading as plotted in Figure 3.24.

Table 3-11 XRF results of Cs-exchanged IONSIV® with Cs loading from 0 wt.% to 12 wt.%. Values shown are atomic percentage (at.%)

Element	0 wt.%	2 wt.%	4 wt.%	6 wt.%	8 wt.%	10 wt.%	12 wt.%
Cs	0.00	0.58	0.96	1.73	2.34	2.85	2.92
Na	3.13	2.60	2.03	1.14	0.67	0.34	0.34
Ti	13.07	12.97	12.67	12.50	12.76	12.62	12.64
Nb	4.84	4.88	4.87	4.86	4.85	4.80	4.85
Si	8.60	8.73	9.05	9.10	9.00	9.02	8.86
Zr	4.46	4.37	4.45	4.66	4.39	4.50	4.56

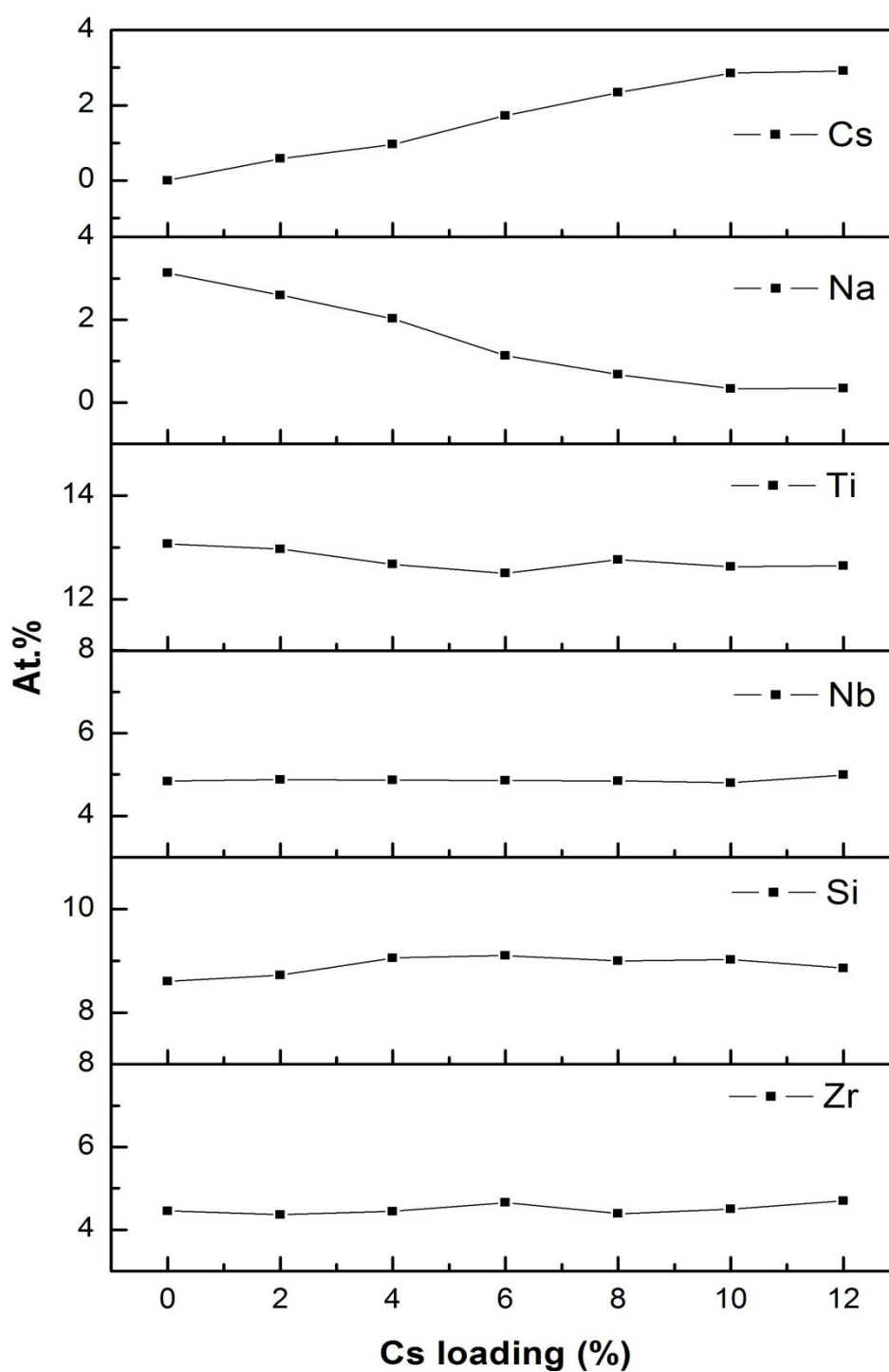Figure 3.24 Plot of atomic percentages of each element in Cs-exchanged IONSIV®s with variable Cs loadings. Shown are the XRF data acquired from fused beads.

To understand the relationship of relative chemical composition between elements with increasing Cs loading, values from Table 3-11 were normalised to Si, giving the values in Table 3-12 and Table 3-13. It illustrates that Nb substitutions with Ti in the samples vary from 27.02 to 28.00%, suggesting the consistency of Nb substitution 30 mol% claimed by UOP and as well as no damage in CST structure after Cs exchanged.

Table 3-12 XRF results of Cs-exchanged IONSIV® with Cs loading from 0 wt.% to 12 wt.%. Values shown are atomic percentage (at.%) normalised to Si.

Element	0 wt.%	2 wt.%	4 wt.%	6 wt.%	8 wt.%	10 wt.%	12 wt.%
Cs	0.00	0.07	0.11	0.19	0.26	0.32	0.33
Na	0.36	0.30	0.22	0.13	0.07	0.04	0.04
Ti	1.52	1.49	1.40	1.37	1.42	1.40	1.43
Nb	0.56	0.56	0.54	0.53	0.54	0.53	0.55
Si	1	1	1	1	1	1	1
Zr	0.52	0.50	0.49	0.51	0.49	0.50	0.51

Table 3-13 Nb substitution and sum of Cs and Na from XRF results. Values shown are the normalised atomic percentage.

	0 wt.%	2 wt.%	4 wt.%	6 wt.%	8 wt.%	10 wt.%	12 wt.%
Nb substitution	27.02%	27.34%	27.77%	28.00%	27.54%	27.55%	27.73%
Cs+Na	0.36	0.36	0.33	0.32	0.33	0.35	0.37
Cs/Cs+Na	0	0.18	0.32	0.60	0.78	0.89	0.90

Furthermore, the sum of Cs and Na contents for exchanged IONSIV® samples remained consistent and the Cs content in the IONSIV® samples increases with increasing Cs loading, reaching equilibrium at a loading between 10 to 12 wt.%. It is suggested that the saturated ion exchange capacity in IONSIV® is about 10 wt.%, giving the composition $H_{1.39}(Cs_{0.32}Na_{0.04})(Ti_{1.40}Nb_{0.53})SiO_7 \cdot xH_2O$. In general, not all channel sites in CST are able to exchange Cs due to space limitation, the reported maximum exchanged composition for Na-CST is $Cs_{0.4}H_{1.6}Ti_2SiO_7 \cdot H_2O$[37] or $Cs_{0.5}H_{1.5}Ti_2SiO_7 \cdot H_2O$[110]. Additionally, IONSIV® utilised in the study is 30% Nb substituted CST with Ti and with $Zr(OH)_4$ as binder, a more favourable Cs incorporation is expected due to a slightly larger unit cell of Na-Nb/CST and a less framework expansion occurred. However, the enhanced selectivity of IONSIV® than that of Na-CST was not observed in the ion exchange study.
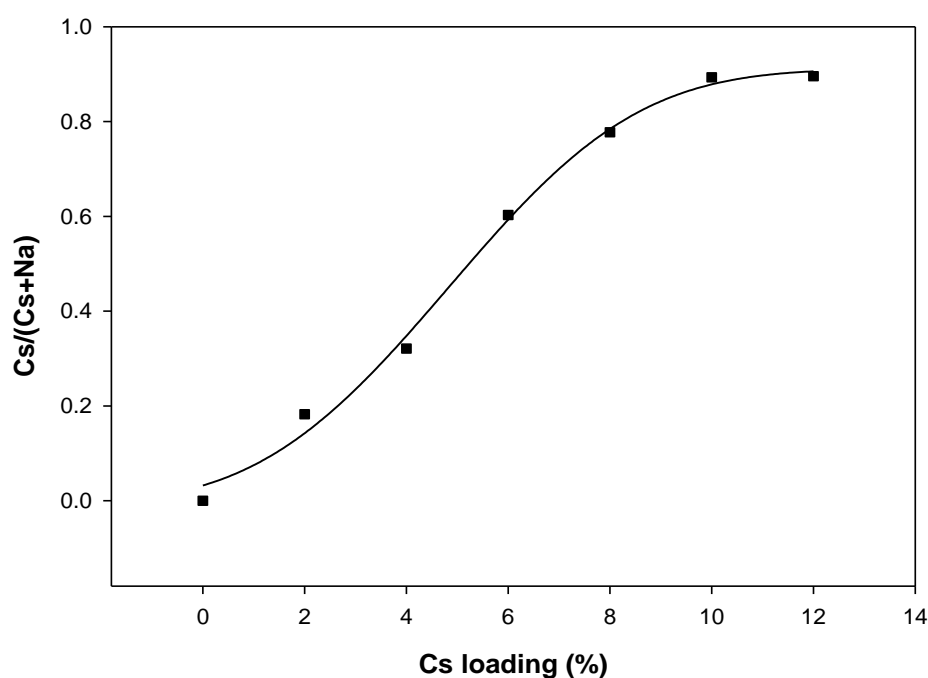

Figure 3.25 Cs to (Cs+Na) ratio as a function of Cs loading

3.6 Conclusions

Framework crystalline silicotitanates, Na-CST and Na-Nb/CST, have been successfully synthesised using the hydrothermal method. Synthesis optimisation, structure solution, chemical composition, morphology, and thermochemistry were investigated using XRD, XRF, SEM/EDX, TGA and Rietveld refinement. The commercial CST product, IONSIV® IE-911, was also studied.

Both Na-CST and Na-Nb/CST can be directly obtained hydrothermally, but sometimes a small amount of an impurity, natisite and Nb_2O_5 in Na-CST and Na-Nb/CST, respectively, can be found. Natisite can be easily removed by applying a 2-step treatment; however, a decrease of crystallinity was sometimes noticed after this treatment. The thermal studies show that CSTs are not stable at higher temperature due to a phase transition to an amorphous material, indicating a potential risk of Cs leaching in terms of long-term storage. The structure information showed that Na-Nb/CST has a slightly larger unit cell than that of Na-CST, thus an enhanced Cs affinity was achieved by accommodating more Cs into the less crowded tunnels. IONSIV® possesses a far smaller particle size than as-synthesised Na-CST and Na-Nb/CST which is beneficial for ion exchange process. From the ion exchange study of IONSIV®, an increase of Cs content and a decrease of Na content were observed as well as nearly constant Zr, Si, Ti and Nb contents with increasing Cs loading, proving a successful Cs exchange process and no damage to the CST structure. However, in the cases of Na-CST and Na-Nb/CST the maximum Cs composition was not achieved, the optimisations of ion exchange condition and activation process still need to be further investigated.

Chapter 4   Immobilisation of Cs from Crystalline

Silicotitanate by Hot Isostatic Pressing

4.1 Introduction

IONSIV® IE-911 is a commercial mixture of a CST with the approximate formula of $(H_3O)_xNa_y(Nb_{0.3}Ti_{0.7})_4Si_2O_{14}\cdot zH_2O$ - where x~2, y~1 and z~4, and a $Zr(OH)_4$ binder. Studies on the mechanism of the good Cs ion selectivity in crystalline silicotitanate[117, 124], the crystal structure of Cs-exchanged CST[37, 116], and the microstructure and phase transformation caused by radiation and heat[137] have been carried out. IONSIV® IE-911 has been widely applied in the nuclear industry as an inorganic ion exchanger to separate ^{137}Cs and ^{90}Sr relative to Na^+, K^+ and H^+ from waste streams due to its excellent selectivity and great performance in a broad pH range.[36] However, options for dealing with a large amount of spent ion exchanger containing long half-life nuclides are still being sought.

The principle used for the immobilisation of radioactive waste materials is to provide a chemically, thermally and radiologically stable and leach-resistant material that can be more easily and safely stored or disposed of than the current liquid or solid wastes.[4] In practice, a monolithic material is usually required to be a viable wasteform. For long term strategy, simple encapsulation of highly radioactive waste in an inert matrix without chemically incorporating the waste elements into a stable host lattice would not normally be employed as it is not considered safe to be disposed of in an underground repository.

Hot isostatic pressing (HIPing) involves heating a powder sample in a mould whilst simultaneously applying pressure and has been utilised for nuclear waste treatment in the past fifteen years.[66, 84, 85, 138-141] It can be used as a route for densifying and consolidating materials with high-level radioactive wastes to produce a monolithic wasteform prior to final disposal. Compared with glass wasteform technology, the waste is enclosed in a can and processed at relatively low temperature under HIP conditions. Therefore there are no high temperature volatility losses and no expensive off-gas emission processing system is required. HIPing provides higher waste loadings than vitrification and also the flexibility in handling problematic waste. It was reported by Harker et al.[83] that consolidation of borosilicate glass containing simulated SRS HLW with waste loadings of up to 50 mass% was successful achieved by hot isostatic pressing at low temperature at 850 °C.

In a later study, Raman[138] studied glass-ceramic wasteforms developed by adding glass and crystal forming components to a high level nuclear waste calcine simulatant containing Cs, Sr and Ce, and then hot isostatic pressing the mixture at 1000 °C and 138 MPa. The resultant wasteforms were composed of zircon, beddeyelite, apatite, fluorite, greenockite and boroaluminosilicate glass. The crystal nucleating, glass forming and volatilising components of the calcine are partitioned into the crystalline and glass phases, such that 95 wt.% of the waste components stoichiometrically reside in the crystalline phases. This results in a high waste loading of 60-80 wt.% calcine in the total glass-ceramic. Both glass and ceramic contribute to high chemical durability (< 1 g·m^{-2}·day^{-1} for all the elements) that resulted from the growth of stable crystalline phases and avoidance of glass devitrification. HIP processing is considered environmentally safe due to the entire processing occurs within the enclosed system and no secondary wastes are produced.

Studies of the interaction between the wasteform and a HIP can have also been carried out.[66, 84, 85] Three titanates, Synroc, pyrochlore and zirconolite, were chosen to incorporate actinides and then HIPed at 1280 °C/100 MPa/3 h. It was reported in these three studies that actinides are mainly incorporated into crystalline phases and the low elemental release rates exhibited that these phases were very durable. It was also found that the reactions at the interface between the titanates and stainless steel do not alter the valence of actinides or generate undesirable phases. Therefore, it was believed that actinides still remain in a stable wasteform created using HIP conditions. The use of stainless steel cans under HIP conditions does not affect the integrity of the wasteform and are unlikely to have a detrimental effect.

Carter et al.[142] investigated the compositional flexibility of pyrochlore-rich wasteforms to incorporate U-rich waste from ^{99}Mo production under HIP conditions. The baseline waste form composition (containing 40 wt.% UO_2) was adjusted by either varying the waste loading or varying the precursor materials. HIPed samples in both cases had very similar phase assemblage but only the amounts of each phase varied. These changes had little effect on chemical durability of the wasteform and the normalised leach rates are very comparable with those from Synroc-C, a well-known stable wasteform for U immobilisation. The results demonstrated that HIPing titanate ceramics is a robust and flexible way for immobilisation of U-rich waste streams.

Other work done by Vance et al.[143] developed the encapsulation of volatile ^{129}I in low-melting metal by hot pressing AgI-bearing alumina beads surrounded by tin powder at 200 °C. Their recent work[144] investigated the sodalite/glass prepared by HIPing at 850 °C/100 MPa for immobilisation of fission product-bearing waste KCl-LiCl pyroprocessing salts. These

valuable results demonstrate again that HIPing is a promising route for radioactive waste immobilisation.

To examine further the technological applicability of HIPing in Cs immobilisation, the high temperature behaviour of Cs-exchanged IONSIV® under HIPing conditions and also the chemical durability of the Cs-IONSIV® products after HIPing were investigated.

One particular focus is the nature of the Cs phase(s) formed in the process. Hollandite, one of the major titanate phases of Synroc, a multiphase ceramic matrix also containing zirconolite and perovskite phases, has been widely studied and shown its promise for immobilising Cs and corrosion products. The hollandite group of minerals has the general formula $A_xB_yC_{8-y}O_{16}$, where $x \leq 2$. In Synroc type hollandite, the A position is occupied by large mono- or divalent cations (Na^+, K^+, Cs^+, Rb^+, Sr^{2+}, Pb^{2+}, Ba^{2+}), the B position by Al^{3+} and Ti^{3+}, and C position by Ti^{4+}. This material has an added benefit that it retains Ba, a decay element of Cs, where charge balance is maintained by Ti^{4+} reducing to Ti^{3+}. Thus Ba can be incorporated elegantly so that hollandite is suitable for long-term storage.

It is of interest to see if hollandite can be produced from HIPing IONSIV® when a suitable condition is created. Most of the Synroc varieties (except for Synroc-C) were produced via hot pressing route. It was reported that three criteria must be met to obtain a hollandite ceramic without minor phases detrimental to the chemical stability of the matrix:[64]

(i) The trivalent elements (Al^{3+} and Ti^{3+}) must be present in sufficient quantities;

(ii) The trivalent elements must be not represented by Al^{3+} alone, but also by Ti^{3+};

(iii) The presence of 'reduced rutile' TiO_{2-x} is also indispensable to prevent the formation of secondary phases.

Therefore, in some experiments, three reductants, metal Ti, Fe and Al, were selected and mixed with Cs-IONSIV® before HIPing. The effect of this metal addition on the phase composition of IONSIV® during HIP is also investigated.

4.2 Experimental

4.2.1 HIPing

Sample pre-treatment

All the pure CST and IONSIV® samples as well as the Cs-exchanged ones were prepared for HIPing. Samples were ground and sintered at 800 °C for 12 hours in order to dehydrate and prevent water re-absorbing into the samples.

Can preparation

Compared with stainless steel, mild steel was chosen as the raw material of the HIP-cans for its less reducing environment, ease to source, good weldability and easy deformation at the high temperature and pressure under HIPing conditions. HIP-cans were designed by connecting two tubes with different diameters and a base plate, as shown in Figure 4.1.

- Top tube (connected to the outgas rig): 3 mm thick wall, 0.6 cm inner diameter, 1/2 inch (1.27 cm) outer diameter, and at least 15 cm in length. 10 cm from the top was saved for crimping.

- Bottom tube: 2 mm thick wall, 1.2 cm inner diameter, 5/8 inch (1.59 cm) outer diameter, and 3 cm in length.

- Base plate: 2 mm thick, 5/8 inch (1.59 cm) in diameter.

Tubes were cut to the required length, and degreased in an ultrasonic acetone bath for 10 minutes before welding. All the joins were welded using tungsten inert gas (TIG) welding. Before filling in powders, these capsules were checked by a leak detector.
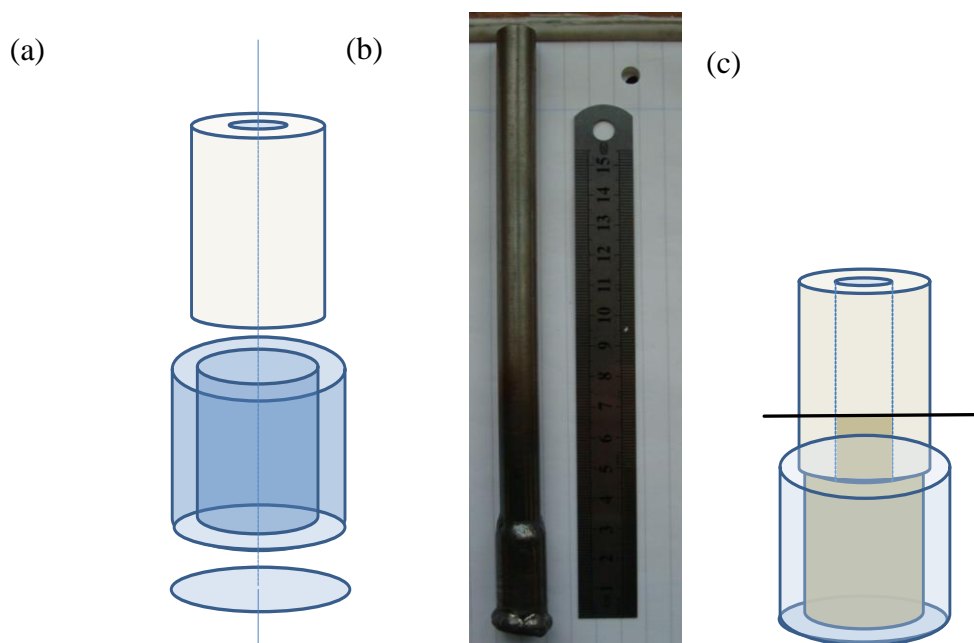
Figure 4.1 HIP-can design (a) The sketch of the design (b) HIP-can after welding (c) The diagram of design after sample filling.

Sample filling/crimping/welding

The samples were compacted firmly by filling small amount of sample each time and then placing the cans on a vibration table to increase the tap density. A ball of quartz wool was packed on the top of the powder to prevent it being sucked up into the vacuum system. The HIP-cans were placed in the outgas rig and vacuumed overnight at 10^{-5} mbar to ensure vacuum tightness. After evacuation was completed, the cans were double-crimped at the mark of sample height and TIG-welded to finish.

HIPing

HIPing was carried out in a EPSI Lab HIP facility operating at 1100 °C, 190 MPa for 2 hrs under an argon atmosphere. The heating and cooling rates were both set at 5 °C per minute.

Can opening

The tubes were firstly opened in a cutting machine with an Al_2O_3 blade. The remaining mild steel capsules were chemically dissolved away by soaking in diluted (~ 20%) nitric acid.

4.2.2 Characterisation

4.2.2.1 SEM/EDX

HIPed samples were sectioned into 5-7 mm thick discs in a cutting machine running with an aluminium oxide blade. The discs were hot-mounted at 175 °C in conductive bakelite. Mounted samples were then prepared by a 4-step metallographic grinding/polishing procedure in a lapping and polishing machine. All of the grinding and final polishing was carried out in a Struers Pedemin DAP-7 polisher. The details of grinding and polishing process for SEM specimens were listed in Table 4-1.

Table 4-1 Grinding/polishing routes for SEM sample preparation

Step	Surface	Lubricant	rpm/Force(N)	Time(mins)
Plane grinding	MD-Primo220	water	250/15	5
Fine grinding	MD-Largo	9 μm diamond paste	125/5	4
Diamond polishing	MD-Dac	3 μm diamond paste	125/5	4
Final polishing	MD-Nap	1 μm diamond paste	125/5	2

Backscattered electron (BSE) imaging with an EDX system was used to examine the microstructure and chemical composition of the samples. For BSE mode observation, polished samples were loaded in the SEM without carbon coating. All the investigations were carried out using a Philips XL30 ESEM-FEG with an Oxford Inca 300 EDX system operating at 10 kV.

4.2.2.2 TEM/EDX

HIPed samples were manually ground to obtain fine powders. The powders were dispersed and sonicated in ethanol for 5 minutes. A few drops of the supernatant liquid were then transferred to the holey carbon film of a Cu-grid. Once the ethanol evaporated, it left a distribution of particles on the film. The samples were examined with an FEI Philips TECNAI F20 operating at 200 kV with an Oxford Inca EDX system to study the microstructure and elemental composition.

4.2.2.3 XRF

Fused borate glass beads were analysed within X-ray fluorescence spectrometry (Bruker S8 Tiger WDXRF) for the determination of the elemental compositions. Circular glass beads with flat surface were prepared by mixing 0.35 g of sample with lithium tetraborate in 1:10 ratio, and the mixture was placed in a platinum/gold crucible and heated at 1050 °C for 7 mins. A non-wetting agent, ammonium iodide (NH_4I), was added to help the bead exfoliate from the crucible. The bubbles in the fusion were removed by swirling the crucible if needed. After cooling, the beads were analysed.

4.2.2.4 XRD and Rietveld Refinement

The phase assembly of HIPed Cs-IONSIV® samples was investigated using XRD and Rietveld refinement. HIPed Cs-IONSIV® samples were ground and data collected with a Bruker D8 Advance diffractometer using Cu K_α radiation operating in transmission mode. Diffraction patterns were collected between 2 theta of 5 and 90° at a step size of 0.0197° with a LynxEye Si-strip detector.

Rietveld refinements were performed using the General Structure Analysis System (GSAS) program. The starting values of the atomic positions, lattice parameters and displacement parameters for each phase were taken from the literature as listed in Table 4-2.

Table 4-2 Starting models for the phases used in Rietveld refinement

Phase	Space group	References	Year
$(Ti_{0.712}Nb_{0.288})O_2$	$P4_2/mnm$	Okrusch et al.[145]	2003
$ZrSiO_4$	$I4_1/amd$	Torres et al.[146]	2002
$NaNbO_3$	$Pbma$	Hewat[147]	1974
$Zr_{0.5}Ti_{0.5}O_2$	$Pbcn$	Troitzsch et al.[148]	2005
SiO_2	$P3_221$	Kihara[149]	1990
$Cs_2TiNb_6O_{18}$	$P\text{-}3m1$	Desgardin et al.[150]	1977
$Cs_2ZrSi_6O_{15}$	$C2/m$	Jolicart et al.[151]	1996

For multi-phases refinements, due to the large number of variables, the atomic displacement parameters were kept at default values of $U_{iso} = 0.02$ Å^2. Lattice parameters

were optimised after the scale factor had converged and the background was graphically fitted. The peak profiles were fitted to symmetric pseudo-Voigt functions (Function type 3).

4.3 HIPed Cs-exchanged Na-CST

4.3.1 Non-activated Na-CST

The microstructure of HIPed Cs-exchanged Na-CST without acid activation was investigated in SEM/BSE. Under SEM observation, the sample exhibits random microstructure, as shown in Figure 4.2. There are a few large crystallites with irregular shape present. Those grains show dark contrast in BSE mode, indicating no heavy elements are present.
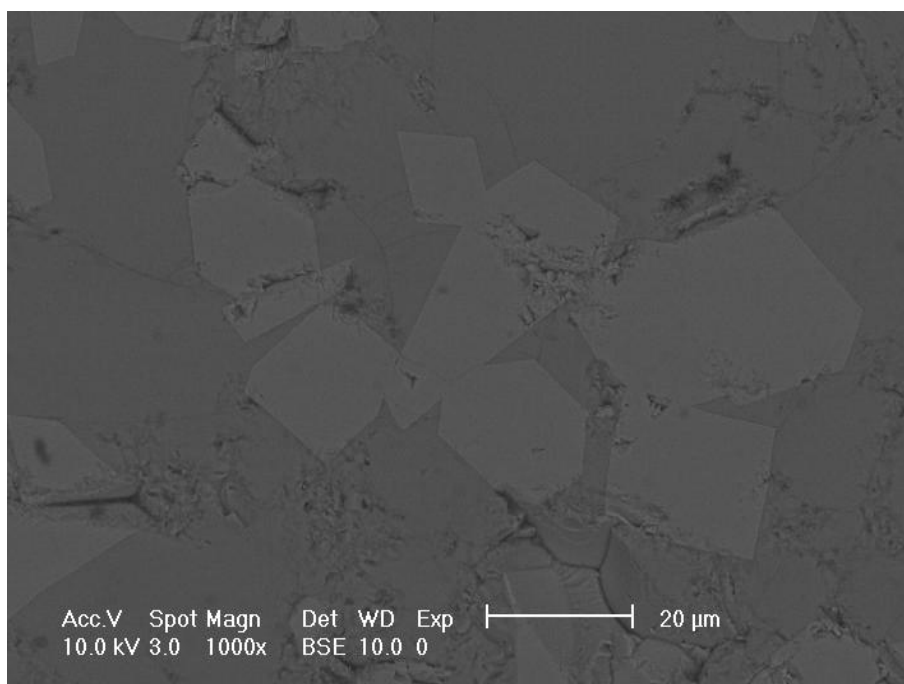

Figure 4.2 SEM/BSE micrograph of HIPed Cs (12 wt.%)- exchanged Na-CST without acid pretreatment applied.

XRD pattern of HIPed 12 wt.% Cs-exchanged Na-CST also supports the SEM findings. No significant difference was observed in the 12 wt.% of Cs-exchanged Na-CST compared with that of pure Na-CST after HIPing (shown in Figure 4.3). It is suggested that the Cs level in exchanged Na-CST was too small to cause any related phase transition during HIPing. However, the phase identification was not able to be completed so far because no matching phase can be found in the PDF database, giving no direct evidence to examine the phase assembly.
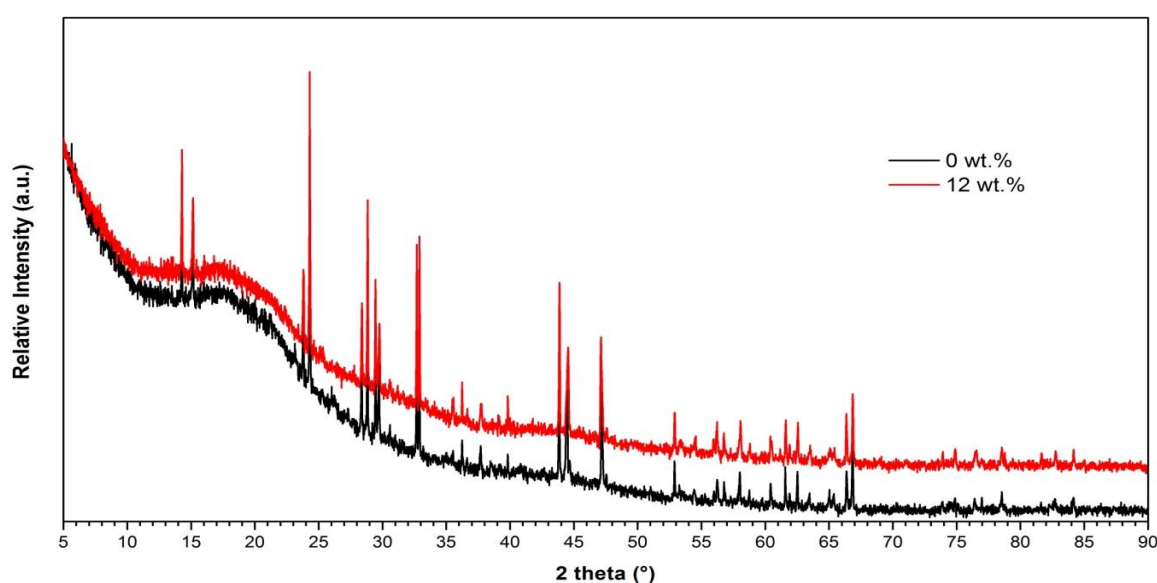
Figure 4.3 XRD patterns of non-activated Na-CST, 0 and 12 wt.% Cs-exchanged Na-CSTs after HIPing

4.3.2 Acid Activated Na-CST

To understand the effect of the presence of Cs on the phase composition of Na-CST-activated after HIPing, 12 wt.% Cs-exchanged Na-CST-activated was analysed using XRD. The XRD pattern shown in Figure 4.4 confirms the sample was thermally decomposed, and unfortunately only one phase, TiO_2-Rutile is present. This finding was also supported by SEM/BSE images and EDX analysis of selected areas.

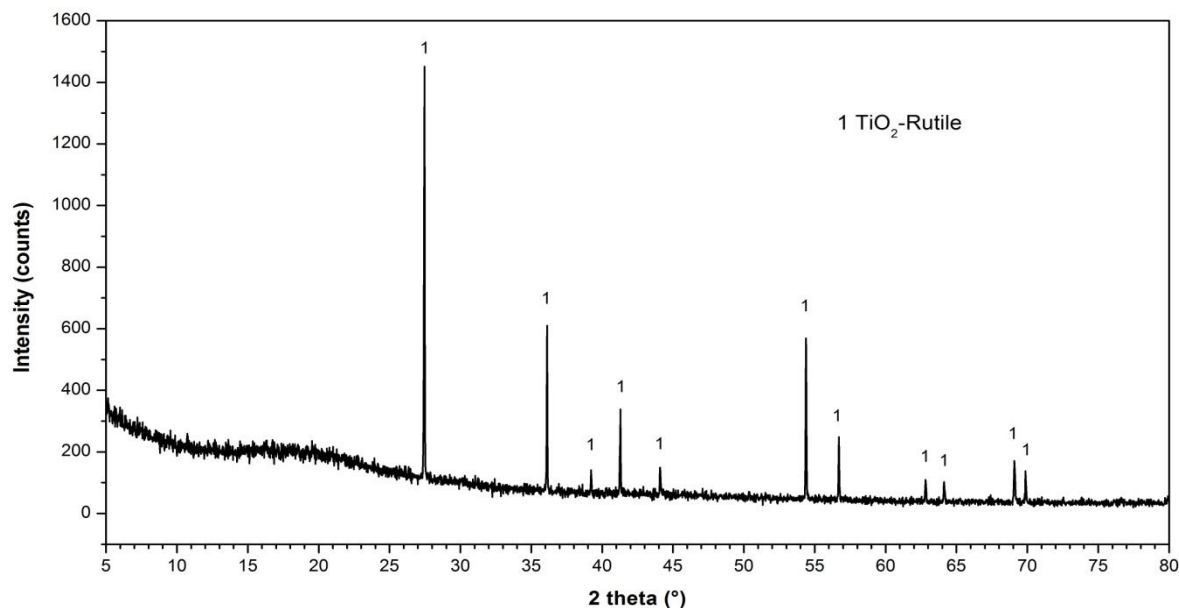Figure 4.4 XRD pattern of 12 wt.% Cs-exchanged Na-CST-activated after HIPing.

The SEM/BSE image (shown in Figure 4.5) reveals that there is one main dark phase of square morphology randomly dispersed in the other bright sections. EDX results confirmed that the dark particle is TiO_2 and the other elements, such as Na, Cs, and Si, were located in the irregular areas, indicating amorphous substances.

This result is of concern because the durability of the particular element is highly relevant to the nature of the host phase. It also means that a high Cs leach rate is expected due to the lack of crystalline phases for retaining Cs ions in the structure. Although HIPing provides an encapsulation in which the radioactive waste can still be well-sealed, there is a risk that the leachable Cs releases from Na-CST material to the environment will occur over a long time scale. HIPed Na-CST is not considered the best candidate for radioactive waste treatment in regards to a long-term solution.

(A)
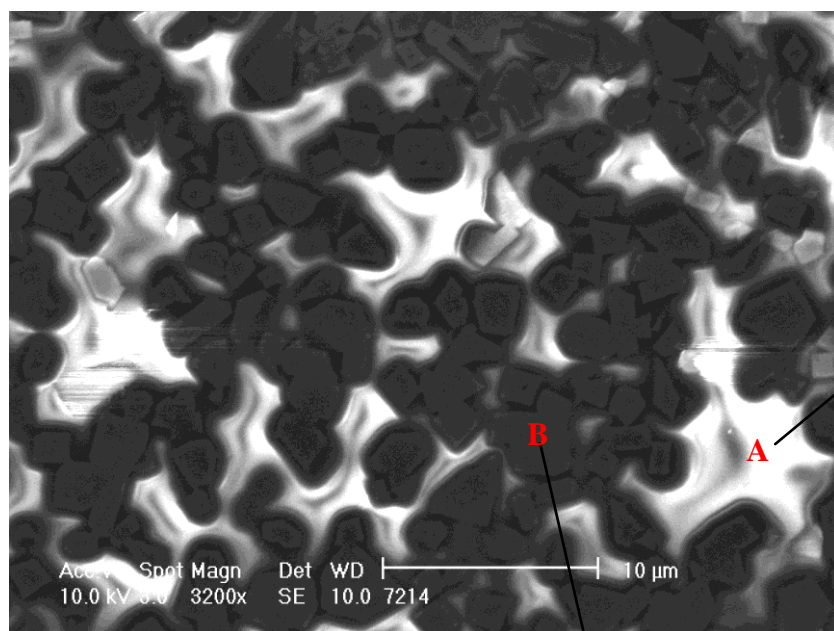
Element	Weight%	Atomic%
O K	43.02	62.83
Na K	9.76	9.92
Si K	23.17	19.28
Ti K	11.97	5.84
Cs L	12.08	2.12
Totals	100.00	

(B)
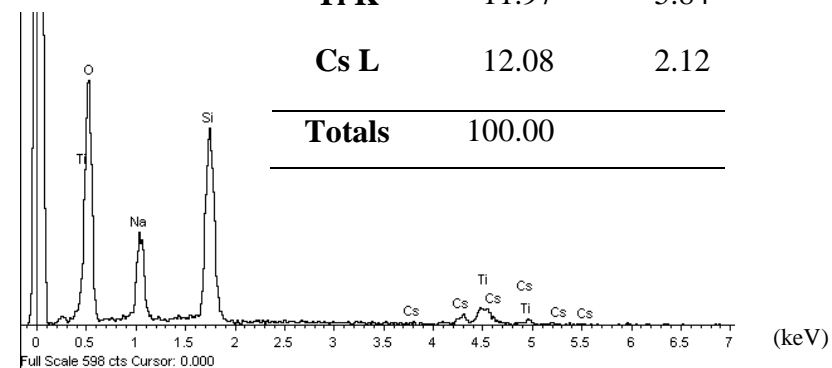
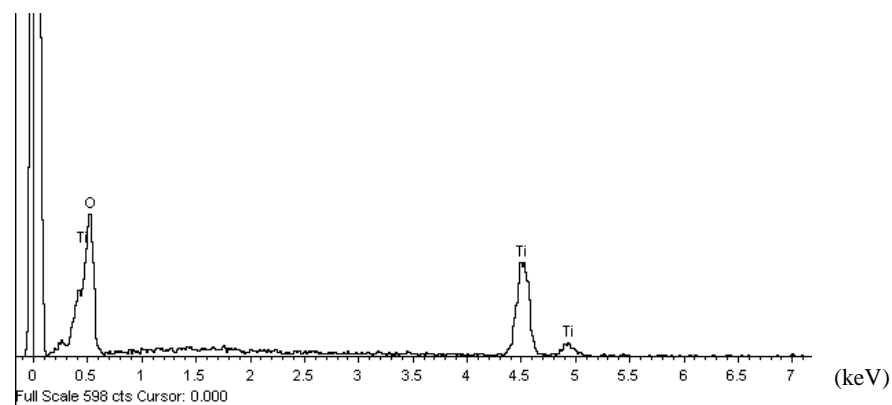| Element	Weight%	Atomic%
O K	42.39	68.78
Ti K	57.61	31.22
Totals	100.00	

Figure 4.5 SEM/BSE image and EDX analysis of HIPed 12 wt.% Cs-exchanged Na-CST-activated.

4.4 HIPed Cs-exchanged Na-Nb/CST

4.4.1 Non-activated Na-Nb/CST

SEM micrographs of HIPed Cs-exchanged Na-Nb/CST without acid pretreatment at different Cs loadings all showed very similar microstructure. Figure 4.6 depicts the SEM micrograph of HIPed 12 wt.% Cs-exchanged Na-Nb/CST without acid treatment. It is composed of some large crystallites with rod shape morphology comprised primarily of Ti, Na, Si and O, as revealed by an EDX analysis, as well as some smaller particles, comprised of Na, Nb and O, with brighter contrast. However, there is some inaccuracy as the larger size of the incident beam can excite an area larger and deeper than the expected single grain, hence will give rise to an unreliable elemental output. Thus, the direct phase identification using EDX was not achieved.
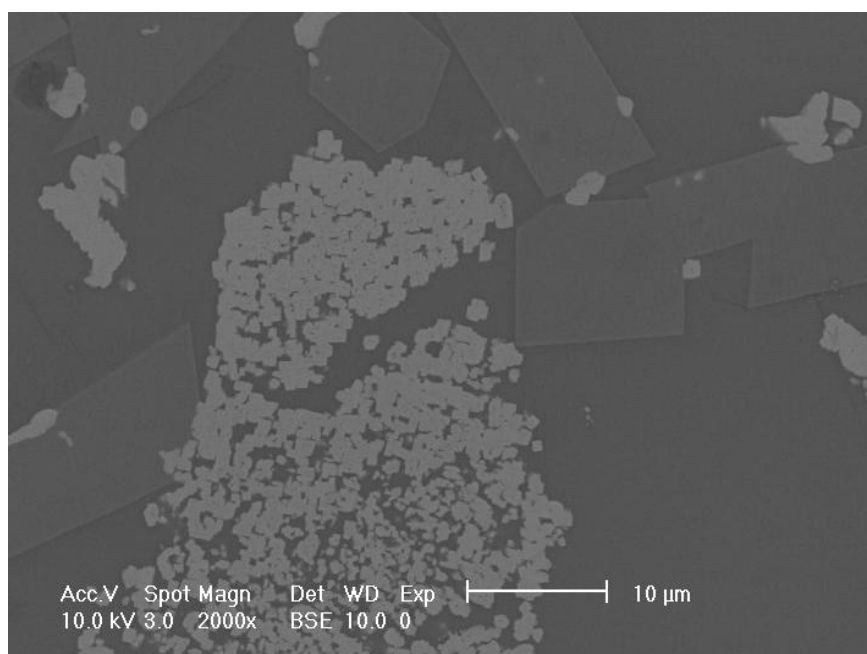

Figure 4.6 SEM/BSE micrograph of HIPed 12 wt.% Cs-exchanged Na-Nb/CST without acid pretreatment.

XRD patterns shown in Figure 4.7 also illustrate that no obvious change between pure HIPed Na-Nb/CST and that with 12 wt.% Cs loading exchanged. The only phase which was identified so far is $NaNbO_3$, corresponding to the finding in EDX. It is proven that the Cs ion exchange was not successful and a further treatment is required to improve the Cs exchange capacity.
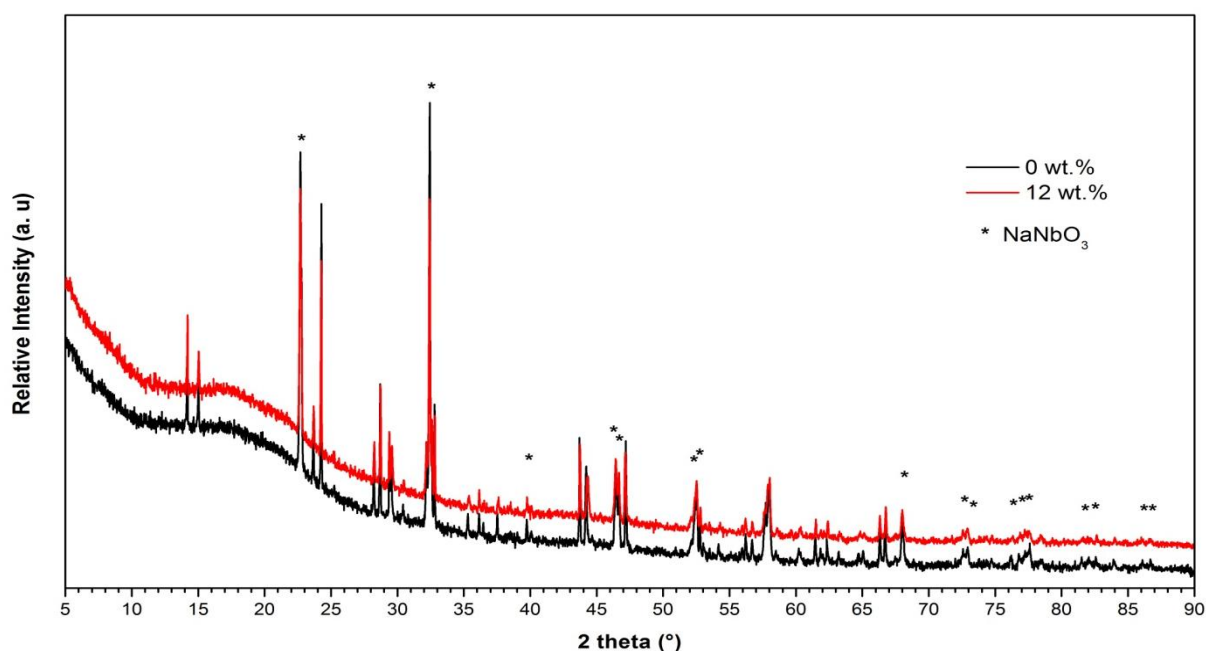
Figure 4.7 XRD pattern of HIPed 12 wt.%Cs-exchanged Na-Nb/CST without acid pre-treatment.

4.4.2 Acid Activated Na-Nb/CST

The main phase observed in the HIPed Cs-exchanged Na-Nb/CST-activated (shown in Figure 4.8) is clusters of grains with bright contrast. At higher magnification, small crystallites of square/rectangular shape morphology were noticed mounting inside the bright grains. The identification of other phases was not succeeded using EDX as the particle size is too small to distinguish individual grains.
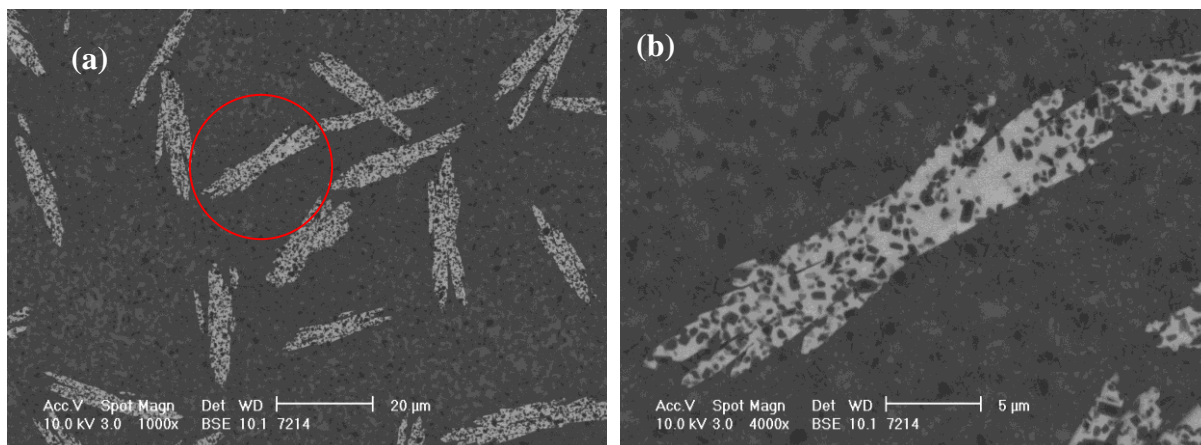
Figure 4.8 SEM/BSE micrographs of HIPed 12 wt.% Cs-exchanged Na-Nb/CST-activated. (a) Magnification of ×1,000 (b) Zoom-in observation of selected area in (a).

The XRD pattern of HIPed Cs-exchanged Na-Nb/CST-activated shows a better insight into the effect of Cs on thermal conversion during the HIPing process. Cs-Na-Nb/CST was thermally converted after HIPing to TiO_2-Rutile with Nb^{4+} substitution, Ti_2O_3, Na_2SiO_3 and a Cs-containing phase- $Cs_8Nb_{10}Si_6O_{41}$. The convincing phase indexing reveals that elements are incorporated into the phases with lower oxidation states, for example, Nb into $(Ti, Nb^{IV})O_2$ and Ti into $Ti^{III}_2O_3$, due to the reducing environment that HIP creates.
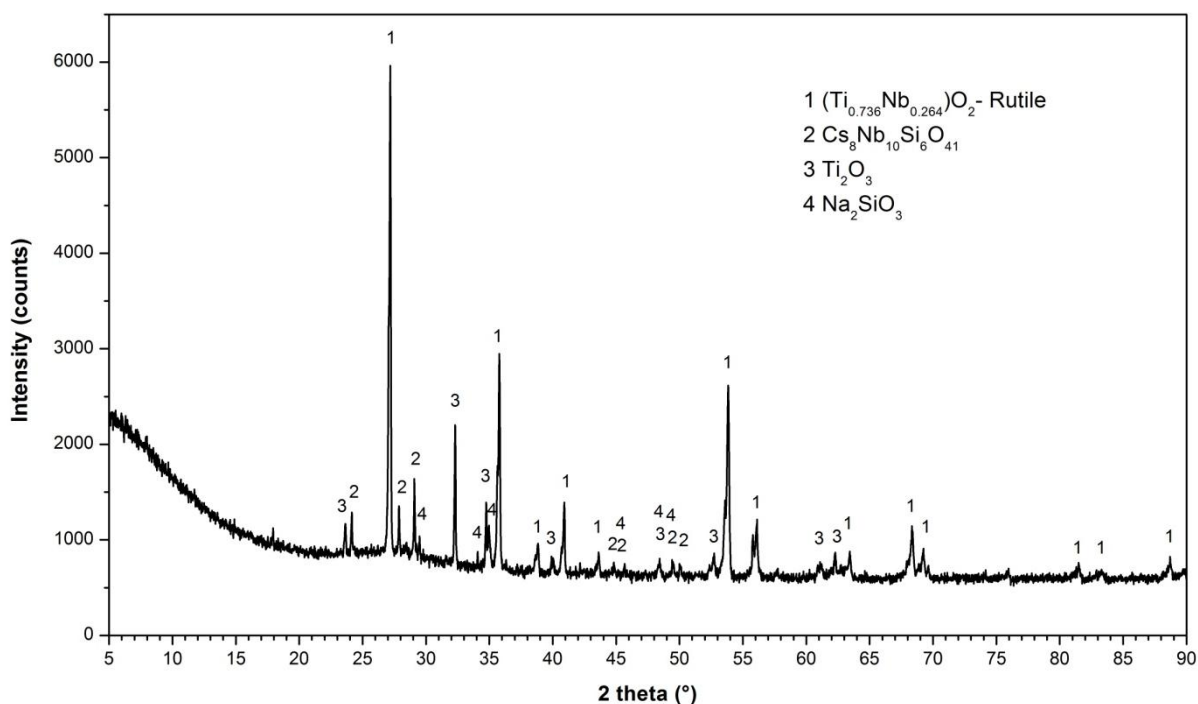
Figure 4.9 XRD pattern of acid activated 12 wt.% Cs-exchanged Na-Nb/CST after HIPing.

It is of particular importance to understand where Cs locates in the material. It was indicated that Cs in the HIPed Cs-Na-Nb/CST sample was incorporated into the phase $Cs_8Nb_{10}Si_6O_{41}$. However, the structure has not been intensively studied so that the Cs behaviour related to the structure properties remains unclear. Crosnier et al.[152] reported that this structure crystallises in the hexagonal system, space group $P6_3/mmc$ with $a = 7.342(1)$ Å, $c = 22.166(3)$ Å. The structure is built up from NbO_6 octahedra sharing corners and three-membered Si_3O_9 single rings sharing corners with the octahedra to form a three-dimensional framework. Cs atoms are well-situated into the cavities of the framework, as shown in Figure 4.10, a great Cs incorporation ability in this crystalline phase is anticipated.
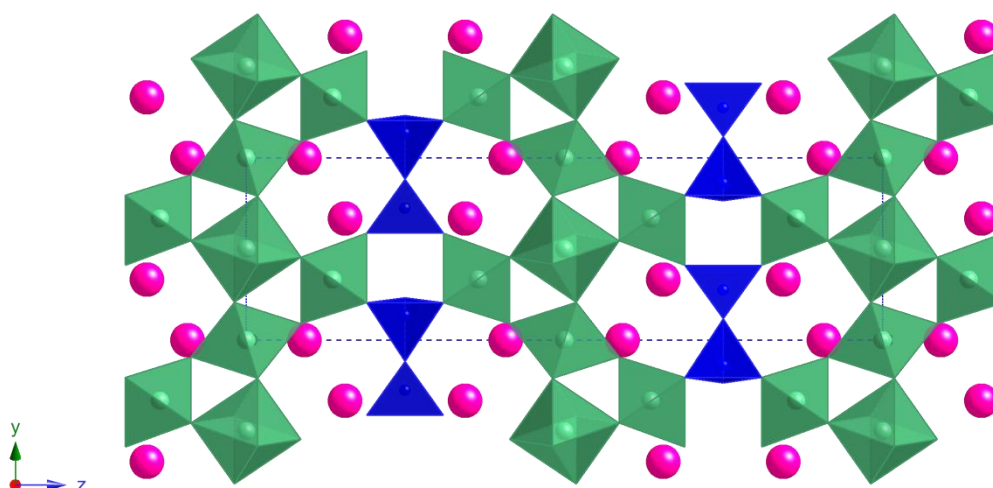
Figure 4.10 Structure of $Cs_8Nb_{10}Si_6O_{41}$ in projection down *a*. Green octahedra represent NbO_6 and blue tetrahedra represent SiO_4.

To sum up, Na-Nb/CST with acid pretreatment has shown more promise as an ion exchanger for Cs. After HIPing, Cs-exchanged Na-Nb/CST-activated samples were converted into several oxides containing substitutions with lower oxidation state. The Cs host phase in the HIPed Na-Nb/CST product, $Cs_8Nb_{10}Si_6O_{41}$, has promise for holding Cs based on the crystal structure. However, the leaching behaviour will need to be studied.

4.5 HIPed Cs-exchanged IONSIV®

The ion exchange property of IONSIV® has been widely studied and it is used for Cs removal in industry. In the previous section (Chapter 3.5.3), the Cs levels in the Cs-exchanged IONSIV® samples were measured using XRF and an increasing Cs content was detected, as expected. In the following discussion, the focus is on the investigation of the phase

assemblage of IONSIIV after HIPing. Phase identification and quantitative phase analysis were carried out and supported by the findings obtained using electron microscopy and X-ray diffraction.

4.5.1 Microstructure

The SEM/BSE images of HIPed Cs-IONSIV® samples with variable Cs loadings (Figure 4.11) revealed that the microstructure reduces in grain size with increase in Cs loading. It was also observed that more bright grains of rectangular shape morphology, suggesting Cs containing phases, exist with the increasing Cs loading.

At higher Cs content, a large number of Cs heterogeneities can act as efficient internal nucleating centres for the growth of small, randomly orientated, and interlocking ceramic crystal during heating process, resulting in the morphology with smaller grains present. Moreover, the other bright phase with hexagonal shape, which is considered the second Cs containing phase, was observed in the samples of Cs loading above 6 wt.%. A locally blurred image at some of the grains of hexagonal shape, as seen in Figure 4.11 (d) and (e), was caused from partial vitrification.

These images exhibit typical "glass-ceramic" microstructures - one with a coarse microstructure and the other with a nano-crystalline structure. IONSIV®, a $CsO-TiO_2-SiO_2-Nb_2O_5-ZrO_2$ system, includes certain oxides that can be nucleating agents (e.g. TiO_2, ZrO_2) and the constituents of a glass (e.g. SiO_2) that can be processed to a glass-ceramic easily under HIP conditions. The microstructure of the glass-ceramic that consists of crystals dispersed in a glassy silica-rich matrix is similar to some examples reported previously.[153]
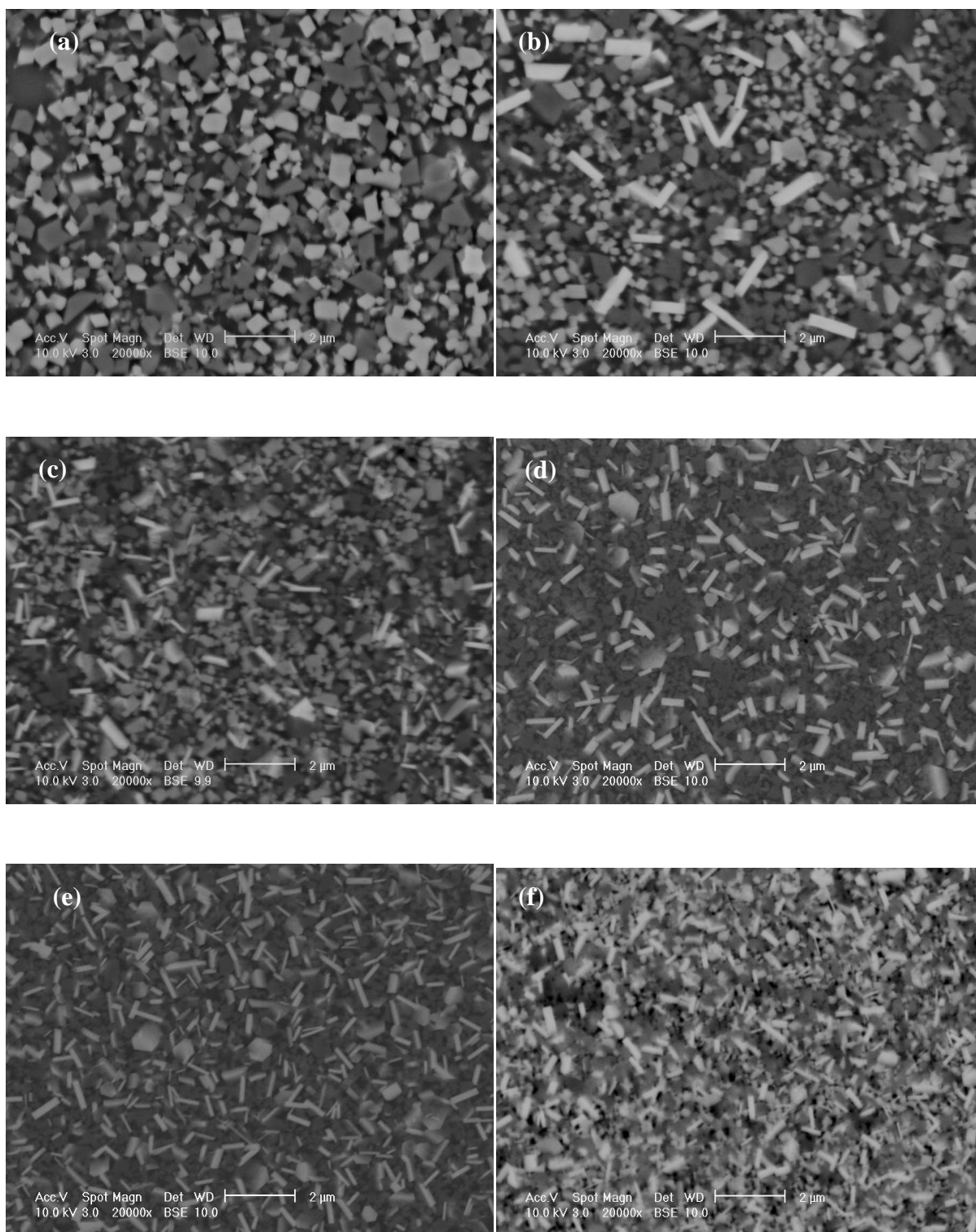
Figure 4.11 SEM/BSE images of HIPed (a) 2 wt.% (b) 4 wt.% (c) 6 wt.% (d) 8 wt.% (e) 10 wt.% (f) 12 wt.% Cs-IONSIV®.

4.5.2 Phase Identification

Due to the failure of direct phase identification using EDX, HIPed Cs-exchanged IONSIV® samples were analysed using TEM. The diffraction pattern of the grain of interest can provide powerful and direct evidence for phase identification. In this case, a thin disc of sample is required. Attempts to prepare a TEM sample by mechanical polishing, dimpling and FIB-thinning (focused ion beam) were made but all failed. Although the sample should be dense enough after HIPing to resist the damage caused during the grinding and polishing procedure, the HIPed samples are still too fragile. In addition, IONSIV® has poor conductivity to react with ions using the FIB-thinning method. The beam drifts whilst defining and shaping the area and causes the job to abort.

An alternative way to prepare the powder sample is to grind and disperse on the holder. This method is relatively easy and time-saving; however, difficulties are usually encountered due to the disadvantages from this preparation method. Firstly, TEM requires a particle that is not merely thin enough for electrons to penetrate but also large enough for the electron beam to cover. This requirement is hard to meet because the size of fragments is hard to control by manual grinding. Secondly, the fragment might contain more than one phase of interests and result in an error in acquiring the diffraction pattern or elemental composition of the desired single grain. Thirdly, it is difficult to search a particular phase in the complicated mixture under TEM observation. Finally, long operating times are required for searching the grains to find the desired one due to the small amount of particles loaded by dropping suspension on the grid. Consequently, gaining direct evidence such as diffraction patterns for discovering phase information using TEM was not successful.

The elemental composition of an individual grain acquired using TEM/EDX can still provide reliable and useful information for phase identification. Figure 4.12 shows the EDX result analysed from the grain found in HIPed 2 wt.% Cs-IONSIV® under TEM observation. It is indicated that this grain contains Ti, Zr and O. The formula is estimated as $(Ti_{0.61}, Zr_{0.39})O_2$ based on the atomic percentage obtained from the EDX result.
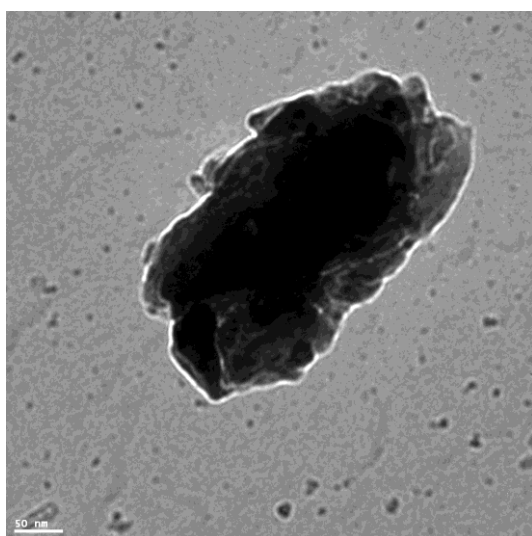
Elemental composition

Element	Weight%	Atomic%
O K	31.74	65.24
Ti K	31.13	21.37
Zr L	37.14	13.39
Totals	100	
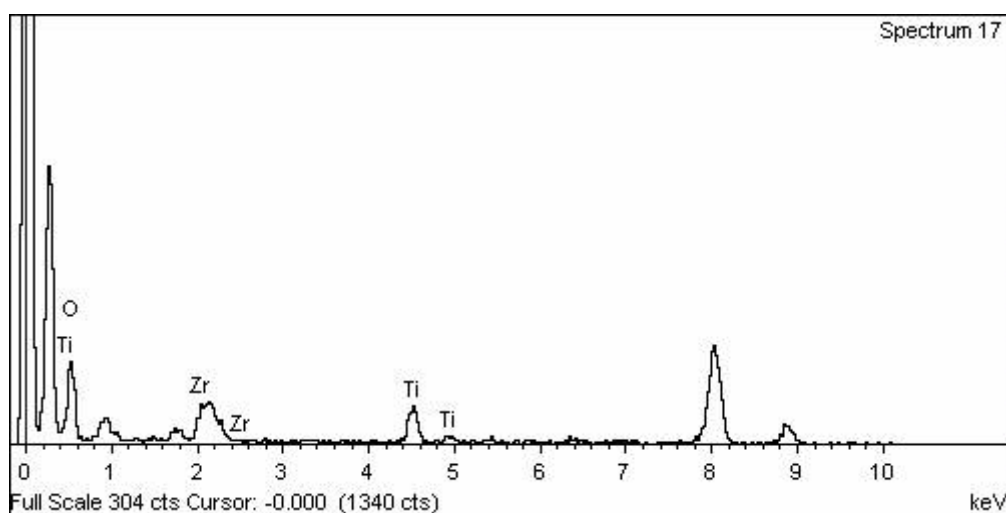
Figure 4.12 Quantitative analysis of a grain found in the HIPed 2 wt.% Cs-IONSIV® using EDX under TEM observation. Scale bar = 50 nm. Peaks at 8.04 keV and 0.277 keV are from Cu K_α and C K_α, respectively, both from sample holder.

The other grain discovered using TEM is more significant. This is a Cs-containing phase with Ti and a fairly high amount of Nb as constituents. It is estimated that the formula has Cs: Ti: Nb = 2: 1: 10 ratio. Although EDX analysis is considered a semi-quantitative method due to the matrix effect and the lack of calibration, the result provides a key clue.
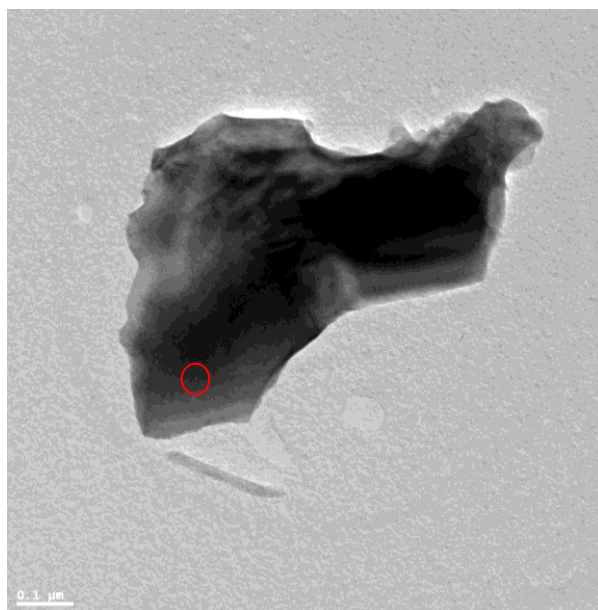
Elemental composition

Element	Weight%	Atomic%
O K	19.47	59.39
Ti K	3.03	3.09
Nb L	57.39	30.14
Cs L	20.11	7.38
Totals	100	
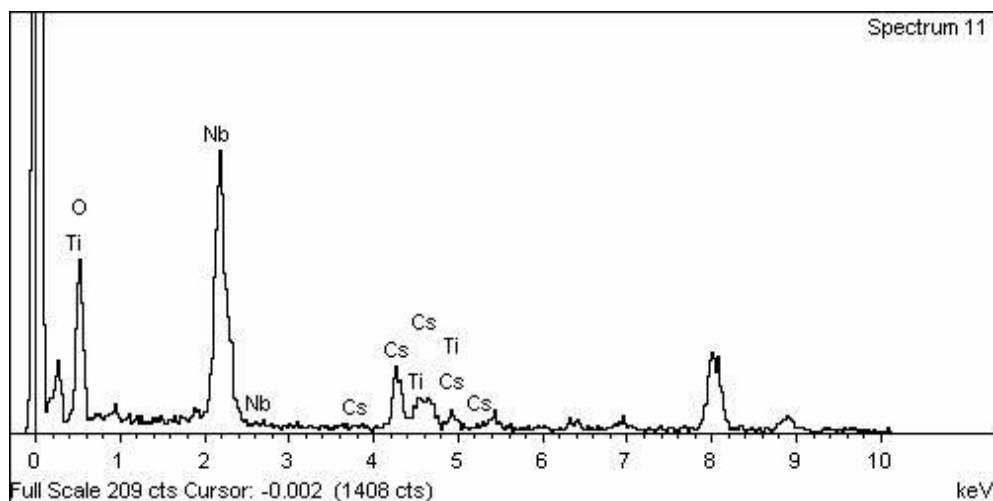
Figure 4.13 Quantitative analysis of HIPed 2 wt.% Cs-exchanged IONSIV® sample using EDX under TEM observation. The red circle represents the area of beam coverage. Scale bar = 0.1 μm.

Another HIPed Cs-exchanged IONSIV® sample with a higher Cs loading (12 wt.%) was also investigated using TEM/EDX. The TEM micrograph shown in Figure 4.14 shows particle of rectangular shape and contains Cs, Zr and Si. The EDX result also shows a great amount of Si content in this phase. The possible phases proposed by searching the ICDD PDF database are $Cs_2ZrSi_3O_9$ or $Cs_2ZrSi_6O_{15}$.
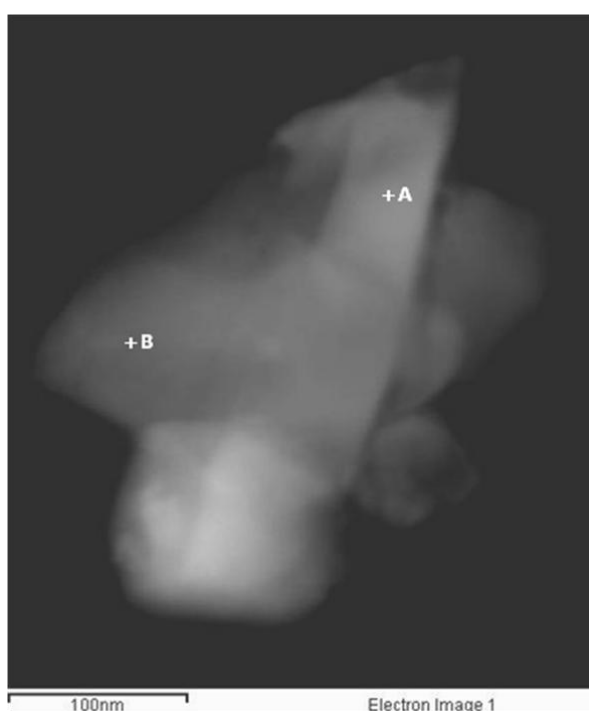
Point A

Element	Weight %	Atomic %
O K	53.87	71.07
Si K	35.98	27.04
Zr L	3.80	0.88
Cs L	6.35	1.01
Total	100	

Point B

Element	Weight %	Atomic %
O K	55.59	75.96
Si K	25.93	20.18
Zr L	10.88	2.61
Cs L	7.60	1.25
Total	100	

Figure 4.14 Quantitative analysis of HIPed 12 wt.% Cs-exchanged IONSIV® sample using EDX under TEM observation. Beam size = 25 nm. Scale bar = 100 nm.

HIPed Cs-IONSIV® samples were analysed using XRD and the patterns were indexed with the help of phase information obtained from the TEM/EDX study. XRD characterisation of HIPed Cs-IONSIV® samples (shown in Figure 4.15) shows the effect of Cs levels on phase assemblages. As shown as in Figure 4.15(a), pure IONSIV® was thermally transformed to a glassy phase $ZrSiO_4$, rutile-TiO_2 with Nb^{4+} substitution due to the reducing HIP condition, and $NaNbO_3$, which is one of the phases found in the Na-Nb/CST after thermal treatment.

At low Cs concentration, a series of oxides and a single Cs containing phase, $Cs_2TiNb_6O_{18}$, are present in both 2 wt.% and 4 wt.% HIPed IONSIV®. In addition, a growth in intensity of $Cs_2TiNb_6O_{18}$ was noticed with an increase of Cs level in the HIPed IONSIV® samples. At Cs loadings more than 6 wt.%, a second Cs-containing phase, $Cs_2ZrSi_6O_{15}$, was observed as well as the absense of SiO_2. It is suggested that Cs was used up to form $Cs_2TiNb_6O_{18}$ and $Cs_2ZrSi_6O_{15}$, and the rest of Zr and Si were consumed for partial vitrification forming $ZrSiO_4$. In the HIPed IONSIV® samples with higher Cs levels (10 wt.% and 12 wt.%), the absence of $ZrSiO_4$ indicated that residual Zi and Si with sufficient Cs provided were converted to $Cs_2ZrSi_6O_{15}$. However, more evidence is required to study the mechanism of phase formation during HIPing.

Early work by Balmer et al.[154] revealed that a number of new phases appear when IONSIV® is heat-treated. NMR, XRD and TEM results indicate that major phases in thermally converted CST are $Cs_2ZrSi_3O_9$, $Na(Ti,Nb)O_3$ and $Na_2Ti_6O_{13}$. However, the Cs host phase, $Cs_2ZrSi_3O_9$, was not found in any of the HIPed IONSIV® samples. It is suggested that a different phase formation route was created due to a more reducing environment in HIP process than normal sintering in addition to the effect of Cs loadings.
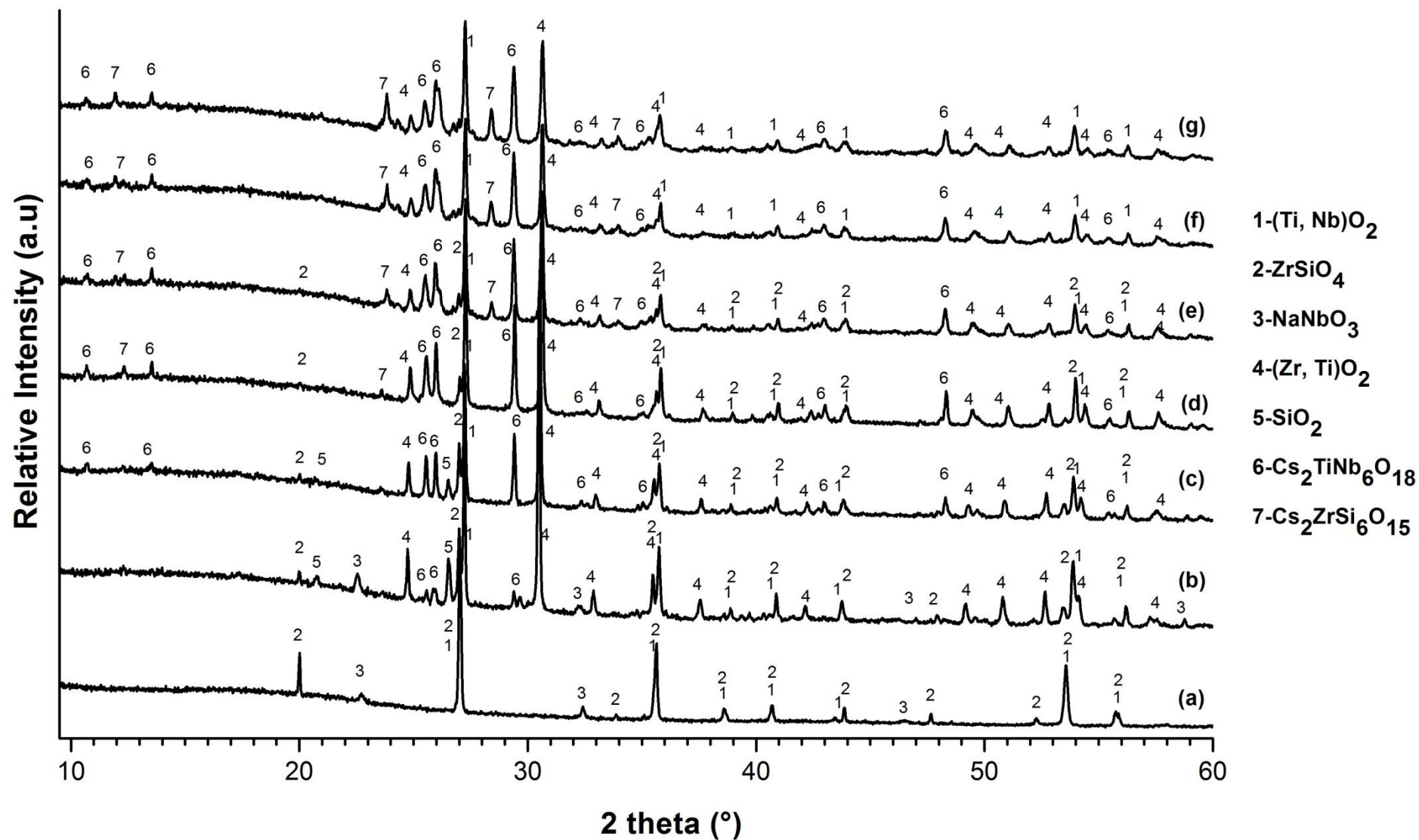
Figure 4.15 XRD patterns of HIPed (a) 0 wt.% (b) 2 wt.% (c) 4 wt.% (d) 6 wt.% (e) 8 wt.% (f) 10 wt.% (g) 12 wt.% Cs-IONSIV®.

4.5.3 Quantitative Phase Analysis using Rietveld Refinement

The use of Rietveld refinement for quantitative analysis has become an important method in material science. The main strength lies in its ability to control and correct various parameters, such as overlapped peaks and the effect of preferred orientation, which influence powder diffraction patterns. The errors come from the differences in properties of the constituents in a multiphase mixture and also the inability to model these consistently. The quantitative phase analysis using Rietveld refinement was originally developed by Hill and Howard[155] for crystal structure refinement using neutron diffraction data and it was now widely applied to evaluate phase weight fraction using X-ray powder diffraction data.[156] Weight fractions of all the phase in a multiphase system can be directly calculated by their scale factors obtained after a good pattern fitting. The relationship between the weight fraction (W_i) for each phase i and its refined scale factor (S_i) determined is obtained from the following equation,[155]

$$Wi = \frac{S_i(ZMV)_i}{\sum_{i=0}^{n} S_i(ZMV)_i}$$

Equation 4-1

where Z is the number of formula units per unit cell, M is the unit molecular weight of the formula, and V represents unit cell volume of phase $_i$ in a mixture of n phases.

Quantitative Rietveld refinements for weight fraction evaluation of each phase found in the HIPed IONSIV® samples were carried out using GSAS (Figure 4.16 to Figure 4.22 and Table 4-3). The phase indexing was confirmed and most of the elemental weight fractions based on the refinement results, which are shown in Table 4-4, generally exhibit good

consistency with the elemental composition obtained from XRF, given in Table 4-5. Additionally, both XRF and refinement results showed the weight fractions of Cs increased as the increasing Cs loadings, as expected.

However, in addition to an insufficient Nb content in HIPed IONSIV® with low (0-4 wt.%) Cs content, a deficiency of Ti in HIPed IONSIV® with 8-12 wt.% Cs loadings and an excess Zr content in HIPed 2-6 wt.% Cs loadings also observed. Those unreliable Zr, Nb, Ti and Si evaluations can be caused from the difficulties in refining these XRD patterns since laboratory X-ray diffraction is not sensitive enough to refine the Ti/Nb and Zr/Ti ratios in the rutile and $(Zr,Ti)O_2$ phases, respectively, so the compositions had to be fixed at suitable levels guided by literature in this area. Furthermore, the much lower Si content in the HIPed IONSIV® 6 wt.% sample determined from the refinement was not acordant with the XRF result. It is suggested that some amorphous substance, which would not be observed using XRD, may possibly form during the HIP treatment. Therefore, an error would occur in the Si content based on the refinement evaluation.

To summarise, two main crystalline Cs-containing phases, $Cs_2TiNb_6O_{18}$ and $Cs_2ZrSi_6O_{15}$, were discovered and confirmed in HIPed Cs-IONSIV® samples using XRD and TEM/EDX, and the weight fractions of phases were evaluated using Rietveld refinement. A series of oxides, such as $NaNbO_3$, $(Ti, Nb)O_2$-rutile, $ZrSiO_4$, $ZrTiO_4$ and SiO_2, were also detected by XRD characterisation. Although the structural stuides of $Cs_2TiNb_6O_{18}$ and $Cs_2ZrSi_6O_{15}$ have only been done by a few groups[150, 151, 157], it is believed that those two phases show promise for hosting Cs due to the structures being dense and having high Cs coordination numbers. To further understand the chemical stability of the wasteforms generated in the HIP process,

leach tests were carried out and the properties of $Cs_2TiNb_6O_{18}$ and $Cs_2ZrSi_6O_{15}$ were studied, the results are discussed in the folowing two chapters.

Figure 4.16 Simulated (green line) and experimental diffraction patterns (red dots) as well as difference pattern (purple) for HIPed Cs-IONSIV® 0 wt.% sample.

Figure 4.17 Simulated (green line) and experimental diffraction patterns (red dots) as well as difference pattern (purple) for HIPed Cs-IONSIV® 2 wt.% sample.
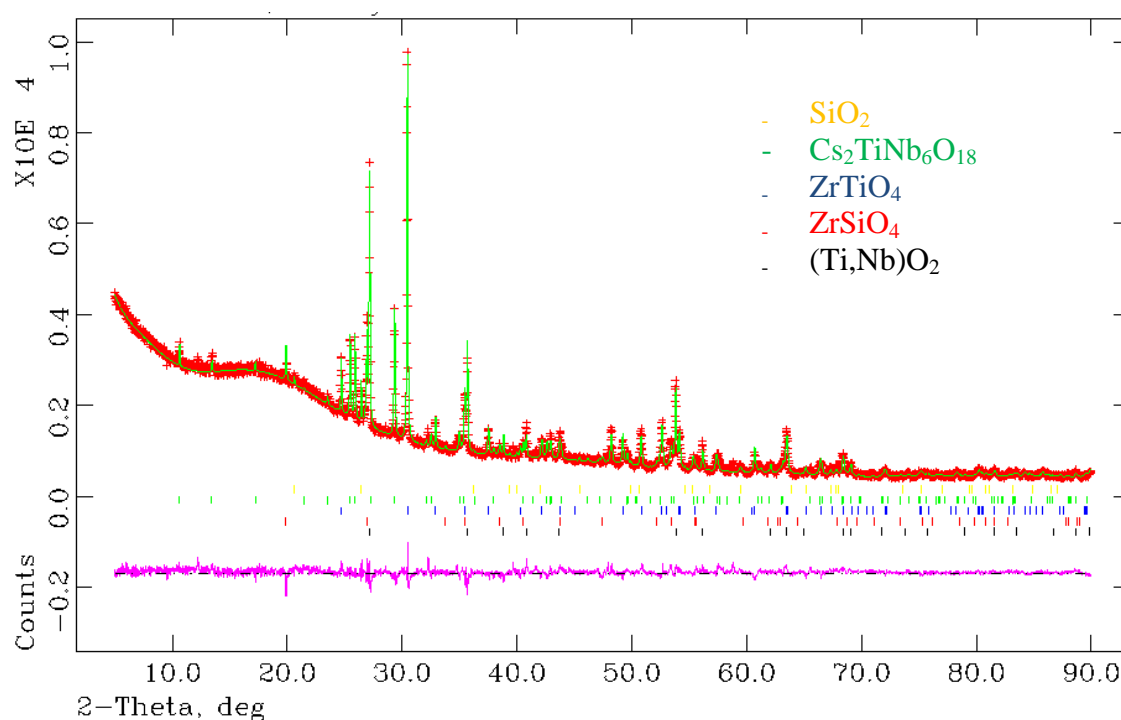
Figure 4.18 Simulated (green line) and experimental diffraction patterns (red dots) as well as difference pattern (purple) for HIPed Cs-IONSIV® 4 wt.% sample.
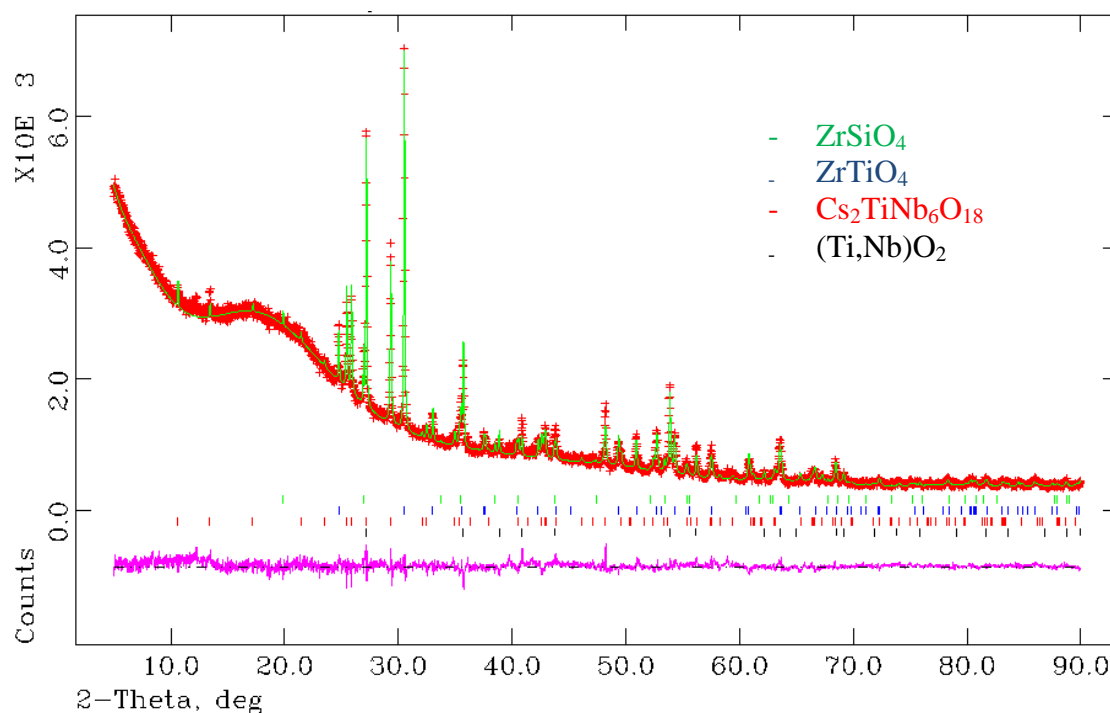
Figure 4.19 Simulated (green line) and experimental diffraction patterns (red dots) as well as difference pattern (purple) for HIPed Cs-IONSIV® 6 wt.% sample.
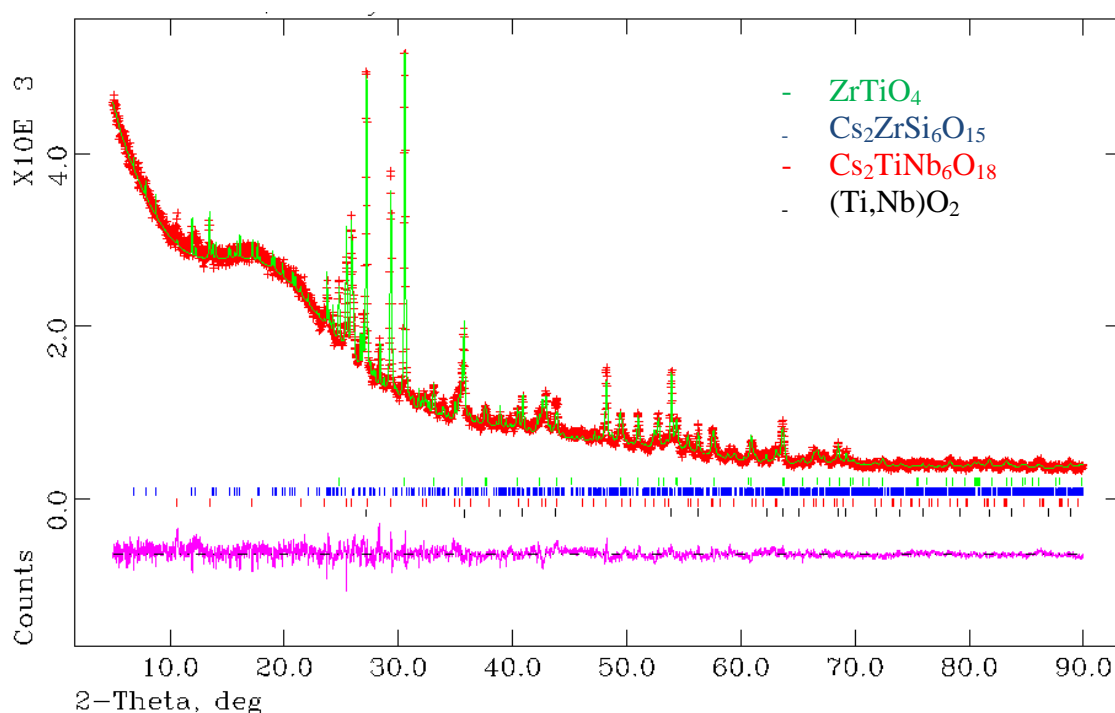
Figure 4.20 Simulated (green line) and experimental diffraction patterns (red dots) as well as difference pattern (purple) for HIPed Cs-IONSIV® 8 wt.% sample.
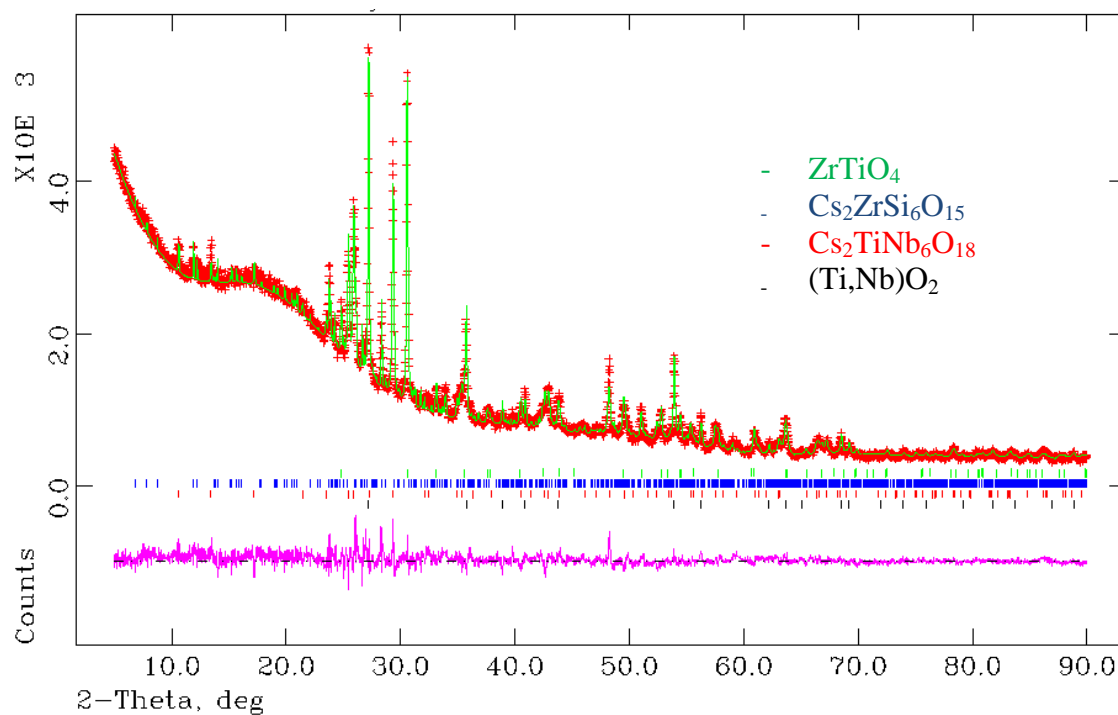
Figure 4.21 Simulated (green line) and experimental diffraction patterns (red dots) as well as difference pattern (purple) for HIPed Cs-IONSIV® 10 wt.% sample.
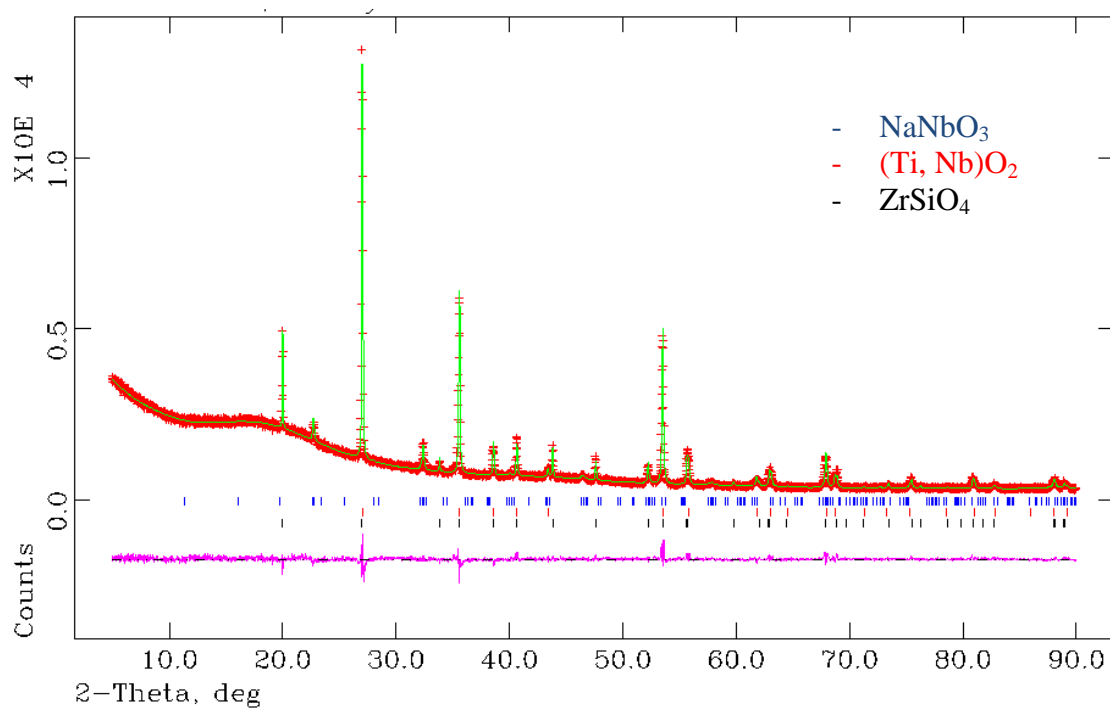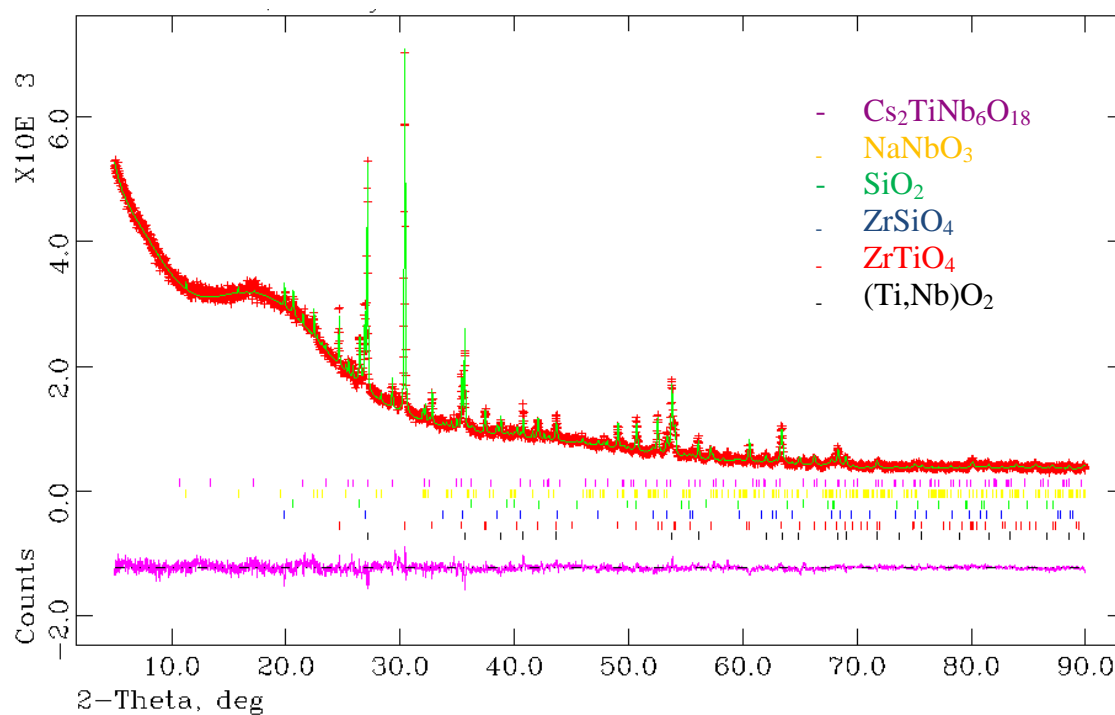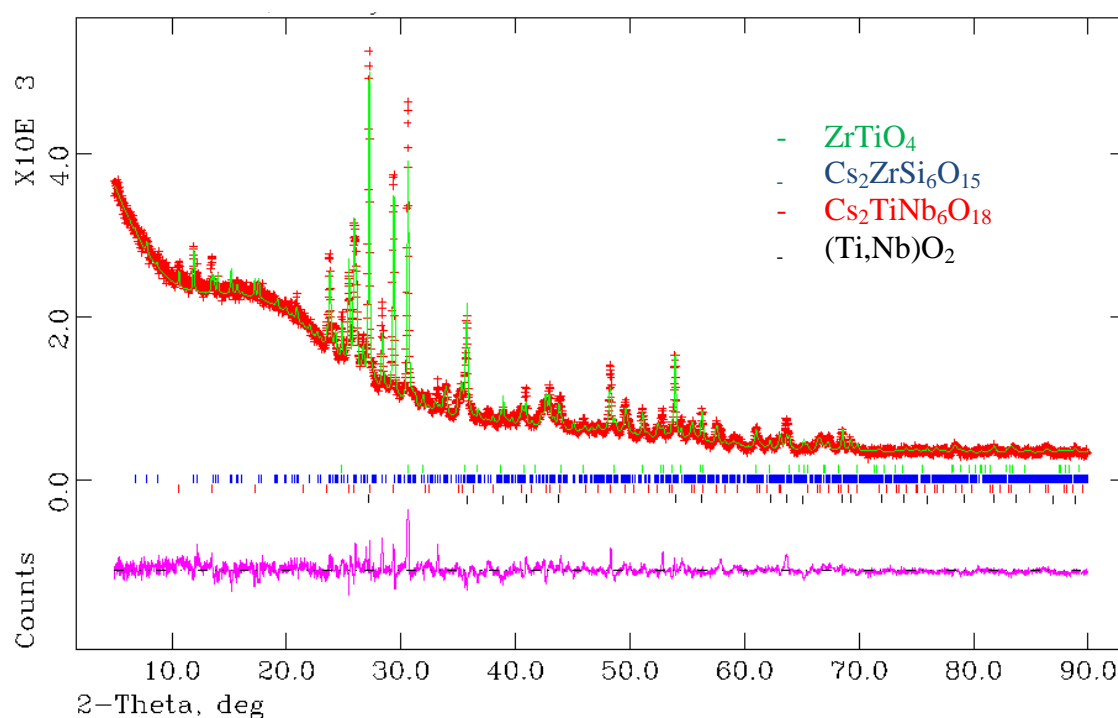

Figure 4.22 Simulated (green line) and experimental diffraction patterns (red dots) as well as difference pattern (purple) for HIPed Cs-IONSIV® 12 wt.% sample.

Table 4-3 Weight fractions of each phase in HIPed Cs-IONSIV® samples from Rietveld refinement results. The refinement parameters, χ^2, R_{wp} and R_p are also listed in the table.

Phase fractions (wt.%)							
	0 wt.%	2 wt.%	4 wt.%	6 wt.%	8 wt.%	10 wt.%	12 wt.%
$(Ti_{0.712},Nb_{0.288})O_2$	59.96	25.73	27.54	28.85	21.04	22.79	24.27
$ZrSiO_4$	32.88	10.06	12.00	3.55	–	–	–
$NaNbO_3$	7.16	5.25	–	–	–	–	–
$(Zr_{0.5},Ti_{0.5})O_2$	–	38.94	37.64	41.54	34.66	29.40	19.91
SiO_2	–	16.80	7.05	–	–	–	–
$Cs_2TiNb_6O_{18}$	–	3.22	17.56	26.07	25.65	28.39	24.56
$Cs_2ZrSi_6O_{15}$	–	–	–	–	18.65	19.42	31.26
Refinement parameters							
	0 wt.%	2 wt.%	4 wt.%	6 wt.%	8 wt.%	10 wt.%	12 wt.%
χ^2	2.504	2.299	3.350	2.582	2.648	3.322	3.751
R_{wp}	4.80%	4.00%	4.92%	4.32%	4.47%	5.02%	5.79%
R_p	3.28%	2.83%	3.49%	3.10%	3.27%	3.66%	4.09%

Table 4-4 Estimated elemental composition of Cs-IONSIV® samples from Rietveld refinement.

Element	0 wt.%	2 wt.%	4 wt.%	6 wt.%	8 wt.%	10 wt.%	12 wt.%
Nb	4.06	4.52	8.45	12.54	12.34	13.65	11.81
Zr	16.36	22.50	22.88	20.42	17.79	15.52	12.67
Ti	18.46	17.23	18.08	19.75	15.71	15.12	13.18
Cs	0.00	0.74	4.03	5.98	12.36	13.26	16.49
Si	5.04	9.40	5.13	0.54	4.11	4.28	6.88
Na	1.00	0.74	0.00	0.00	0.00	0.00	0.00

Table 4-5 Elemental compositions (weight percentage) of Cs-IONSIV® samples acquired using XRF.

Element	0 wt.%	2 wt.%	4 wt.%	6 wt.%	8 wt.%	10 wt.%	12 wt.%
Nb	14.92	14.96	15.81	15.56	15.41	16.21	15.01
Zr	13.49	13.15	14.18	14.64	13.69	14.91	13.87
Ti	20.76	20.49	21.21	20.62	20.89	21.96	20.16
Cs	−	2.55	4.47	7.90	10.63	13.79	12.92
Si	8.02	8.09	8.89	8.81	8.64	9.21	8.29
Na	2.39	1.97	1.63	0.90	0.53	0.28	0.26

(The refinement results of the HIPed samples in this chapter are included in the CD attached)

4.6 HIPed IONSIV® with Additive

Three metals, Ti, Fe and Al, were selected as reductants and added to Cs-IONSIV® in the HIP process. 2 and 4 total weight percent of metal Ti, Fe and Al were mixed with 6 wt.% Cs-IONSIV® and 12 wt.% Cs-IONSIV®, respectively. Metals were chosen that might provide sufficient trivalent metal content to form hollandite-like compound as well as to control the redox state of the multivalent metal in hollandite once it forms. The expected formula of a hollandite-like ceramic is $A_xB_yC_{8-y}O_{16}$. (A: Cs^+ or its decay product Ba^{2+}, B: Ti^{3+}, Fe^{3+}, Al^{3+}, and C: Ti^{4+})

4.6.1 Metal Ti Addition

Figure 4.23 shows the SEM/BSE micrograph of 6 wt.% Cs-IONSIV® HIPed with 2% (total weight percentage) Ti metal added. It suggests that several phases formed, distinguished by the shape and size.

Phase A- Brightest particle of round shape morphology.

Phase B- Grey area of square shape morphology and sized about 1 μm^2.

Phase C- Grey area with round shape morphology and sized ~ 25 nm in diameter.

Phase D- Darkest area without regular shape.

However, the microstructure of this sample did not provide information of much value; phase identification was then conducted using XRD.

Figure 4.23 SEM/BSE image of 6 wt.% Cs-IONSIV® HIPedwith 2% (total weight percentage) Ti metal.

XRD characterisation reveals the phase assemblage in the sample. $(Ti,Nb)O_2$-Rutile, $ZrSiO_4$, and a Cs-containing phase – $Cs_2ZrSi_6O_{15}$, were detected as main phases. The absence of $Cs_2TiNb_6O_{18}$, which was found in the HIPed Cs-IONSIV® without a metal additive, indicated that the phase transformation has been affected due to a more reducing environment.

It was noticed that Nb is more likely to form Nb^{4+} and to be stabilised forming the $(Ti, Nb)O_2$-Rutile phase. Furthermore, it is suggested that the presence of $ZrSiO_4$, a typical

vitrification product, was from the excess ZrO_2 and SiO_2 remaining after part of them were converted with the limited amount of Cs to form $Cs_2ZrSi_6O_{15}$.

Figure 4.24 The XRD pattern of 6 wt.% Cs-IONSIV® HIPed with 2% (total weight percentage) of Ti metal.

Quantitative phase analysis was carried out using Rietveld refinement, as shown in Figure 4.25. The result reveals that the sample formed when 6 wt.% Cs-IONSIV® is HIPed with 2% (total weight percentage) of Ti metal is comprised of 49.89 % of $Ti_{0.88}Nb_{0.12}O_2$, 26.60% of $ZrSiO_4$ and 23.51% of $Cs_2ZrSi_6O_{15.}$ However, the fitting is not as good as hoped because most of the peaks of $ZrSiO_4$ overlap with those of $(Ti, Nb)O_2$. In addition, X-ray diffraction is not sensitive enough to distinguish the Ti/Nb ratio in the $(Ti, Nb)O_2$ phase, especially when the matrix is rather complicated. As a result, an uncertainty was left in the phase weight fraction evaluation.
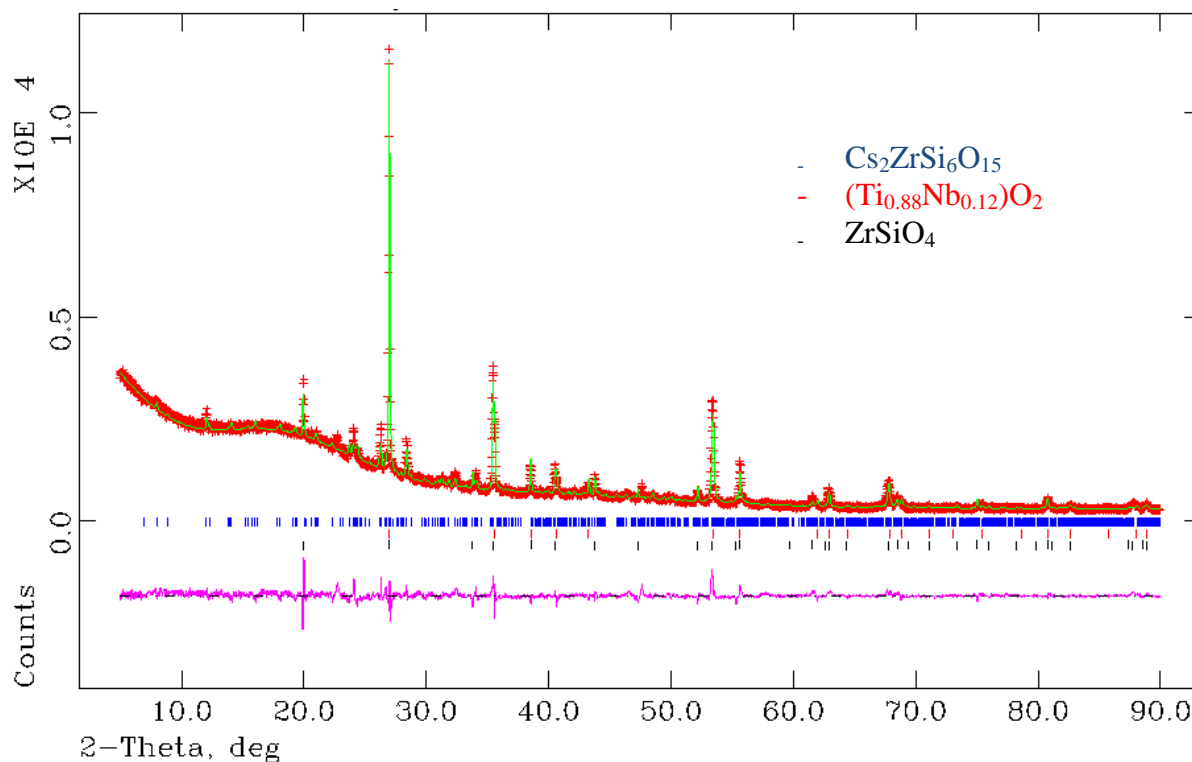
Figure 4.25 Rietveld refinement of 6 wt.% Cs-IONSIV® HIPed with 2 wt.% Ti metal for quantitative phase analysis. (χ^2=4.443, R_{wp}=6.45 % and R_p=4.30 %)

Figure 4.26 shows the SEM/BSE micrograph of 12 wt.% Cs-IONSIV® HIPed with 4% (total weight percentage) Ti metal. The microstructure exhibits 4 phases, distinguished by the shape, size and contrast. Phase A to D are grouped by the contrast from brightest to darkest, as shown in Figure 4.26.
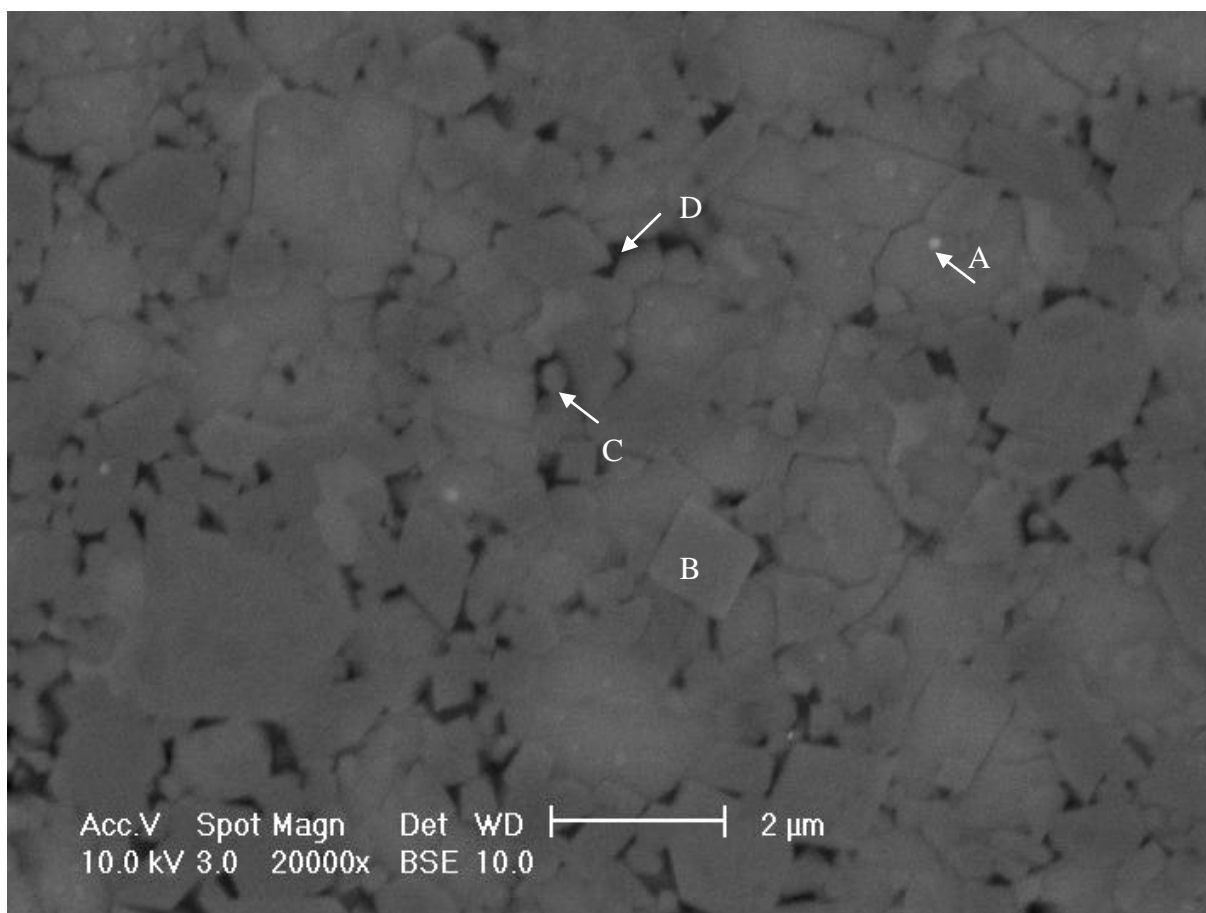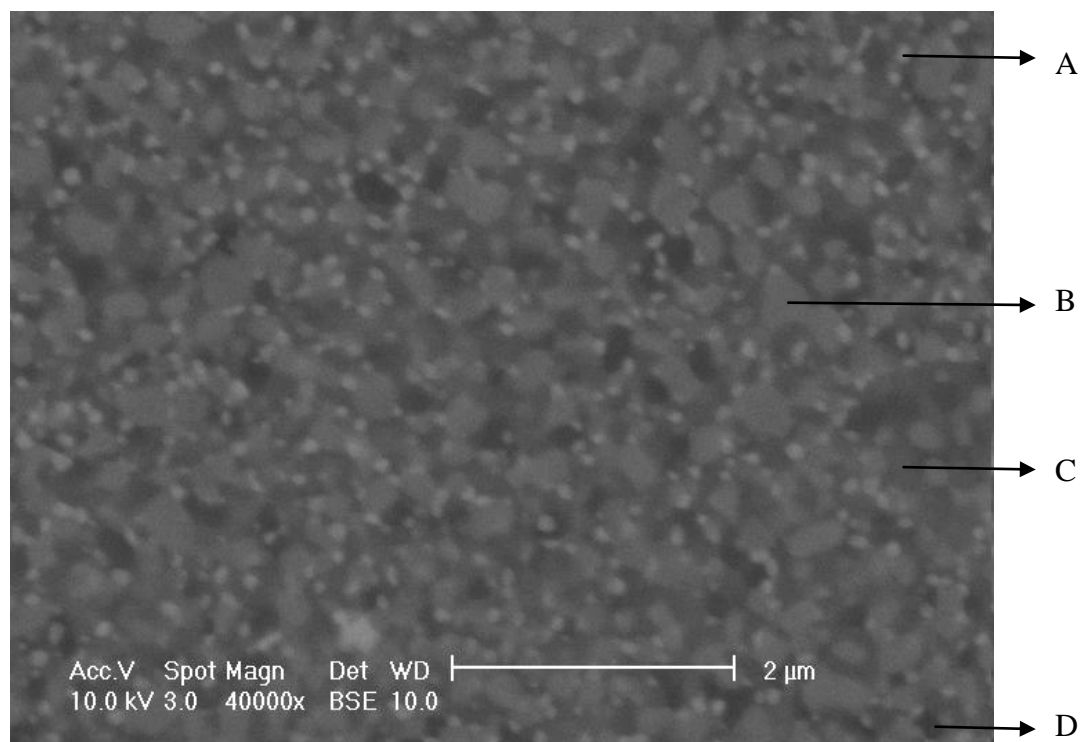
Figure 4.26 SEM/BSE image of 12 wt.% Cs-IONSIV® HIPed with 4% (total weight percentage) Ti metal.

XRD characterisation (shown in Figure 4.27) reveals a slightly different phase assemblage than the previous sample. With the higher Cs content and more Ti added, (Ti, Nb)O_2-Rutile, $Cs_2ZrSi_3O_9$ and $Cs_2ZrSi_6O_{15}$, were detected as main phases in the sample. No $Cs_2TiNb_6O_{18}$ or $ZrSiO_4$ were discovered, as expected.
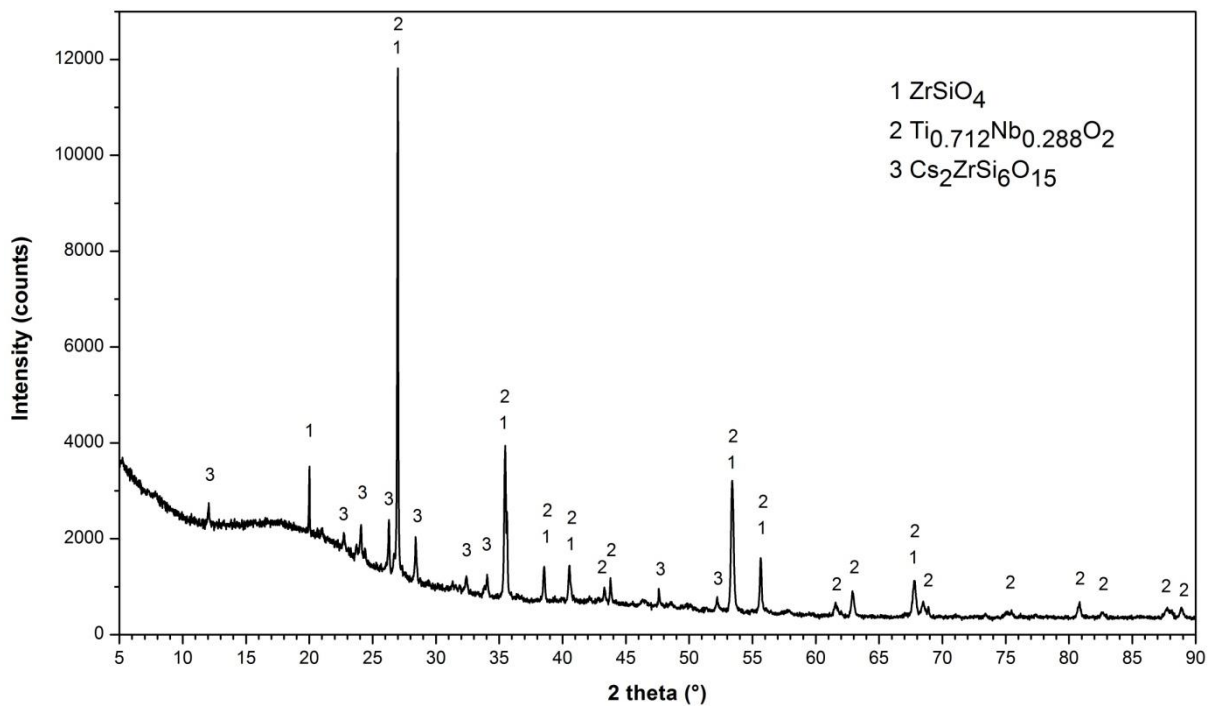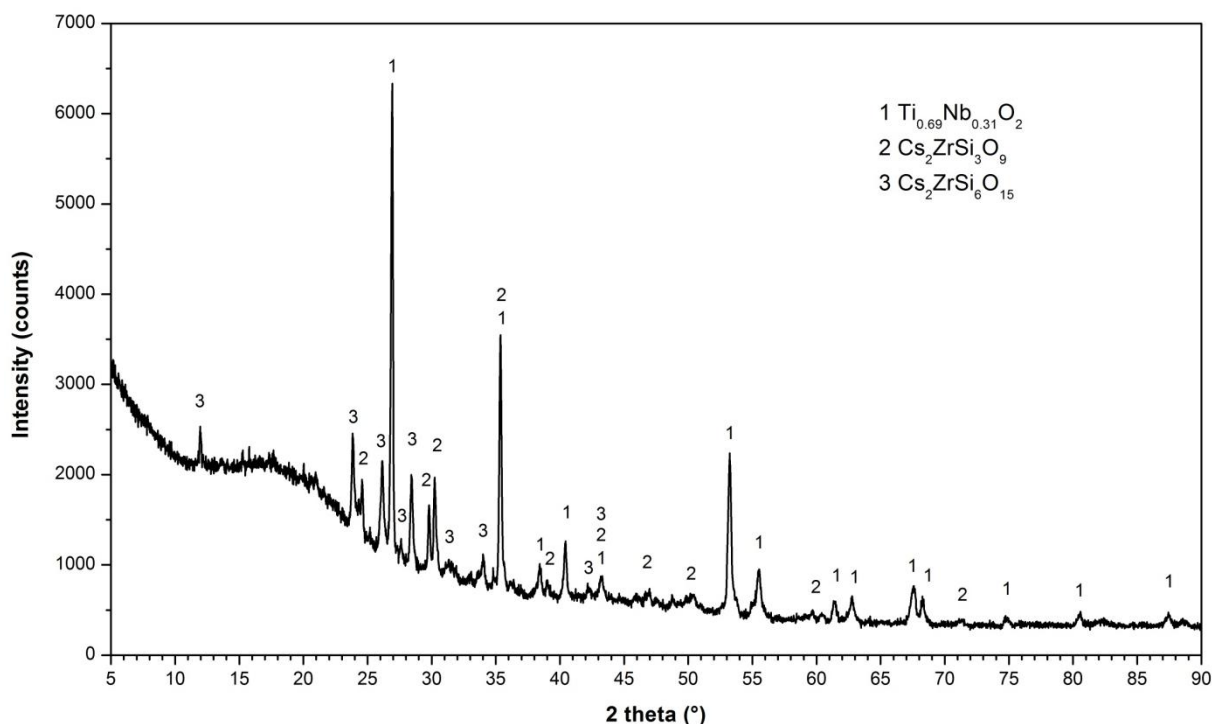
Figure 4.27 The XRD pattern of 12 wt.% Cs-IONSIV® HIPed with 4% (total weight percentage) of Ti metal.

Quantitative phase analysis using Rietveld refinement (shown in Figure 4.28) indicates that 12 wt.% Cs-IONSIV® HIPed with 4% (total weight percentage) of Ti metal forms a sample that is comprised of 61.52% of $Ti_{0.712}Nb_{0.288}O_2$, 9.45% of $Cs_2ZrSi_3O_9$ and 29.03% of $Cs_2ZrSi_6O_{15.}$ The phase assembly was confirmed by the reasonable fitting, and the weight fraction is considered convincing.
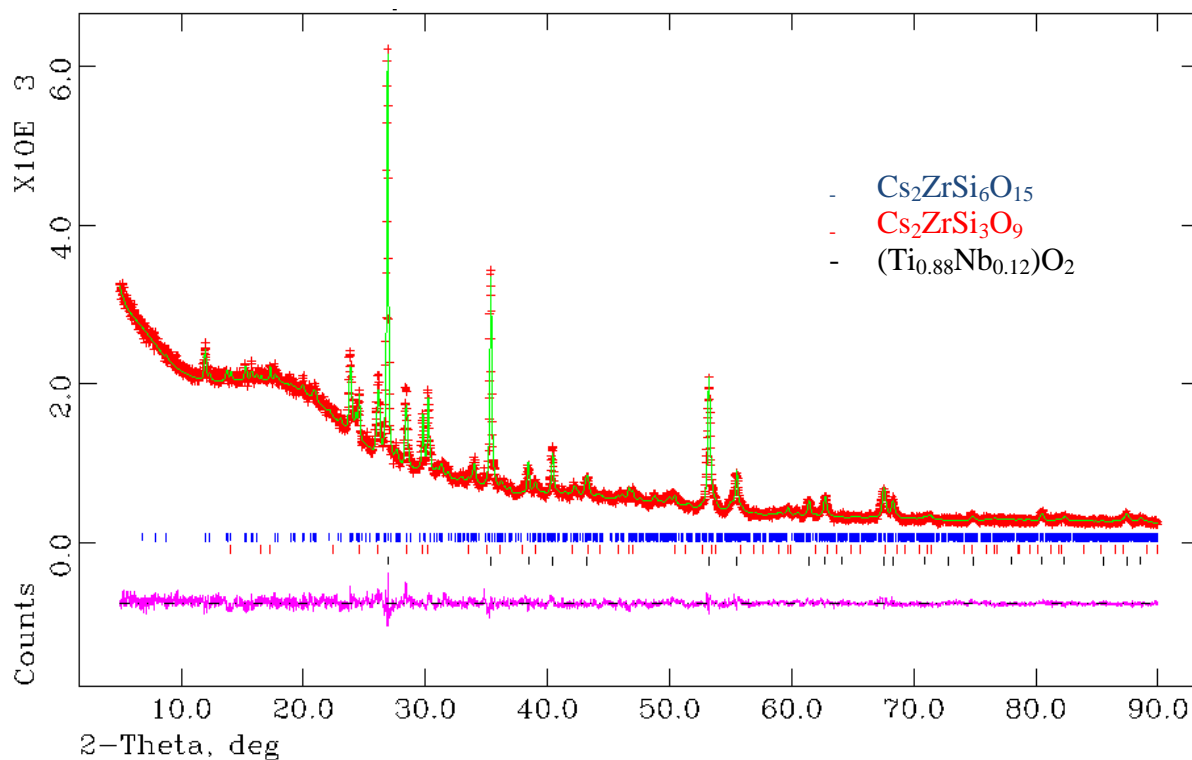
Figure 4.28 Rietveld refinement of the sample from Cs-IONSIV® 6 wt.% sample HIPed with total weight percentage 2% Ti metal. (χ^2=1.766, R_{wp}=4.24% and R_p=3.12%)

A possible explanation for the change in phases present can be proposed based on the findings from XRD refinement. In order to moderate the redox state during the HIP process, the charge can be balanced by reducing Ti^{4+} to Ti^{3+} or Nb^{5+} to Nb^{4+}. Zr^{4+}/Zr^{2+} can only occur in an extremely reducing environment. Therefore, since more Ti was added it is sufficient to accommodate all the Nb^{4+} that forms in $(Ti^{4+}, Nb^{4+})O_2$, so an abundance of $(Ti^{4+}, Nb^{4+})O_2$ was expected. No Nb^{5+} was discovered in any Nb-containing phase, for example, $Cs_2TiNb_6O_{18}$ is not found.

Moreover, $Cs_2ZrSi_6O_{15}$ seems to be the first Cs-containing phase to form in this Cs_2O-TiO_2-Nb_2O_5-SiO_2-ZrO_2 system under these reducing conditions. Phase fractions of $Cs_2ZrSi_6O_{15}$ in both HIPed Cs-IONSIV® samples with added Ti are very similar. It is

suggested that $Cs_2ZrSi_3O_9$ forms after most of the Cs was consumed for forming $Cs_2ZrSi_6O_{15}$ in such a reducing environment. However, more evidence is required to prove this mechanism.

4.6.2 Metal Fe Addition

2 total weight percent of Fe metal was mixed with 6 wt.% Cs-IONSIV[®] and the mixture was HIPed. The XRD characterisation shown in Figure 4.29 reveals that this sample is nearly amorphous. Only few peaks with very weak intensity were observed, as a result, phase indexing was not successful. It was also discovered in SEM examination that no uniform or repeat microstructure was found.

Figure 4.29 XRD pattern of 6 wt.% Cs-IONSIV[®] HIPed with 2% (total weight percentage) of Fe metal.

When a larger amount of Fe is added and a higher Cs content is used, thermal conversion occurs to produce ceramic phases. Figure 4.30 displays the microstructure of 12 wt.% Cs-exchanged IONSIV® HIPed with 4% (total weight percentage) Fe metal. There are five main phases in the sample distinguished by contrast, one needle shape with the brightest (A), one bright spherical grain (B), one light grey with square/rectangular shape (C), one darker grey square/rectangular (D), and the other black area (E), as marked in Figure 4.31. It was suggested that Cs was possibly located in phase A and B since those two phases show the brightest contrast.
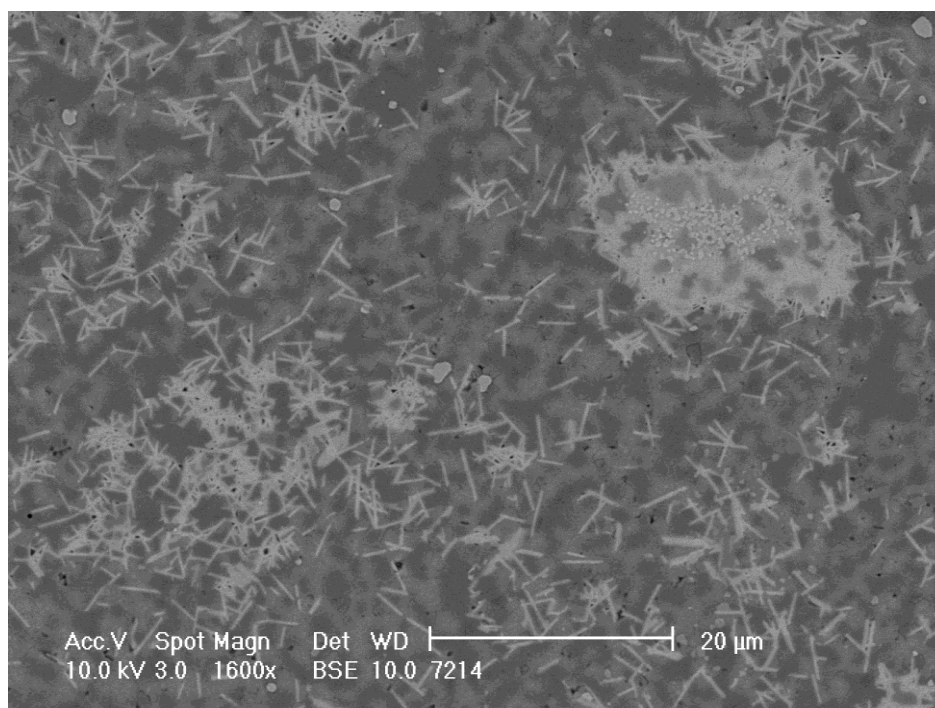
Figure 4.30 SEM/BSE micrograph of 12 wt.% Cs-IONSIV® HIPed with 4% (total weight percentage) Fe metal. (Magnification ×1,600)
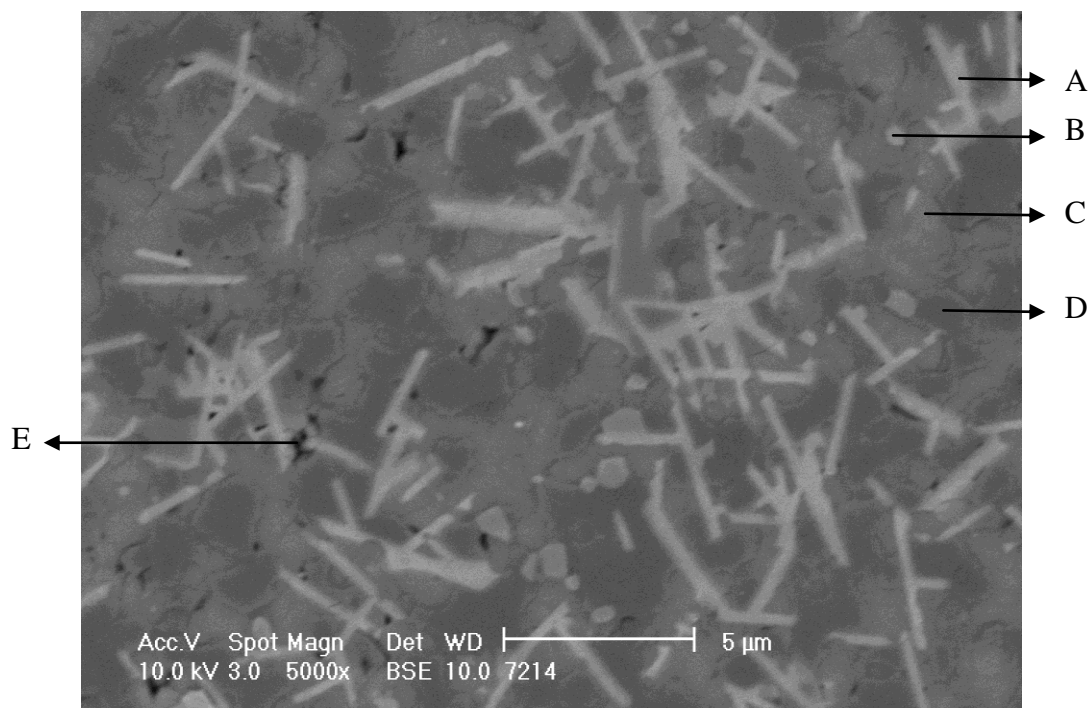
Figure 4.31 SEM/BSE micrograph of 12 wt.% Cs-IONSIV® HIPed with 4% (total weight percentage) Fe metal. (Magnification ×5,000)

XRD characterisation was also carried out, the pattern exhibits a high background due to the presence of Fe but three main phases, $(Ti_{0.712}Nb_{0.288})O_2$, $Cs_2ZrSi_3O_9$ and $Cs_2ZrSi_6O_{15}$, were indentified. The phase assemblage is similar to that in HIPed Cs-IONSIV® with added Ti metal, and the same mechanism in terms of phase formation is proposed. Quantitative phase analysis using Rietveld refinement reveals that the sample is composed of 52.50 wt.% of $Ti_{0.743}Nb_{0.257}O_2$, 5.58 wt.% of $Cs_2ZrSi_3O_9$ and 41.92 wt.% of $Cs_2ZrSi_6O_{15}$. However, from the SEM observations and XRD pattern, it is suggested that a large amount of amorphous material may be present in the sample and this would result in an inaccurate quantitative phase evaluation.
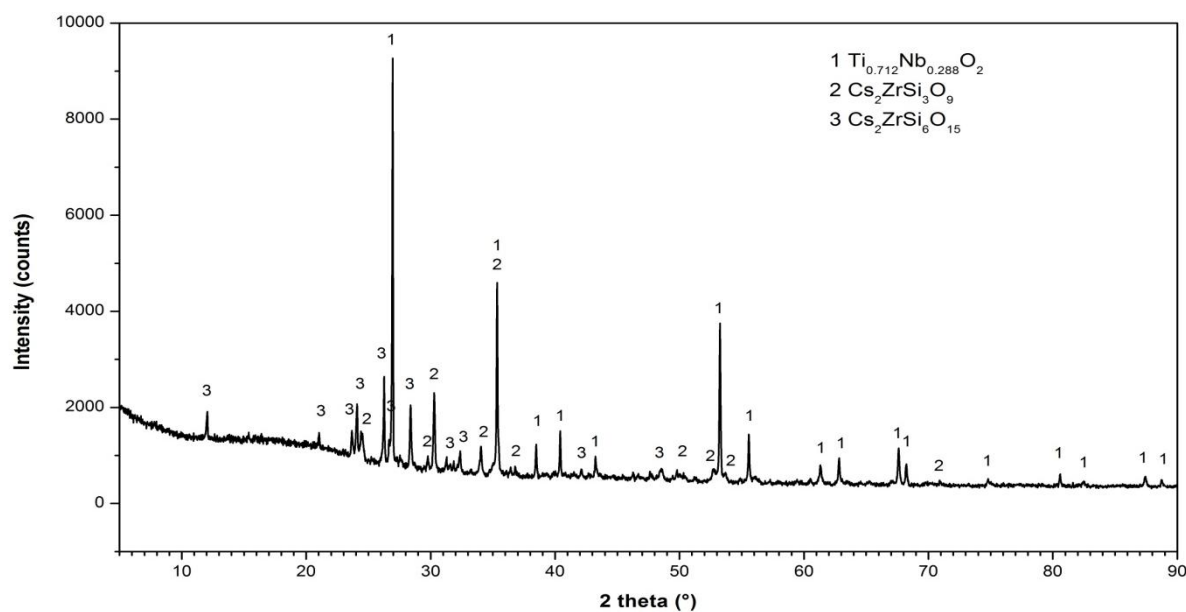
Figure 4.32 XRD pattern of 12 wt.% Cs-IONSIV® HIPed with 4% (total weight percentage) of Fe metal.
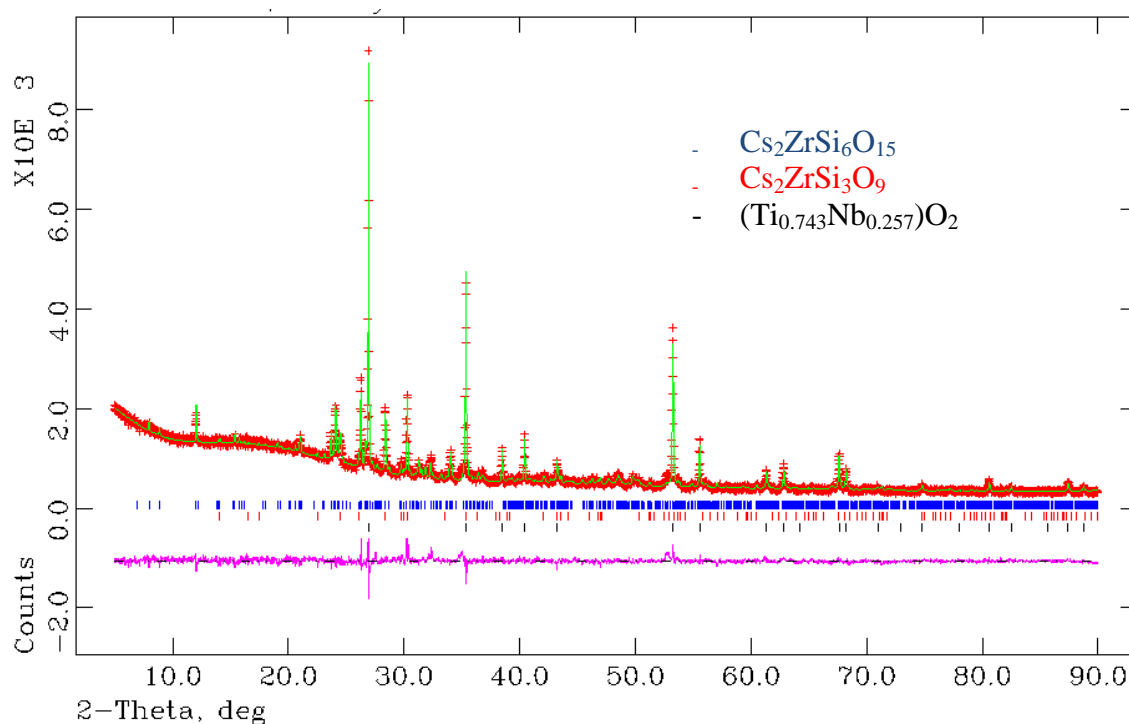
Figure 4.33 Rietveld refinement of the sample of Cs-IONSIV® 12 wt.% HIPed with a total weight percentage of 4% Fe metal. ($\chi^2 = 2.461$, $R_{wp} = 5.74\%$ and $R_p = 4.22\%$)

4.6.3 Metal Al Addition

2% (total weight percentage) of Al metal was added to 6 wt.% Cs-IONSIV® and the sample HIPed. The SEM images exhibits no particular microstructure of interests. The XRD pattern, Figure 4.34, displays a high background and many peaks with low intensity. It is difficult to confirm all the phases present in this sample. The lack of crystalline Cs-containing phases, such as $Cs_2TiNb_6O_{18}$, $Cs_2ZrSi_6O_{15}$ or $Cs_2ZrSi_3O_9$, was confirmed by searching the ICSD-PDF database.
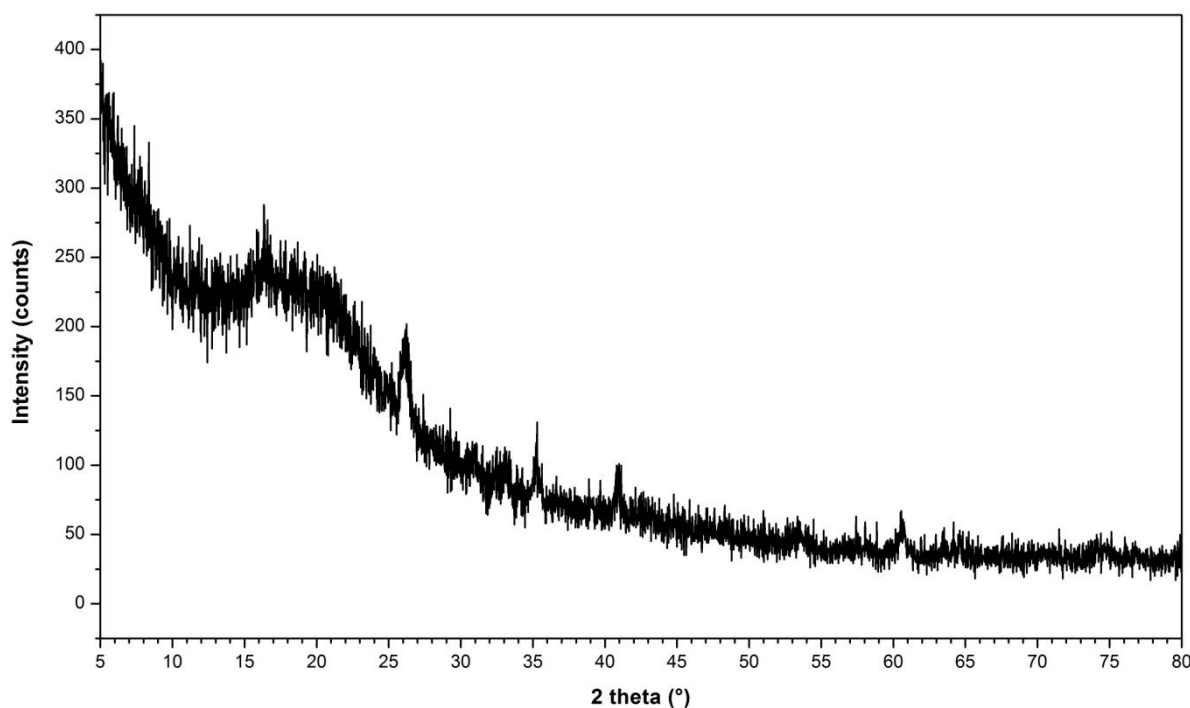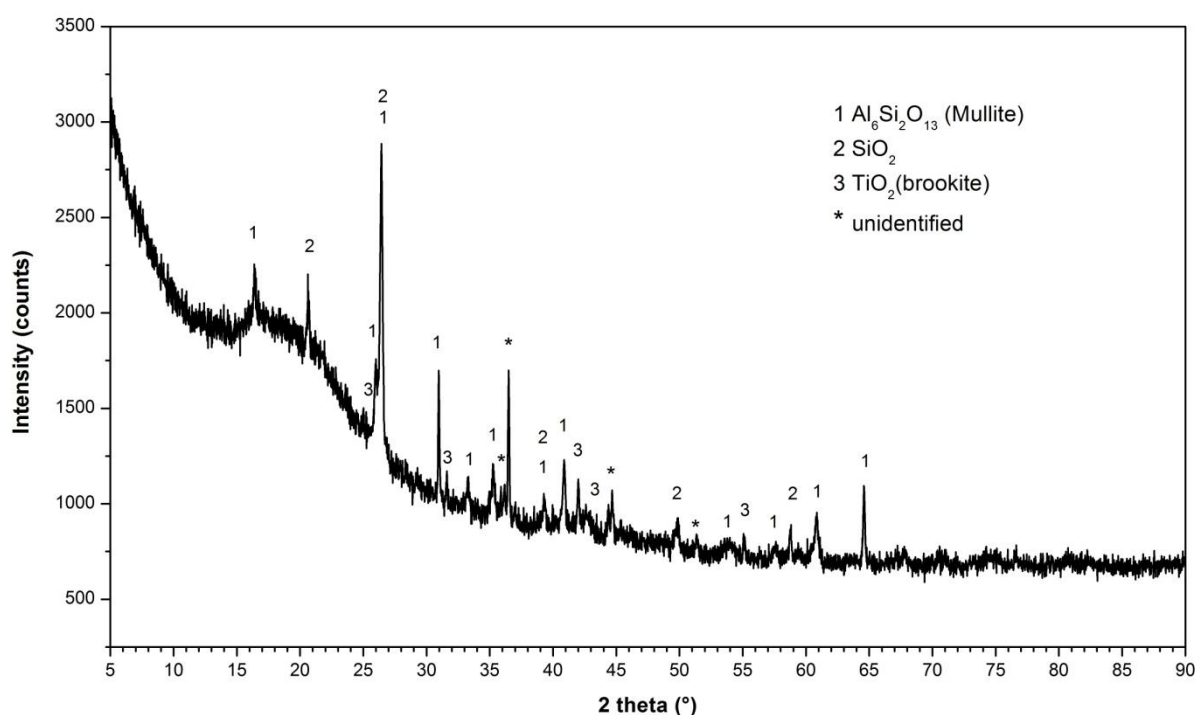

Figure 4.34 The XRD pattern of 6 wt.% Cs-IONSIV® HIPed with 2% (total weight percentage) of Al metal.

In the sample with a larger amount of added Al and a higher Cs content, a more crystalline sample was produced. The XRD pattern of 12 wt.% Cs-IONSIV® HIPed with 4% (total weight percentage) of Al metal is shown in Figure 4.35 and quantitative phase analysis using Rietveld technique is shown in Figure 4.36. This sample contains 4 main phases, 45.88 wt.% of $(Ti_{0.413},Nb_{0.587})O_2$, 13.01 wt.% of $Cs_2ZrSi_3O_9$, 37.64 wt.% of $Cs_2ZrSi_6O_{15}$ and 3.46 wt.% of Al_2O_3, were indexed.
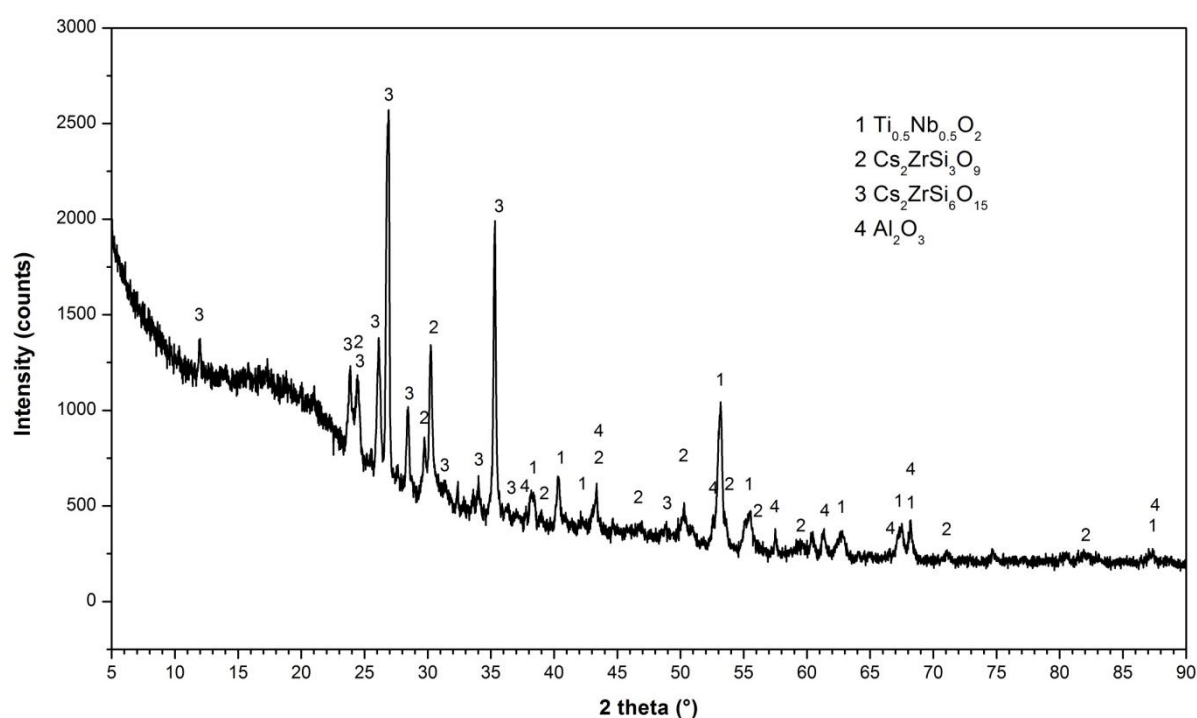
Figure 4.35 The XRD pattern of 12 wt.% Cs-IONSIV® HIPed with 4% (total weight percentage) of Al metal.
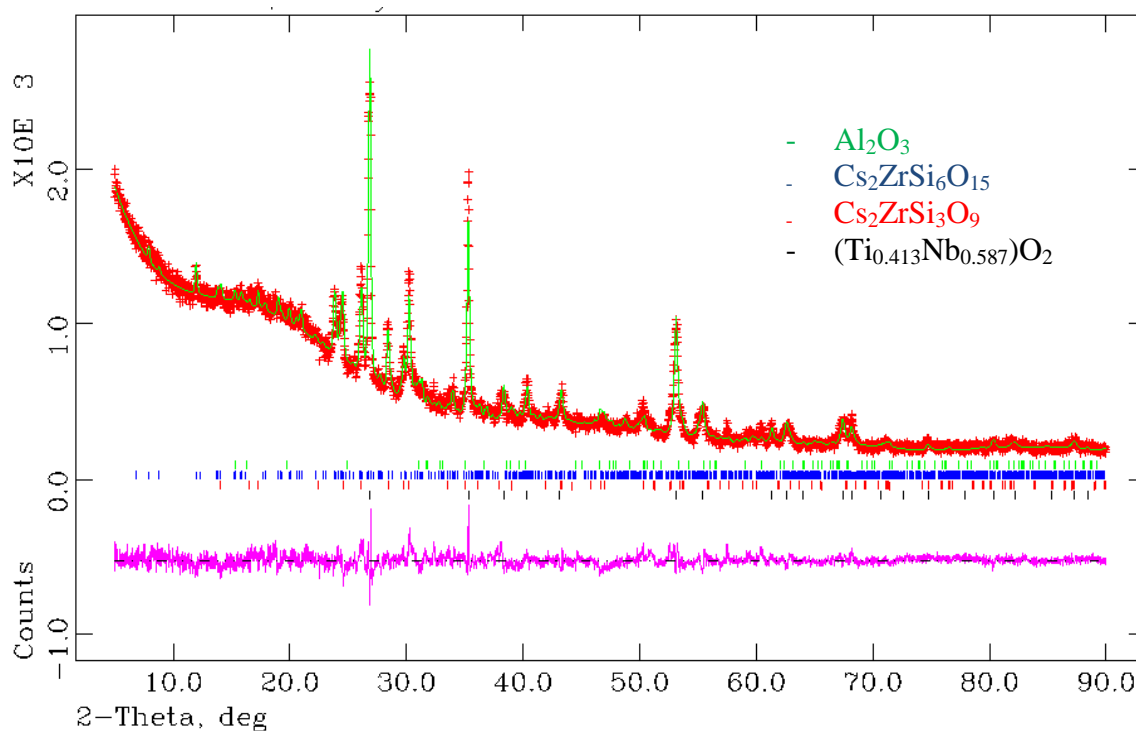
Figure 4.36 Rietveld refinement of the sample from Cs-IONSIV® 12 wt.% HIPed with a total weight percentage of 4% Al metal. ($\chi^2 = 2.251$, $R_{wp} = 6.29\%$ and $R_p = 4.65\%$)

To conclude, three metals (Ti, Fe and Al) have been mixed with Cs-IONSIV® and then the samples HIPed to investigate the effect of the metal additive on phase formation, as well as the possibility of producing hollandite-like compounds. Unfortunately, hollandite phases were never found.

However, the phase assemblage has been affected due to the more reducing environment formed by the metal. It appears that the redox status of the sample during HIPing was changed leading to Nb^{5+} being reduced to Nb^{4+} to form $(Ti^{VI}, Nb^{VI})O_2$, and $Cs_2TiNb_6O_{18}$ was not observed. It was also suggested that the nature of metal itself does not influence which phases form.

4.7 Conclusions

In this chapter, the thermal conversion, phase assemblage and quantitative phase evaluation of HIPed Cs-exchanged IONSIV® at various Cs levels were investigated. Two main Cs-containing phases, $Cs_2TiNb_6O_{18}$ and $Cs_2ZrSi_6O_{15}$, were detected, and they are considered possible Cs leach resistant hosts due to the structures. These findings show promise that a durable wasteform has been created by HIPing IONSIV®.

From the further studies of HIPing Cs-IONSIV® with added metal, it was found that these change the phase assemblage of Cs-IONSIV®s during HIPing. The redox state created by metal plays a key role in phase formation. It was indicated that Cs was gently locked in the crystalline phases regardless of the variety of metal addition.

However, the mechanism of phase formation and the element partitioning during HIPing still need to be further investigated. For example, the Ti/Nb ratio in $(Ti, Nb)O_2$ phase is not able to be determined accurately using X-ray diffraction and, as a consequence, proposing the sequence of $Cs_2TiNb^V_6O_{18}$ and $(Ti, Nb^{IV})O_2$ formation is rather difficult. In addition, further studies of the TEM microstructure with diffraction patterns of HIPed Cs-IONSIV® sample is of great interests because the crystallography studies of the individual grains can be achieved therefore phase identification can be further proved.

Chapter 5   Properties, Structure Determination and Ba Substitution of Cs-Containing Phases as Potential Ceramic Wasteforms

5.1 Introduction

Three Cs-rich phases, $Cs_2TiNb_6O_{18}$, $Cs_2ZrSi_6O_{15}$ and $Cs_2ZrSi_3O_9$, were discovered in the HIPed Cs-IONSIV® samples with and without metal additives. Cs^+ ions are water soluble and will transport rapidly in the environment with groundwater. It is crucial to understand if a ceramic composed of one or more of these condensed phases can potentially serve as a good host for radioactive Cs immobilisation. Therefore, knowledge of the structures of these phases, specifically how Cs is bonded, and properties such as leach rates in the solid wasteforms produced by HIPing are of importance.

The $Cs_2TiNb_6O_{18}$ structure is a pyrochlore analogue. Although materials with the pyrochlore structure have been widely studied as ceramic wasteforms (as discussed in Chapter 1), $Cs_2TiNb_6O_{18}$ has received very little attention for the immobilisation of Cs. The $Cs_2TiNb_6O_{18}$ structure was only studied by one research group[150] in the late 1970s along with a related series of phases of composition $A_2B_6TiO_{18}$ (A = Cs, Rb, Tl, and B = Ta, Nb). The interest in these materials was stated to be ion conductivity due to the tunnel structures.[150, 158] The cation mobility in the intersecting tunnel structures can also lead to ion exchange[159], but no further investigation of $Cs_2TiNb_6O_{18}$ particularly has been reported ever since.

$Cs_2TiNb_6O_{18}$ can be synthesised via solid state reaction, the easiest and most straightforward way as reported by Desgardin et al.[150] However, due to the volatility of Cs at high temperature a solid state reaction which requires high firing temperature and long duration is not ideal for $Cs_2TiNb_6O_{18}$ synthesis. Alternatively a sol-gel method, which has been used to obtain homogeneous glasses and ceramics in other systems, may be preferable. Although the sol-gel method is generally well developed, the use of metal alkoxides for $Cs_2TiNb_6O_{18}$ synthesis via the sol-gel method has never been explored. In this work, an easy-to-control and efficient method for synthesising $Cs_2TiNb_6O_{18}$ using the sol-gel method is studied and the product compared to one made by a solid state reaction.

Alkali zirconosilicates occur widely in nature and the microporous analogues, such as dalyite [$(K,Na)ZrSi_6O_{15}$],[160] elpidite ($Na_2ZrSi_6O_{15}\cdot3H_2O$),[161, 162] umbite ($K_2ZrSi_3O_9\cdot H_2O$)[163, 164] and wadeite ($K_2ZrSi_3O_9$),[165-167] have been successfully synthesised using the hydrothermal method. The topological structures of zirconosilicates and their analogues were investigated and systematically described by Ilyushin and Blatov.[168] Zirconosilicate materials display interesting crystal structures which contain mixed tetrahedral-octahedral frameworks and these zeolite-type materials have received considerable attention in recent years.[169, 170] Zirconosilicates have also been investigated as ion exchangers and show potential applications in separation technology due to the flexibility in optimisation of cation selectivity by varying the different substitutions within the framework.[170]

$Cs_2ZrSi_6O_{15}$ and $Cs_2ZrSi_3O_9$ have drawn much attention as potential wasteforms for Cs retention due to their structures. Investigations of the synthesis, structure and aqueous durability of $Cs_2ZrSi_3O_9$ were carried out by Balmer et al.[90] when following up their previous findings that thermal conversion of Cs-loaded CST produces a durable wasteform -

$Cs_2ZrSi_3O_9$ crystalline phase.[171] Cs is locked in the framework which limits Cs migration. $Cs_2ZrSi_3O_9$ has hexagonal symmetry and is isostructural with wadeite. Both PCT and MCC leach tests showed the great ability of this material to retain Cs in aqueous environments which was attributed to the condensed structure where the channel openings are smaller than the diameter of a Cs ion, hence the mobility of Cs atoms is restricted.[90]

A complete structure determination of $Cs_2ZrSi_6O_{15}$ has been performed by Jolicart et al.[151] The connection of ZrO_6 octahedra and $[Si_6O_{15}]$ layers leaves large cavities where Cs atoms can locate. Generally the MSi_6O_{15} network formed in $A_nMSi_6O_{15}$ compounds exhibit two types of frameworks, open and compact frameworks, as illustrated in Figure 5.1.
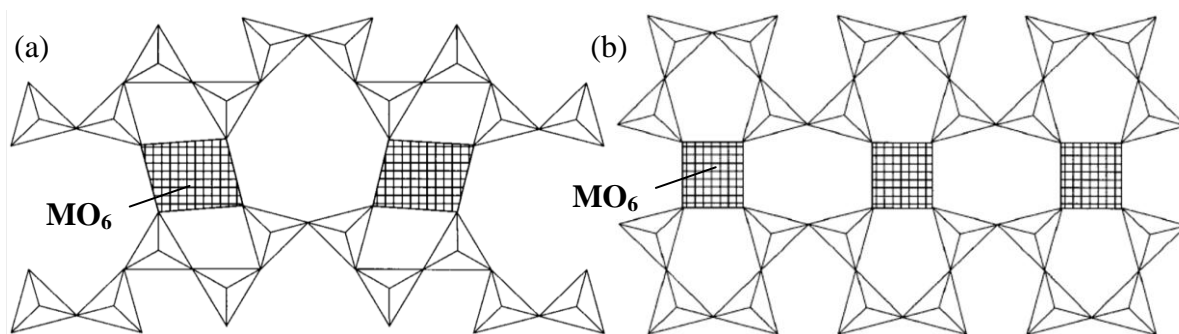
Figure 5.1 Schematic diagram depicting two types of MSi_6O_{15} frameworks: (a) the open frameworks encountered with large M cations (b) the compact frameworks encountered with small M cations. Adapted from reference [172].

The structural study of alkali silicates ($A_nMSi_6O_{15}$, A = alkali atoms, M = Nd, Ce, Zr) as fast ion conductors was previously reported by Haile et al.[172] The framework which contains larger M cations (e.g. Nd or Ce) is more open than that contains smaller cations (e.g. Zr or Ti). The large channels formed in the $A_nMSi_6O_{15}$ framework may serve as pathways for fast alkali

ion transport. In $A_nNdSi_6O_{15}$ and $A_nCeSi_6O_{15}$ systems, it was noticed that the open structure creates the conduction channels for alkali to migrate, therefore, they can act as good conductors.[173] Whereas in $Cs_2ZrSi_6O_{15}$, it was proved that $Cs_2ZrSi_6O_{15}$ adopts the compact structure, which is rather rigid, allowing no Cs to travel along a diffusion pathway. Thus, $Cs_2ZrSi_6O_{15}$ is a promising candidate for caesium storage due to its structural features.

To better understand the behaviours of Cs-rich phases as ceramic wasteforms, pure phases of $Cs_2TiNb_6O_{18}$, $Cs_2ZrSi_6O_{15}$ and $Cs_2ZrSi_3O_9$ were synthesised using ceramic and the sol-gel methods. For these three Cs phases, characterisation of morphologies, thermal gravimetric studies, elemental compositions, and crystal determinations were carried out and compared to previous work.

$^{137}Cs^+$ will radioactively decay to $^{137}Ba^{2+}$ with one or two high energy beta particles, as shown in Figure 5.2. The stability of Cs-containing compounds to incorporate both Cs^+ and Ba^{2+} ions and if any constituents in the structure can act as electron traps during β-decay (e.g $Ti^{4+}+\beta^-\rightarrow Ti^{3+}$ or $Nb^{5+}+\beta^-\rightarrow Nb^{4+}$) are also of concern. To determine whether Ba could also reside in the Cs-containing phases, syntheses with Ba substitution using sol-gel methods were attempted and the products characterised. The knowledge developed in this part of the project such as the structures and Ba substitution can be used to develop more effective materials. The evaluation of practical viability of the use of these Cs-containing phases for radionuclide storage by studying their aqueous durabilities will be presented and discussed in Chapter 6.
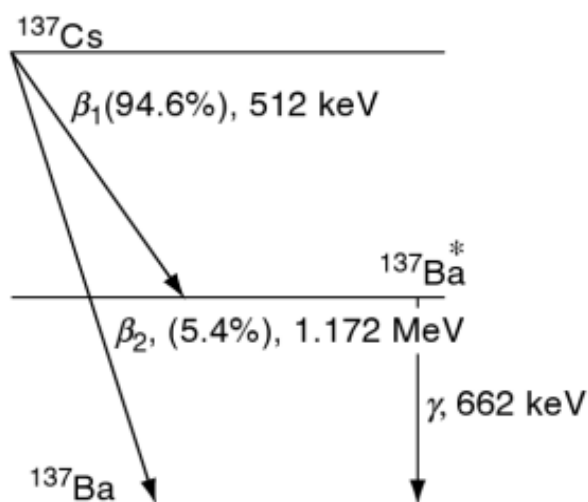
Figure 5.2 Schematic diagram of ^{137}Cs decay. Adapted from reference[80].

5.2 Experimental

5.2.1 Synthesis

5.2.1.1 Solid State Reaction

A mixture of Cs_2CO_3, TiO_2 and Nb_2O_5 at a molar ratio of Cs:Ti:Nb of 2:1:6, and mixtures of $CsCO_3$, ZrO_2 and SiO_2 at molar ratio Cs:Zr:Si of 2:1:6 and 2:1:3 were prepared for syntheses of $Cs_2TiNb_6O_{18}$, $Cs_2ZrSi_6O_{15}$ and $Cs_2ZrSi_3O_9$, respectively. The mixtures were ground together by hand using a pestle and mortar and then pressed into pellets. Pellets were fired within a platinum crucible at 1200 °C for 12 hrs with a heating rate of 10 °C/min. Sintered pellets were ground, pressed again and repeatedly annealed for 4-5 times to increase the purity.

5.2.1.2 Sol-gel Synthesis

(1) $Cs_2TiNb_6O_{18}$

50 wt.% of caesium hydroxide (CsOH) was dissolved in an equal volume of ethanol. A 1 mL portion of the mixture was injected into a mixture of titanium isopropoxide (TTIP) and niobium ethoxide under stirring, followed by the injection of 1 mL of ethanol. The injections of CsOH-EtOH and ethanol additions were repeated until the CsOH-EtOH was depleted. Then an extra 2 mL of ethanol and water were added to the mixture. The concentrations of the reactants were based on a final Cs:Ti:Nb cation ratio of 2:1:6. The mixture was aged overnight and then dried in an oven at 100 °C overnight. The precursor was ground and pressed into pellets before heat treatment. Pellets were placed in a platinum crucible and heated in air at a rate of 10 °C/min to 1200 °C and held for 12 hrs.

(2) $Cs_2ZrSi_6O_{15}$ and $Cs_2ZrSi_3O_9$

$Cs_2ZrSi_6O_{15}$ and $Cs_2ZrSi_3O_9$ were obtained by the same as-mentioned sol-gel synthesis procedure apart from using tetraethyl orthosilicate (TEOS) and 70 wt.% zirconium propoxide (ZrP) as starting materials. For $Cs_2ZrSi_6O_{15}$ and $Cs_2ZrSi_3O_9$, the concentrations of the reactants were mixed at a final Cs:Zr:Si cation ratio of 2:1:6 and 2:1:3, respectively.

(3) Ba substitution in three Cs-containing phases

Three series of nominal formula $Cs_{2-x}Ba_xTiNb_6O_{18}$, $Cs_{2-x}Ba_xZrSi_6O_{15}$ and $Cs_{2-x}Ba_xZrSi_3O_9$ (x = 0, 0.05, 0.1, 0.15 and 0.2) were synthesised using the sol-gel method. $Ba(NO_3)_2$ was used as Ba source in the synthesis. The reactants were mixed based on the desired Cs:Ba:Ti:Nb and Cs:Ba:Zr:Si ratios. The starting gels were aged and dried following

the as-mentioned procedure. Dried precursors were then pressed into pellets and fired at 1200 °C for 12 hrs at a heating rate of 10 °C/min.

5.2.2 Characterisations

5.2.1.1 XRD

Powder X-ray diffraction patterns were collected on a Bruker D8 Advance diffractometer operating in transmission mode using Cu $K_{\alpha 1}$ radiation (λ = 1.5406 Å) in the range of 2 theta from 5° to 90° at a step size of 0.0197° with a LynxEye Si-strip detector.

5.2.1.2 Synchrotron X-ray Diffraction

Synchrotron X-ray powder diffraction data for samples of $Cs_2TiNb_6O_{18}$, $Cs_2ZrSi_6O_{15}$ and $Cs_2ZrSi_3O_9$ synthesised via the sol-gel route were collected at the I11 beamline, Diamond, UK using the high resolution multi-analyser crystal array. For the $Cs_2TiNb_6O_{18}$ data collection, the calibrated wavelength was 0.826118(2) Å and collection time 2 mins. For $Cs_2ZrSi_6O_{15}$ and $Cs_2ZrSi_3O_9$, the calibrated wavelength was 0.827154(2) Å and collection times of 15 mins.

5.2.1.3 Neutron Diffraction

Neutron powder diffraction data for $Cs_2TiNb_6O_{18}$ (synthesised via solid state reactions) were collected using the high-resolution diffractometer GEM, ISIS, UK. About 8 g of sample was used.

5.2.1.4 SEM/EDX

SEM with secondary electron imaging (SEI) and an EDX system was used to determine the morphology and chemical composition of the samples. Loose powder was spread on a conductive carbon film and coated with carbon for SEM/EDX observations. All the investigation was carried out using a Philips XL30 ESEM-FEG with an Oxford Inca 300 EDX system operating at 10 kV.

5.2.1.5 TGA

The dried sol-gel precursors to $Cs_2TiNb_6O_{18}$, $Cs_2ZrSi_6O_{15}$ and $Cs_2ZrSi_3O_9$ were analysed in TGA/DTA experiments with mass spectral analysis preformed on a NETZSCH STA 449FA instrument. Samples (30-40 mg) were heated to 1200 °C at a heating rate of 10 °C/min under oxygen atmosphere. The mass spectrometer was set up to monitor a molecule mass of 44 amu for CO_2.

5.2.1.6 XRF

Fused borate glass beads were analysed for the quantitative determination in Cs-rich phases using XRF. A 0.35 g portion of sample was mixed with 3.5 g of lithium tetraborate, and the mixture was placed in a platinum/gold crucible and heated at 1050 °C for 7 mins. A non-wetting agent, ammonium iodide (NH_4I), was added and the sample was then returned to heat for another 7 mins. The bubbles in the fusion were removed by swirling the crucible if needed and the crucible was returned into the furnace for an additional 2 mins. After cooling, the beads were removed from the crucible and analysed by XRF (Bruker S8Tiger WDXRF).

5.2.1.7 Rietveld Refinement

For the structure refinements, the starting values of the atomic positions and atomic displacement parameters for $Cs_2TiNb_6O_{18}$, $Cs_2ZrSi_6O_{15}$ and $Cs_2ZrSi_3O_9$ were taken from the references [150], [151] and [90], respectively. For the $Cs_2TiNb_6O_{18}$ structure refinement, atomic positions and U_{iso} of Ti and Nb which share the same site were constrained. The U_{iso} values for all of the oxygen atoms were considered to be the same. The occupancies of the Cs and Ti/Nb sites were also refined.

Neutron diffraction refinement using GSAS

The refinement strategy for neutron diffraction in this work is based on the information in reference [174].

(1) Diffractometer parameters:

Neutron diffraction and laboratory XRD data of $Cs_2TiNb_6O_{18}$ were collected and jointly refined using GSAS. For time-of-flight neutron diffraction refinement, the three diffractometer constants in GSAS - DIFC, DIFA and ZERO - relate the time of flight (*t*) of a reflection to its *d*-spacing (*d*) as follows:

$$t = DIFC \times d + DIFA \times d^2 + ZERO$$

Equation 5-1 Relations between time of flight (t) and diffractometer constants in GSAS

DIFC

Combing Equation 5-1 and Bragg's Law (Equation 2-1), DIFC is equal to 505.56 L sinθ where L is total flight of length (assuming that DIFA and ZERO are equal to 0 in Equation

5-1). The DIFC values were refined for the lower resolution histograms (Banks 1-5) and it remained fixed for the highest resolution histogram (Bank 6). During multi-histogram refinement, refining DIFC can prevent the refinement becoming unstable due to the very high degree of correlation between DIFC and the lattice parameters.

DIFA

DIFA values for all of the histograms were refined. The neutron absorption cross-section of an atom is wavelength dependent. In TOF measurements, the short wavelength (low time of flight) neutrons will experience less absorption than the larger wavelength (longer time of flight) neutrons. Therefore, refining DIFA introduces small corrections to the expected time-of-flight of a reflection to allow for peak shifts due to absorption in the sample.

ZERO

This parameter accounts for small differences between the various timing signals in the ISIS accelerator and the instrument data acquisition system, and also allows for the finite response times in the detector electronics. It is instrument dependent and must remain fixed for all the histograms.

(2) Profile parameters:

The pseudo-Voigt function (Peak shape function 2) was used to model the peak shapes. In GSAS, sig-0, sig- 1 and sig-3 are the commonly used terms for Gaussian width and gam-0, gam-1, gam-2 are for Lorentzian width. Although theoretically it is possible to refine these parameters, in practice it may result in unstable and unsatisfactory refinements. In structure refinement, only sig-1 and gam-1 were refined. Exponential parameters such as alp, bet-0 and

bet-1 are the rise and decay coefficients for the two exponential functions. These parameters were kept fixed during structure refinement.

Synchrotron PXRD refinement using GSAS

In GSAS, the specimen displacement and lattice parameters were refined after zero and scale factor had converged and background was graphically fitted. Then, the peak profiles were fitted to symmetric pseudo-Voigt functions (Type 3). GU, GV and GW were firstly refined for Gaussian coefficients and LX and LY were then refined for Lorentzian coefficients.

After a satisfactory profile was achieved, the effect of preferred orientation was refined as well as the Cs occupancy (also the Ti/Nb mixed occupancy for the $Cs_2TiNb_6O_{18}$ phase). For $Cs_2ZrSi_6O_{15}$ and $Cs_2ZrSi_3O_9$ refinements, Si-O bond distances restraints of 1.624 Å were set up with 0.02 Å tolerances.

5.2.1.8 TEM Diffraction Pattern

$Cs_2ZrSi_6O_{15}$ powder was ground and dispersed in ethanol. The suspension was sonicated for 5 mins and then transferred to a holey Cu grid. The sample was loaded in FEI Philips TECNAI F20 operating at 200 kV with an Oxford Inca EDX system.

5.3 Cs$_2$TiNb$_6$O$_{18}$

5.3.1 Synthesis and Optimisation

Cs$_2$TiNb$_6$O$_{18}$ has been successfully synthesised using both solid state reactions and the sol-gel method. The diffraction patterns in Figure 5.3 show the phase growth of Cs$_2$TiNb$_6$O$_{18}$ with repeated sintering of a solid state reaction, and a highly crystalline end product was obtained. A very small amount of impurity, possibly Nb$_2$O$_5$, was found in the final product. However, the impurity remained uncertain due to the relatively weak intensity. Incomplete reaction or undesired phase formation are sometimes observed in solid state reactions due to the slow diffusion rates and the low reactivity of the solid materials and the high firing temperature. Although this method is very economical and easy to perform, a better synthesis route was required to achieve a pure product.
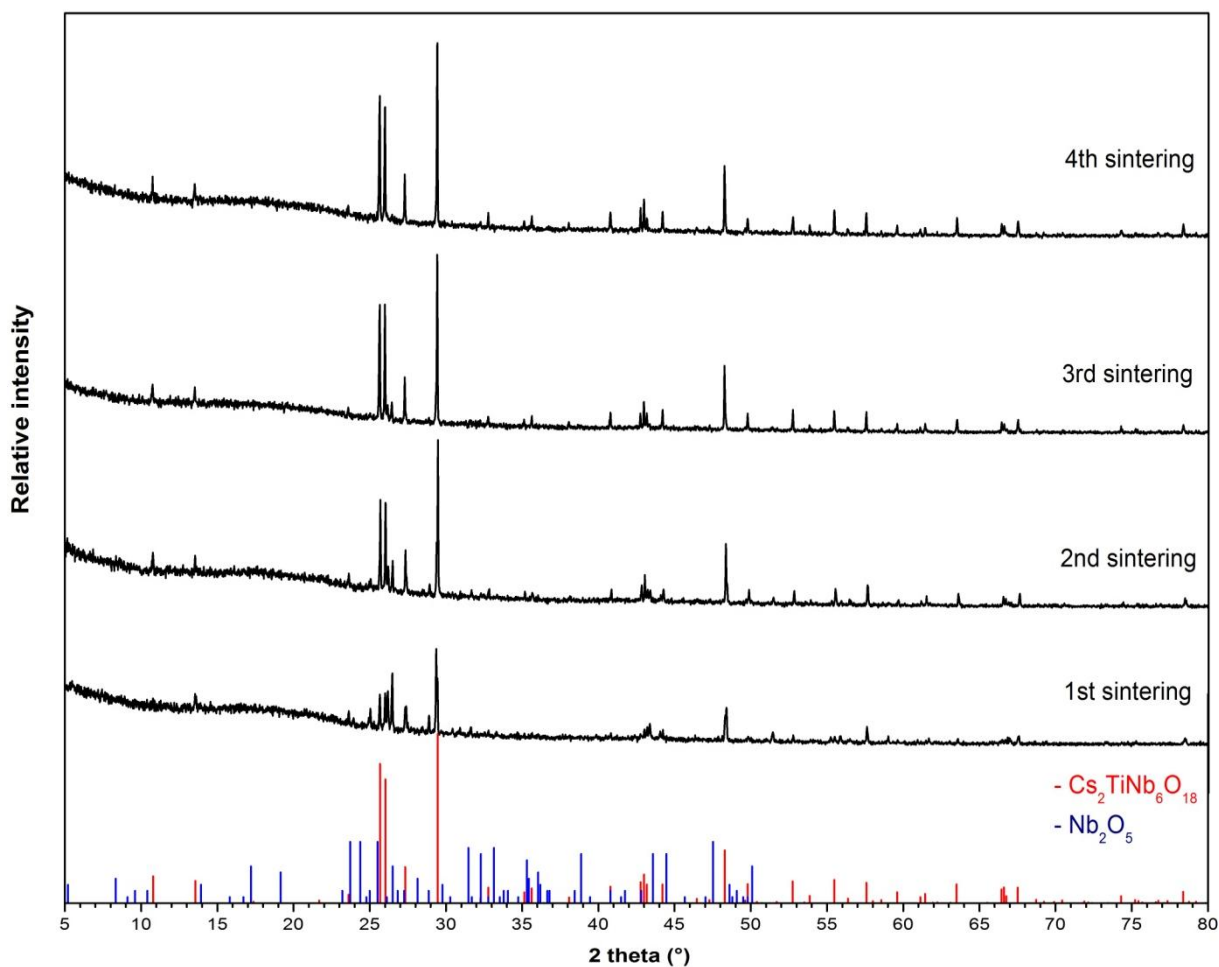
Figure 5.3 XRD patterns showing the phase growth of $Cs_2TiNb_6O_{18}$ during repeating sintering. The red and blue lines are the indexed peaks from the ICDD PDF 01-070-0674 ($Cs_2TiNb_6O_{18}$) and 00-005-0379 (Nb_2O_5), respectively.

Alternatively, $Cs_2TiNb_6O_{18}$ can be obtained using a sol-gel route. Figure 5.4 shows the XRD pattern of $Cs_2TiNb_6O_{18}$ synthesised through the sol-gel route, in this case a highly crystalline and pure product was successfully made in one firing.
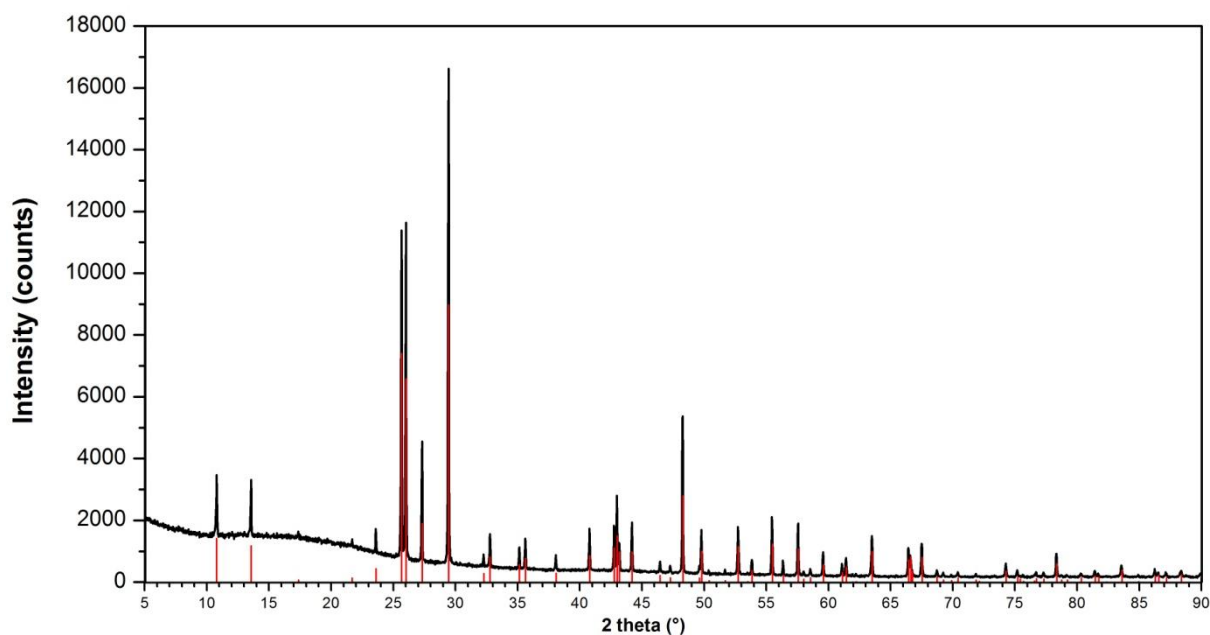
Figure 5.4 XRD pattern of $Cs_2TiNb_6O_{18}$ synthesised via sol-gel route. The red lines are the indexed peaks from the ICDD PDF 01-070-0674.

The advantages of the sol-gel method for this phase are the ease of composition control, reduced firing duration and high quality of the final product. However, the cost of the product is much higher due to the use of niobium ethoxide as starting material. Furthermore, this method is not easy to scale-up since a large amount of organic solvent is used.

5.3.2 Morphology and Elemental Composition

The pure $Cs_2TiNb_6O_{18}$ synthesised using the sol-gel route was subjected to SEM for morphology observation. As shown in Figure 5.5, particles of $Cs_2TiNb_6O_{18}$ do not show uniform size or shape, but generally the particles display hexagonal shape.
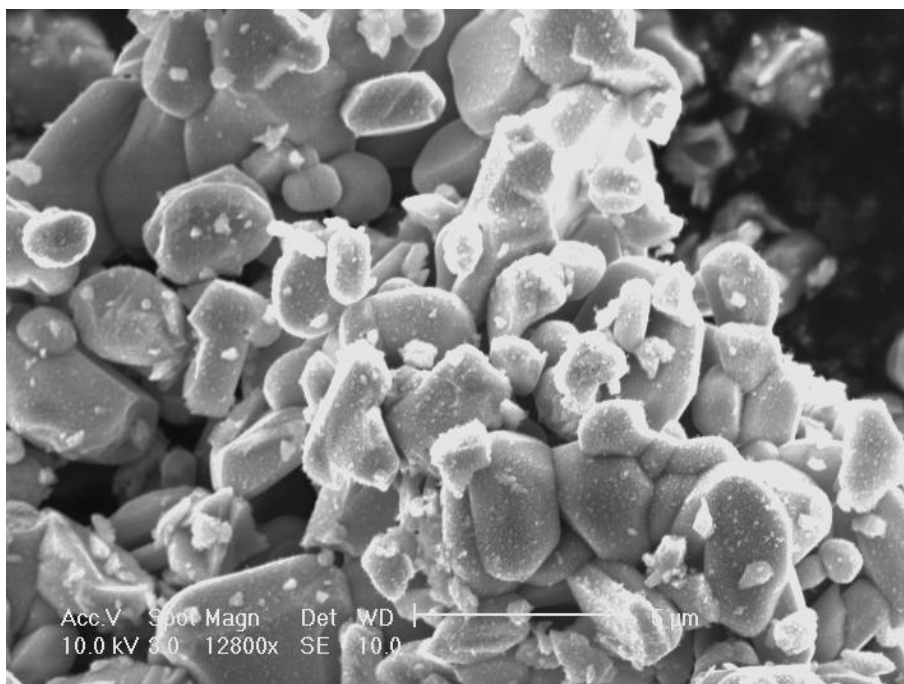
Figure 5.5 Morphology of $Cs_2TiNb_6O_{18}$ synthesised via sol-gel route

In-situ elemental analysis using EDX was not successful because the energy resolution is poor in EDX and peaks of Cs and Ti overlap (as shown in Table 5-1). In principle, the atomic percentage of Ti and Nb should exhibit a 1:6 ratio, however the detected Ti/Nb ratio (atomic percentage) is nearly 1:10 (average of 5 analyses). The errors were possibly from the surface roughness, matrix effect and the lack of calibration in EDX.

Table 5-1 Principal line of the elements in energy[175]

Element	Principal line	Energy (keV)
Cs	L_α	4.2865
Ti	K_α	4.5089
	L_α	0.4522
Nb	K_α	16.584
	L_α	2.1659

Wavelength dispersive XRF was also used to analyse the elemental composition in the samples. The better energy resolution of this method provided a more accurate quantitative analysis. Table 5-2 contains both the weight and atomic percentage of each element as well as the molar ratios normalised to Ti and Nb, respectively, in the $Cs_2TiNb_6O_{18}$ sample synthesised via solid state reactions.

The composition determined using XRF is consistent with the expected one, according to the molar ratio normalised to Nb, which makes the assumption that most of the Nb is incorporated within the $Cs_2TiNb_6O_{18}$. However, the presence of impurity suggests that some of the starting materials, possibly Nb_2O_5, may not be completely converted to $Cs_2TiNb_6O_{18}$ phase. Thus, the calculated molar ratio normalised to Ti should reveal another interpretation in elemental composition. The 4.5% Cs deficiency observed in the XRF result is possibly from the volatility of Cs at high temperature and long firing duration in synthesis procedure as well as in the fused bead preparation step. Additionally, it is also suggested that the impurity may exist as Nb-containing phase.

Table 5-2 XRF result of $Cs_2TiNb_6O_{18}$ synthesised from solid state reactions (fused bead)

Elements	Weight %	Atomic %	Molar ratio (normalised to Nb)	Molar ratio (normalised to Ti)
Cs	23.14	7.47	2.04	1.91
Ti	4.37	3.91	1.06	1
Nb	47.68	22.02	6	5.63
O	24.82	66.59	18.14	17.03

Table 5-3 shows the elemental composition determined by XRF for $Cs_2TiNb_6O_{18}$ synthesised using the sol-gel method. The molar ratio normalised to Nb is consistent to that normalised to Ti. It is suggested that 9.0% and 6.5% of Cs deficiency was observed from the molar ratios normalised to Nb and Ti, respectively. It is suggested that Cs loss was the consequence of the firing procedure in synthesis and/or the fused bead preparation step.

Table 5-3 XRF result (fused bead) of $Cs_2TiNb_6O_{18}$ synthesised via the sol-gel route

Elements	Weight %	Atomic %	Molar ratio (normalised to Nb)	Molar ratio (normalised to Ti)
Cs	21.29	6.83	1.82	1.87
Ti	4.13	3.66	0.97	1.00
Nb	49.31	22.52	6.00	6.16
O	25.27	67.00	17.85	18.32

5.3.3 Thermal Analysis

The results from simultaneous TG/DTA/MS analysis of the dried sol-gel precursor of $Cs_2TiNb_6O_{18}$ are shown in Figure 5.6. The majority of the weight loss (4.77%) occurred below 600 °C. The weight loss and corresponding exothermic event were attributed to the decomposition of residual organics from the sol-gel precursor. It was also supported by the CO_2 emission observed in the mass spectrum of 44 amu. An additional 0.96% of weight loss observed in the range between 600 °C to 1200 °C was likely due to a very mild Cs loss. It is suggested that the synthesis procedure at high temperature does not cause a significant Cs deficiency. The exothermic event in the DTA curve observed above 800 °C indicates the commencement of the crystallisation of $Cs_2TiNb_6O_{18}$.
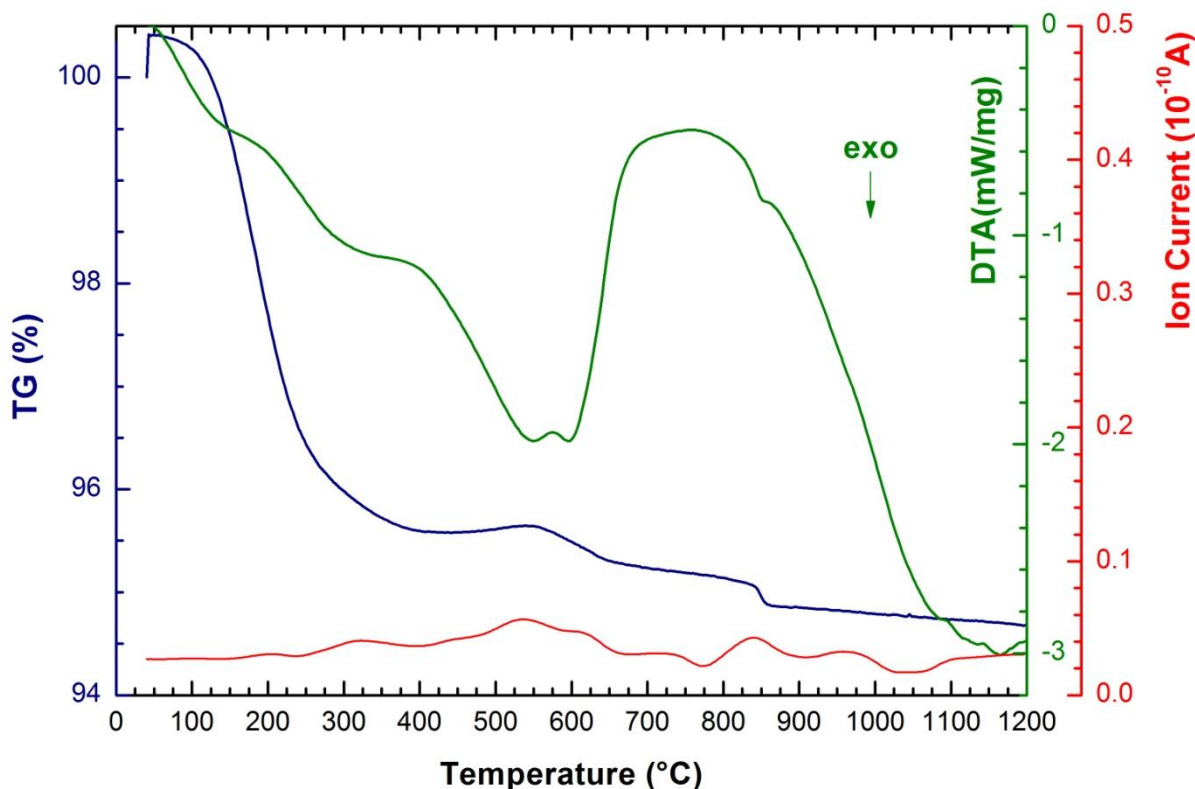
Figure 5.6 TG/DTA/MS plot for the reaction of the sol-gel precursor converting to $Cs_2TiNb_6O_{18}$ (blue- TG curve, green- DTA curve and red-MS curve of 44 amu.)

5.3.4 Structure Refinement

By combining laboratory XRD data and neutron diffraction data of $Cs_2TiNb_6O_{18}$ (synthesised via solid state reactions), a better evaluation of the Ti/Nb mixed occupancy due to the different neutron scattering lengths in Ti (-3.438 fm) and Nb (7.054 fm)[96] can be achieved. A multi-histogram refinement was performed and the fits to the data are shown in Figure 5.7 for histograms 3-7. The refinement parameters are summarised in Table 5-4.

.
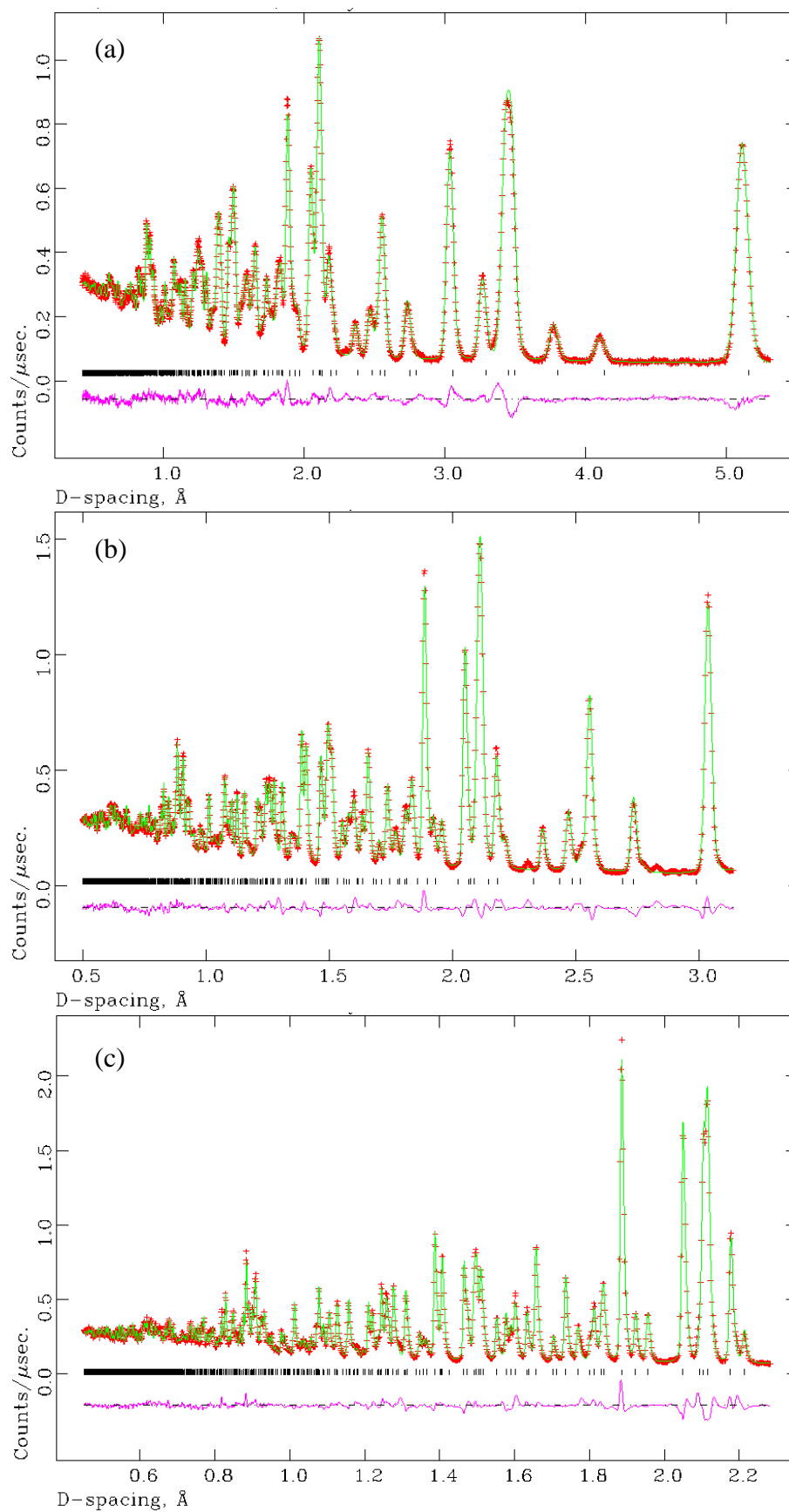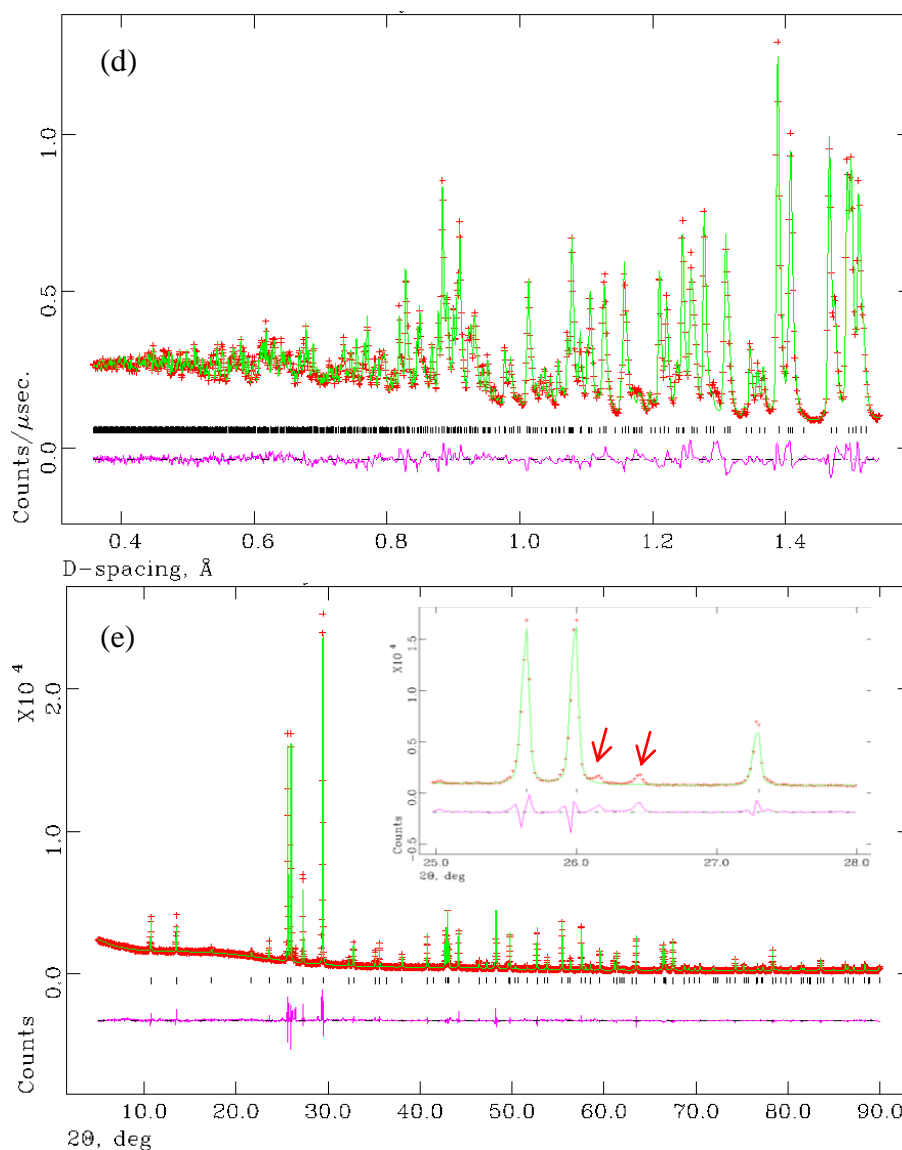
Figure 5.7 Simulated (green line) and experimental diffraction patterns (red dots) as well as difference pattern (purple) for $Cs_2TiNb_6O_{18}$ (solid state reaction) using neutron diffraction data (a) Bank 3, $2\theta = 34.96°$ (b) Bank 4, $2\theta = 63.62°$ (c) Bank 5, $2\theta = 91.30°$ (d) Bank 6, $2\theta = 154.40°$, and (e) using laboratory XRD data.

Table 5-4 Refinement parameters, unit cell parameters, refined atom positions, multiplicities, occupancies and isotropic displacement parameters from the refinement of joint neutron diffraction and laboratory XRD for $Cs_2TiNb_6O_{18}$ synthesised via solid state reactions

Refinement parameters

	Diffraction data		R_{wp}	R_p
Hstgm 3	Neutron	Bank 3	4.82%	4.04%
Hstgm 4	Neutron	Bank 4	4.73%	4.04%
Hstgm 5	Neutron	Bank 5	5.58%	4.64%
Hstgm 6	Neutron	Bank 6	4.73%	3.87%
Hstgm 7	Laboratory	X-ray	8.83%	5.92%
χ^2	9.193			

Lattice parameters

$a\ /Å$	7.535883(2)
$c/\ Å$	8.19086(10)
$Volume/\ Å^3$	402.836(11)

Refined atom positions, multiplicities, occupancies and isotropic displacement parameters

	x	y	z	$Mult$	$Occup$	U_{iso}
Cs1	0.3333	0.6667	0.63336(30)	2	0.999(4)	0.0286(7)
Nb1	0	0	0.5	1	0.728(4)	0.0045(8)
Ti1	0	0	0.5	1	0.272(4)	0.0045(8)
Nb2	0.16872(6)	-0.16872(6)	0.14496(13)	6	0.879(1)	0.0044(2)
Ti2	0.16872(6)	-0.16872(6)	0.14496(13)	6	0.121(1)	0.0044(2)
O1	0.44965(6)	-0.44965(6)	0.15967(13)	6	1	0.0074(1)
O2	0.85720(6)	-0.85720(6)	0.10177(10)	6	1	0.0074(1)
O3	0.12373(6)	-0.12373(6)	0.36269(13)	6	1	0.0074(1)

The unsatisfactory refinement was mainly due to the presence of an unidentified impurity, as indicated with the red arrows in the zoom-in area of Figure 5.7. Neutron data collected from Banks 1-2 were discarded from the structure refinement due to the lack of meaningful data points.

It was observed that the U_{iso} of Cs exhibits a relatively high value, indicating that the Cs occupancy may be overestimated. In general, the displacement parameters highly correlate with the occupancies. With neutron and XRD diffraction data, there are not enough data to allow both to be determined. To better estimate the occupancy of Cs, a second refinement strategy, where the U_{iso} of Cs was fixed at a reasonable value of 0.004 Å^2, close to the ones of the same atom types in the phase, and the constraint of U_{iso} for all the three oxygens was released, was therefore performed. The results are given in Table 5-5. (More information including simulated, experimental diffraction patterns and difference pattern are shown in Appendix 3)

Most of the results remain consistent with the previous refinement except a significant change in Cs occupancy. With all the U_{iso} values reasonably present, the results show a Cs deficiency in this phase. Due to a severe firing procedure applied in solid state synthesis, loss of Cs was anticipated. In comparison, the first strategy exhibits better result in the refinement according to the lower R_{wp} and χ^2 values than the ones from second strategy. However, this further refinement can only provide estimation based on a reasonable fixed U_{iso} value, but this value is related to the material itself, temperature, absorption and the atomic mass. Hence it is usually hard to decide the "true" U_{iso} value from Rietveld refinement.

Table 5-5 Refinement results from the modified refinement of joint neutron diffraction and laboratory XRD for $Cs_2TiNb_6O_{18}$ synthesised via solid state reactions (U_{iso} of Cs is fixed at a value of 0.004 Å^2)

Refinement parameters

	Diffraction data		R_{wp}	R_p
Hstgm 3	Neutron	Bank 3	5.35%	4.98%
Hstgm 4	Neutron	Bank 4	4.93%	4.25%
Hstgm 5	Neutron	Bank 5	5.92%	4.88%
Hstgm 6	Neutron	Bank 6	5.42%	4.44%
Hstgm 7	Laboratory	X-ray	9.46%	6.39%
χ^2	10.59			

Lattice parameters

a /Å	7.53585(8)
c/ Å	8.19086(10)
Volume/ $Å^3$	402.833(11)

Refined atom positions, multiplicities, occupancies and isotropic displacement parameters

	x	y	z	Mult	Occup	U_{iso}
Cs1	0.3333	0.6667	0.63534(26)	2	0.880(3)	0.004
Nb1	0	0	0.5	1	0.732(4)	0.0012(7)
Ti1	0	0	0.5	1	0.268(4)	0.0012(7)
Nb2	0.16850(6)	0.16850(6)	0.14499(14)	6	0.878(1)	0.0054(18)
Ti2	0.16850(6)	0.16850(6)	0.14499(14)	6	0.122(1)	0.0054(18)
O1	0.44965(6)	0.44965(6)	0.15951(15)	6	1	0.0072(2)
O2	0.85716(7)	0.85716(7)	0.10163(11)	6	1	0.0060(2)
O3	0.12375(6)	0.12375(6)	0.36243(14)	6	1	0.0078(2)

Cs$_2$TiNb$_6$O$_{18}$, a pyrochlore analogue, crystallises in the hexagonal system, and the unit cell parameters *a* and *c* are 7.535883(2) Å and 8.19385(3) Å, respectively. Figure 5.8 shows the crystal structure. It consists of layers of (M$_6$O$_{15}$)$_n$ sheets linked by the (MO$_3$)$_n$ octahedral parallel to the *c* axis by sharing corners (shown in Figure 5.9), thus cavities bounded by 21 oxygens are formed. Cs cations are located between two (M$_6$O$_{15}$)$_n$ layers and almost occupy the entire volume of the cages "O$_{21}$". The structure of Cs$_2$TiNb$_6$O$_{18}$ is rigid, thus the mobility of the Cs cation is limited.[158, 159]
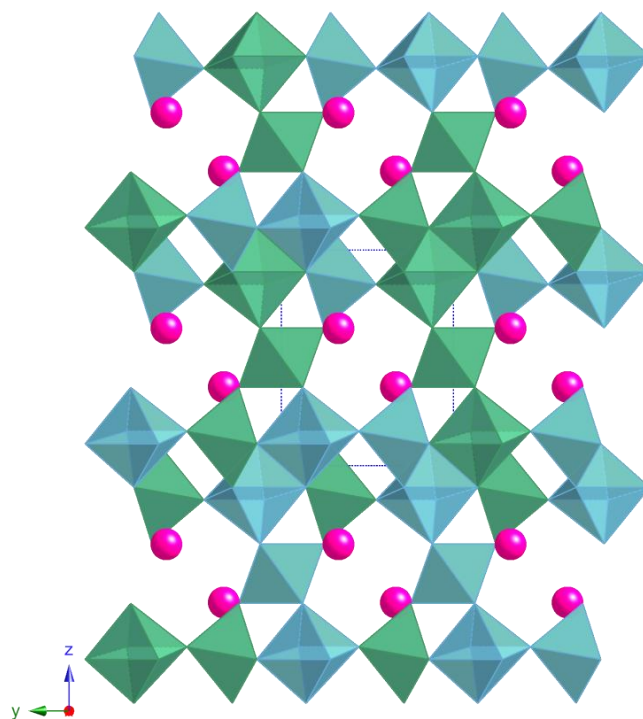
Figure 5.8 Crystal structure of Cs$_2$TiNb$_6$O$_{18}$ as viewed down the *a* zone axis. Green octahedra represent Nb/TiO$_6$, blue octahedra represent Ti/NbO$_6$ and pink spheres represent Cs atoms.
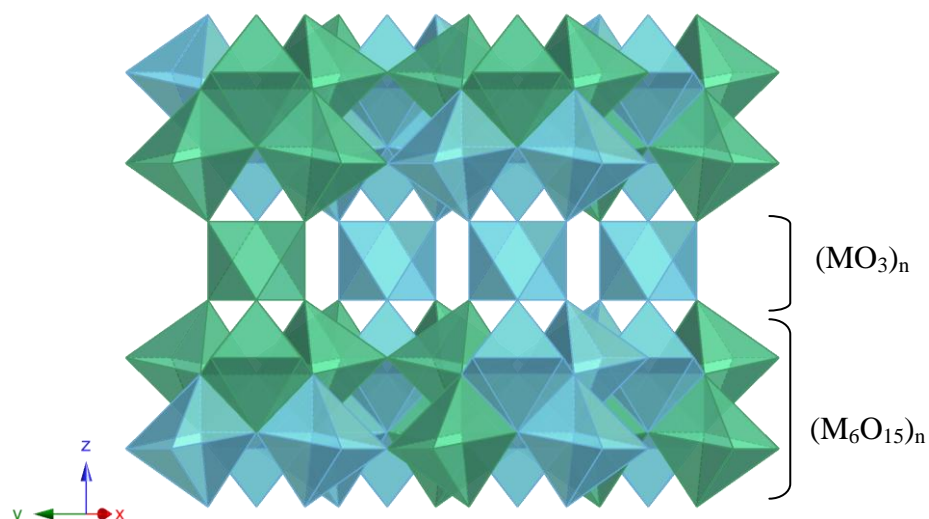
Figure 5.9 Polyhedral representation of $Cs_2TiNb_6O_{18}$ viewed along [100].

Synchrotron PXRD data of $Cs_2TiNb_6O_{18}$ synthesised using the sol-gel method were collected and the Rietveld refinement was performed. Figure 5.10 shows the difference between the simulated and experimental diffraction patterns for $Cs_2TiNb_6O_{18}$ (sol-gel).
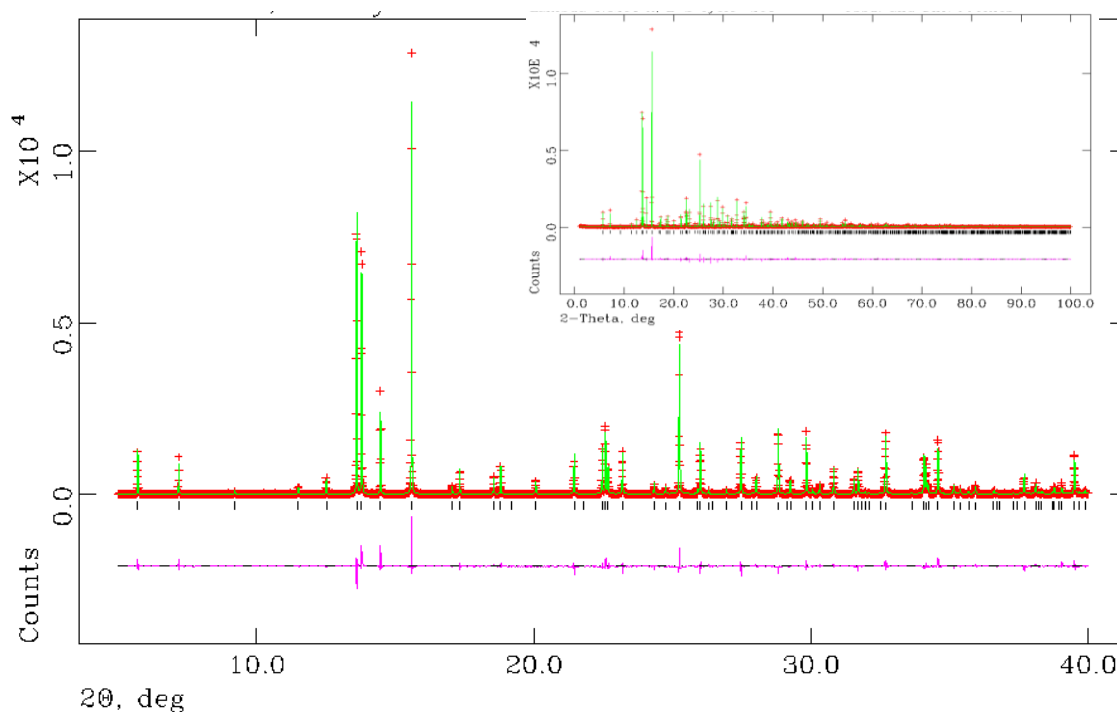
Figure 5.10 Simulated (green line) and experimental diffraction patterns (red dots) as well as difference pattern (purple) for $Cs_2TiNb_6O_{18}$ (sol-gel) using synchrotron X-ray diffraction data

In general, the structural information from Rietveld refinement, such as lattice parameters and atomic positions, of $Cs_2TiNb_6O_{18}$ obtained from solid state reactions and the sol-gel method shows consistent results (see Table 5-4 and Table 5-6). Both neutron and synchrotron diffraction data showed that $Cs_2TiNb_6O_{18}$ possesses a structure where there is only a slight ordering of the Ti and Nb cations over the two sites in the lattice.

Table 5-6 Refinement parameters, unit cell parameters, refined atom positions, multiplicities, occupancies and isotropic displacement parameters from the refinement of synchrotron PXRD for $Cs_2TiNb_6O_{18}$ synthesised via a sol-gel method

Refinement parameters		*Lattice parameters*	
R_{wp}	17.40%	a /Å	7.535883(2)
R_p	13.42%	c/ Å	8.19385(3)
χ^2	3.684	*Volume*/ $Å^3$	402.833(11)

Refined atom positions, multiplicities, occupancies and isotropic displacement parameters

	x	*y*	*z*	*Mult*	*Occup*	U_{iso}
Cs1	0.3333	0.6667	0.63406(19)	2	1.025(3)	0.0204(3)
Nb1	0	0	0.5	1	0.776(10)	0.0044(6)
Ti1	0	0	0.5	1	0.224(10)	0.0044(6)
Nb2	0.16946(6)	-0.16946(6)	0.14625(11)	6	0.871(2)	-0.0030(1)
Ti2	0.16946(6)	-0.16946(6)	0.14625(11)	6	0.129(2)	-0.0030(1)
O1	0.4481(4)	-0.4481(4)	0.1603(8)	6	1	-0.0007(7)
O2	0.8594(4)	-0.8594(4)	0.0967(7)	6	1	-0.0007(7)
O3	0.1232(4)	-0.1232(4)	0.3575(8)	6	1	-0.0007(7)

5.3.5 Bond Valence Sum

The metal-oxygen distances in the cages (Cs-O) and octahedral (Ti-O and Nb-O) sites of $Cs_2TiNb_6O_{18}$ from both solid state synthesis and the sol-gel method are listed in Table 5-7 and Table 5-8, respectively, along with bond valence sums.

Ti and Nb atoms adopt classic octahedral coordination. Compared with $Cs_2TiNb_6O_{18}$ (solid state), the mean Ti-O and Nb-O bond distances in $Cs_2TiNb_6O_{18}$ (sol-gel) are closer to the sum of ionic radii of Ti^{4+} (0.605 Å) and O^{2-} (1.40 Å), and Nb^{5+} (0.64 Å) and O^{2-}, respectively.[176] The calculated bond valence sum for each of the distinct positions are consistent with the proposed formula $Cs_2TiNb_6O_{18}$. Moreover, it is suggested that the slightly overbonded Nb and underbonded Ti observed in both cases were due to the partial disorder of the Ti and Nb cations over the two six-coordinate sites in the octahedral framework.

The bonding environment of Cs in the structure may be important for understanding its use as a wasteform and a simple measure is to calculate the coordination number of Cs. However, there is no rigorous definition of bond length cut-off that has been successfully set. Conventionally a definition that is based on the electrostatic linkages between atoms and therefore directly reflects the contribution of each bond to the cohesion energy of the crystal is applied. It sometimes contains bonds to the second nearest neighbouring atoms that would have small fluxes (< 0.05 v.u.) and not be considered chemically bonded. To better determine the coordination number of Cs which the electrostatic fluxes that make major contribution to the chemical bonding, a simple criterion was applied to decide if two atoms are bonded.

In this work, the determination of coordination number is to set an lower threshold for the experimental bond valence proposed by Altermatt and Brown.[101, 177]

A bond exists between a cation and an anion if its experimental bond valence is larger than 0.04 × the cation valence.[101]

The rule is considered reasonable and appropriate because it takes the chemical and geometric considerations into account. The definition can be justified for use with the bond valence model since any true bond that is excluded by this definition contributes at most 4% to the cation bond valence sum.

Using this criteria the few long distances between Cs1 and O3 (as marked * in Table 5-7 and Table 5-8) were too weak to contribute the valence to the cation and excluded. Thus, Cs exhibits coordination number 9 in the $Cs_2TiNb_6O_{18}$ structure.

Table 5-7 Inter-atomic Cs-O, Ti-O, and Nb-O distances (Å) in $Cs_2TiNb_6O_{18}$ (solid state reaction) calculated based on the joint refinement result using neutron diffraction data and laboratory XRD data.

Atom		Bond length (Å)		Mean distance(Å)	Valence sum	Coordination
Cs1	O1	3.3015(15)	× 1			
	O1	3.3010(15)	× 2			
	O2	3.2999(18)	× 1	3.37		
	O2	3.3004(18)	× 2	(for 9 existing Cs-O bonds)		
	O3	3.5210(18)	× 1		0.84	9
	O3	3.5215(18)	× 2	3.55		
	O3	3.80959(12)	× 2*	(for all Cs-O bonds)		
	O3	3.80912(12)	× 2*			
	O3	3.80986(12)	× 2*			

Atom		Bond length (Å)		Mean distance (Å)	Valence sum	Coordination
Nb1	O3	1.9681(9)	× 6	1.97	5.14	6

Atom		Bond length (Å)		Mean distance (Å)	Valence sum	Coordination
Ti1	O3	1.9681(9)	× 6	1.97	3.97	6

Atom		Bond length (Å)		Mean distance (Å)	Valence sum	Coordination
Nb2	O1	1.9168(6)	× 2			
	O2	2.0843(6)	× 2	1.99	5.00	6
	O2	2.0491(13)	× 1			
	O3	1.8775(14)	× 1			

Atom		Bond length (Å)		Mean distance (Å)	Valence sum	Coordination
Ti2	O1	1.9168(6)	× 2			
	O2	2.0843(6)	× 2	1.99	3.86	6
	O2	2.0491(13)	× 1			
	O3	1.8775(14)	× 1			

Average bond valence sum			
Nb	5.07		
Ti	3.92		

*: Distances considered too long for bonds.

Table 5-8 Inter-atomic Cs-O, Ti-O, and Nb-O distances (Å) in $Cs_2TiNb_6O_{18}$ (sol-gel) calculated based on the refinement result using synchrotron X-ray diffraction data

Atom		Bond length (Å)		Mean distance (Å)	Valence sum	Coordination
Cs1	**O1**	3.315(5)	× 3	3.41 (for 9 existing Cs-O bonds)	0.78	9
	O2	3.347(5)	× 3			
	O3	3.558(5)	× 1			
	O3	3.559(5)	× 2			
	O3	3.8126(8)	× 2*	3.57 (for all Cs-O bonds)		
	O3	3.8121(7)	× 2*			
	O3	3.8129(7)	× 2*			

Atom		Bond length (Å)		Mean distance (Å)	Valence sum	Coordination
Nb1	**O3**	1.987(6)	× 6	1.99	4.89	6

Atom		Bond length (Å)		Mean distance (Å)	Valence sum	Coordination
Ti1	**O3**	1.987(6)	× 6	1.99	3.77	6

Atom		Bond length (Å)		Mean distance (Å)	Valence sum	Coordination
Nb2	**O1**	1.9054(14)	× 2	1.96	5.23	6
	O2	2.0900(21)	× 2			
	O2	2.026(6)	× 1			
	O3	1.834(6)	× 1			

Atom		Bond length (Å)		Mean distance (Å)	Valence sum	Coordination
Ti2	**O1**	1.9054(14)	× 2	1.96	4.03	6
	O2	2.0900(21)	× 2			
	O2	2.026(6)	× 1			
	O3	1.834(6)	× 1			

Average bond valence sum	
Nb	5.06
Ti	3.90

*: Distances considered too long for bonds.

5.4 $Cs_2ZrSi_6O_{15}$

5.4.1 Synthesis and Optimisation

Attempts to prepare $Cs_2ZrSi_6O_{15}$ were made using solid state reactions and also the sol-gel method.

The synthesis via a solid state reaction was not successful. The starting reagents ZrO_2 and SiO_2 were too chemically stable and the particle sizes were too large to react. To achieve a solid state reaction, reagents with high surface area can be used to increase the reactivity. For example, Balmer et al.[90] used m-ZrO_2 with a small particle size (30 nm in average) and high surface area (40 m^2/g) as reactant and milled the mixture before heat treatment to synthesise $Cs_2ZrSi_3O_9$, the other phase in the same Cs_2O-ZrO_2-SiO_2 system.

Alternatively, $Cs_2ZrSi_6O_{15}$ can be obtained hydrothermally by sealing the reagents ($2Cs_2O$-$1ZrO_2$-$3SiO_2$-$4.9H_3PO_4$-$13.5H_2O$) in a platinum tube and submitting to an external pressure of nitrogen (80 MPa) in an autoclave, as reported by Jolicart et al.[151] However, this method involves high temperature (813 °C), high pressure (up to 218 MPa in nitrogen atmosphere) and long duration (~ 500 hrs), thus it is hard to perform in a normal laboratory.

As found here, the sol-gel route is better because a product of good quality can be synthesised in an easily controlled manner. In addition, syntheses of various caesium zirconium silicates phases can be performed by modulating the starting gel to the desired Cs:Zr:Si ratio. Furthermore, the relatively gentle firing conditions and cheaper cost have made sol-gel methods generally attractive. The XRD pattern of $Cs_2ZrSi_6O_{15}$ shown in Figure 5.11 shows that a highly pure and crystalline final product can be obtained using the sol-gel method.
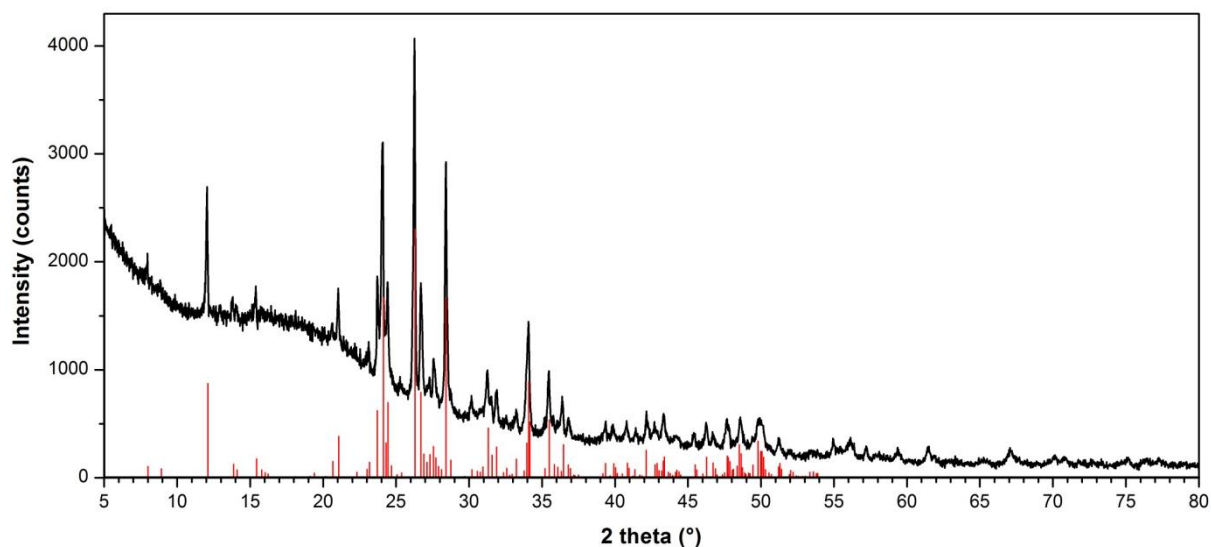
Figure 5.11 XRD pattern of $Cs_2ZrSi_6O_{15}$ synthesised via sol-gel method. The red lines are the indexed peaks from the ICDD PDF 01-086-0738 ($Cs_2ZrSi_6O_{15}$)

5.4.2 Morphology and Elemental Composition

The SEM micrograph of $Cs_2ZrSi_6O_{15}$ is shown in Figure 5.12 and clearly it does not exhibit uniform particles. The particle sizes vary from 1 μm to 5 μm in length. However, some grains do have similar morphology, as indicated with the red arrows in Figure 5.12 (a). The particle seems to appear as hill shaped with corrugated surface, as seen in Figure 5.12 (b).
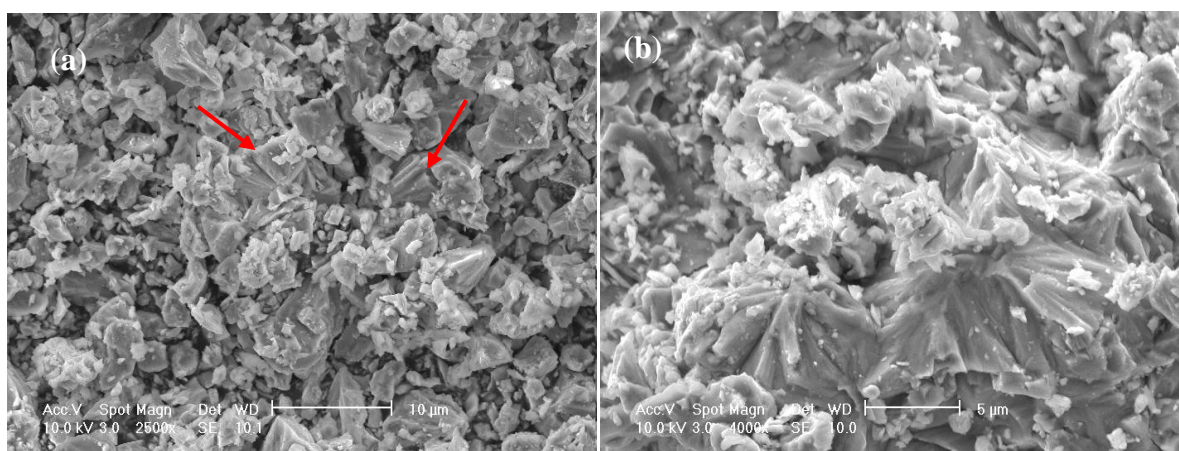
Figure 5.12 SEM micrographs $Cs_2ZrSi_6O_{15}$ at magnification of (a) ×2,500 (b) ×4,000

181

To determine the exact chemical composition of $Cs_2ZrSi_6O_{15}$, some powder was fused into a glass bead and analysed by XRF. Table 5-9 shows the elemental ratio normalised to Zr and Si in this $Cs_2ZrSi_6O_{15}$ sample. Unfortunately, the results are not consistent with the expected composition no matter which normalised data are used. The reduced Cs content suggests that some mass absorption effects might occur during the analysis. Mass absorption effects are normally from two main sources, fluorescence radiation being absorbed by coexisting elements (reduced intensity), or enhancement of fluorescence radiation due to secondary radiation from itself or coexisting elements (increased intensity). This phenomenon was observed in the quantitative analysis in other Cs-Zr-Si systems using XRF. Attempts to better calibrate were made, however the effect was still not solved.

Table 5-9 Elemental composition of $Cs_2ZrSi_6O_{15}$ using XRF (fused bead)

Element	Weight %	Atomic %	Molar ratio (normalised to Zr)	Molar ratio (normalised to Si)
Cs	27.89	0.21	1.35	1.21
Zr	14.20	0.16	1	0.90
Si	23.94	1.04	6.69	6
O	33.96	2.12	13.63	12.23

5.4.3 Thermal Analysis

Simultaneous TG/DTA/MS analyses of the dried sol-gel precursor of $Cs_2ZrSi_6O_{15}$ are shown in Figure 5.13 and indicate that the majority of the weight loss (7.26%) occurred below 600 °C. The mass spectrum of 44 amu was monitored for CO_2 emission, from this the weight loss and corresponding exothermic event are attributed to the decomposition of residual

organics from the sol-gel precursor. An additional 0.43% of weight loss observed in the range above 600 °C was likely due to a small Cs loss. This suggests that the sol-gel method is an ideal synthesis route for $Cs_2ZrSi_6O_{15}$. Unlike $Cs_2TiNb_6O_{18}$, the exothermic event associated with a crystallisation stage was not observed in the DTA curve shown in Figure 5.13.
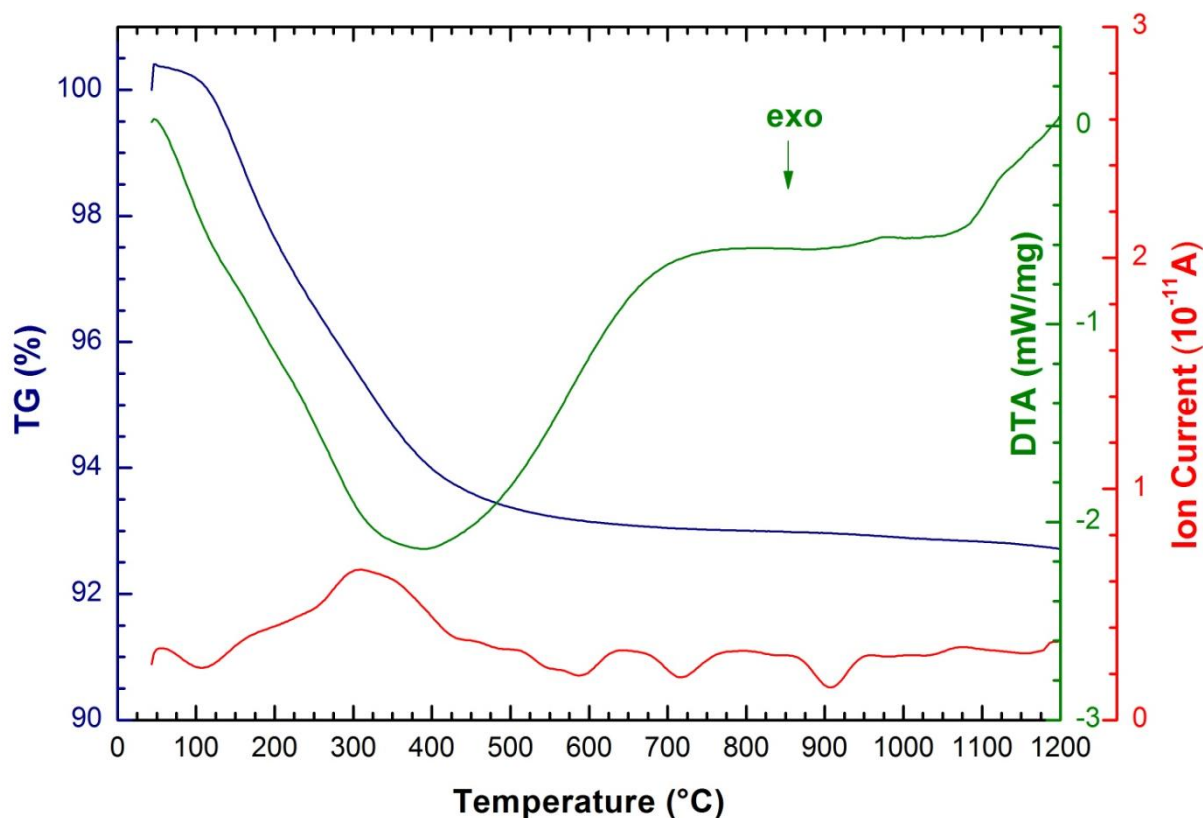
Figure 5.13 TG/DTA/MS plot for the reaction of the sol-gel precursor converting to $Cs_2ZrSi_6O_{15}$ (blue- TG curve, green- DTA curve and red- MS curve of 44 amu)

5.4.4 Structure Refinement

Synchrotron X-ray powder diffraction data from a sample of $Cs_2ZrSi_6O_{15}$ were collected and analysed by Rietveld refinement. To keep Si in tetrahedral coordination, Si-O bond lengths were restrained to 1.624 Å, the bond valence parameter reported by Brown and Altermatt,[102] with a tolerance of 0.02 Å. The difference between the simulated and experimental diffraction patterns for $Cs_2ZrSi_6O_{15}$ (sol-gel) are shown in Figure 5.14 and refined atomic parameter are given in Table 5-10. The refinement confirmed that this compound is monoclinic (space group $C2/m$), and its lattice parameters were $a = 26.6225(5)$ Å, $b = 7.4846(1)$ Å, $c = 11.6155(2)$ Å and $\beta = 107.495(1)$ °.
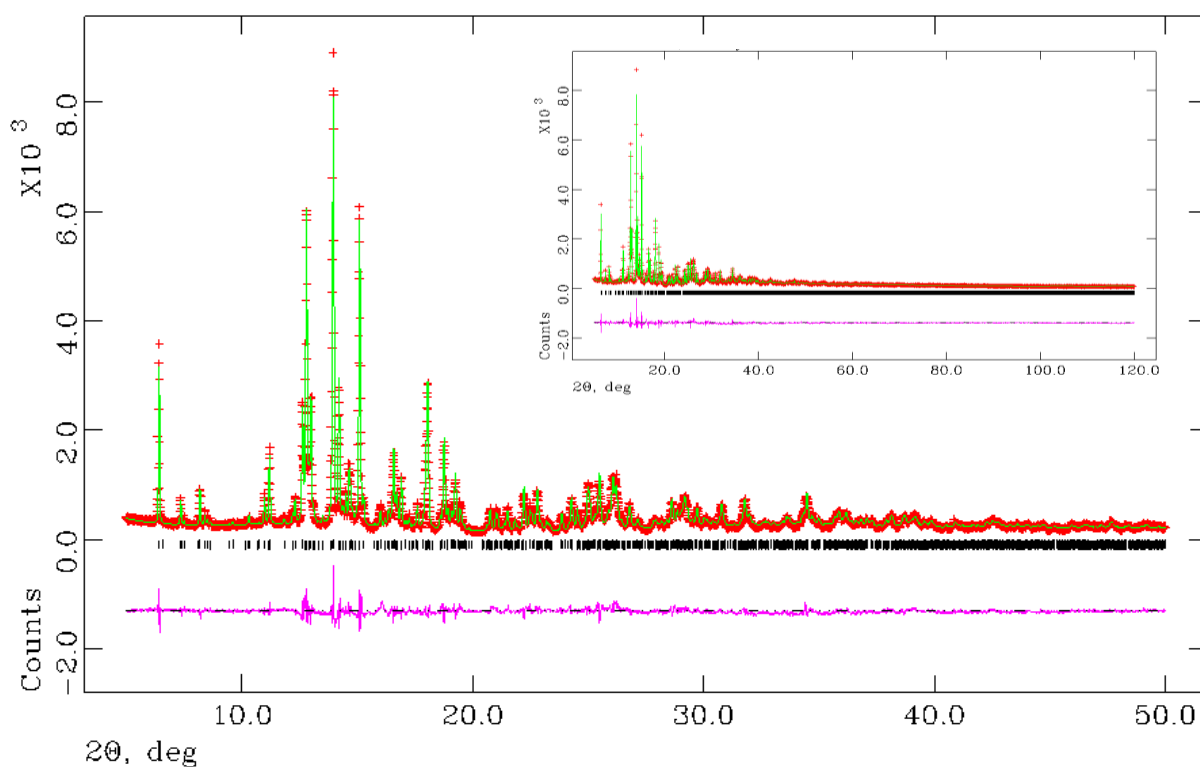
Figure 5.14 Simulated (green line) and experimental diffraction patterns (red dots) as well as difference pattern (purple) for $Cs_2ZrSi_6O_{15}$ (sol-gel). ($\chi^2 = 8.959$, $R_{wp} = 9.33\%$, $R_p = 7.28\%$)

Table 5-10 Refinement parameters, unit cell parameters, refined atom positions, multiplicities, occupancies and isotropic displacement parameters from the refinement of synchrotron PXRD for $Cs_2ZrSi_6O_{15}$ synthesised via a sol-gel method

Refinement parameters		*Lattice parameters*	
R_{wp}	9.33%	$a/Å$	26.6225(5)
R_p	7.28%	$b/Å$	7.4846(1)
χ^2	8.959	$c/Å$	11.6156(2)
		$Volume/Å^3$	2207.44(9)
		$\beta/°$	107.495(1)

Refined atom positions, multiplicities, occupancies and isotropic displacement parameters

	x	y	z	*Mult*	*Occup*	U_{iso}
Cs1	0.57496(15)	0	0.01211(32)	4	0.981(5)	0.026(1)
Cs2	0.89817(13)	0	0.37456(30)	4	0.929(5)	0.026(1)
Cs3	0.75359(14)	0	0.35801(34)	4	1.006(5)	0.054(2)
Zr1	0	0	0	2	1	0.047(3)
Zr2	0.32019(14)	0	0.3568(4)	4	1	0.001(7)
Si1	0.62609(34)	0.2045(9)	0.3680(7)	8	1	0.049(4)
Si2	0.30766(16)	0.1978(10)	0.0900(6)	8	1	0.032(4)
Si3	0.4631(4)	0	0.3604(4)	4	1	0.019(5)
Si4	0.1356(5)	0	0.0007(9)	4	1	0.004(4)
Si5	0.1816(5)	0	0.2536(12)	4	1	0.050(5)
Si6	0.51398(29)	0.3089(11)	0.2745(9)	8	1	0.031(4)
O1	0.6606(5)	0.2056(22)	0.5095(8)	8	1	0.014(1)
O2	0.4006(5)	0	0.3474(17)	4	1	0.014(1)
O3	0.25	0.25	0	4	1	0.014(1)
O4	0	0.5	0	2	1	0.014(1)
O5	0.8114(6)	0.2743(20)	0.2310(8)	8	1	0.014(1)
O6	0.6572(5)	0.3185(14)	0.2919(11)	8	1	0.014(1)
O7	0.57008(32)	0.2782(22)	0.3773(10)	8	1	0.014(1)
O8	0.6236(8)	0	0.3198(17)	4	1	0.014(1)
O9	0.1874(6)	0	0.1184(11)	4	1	0.014(1)
O10	0.3537(5)	0.3315(16)	0.0768(13)	8	1	0.014(1)
O11	0.5191(6)	0.3012(21)	0.1387(10)	8	1	0.014(1)
O12	0.3232(8)	0	0.0543(17)	4	1	0.014(1)
O13	0.2400(6)	0	0.3508(17)	4	1	0.014(1)
O14	0.9929(8)	0	0.3076(20)	4	1	0.014(1)
O15	0.4666(4)	0.1784(14)	0.2835(13)	8	1	0.014(1)
O16	0.0857(6)	0	0.0538(17)	4	1	0.014(1)

A projection of the refined $Cs_2ZrSi_6O_{15}$ structure along [010] is shown in Figure 5.15. The crystal structure consists of corrugated double chain $(Si_6O_{15})_n$ silicate layers that form a three-dimensional framework by sharing corners with ZrO_6 octahedra. The Cs cations occupy the channels created by the network structure. The typical structure formation is also observed in many alkali zirconosilicate (alkai = Li-Cs)[160, 178] and alkali silicates, such as $Cs_2TiSi_6O_{15}$ and $K_2TiSi_6O_{15}$.[157, 173, 179]
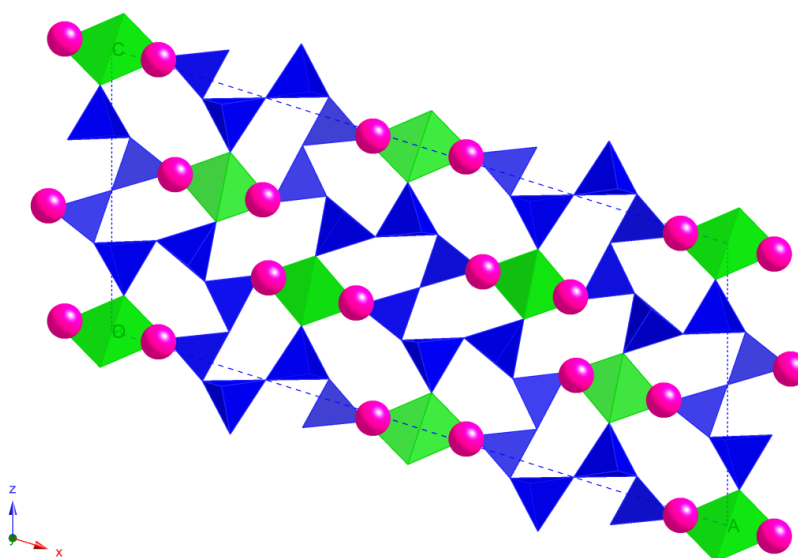
Figure 5.15 Projection along [010] of the structure of $Cs_2ZrSi_6O_{15}$. Green ZrO_6 octahedra and blue SiO_4 tetrahedra are represented. Caesium atoms are shown in pink spheres.

5.4.5 Bond Valence Sum

The interatomic Cs-O, Zr-O and Si-O distances in $Cs_2ZrSi_6O_{15}$ synthesised via the sol-gel method are listed in Table 5-11. Bond valence sums and coordination numbers of atoms are also reported. The refined bond lengths and angles as well as the lattice parameters are consistent with the reported ones in the literature.[151]

It was reported by Jolicart[151] that Cs atoms have three coordinations (X, XI and XII) in $Cs_2ZrSi_6O_{15}$. The oxygen atoms which define the Cs coordination polyhedral were taken at distances smaller than the shortest Cs-Si or Cs-Cs distances. Whilst Cs atoms exhibit three types of coordination, they are VIII, IX and X when determined using the rule proposed by Altermatt and Brown.[101, 177] The weak bonds which contribute less than 4% of the bond valence sum to cations are excluded. It is also noticed that the bond valence sums of site Cs1 and site Cs3 to framework oxygen atoms are 0.84 and 0.89, respectively, suggesting these have a less stable bonding environment than Cs2.

Zr atoms are octahedrally coordinated by six oxygen atoms. The mean Zr-O distances are very close to the sum of the radii of Zr^{4+} (0.72 Å) and O^{2-} (1.40 Å), and it is similar to those found in the analogous system with three-membered silicon-oxygen rings, such as elpidite $Na_2Zr(Si_6O_{15})\cdot 3H_2O$.[161] However, the bond valence sum calculations reveal that both sites Zr1 and Zr2 are seriously underbonded. This phenomenon was not consistent with the observations reported by Jolicart et al.[151]. The reasons that the Zr atoms possess a much lower valence sum than expected are still unclear. Further investigations, such as structure distortion and contraction/expansion in ZrO_6/SiO_4 polyhedra, are required.

Table 5-11 Inter-atomic Cs-O, Zr-O, and Si-O distances (Å) in $Cs_2ZrSi_6O_{15}$ as well as bond valence sum and coordination numbers of atoms.

Atom		Bond length (Å)		Mean distance (Å)	Valence sum	Coordination
Cs1	**O8**	3.415(19)	× 1	3.39 (for 10 existing Cs-O bonds)		
	O10	3.466(16)	× 2			
	O11	3.282(14)	× 2			
	O11	3.434(15)	× 2		0.84	10
	O12	3.035(20)	× 1			
	O15	3.538(17)	× 2	3.45 (for all Cs-O bonds)		
	O16	3.7732(26)	× 2*			

Atom		Bond length (Å)		Mean distance (Å)	Valence sum	Coordination
Cs2	**O1**	3.223(16)	× 2			
	O2	3.7578(16)	× 2*	3.20 (for 9 existing Cs-O bonds)		
	O5	3.165(15)	× 2			
	O7	3.212(13)	× 2		1.34	9
	O10	3.535(16)	× 2			
	O14	2.855(16)	× 1	3.38 (for all Cs-O bonds)		
	O14	3.950(23)	× 1*			
	O15	3.374(16)	× 2			

Atom		Bond length (Å)		Mean distance (Å)	Valence sum	Coordination
Cs3	**O1**	3.769(15)	× 2*			
	O1	3.213(14)	× 2	3.29 (for 8 existing Cs-O bonds)		
	O5	3.182(14)	× 2			
	O6	3.417(14)	× 2		0.89	8
	O8	3.353(21)	× 1	3.48 (for all Cs-O bonds)		
	O13	3.334(20)	× 1			
	O13	3.7582(14)	× 2*			

Atom		Bond length (Å)		Mean distance (Å)	Valence sum	Coordination
Zr1	**O11**	2.139(14)	× 4	2.15	3.26	6
	O16	2.176(15)	× 2			

Atom		Bond length (Å)		Mean distance (Å)	Valence sum	Coordination
Zr2	**O1**	2.137(13)	× 2			
	O2	2.177(13)	× 1	2.16	3.49	6
	O5	2.199(12)	× 2			
	O13	2.114(17)	× 1			

Atom		Bond length (Å)		Mean distance (Å)	Valence sum	Coordination
Si1	**O1**	1.6100(6)	× 1			
	O6	1.6240(6)	× 1	1.62	4.00	4
	O7	1.6240(6)	× 1			
	O8	1.6242(6)	× 1			

Atom		Bond length (Å)		Mean distance (Å)	Valence sum	Coordination
Si2	**O3**	1.6239(6)	× 1			
	O5	1.6240(6)	× 1	1.62	4.00	4
	O10	1.6240(6)	× 1			
	O12	1.6242(6)	× 1			

Atom		Bond length (Å)		Mean distance (Å)	Valence sum	Coordination
Si3	**O2**	1.6238(6)	× 1			
	O4	1.6238(6)	× 1	1.62	4.00	4
	O15	1.6240(4)	× 2			

Atom		Bond length (Å)		Mean distance (Å)	Valence sum	Coordination
Si4	**O9**	1.6239(6)	× 1			
	O10	1.6241(4)	× 2	1.62	4.00	4
	O16	1.6239(6)	× 1			

Atom		Bond length (Å)		Mean distance (Å)	Valence sum	Coordination
Si5	**O6**	1.6239(4)	× 2			
	O9	1.6239(6)	× 1	1.62	4.00	4
	O13	1.6241(6)	× 1			

Atom		Bond length (Å)		Mean distance (Å)	Valence sum	Coordination
Si6	**O7**	1.6241(6)	× 1			
	O11	1.6239(6)	× 1	1.62	4.00	4
	O14	1.6239(6)	× 1			
	O15	1.6240(6)	× 1			

Average bond valence sum				
Cs	1.02			
Zr	3.38			
Si	4.00			

*: Distances that are considered too long for bonds.

189

5.4.6 TEM Diffraction Pattern

A powder of $Cs_2ZrSi_6O_{15}$ synthesised using the sol-gel method was analysed by TEM. The diffraction patterns were collected and indexed based on the values reported by Jolicart et al.[151] with space group *C2/m* and cell parameters $a = 26.610$ Å, $b = 7.506$ Å, $c = 11.602$ Å, and $\beta = 107.43°$. Diffraction patterns of $Cs_2ZrSi_6O_{15}$ from zone axes [101], [110] and [112] are shown in Figure 5.16. The indexing of the patterns is consistent with the reported space group and structure. The structure determined from the TEM diffraction pattern is also consistent with the structure studies based on X-ray and neutron diffraction data.
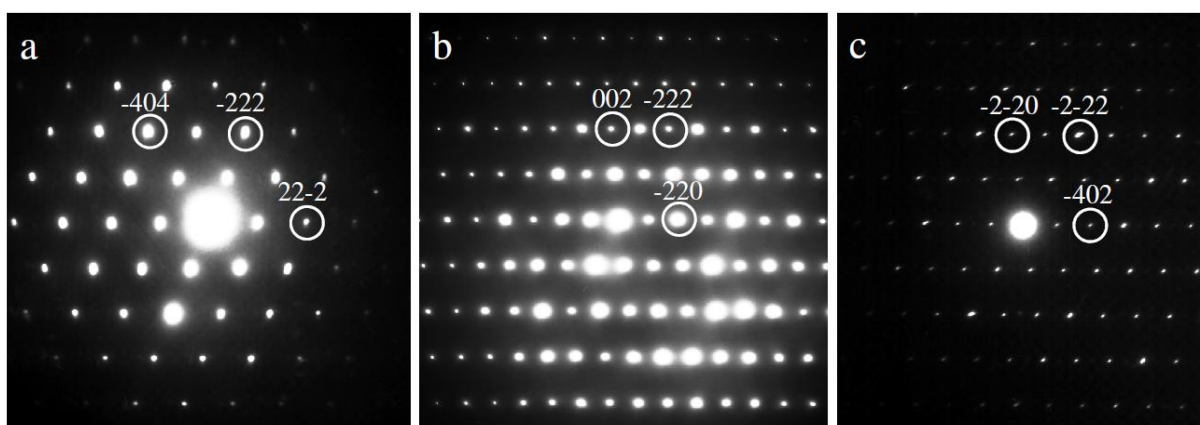

Figure 5.16 Electron diffraction patterns of $Cs_2ZrSi_6O_{15}$ from zone axis of (a) [101] (b) [110] (c) [112]

5.5 Cs₂ZrSi₃O₉

5.5.1 Synthesis and Optimisation

$Cs_2ZrSi_3O_9$ was synthesised using the sol-gel method as reported by Balmer et al.[90] Basically the whole procedure was followed as reported except the reaction was conducted in air rather than in a glove box. Even though the synthesis was undertaken in an open condition, pure and crystalline $Cs_2ZrSi_3O_9$ product was obtained successfully, as seen in Figure 5.17. Although synthesis of $Cs_2ZrSi_3O_9$ using solid state reactions was also proposed in the paper, it was not carried out due to the failed experience in synthesising $Cs_2ZrSi_6O_{15}$.
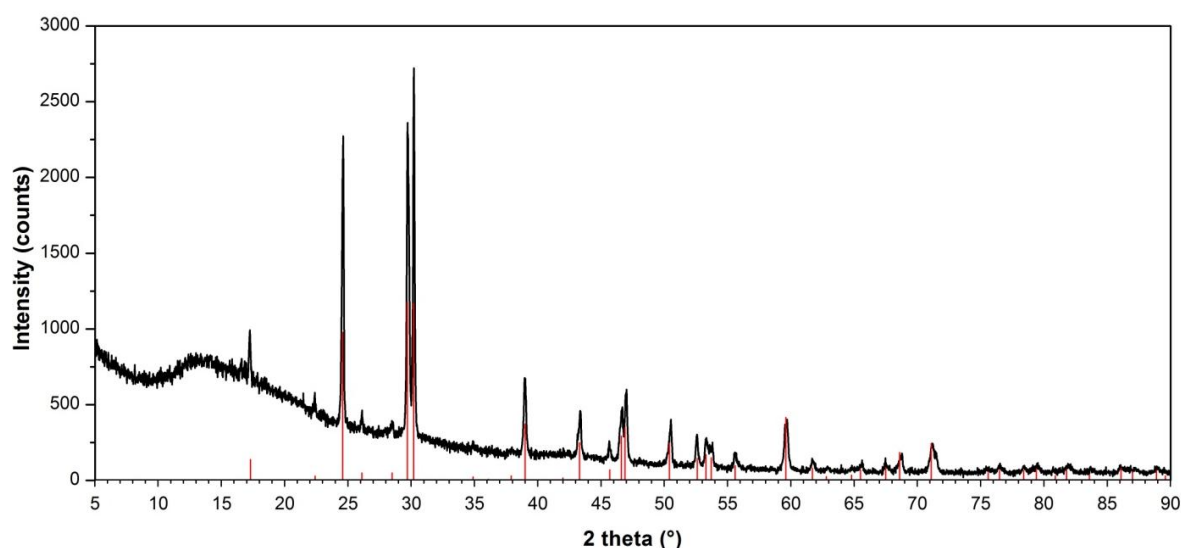

Figure 5.17 XRD pattern of $Cs_2ZrSi_3O_9$ synthesised using sol-gel method. The red lines are the indexed peaks from the ICDD PDF 01-074-2829 ($Cs_2ZrSi_3O_9$)

5.5.2 Morphology and Elemental Composition

The SEM micrograph of $Cs_2ZrSi_3O_9$ is shown in Figure 5.18. $Cs_2ZrSi_3O_9$ exhibits spherical shaped particles sized < 500 nm in diameter.
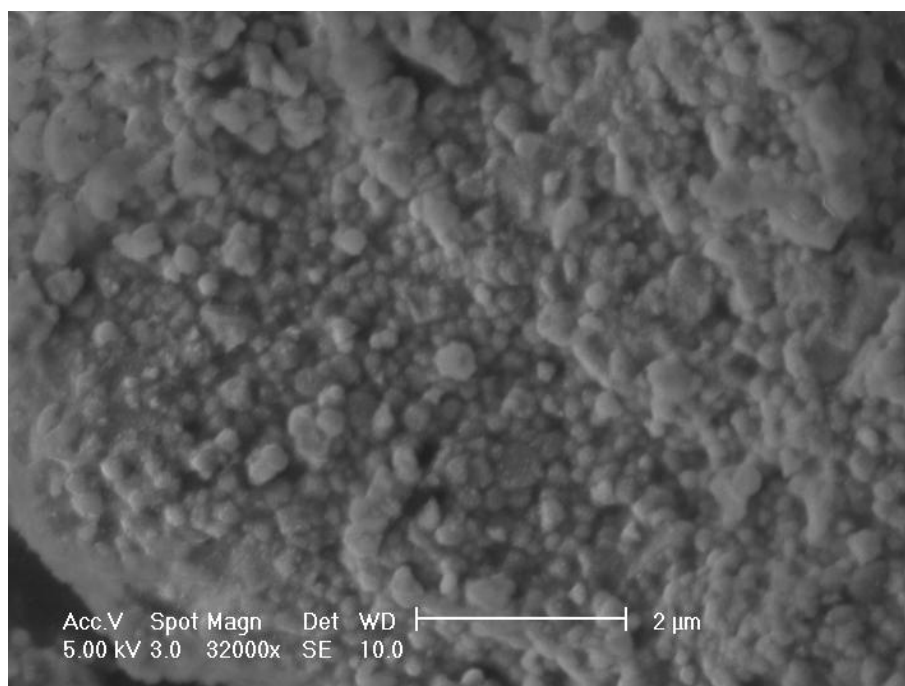
Figure 5.18 SEM micrograph of $Cs_2ZrSi_3O_9$

$Cs_2ZrSi_3O_9$ was fused into a glass bead and analysed by XRF for quantitative analysis. Table 5-12 reveals the elemental compositions normalised to Zr and Si, like $Cs_2ZrSi_6O_{15}$ the results are not consistent with the expected composition. So far, the correction or calibration in the Cs-Zr-Si system has not succeeded; therefore the results remain inaccurate due to appreciable error observed in XRF analyses.

Table 5-12 Elemental composition of $Cs_2ZrSi_3O_9$ using XRF (fused bead)

Element	Weight %	Atomic %	Molar ratio (normalised to Zr)	Molar ratio (normalised to Si)
Cs	32.35	7.84	1.12	0.92
Zr	19.76	6.98	1	0.82
Si	18.24	25.53	3.66	3
O	29.65	59.66	8.55	7.01

5.5.3 Thermal Analysis

TG/DTA/MS analysis of the dried $Cs_2ZrSi_3O_9$ precursor obtained by the sol-gel synthesis is shown in Figure 5.19. The majority of the weight loss (10.10%) occurred below 600 °C and it and the corresponding exothermic event were attributed to the decomposition of residual organics from the sol-gel precursor, which was proved by the evidence of CO_2 emission in the mass spectrum of 44 amu. An additional 0.52% of weight loss was observed in the range above 600 °C, so again little measurable Cs loss. It is indicated that sol-gel method is an ideal synthesis route for $Cs_2ZrSi_3O_9$. The exothermic event observed at 950 °C in the DTA curve without a corresponding weight loss was due to the crystallisation stage.
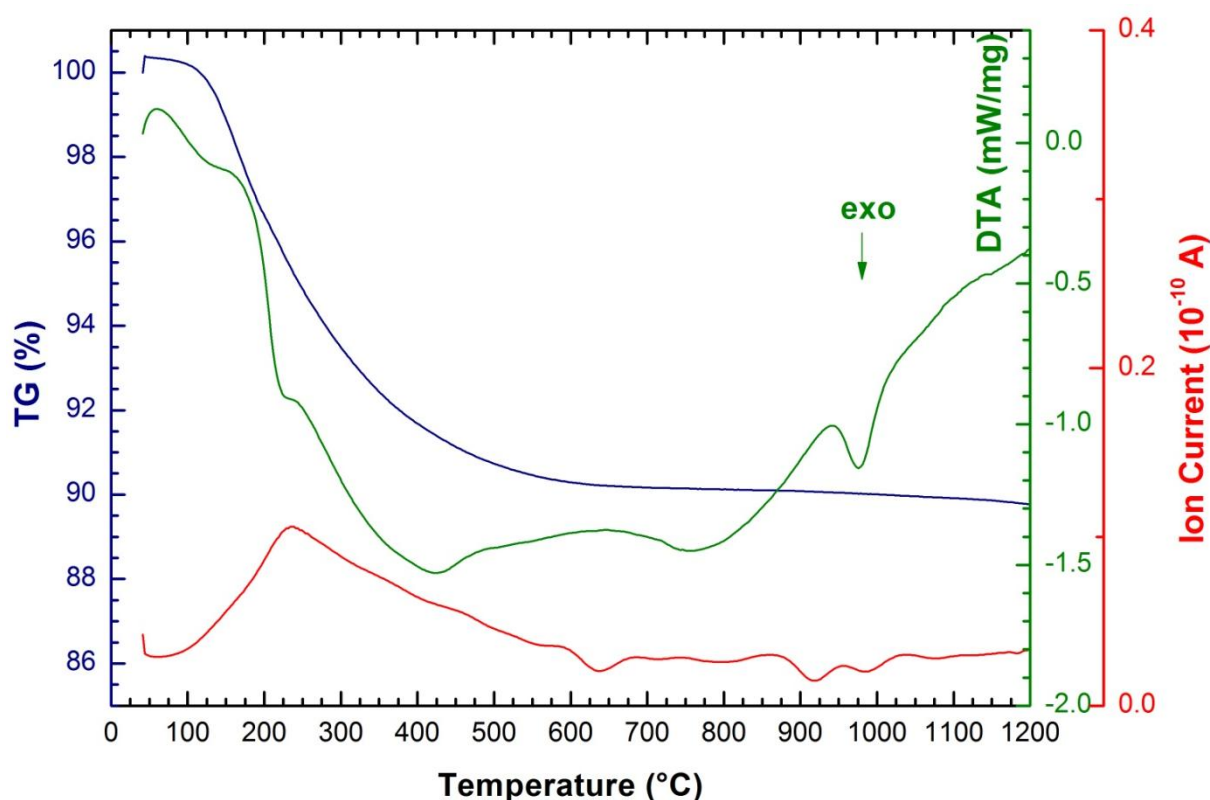
Figure 5.19 TG/DTA/MS plot for the reaction of the sol-gel precursor converting to $Cs_2ZrSi_3O_9$ (blue- TG curve, green- DTA curve and red- MS curve of 44 amu)

5.5.4 Structure Refinement

Synchrotron PXRD data of $Cs_2ZrSi_3O_9$ were collected and a Rietveld refinement was performed. The experimental and calculated XRD patterns of $Cs_2ZrSi_3O_9$, and also the difference are shown in Figure 5.20. The refinement confirmed that this compound has the same structure as the mineral wadeite, $K_2ZrSi_3O_9$, and crystallises in a hexagonal structure (space group $P6_3/m$) with lattice parameters were $a = 7.22560(6)$ Å and $c = 10.2729(1)$ Å. It is indicated that the refined unit cell parameters are consistent with the ones reported by Caruba et al.[166] and Balmer et al.[90] .
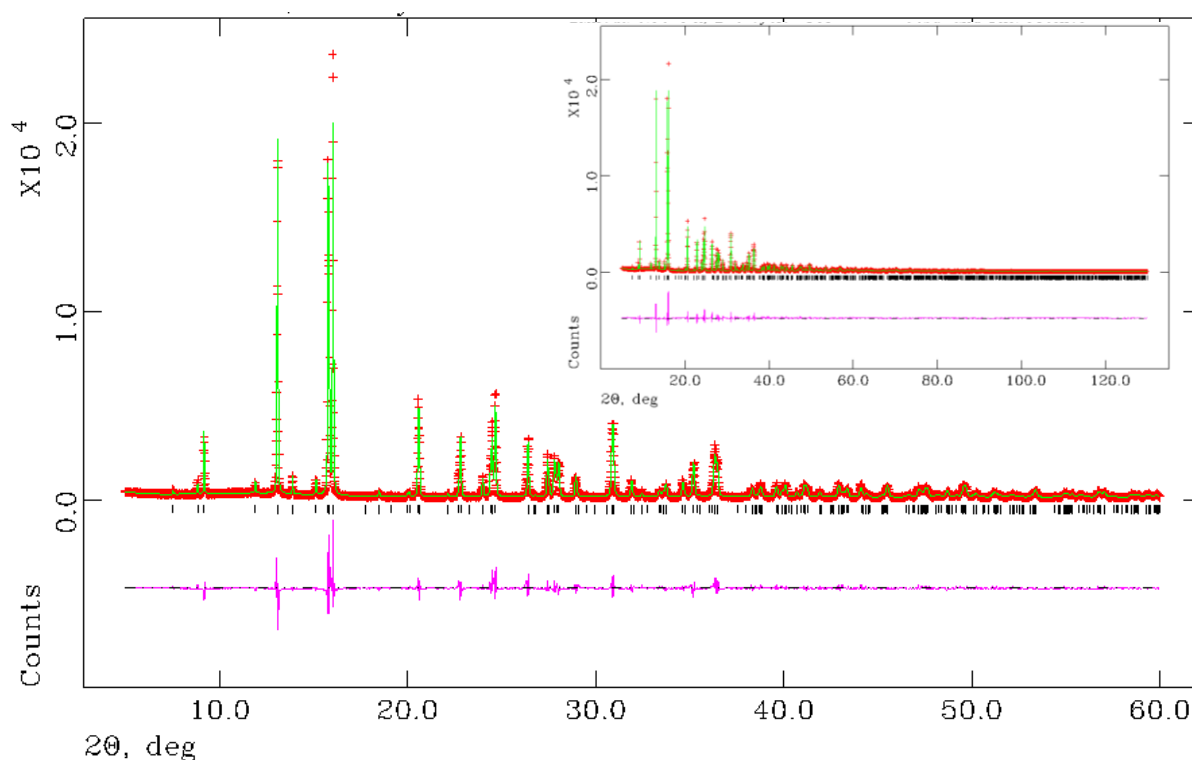
Figure 5.20 Simulated (green line) and experimental diffraction patterns (red dots) as well as difference pattern (purple) for $Cs_2ZrSi_3O_9$ (sol-gel). ($\chi^2 = 15.67$, $R_{wp} = 11.68\%$, $R_p = 9.15\%$)

Figure 5.21 illustrates the crystal structure of $Cs_2ZrSi_3O_9$. The structure consists of layers of $[Si_3O_9]$ rings (shown in blue colour) parallel to the (001) plane linked by $[ZrO_6]$ octahedral (shown in green colour) via corner-sharing into a hexagonal framework. Cs atoms reside in the cages between the neighbouring layers of three-membered silicate $[Si_3O_9]$ rings.[167] The structural formation is commonly observed in the classic wadeite structure[165] and many other wadeite-like alkali zirconosilicates are known.[167, 178] There are two types of oxygens: O1, which is bonded to two Si and two Cs atoms, and O2, which is bonded to one Si, one Zr and two Cs atoms.
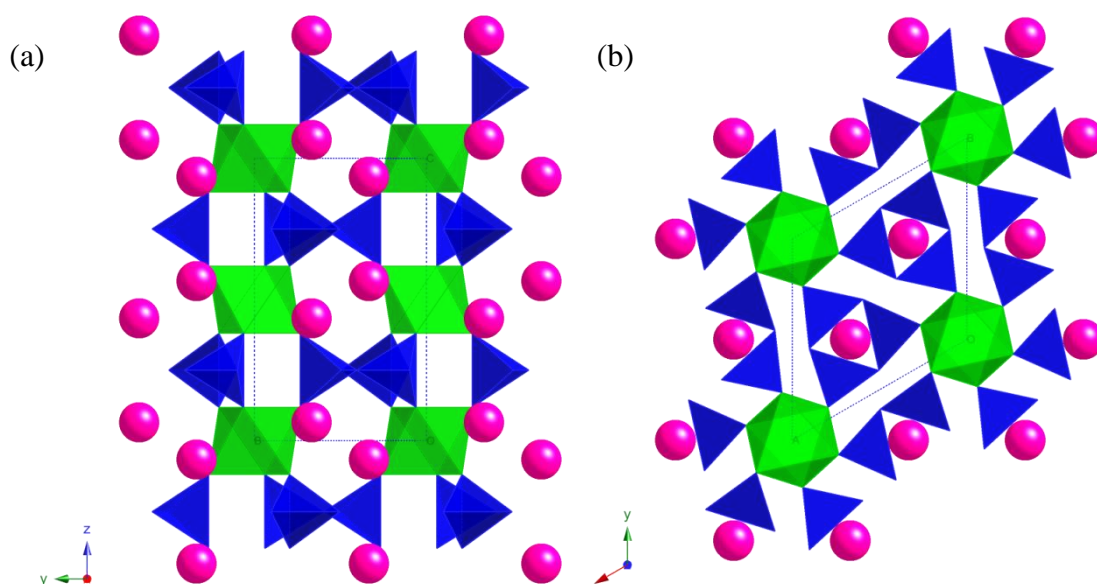
Figure 5.21 Crystal structure of $Cs_2ZrSi_3O_9$ as viewed down the (a) *a* (b) [010] zone axes

5.5.5 Bond Valence Sum

The refined bond parameters for Cs, Zr and Si are shown in Table 5-13. The Zr site is octahedrally coordinated by six oxygen atoms with Zr-O distances of 2.0684(20) Å, which are

close to the sum of radii of Zr^{4+} and O^{2-}. The Zr-O and Si-O bond lengths are similar to those found in other zirconosilicates.[160, 169, 173] Furthermore, the bond valence sum calculations show that calculated bond valences of Cs1 (1.18 v.u.) to framework O^{2-} as well as Zr (4.11 v.u.) are consistent with the expected valence states of the Cs and Zr cations, suggesting Cs and Zr have a stable bonding environment.

In the wadeite structure, alkali A cations usually occupy the nine-coordinated cage sites between the neighbouring layers of $[Si_3O_9]$ rings. However, according to the as-mentioned rule that a distance where the experimental bond valence is smaller than $0.04 \times$ the cation valence is excluded from bonding, Cs possesses the coordination number 12. Although three long bonds (marked with #) were counted based on the rule, the valences of these three bonds are very close to the threshold values resulting in an ambiguous coordination number determination. As discussed in section 5.3.8, there is no rigorous definition yet to be applied for this purpose, so the coordination number of either 9 or 12 demonstrates that Cs atoms have a good bonding environment in $Cs_2ZrSi_3O_9$.

Table 5-13 Interatomic Cs-O, Zr-O and Si-O distances (Å) in $Cs_2ZrSi_3O_9$

Atom		Bond length (Å)		Mean distance (Å)	Valence sum	Coordination
Cs1	**O1**	3.3519(28)	× 2			
	O1	3.5486(18)	× 1[#]			
	O1	3.5484(18)	× 1[#]			
	O1	3.3524(28)	× 1			
	O1	3.5483(18)	× 1[#]	3.33	1.18	9
	O2	3.2013(34)	× 2			
	O2	3.2010(34)	× 1			
	O2	3.2006(34)	× 1			
	O2	3.1841(33)	× 1			
	O2	3.1835(33)	× 1			
	O2	3.1840(33)	× 1			

Atom		Bond length (d)		Mean distance (Å)	Valence sum	Coordination
Zr 1	**O2**	2.0684(20)	× 6	2.08	4.11	6

Atom		Bond length (d)		Mean distance (Å)	Valence sum	Coordination
Si1	**O1**	1.6163(11)	× 1			
	O1	1.637(4)	× 1	1.61	4.01	4
	O2	1.6198(8)	× 2			

5.6 Ba Substitution

To determine whether small amounts of Ba could reside in the Cs-containing phases, various solid substitution series were synthesised and characterised using XRD, XRF and SEM/EDX.

5.6.1 Ba Substitution in the $Cs_2TiNb_6O_{18}$ Phase

A series of $Cs_{2-x}Ba_xTiNb_6O_{18}$ (x = 0, 0.05, 0.1, 0.15 and 0.2) were synthesised using the sol-gel method. From the XRD patterns of the series shown in Figure 5.22, $Cs_2TiNb_6O_{18}$ with

varied Ba substitution remains the same structure as pure $Cs_2TiNb_6O_{18}$. An impurity was firstly observed when nominal Ba content increased to x = 0.2 ($Cs_{1.8}Ba_{0.2}TiNb_6O_{18}$).

There are two possibilities. Firstly, Ba is not incorporated inside the lattice at all but exists as amorphous materials at lower Ba content. The impurity observed in the sample of nominal composition $Cs_{1.8}Ba_{0.2}TiNb_6O_{18}$ may be the crystalline Ba-containing compound. However, the impurity was not identified yet due to the relatively weak intensity of peaks for indexing. Therefore this hypothesis cannot be proved yet.

Secondly, the lattice can enable a certain amount of Ba to be incorporated inside without changing the symmetry of the structure. The excess Ba which cannot be accommodated in the lattice exists as an impurity. However, to quantify the Ba composition in the $Cs_{2-x}Ba_xTiNb_6O_{18}$ is rather difficult. Ti-K_α (4.510 keV) and Ba-L_α (4.467 keV) are major overlapping peaks in EDX and XRF, hence it is not easy to distinguish Ba from Ti using either technique. Furthermore, Rietveld refinements on XRD patterns are not definitive as Cs and Ba are neighbouring elements in the periodic table, thus they contribute identical scattering behaviour of X-rays. Additionally, $Cs_2TiNb_6O_{18}$ is such an extremely durable phase that chemically destructive digestion for ICP sample preparation was not possible.

Another route to incorporate both Cs^+ and Ba^{2+} ions inside the structure is possible if Nb^{5+} ions act as electron traps during β-decay (i.e. $Nb^{5+}+ β^-{\rightarrow}Nb^{4+}$). Therefore, attempts of synthesising $Cs_{2-x}Ba_xTi(Nb^{4+},Nb^{5+})_6O_{18}$ via solid state reaction using both $Nb^{(IV)}O_2$ and $Nb^{(V)}_2O_5$ for Nb sources at N_2 atmosphere were made. XRD patterns show that the product remains single phase during 4 times of sintering, however, the success of synthesising the desire product $Cs_{2-x}Ba_xTi(Nb^{4+},Nb^{5+})_6O_{18}$ has not been proved due to the difficulties in characterisation.
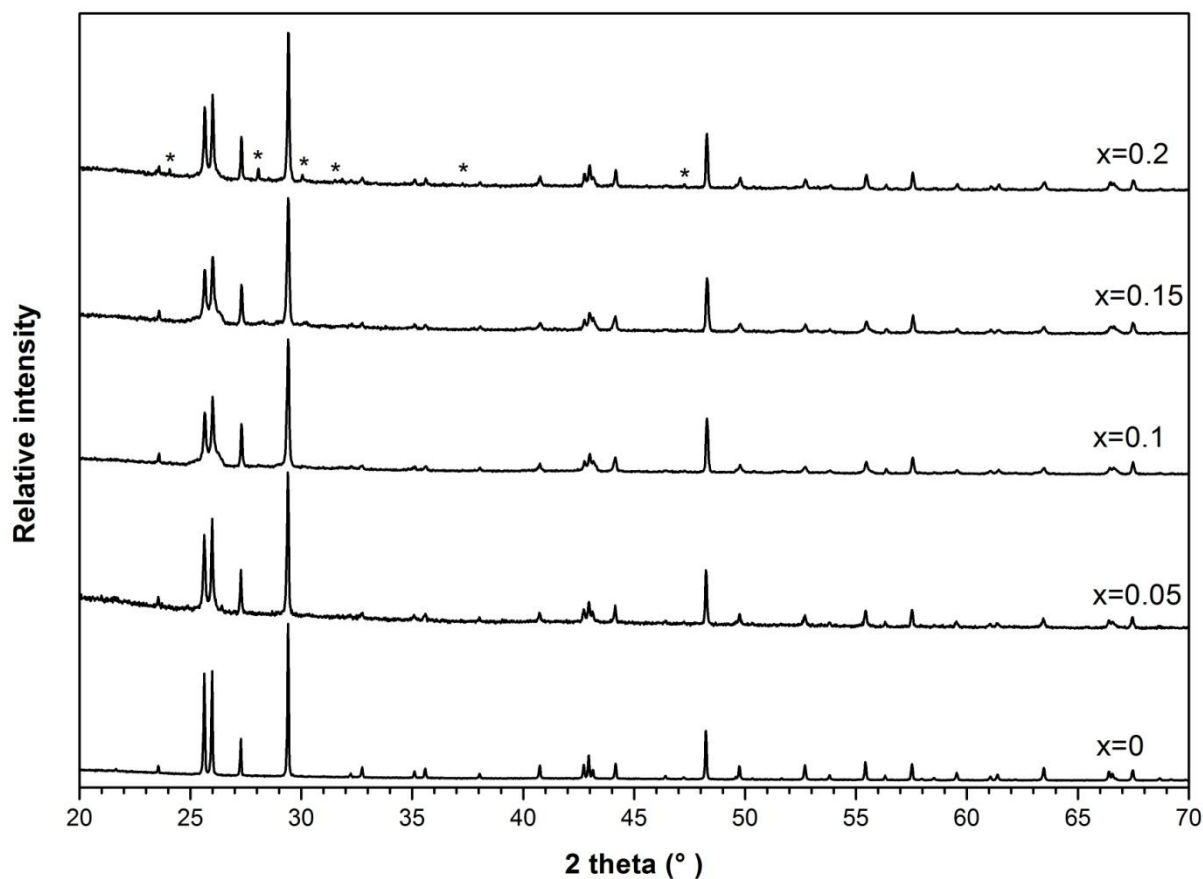
Figure 5.22 XRD patterns of $Cs_{2-x}Ba_xTiNb_6O_{18}$ (x = 0, 0.05, 0.1, 0.15 and 0.2)

Characterisation using neutron powder diffraction seems to be the potential method to examine Ba substitution in the $Cs_2TiNb_6O_{18}$ phase. Neighbouring elements Cs and Ba have different scattering lengths of 5.438 fm and 5.07 fm[96], respectively, therefore neutron scattering provides moderate resolution for detecting Cs/Ba content. However, a large amount of sample is required for neutron diffraction experiments and drawbacks in scaling up the synthesis using the sol-gel method and a relatively high cost produced when using niobium ethoxide as a starting material need to be considered.

5.6.2 Ba Substitution in the $Cs_2ZrSi_6O_{15}$ Phase

A series of nominal formula $Cs_{2-x}Ba_xZrSi_6O_{15}$ (x = 0, 0.05, 0.1, 0.15 and 0.2) were synthesised and characterised using XRD. From the XRD patterns of the series shown in Figure 5.23, Ba substituted samples retain the same structure with pure $Cs_2ZrSi_6O_{15}$. The presence of single phase indicates that Ba either was incorporated inside the lattice or existed as in amorphous or undetectable impurity. As mentioned earlier, quantitative analysis using XRD was not ideal due to the low resolution in distinguishing Cs from Ba. In addition, Cs and Ba are partially overlapping elements in SEM/EDX, thus EDX results will not be accurate for evaluating Ba substitution. Unlike SEM/EDX which performs quantitative analysis on the selected grain of interests, XRF provides bulk information. If the assumption of Ba existing as amorphous materials rather than being incorporated inside the lattice is correct, XRF results will be meaningless. Unfortunately, so far no characterisation can evidence that Ba has any solubility in the $Cs_2ZrSi_6O_{15}$ phase.
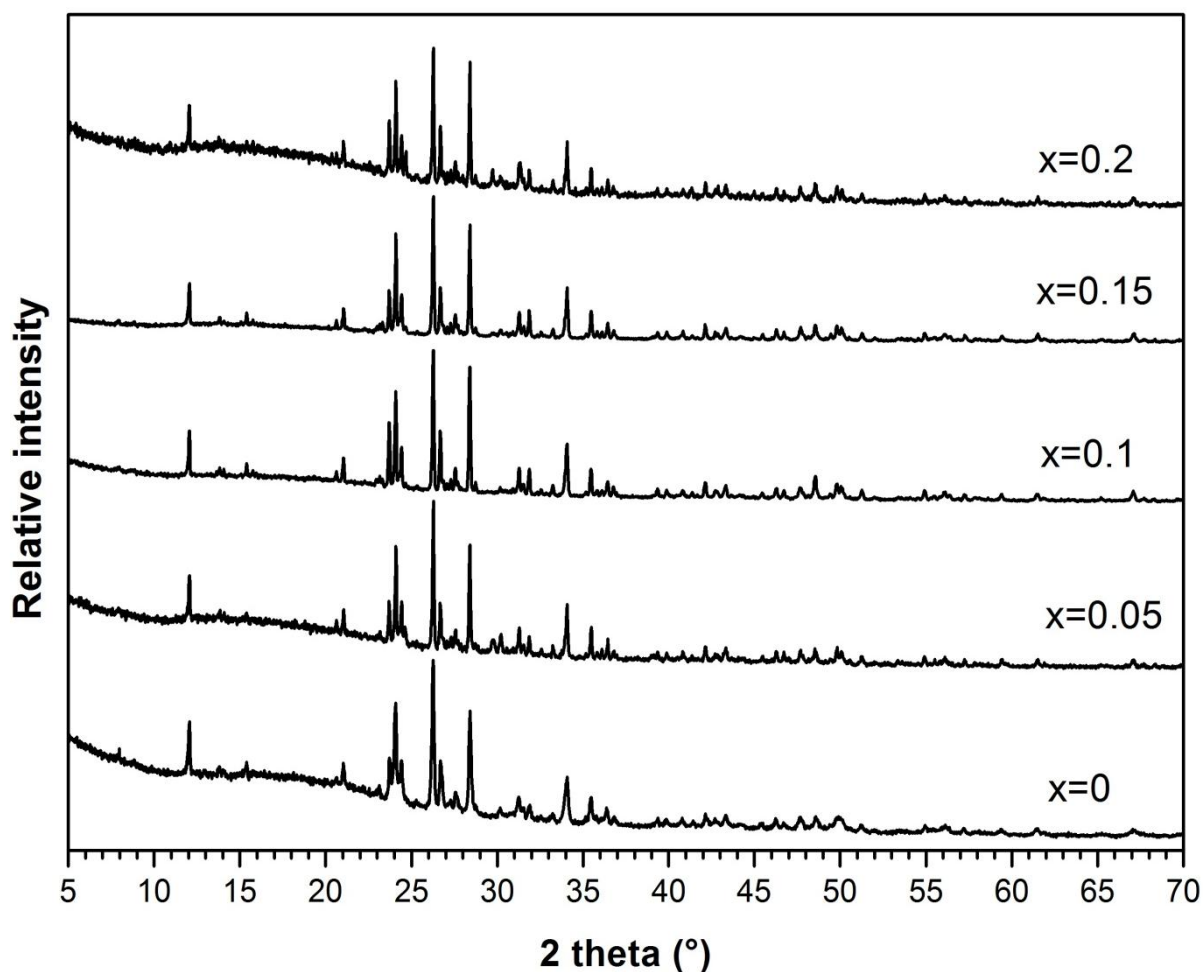
Figure 5.23 XRD patterns of $Cs_{(2-x)}Ba_{(x)}ZrSi_6O_{15}$ (x = 0, 0.05, 0.1, 0.15 and 0.2)

5.6.3 Ba Substitution in the Cs₂ZrSi₃O₉ Phase

A series of $Cs_{2-x}Ba_xZrSi_3O_9$ (x = 0, 0.05, 0.1, 0.15 and 0.2) were synthesised and characterised using XRD and the patterns of the series are shown in Figure 5.24. The samples all appear single phase and with the same structure as the pure $Cs_2ZrSi_3O_9$ material meaning that Ba either was incorporated inside the lattice or existed as an amorphous impurity.

Similar work has been reported by Su et al.[180] (Project report published by Pacific Northwest National Laboratory). The thermal conversion of Cs-loaded CST was investigated

and it was discovered that Cs is trapped in the $Cs_2ZrSi_3O_9$ crystalline phase. They also studied Ba substitution in $Cs_2ZrSi_3O_9$ using XRD, SEM/EDX and TEM/EDX. TEM studies showed that there is no measurable substitution of Ba for Cs on the $Cs_2ZrSi_3O_9$ lattice. Therefore, it appears Ba has no solubility in the $Cs_2ZrSi_3O_9$ phase.

However, the conclusion seems arbitrary due to the insufficient evidence. Although TEM has better energy resolution than SEM, it is still difficult to distinguish Ba and Cs using EDX and this might cause a misleading interpretation. As discussed earlier, no characterisation to date can evidence Ba substitution in $Cs_2ZrSi_3O_9$. Further investigations are still required.

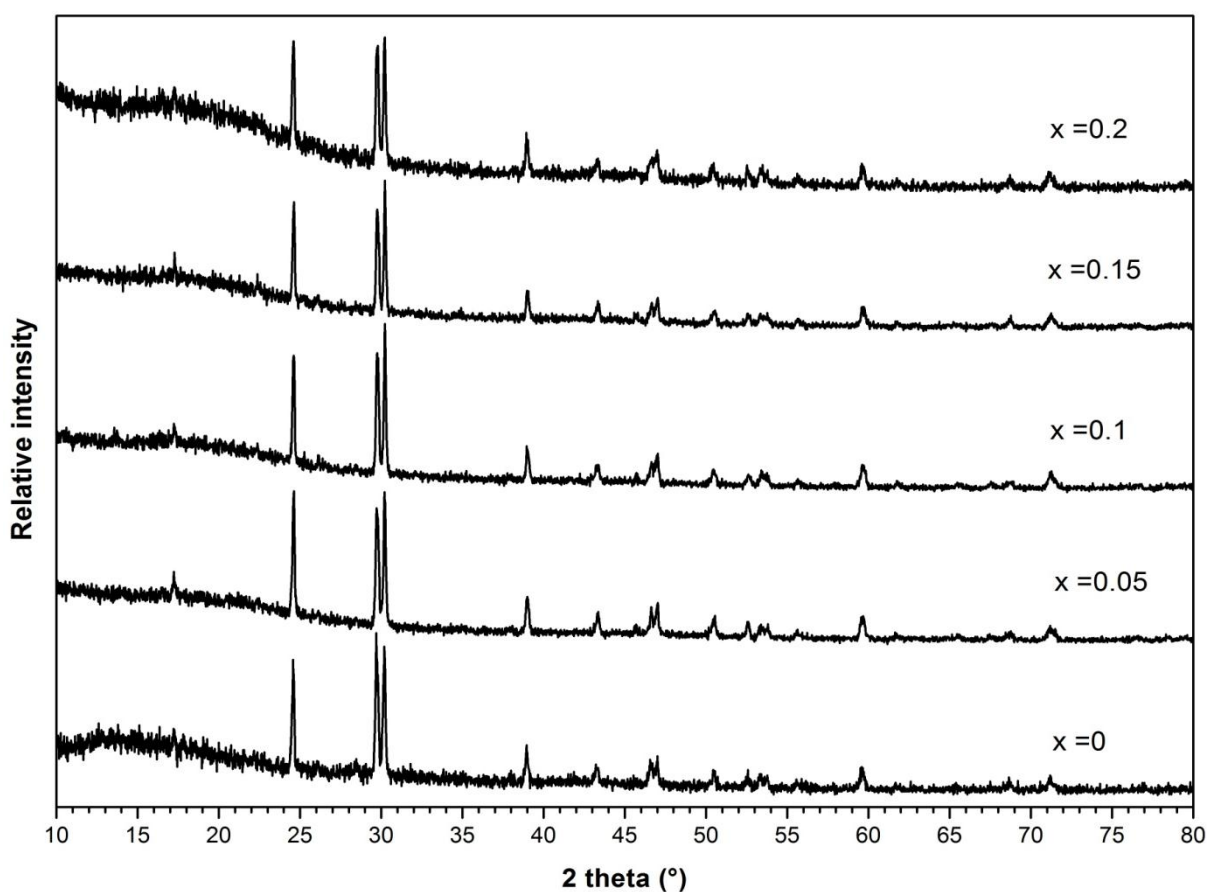Figure 5.24 XRD patterns of $Cs_{2-x}Ba_xZrSi_3O_9$ (x = 0, 0.05, 0.1, 0.15 and 0.2)

5.7 Conclusions

Three Cs-containing phases, $Cs_2TiNb_6O_{18}$, $Cs_2ZrSi_6O_{15}$ and $Cs_2ZrSi_3O_9$, were synthesised and analysed for thermal analysis, chemical composition and structural studies. A modified sol-gel method was used and highly pure and crystalline products can be obtained under the less harsh conditions (e.g. shorter firing duration). The sol-gel method has been proven to be a better route for synthesising these Cs-rich phases compared with solid state reactions and hydrothermal synthesis reported in the literature. Quantitative analysis was not successful due to the errors observed in XRF as well as the frustration in digesting the samples into solution for ICP-MS analysis.

Structurally speaking, these three Cs-containing phases have potential for Cs storage due to the excellent structure features. Cs cations were nicely packed inside the vacancies in the crystals. Consequently, no Cs should migrate along a diffusion pathway in the rigid crystal structures. Cs atoms in these phases are located in the cavities with high coordination numbers, indicating that Cs atoms have a stable bonding environment. This feature explains the outstanding aqueous durability, which will be discussed in the next chapter.

Ba solubility in these three Cs-containing phases was also attempted to investigate the long-term behaviour to accommodate Ba, the decay product of Cs. However, it is challenging to prove the presence of Ba inside the lattice due to the difficulties encountered in characterisation, such as the failure to distinguish the neighbouring elements Cs/Ba using XRD and Ti/Ba signal lines overlapping in SEM/EDX and XRF. Further work should include the syntheses and characterisations of Ba inserted Cs-rich phases using neutron diffraction and Rietveld refinements. In addition, chemical and thermal durabilities of the Ba inserted Cs-rich phases should be evaluated.

Chapter 6   Aqueous Durability of HIPed Materials

6.1 Introduction

As the wasteforms for Cs immobilisation designed in this project are envisioned to be deposited in a geological environment, it is important to assess their chemical durability for long-term behaviour. Many different approaches have been established for examining the leachability of wasteforms. In general, these tests are accelerated, with elevated temperatures and/or an increased ratio of sample surface area to volume of the leachant (SA/V). The use of different methods is required to elucidate the release behaviour from wasteform materials under different conditions. Owing to the different methods applied, the results are often difficult to compare and also inadequacies in experimental design or procedure may lead to misleading results. Therefore, the importance of choosing an applicable method to monitor the chemical durability of critical elements in candidate wasteforms cannot be overemphasised.

The selection of a particular test for a specific wasteform basically depends on the release mechanism of the material. For example, standard tests established for glass that preferentially release constituents controlled by reaction affinity under non-saturated conditions, cannot necessarily be applied to materials that release by a different mechanism, such as cement that releases constituents by diffusion.[181] Generally, leach rate test methods can be divided into two categories: dynamic tests in which samples are in contact with continuously renewed leachant and static tests in which samples are exposed to a fixed volume of water or other leachant.

Each of the wide variety of tests has advantages and disadvantages.[182, 183] It is of course impossible to directly assess the leaching behaviours of critical elements in a real situation by carrying out laboratory experiments with such short durations. However, the flow rate used in a static system is so slow that static experiments can often be regarded as the best approximation for laboratory scale experiments.[183] Dynamic experiments, in which a high flow rate is applied, such as Soxhlet, are not close to geological storage conditions and not employed to leach studies in this project. Some important and commonly used leach tests are summarised in Table 6-1.

Table 6-1 Summary of important standard leach tests

Test name		Sample	Conditions	Note	Ref.
Materials Characterisation Centre Tests (MCC)	MCC-1	Monolith (*SA*/*V* usually 10 m^{-1})	Static. DI-water or simulated ground water. Temperature 40, 70, 90°C.	Used to compare the durability of wasteforms. MCC-1 and MCC-2 have become ASTM C1220 standard test method.	[3, 51, 181, 184]
	MCC-2		Similar to MCC-1 at an elevated temperature in a closed system. Teflon-lined steel capsule.		
	MCC-3	Crushed glasses or glass-ceramics (*SA*/*V* ~ 1000 m^{-1})	DI-water or simulated ground water stirred with glass powder. Fixed SA/V. Temperature 40, 90, 110, 150, 190 °C with stirring.	MCC-3 has become ASTM C-1285, commonly known as PCT. Powered sample mixed with a fixed volume of extracting solution ("solubility limited").	[3, 51, 181]
	MCC-4	Best for crushed glasses but can be monolith	DI-water. Open to atmosphere. Temperature less than 100 °C.	Low flow rate. Used to determine leachability of glasses, glass-ceramics, and ceramics. ASTM C1662, known as SPFT.	[3, 51, 181]
	MCC-5	Monolith or powder	Dynamic. Continuously flowing stream of redistilled water. Open to atmosphere.	Soxhlet (most aggressive) Low flow rate. Used to accelerate the rate of dissolution.	[3]

Product Consistency Tests (PCT)	PCT-A	Powder (*75-150 μm*)	ASTM-Type I water. Static in stainless steel vessels.	Same as MCC-3. Used to determine dissolution mechanisms or used as a scoping test to compare wasteforms or interpret a mechanism.	[3, 51, 181, 185]
	PCT-B		Various solutions, duration, and temperatures.		
Single-Pass Flow-Through Tests	SPFT	Crushed glass/ monolith	DI-water. Various flow rate, various temperatures, and solution pH. Open to atmosphere.	Same as MCC-4. Used to give kinetic parameters of leaching.	[3, 51, 181]
International Atomic Energy Agency Tests	IAEA	Monolith	Leachant is replaced every day for the first 7 d, and every week thereafter. 25 °C.	Similar to MCC-1 at R.T. Used for low and intermediate level wasteforms.	[3, 51, 181]
Toxicity Characteristics Leaching Procedure	TCLP	Powder 100g (< 9.5 mm)	Dilute acetic acid/NaOH. Liquid-to-solid ratio of 20. An end-over-end agitation for 18 h.	Used to determine the mobility of both organic and inorganic analytes present in liquid, solid, and multiphasic wastes.	[186]

Two static leach tests, MCC-1 for monoliths and PCT-B for powder wasteforms, were conducted in this project. The main reason to adopt these two methods is simply because they are the most widely used test methods; therefore a better comparison with other materials with the same test method is available. Furthermore, the MCC-1 test is easy to perform, provides a large solution volume for analysis, and is economical. It can also be conducted under a range of conditions. For instance, MCC-1 can be carried out at temperatures of 40 °C, 70 °C and 90 °C as well as various duration times, normally 28 days but shorter periods of time (1, 3, 5, 7, and 14 days) or longer duration up to several years can be performed.

The PCT-B test is highly reproducible and yields rapid results, usually in seven days, for predicting long-term dissolution rates of wasteform materials. This test has a high surface area to leachate volume and the entire purpose is to determine the maximum solubility limit of the wasteform in solution. It also allows testing at various durations, temperatures, mass of sample, leachant volume and leachant composition, including simulated or actual groundwaters.

In this chapter, chemical durabilities of HIPed samples were assessed using both MCC-1 and PCT-B test methods. Leach rate values of some of the known ceramic materials already studied for Cs immobilisation and some glass wasteforms are also provided and discussed for comparison.

6.2 Experimental

New PTFE test vessels and supports were heated in a 200 ± 10 °C oven for a week prior to cleaning. The support was designed to maximise the surface area of monolith in contact

with leachant. The PTFE vessels and supports were then cleaned according to the procedure described in ATSM "Standard Test Method for Static Leaching of Monolithic Waste Forms for disposal of Radioactive Waste" [184] and ATSM "Standard Test Methods for Determining Chemical Durability of Nuclear, Hazardous, and Mixed Waste Glasses and Multiphase Glass Ceramics: The Product Consistency Test (PCT)" [185]. All the vessels were tested with a pH meter equipped with a fluoride ion selective electrode (ISE) to assure the pH is between 5.0 - 7.0 and the F⁻ level is below 0.5 μg/mL. Between uses, all the vessels and supports were cleaned and then tested using this standard procedure.

6.2.1 Static Leaching Test of Monolithic Waste Forms (MCC-1)

For MCC-1 tests, monolithic specimens of HIPed 6 wt.% Cs-IONSIV®, 12 wt.% Cs-IONSIV®, $Cs_2TiNb_6O_{18,}$ $Cs_2ZrSi_6O_{15}$ and $Cs_2ZrSi_3O_9$, were prepared. Samples were sectioned and soaked in diluted nitric acid for can removal. Some of the samples were irregular due to the deformation that occurred in the HIP procedure such that their geometric surface area was calculated using the image processing software "Image J" as shown in Figure 6.1.
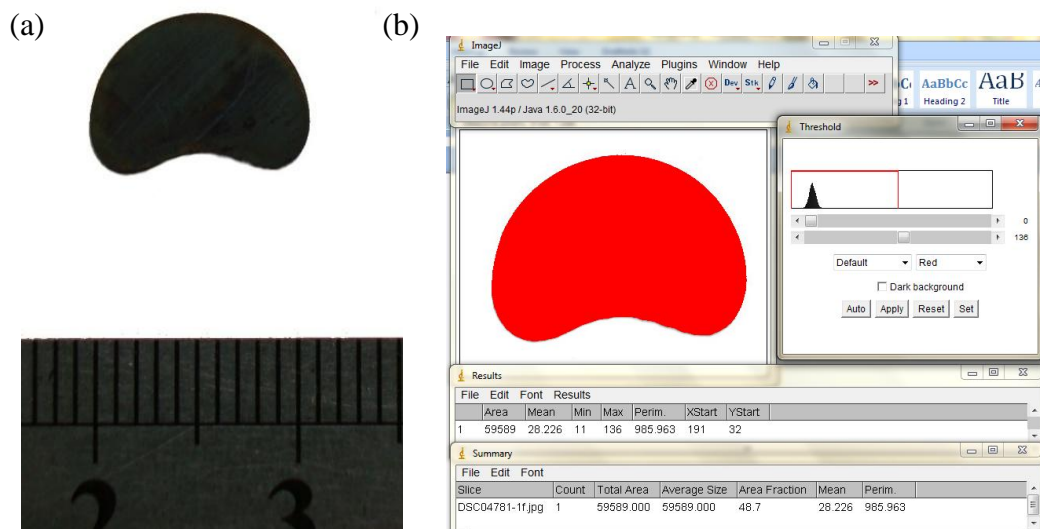
Figure 6.1 An example of the surface area calculation procedure using Image J (a) An image of a specimen with scale bar (b) Defining the area and scale in Image J for geometric surface area

Once the surface area was known, the volume of leachant for each sample was determined to keep a constant surface-area-to-leachant-volume ratio within 0.5 of 10 m^{-1}. Specimens with known surface area were immersed in DI-water without agitation at 90 °C for 3, 7, 14 and 28 days. Two blanks (no specimen) of each leachant for 28 days under identical test conditions were also prepared and tested. For 3, 7 and 14 days, the original leachant was used as the blank. 5-10 mL of each solution was submitted for ICP-MS (Agilent 7500ce) at University of Birmingham.

6.2.2 Product Consistency Test Method B (PCT-B)

For PCT-B tests, specimens were ground and sieved to a 75-150 μm range by hand. Specimens were then washed and dried based on the standard procedure.[185] 1 g of sample with 10 mL of leachant was placed and sealed in the vessel. Tests for each sample were carried out in triplicate to provide estimates of experimental variability, and two vessel blanks from the same batch of cleaned vessels were used. Samples and blanks were placed in the oven at 90 °C for 7 days. The weighing, leachate pH measurements, and filtration through 0.45 μm syringe filter were completed once the leachate had cooled down to ambient temperature. 10 mL of solution was submitted to ICP-MS.

6.2.3 Data Processing

6.2.3.1 MCC-1

The **Normalised elemental mass loss (NL)$_i$**, in g·m^{-2}, was calculated using the following equation:

$$(NL)_i = \frac{(C_{ij} - B_i) \times V_j}{f_i \times SA}$$

Where,

C_{ij} = concentration of element *i* observed in the leachate from specimen *j*, averaged over replicate aliquots.

B_i = average concentration of element *i* observed in the leachate from blank, averaged over replicate aliquots and replicate blanks,

V_j= initial volume of leachate in test vessel containing specimen j,

f_i = mass fraction of element i in the unleached specimen, and

SA= specimen surface area, m^2.

(The mass fraction used for the calculation was from the XRF result.)

The **Normalised elemental leach rate (NR)$_i$,** in g·m^{-2}·day^{-1}, was calculated using the following equation**:**

$$(NR)_i = \frac{(NL)_i}{t}$$

Where,

$(NL)_i$ = Normalised elemental mass loss in g·m^{-2}, and

t = duration of leach test performed, in days.

6.2.3.2 PCT-B

The **Normalised elemental leach rate (NR)$_i$,** in g·m^{-2}day^{-1}, was calculated using the following equation:

$$(NR)_i = \frac{C_i(n) - C_i(Blank)}{(f_i) \times (\frac{SA}{V}) \times t}$$

Where,

n = total number of replicate wasteform sample tests performed,

$C_i(n)$ = concentration observed in the nth wasteform sample, in g·L^{-1},

$C_i(Blank)$ = average blank concentration, in g·L^{-1}.

f_i = mass fraction of element i in the unleached specimen,

SA = specimen surface area, in m^2,

V = volume of leachate in test vessel containing specimen, in L, and

t = duration of leach test performed, in days.

The mass fraction used for the calculation was from the XRF results. The surface area used was estimated using the following equation. (see Appendix 4).

$$Surface\ Area = \frac{Mass\ of\ sample \times 862.2}{Theoretical\ density}$$

6.3 Results

6.3.1 MCC-1 Results

(1) HIPed 6 wt.% Cs-IONSIV®

The normalised mass loss of HIPed 6 wt.% Cs-IONSIV®, as shown in Table 6-2 and Figure 6.2, was found to follow the order: Na > Cs ~ Si >> Ti ~ Zr ~ Nb. Generally an increase in normalised mass loss of Na, Si and Cs against time was observed. Ti was not detected in 3 days period.

As shown in Table 6-2 and Figure 6.3, the normalised leach rate of Na significantly decreased as MCC-1 progressed. Those of Cs and Si decreased in 14 days and then increased in 28 days period. The normalised leach rates of Ti, Zr and Nb were extremely low and no particular trend for these three elements was observed.

Table 6-2 Normalised mass losses (g·m^{-2}) and normalised leach rates (g·m^{-2}day^{-1}) of HIPed 6 wt.% Cs-IONSIV$^{®}$

Normalised Mass Loss (gm^{-2})

Day	Na	Si	Ti	Zr	Nb	Cs
3	1.154E+00	4.191E-01	ND	1.058E-04	3.087E-05	3.757E-01
7	1.078E+00	6.540E-01	1.050E-05	6.781E-05	1.183E-04	6.450E-01
14	1.579E+00	5.302E-01	1.408E-04	9.818E-05	5.043E-04	3.576E-01
28	2.806E+00	3.809E+00	7.940E-04	8.035E-04	3.061E-03	4.319E+00

Normalised Leach Rate (gm^{-2}day^{-1})

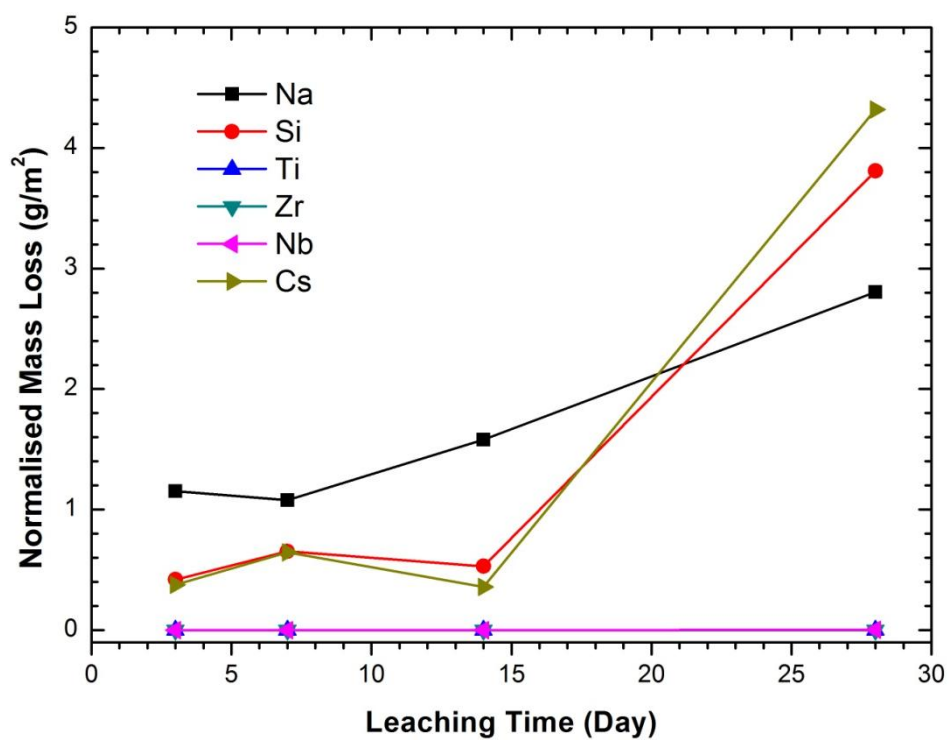| Day	Na	Si	Ti	Zr	Nb	Cs
3	3.848E-01	1.397E-01	ND	3.525E-05	1.029E-05	1.252E-01
7	1.540E-01	9.343E-02	1.499E-06	9.687E-06	1.689E-05	9.215E-02
14	1.128E-01	3.787E-02	1.006E-05	7.013E-06	3.602E-05	2.554E-02
28	1.002E-01	1.360E-01	2.836E-05	2.870E-05	1.093E-04	1.542E-01

ND: not detectable.

Figure 6.2 Plot of normalised mass losses (g·m^{-2}) of HIPed 6 wt.% Cs-IONSIV®
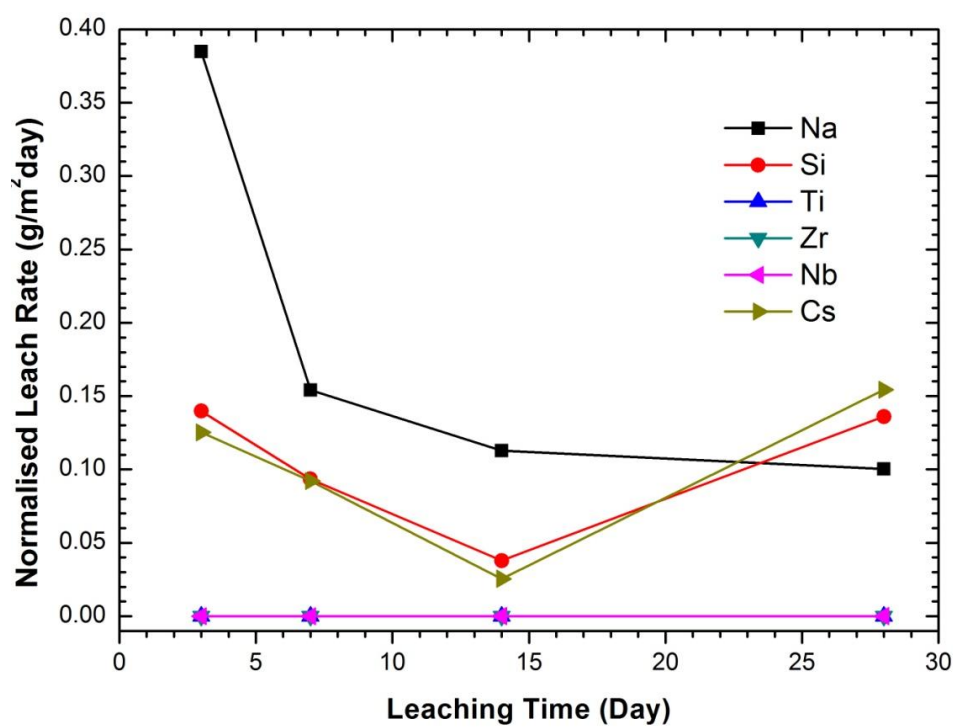
Figure 6.3 Plot of normalised leach rates (g·m^{-2}·day^{-1}) of HIPed 6 wt.% Cs-IONSIV®

(2) HIPed 12 wt.% Cs-IONSIV®

The normalised mass losses of HIPed 12 wt.% Cs-IONSIV® as shown in Table 6-3 and Figure 6.4 reveal that the mass loss of Na was at least one order of magnitude higher than any other element. Cs and Si have very similar behaviour in that the concentrations in their leachates increased with time. Mass losses of Ti, Zr and Nb were about 4-5 orders of magnitudes smaller than that of Si or Cs. Generally, normalised mass losses for all of the elements increased as the test progressed. Concentrations of Zr and Nb in the 3 day period were below ICP-MS detection limits.

As shown in Figure 6.5, the normalised leach rate of Na significantly decreased by one order of magnitude as MCC-1 progressed. Ti, Zr and Nb exhibit extremely low normalised leach rate and no particular trend for these three elements was observed.

Table 6-3 Normalised mass losses (g·m^{-2}) and normalised leach rates (g·m^{-2}·day^{-1}) of HIPed 12 wt.% Cs-IONSIV®

Normalised Mass Loss (g·m^{-2})

Day	Na	Si	Ti	Zr	Nb	Cs
3	2.659E+00	1.842E-01	0.000E+00	ND	ND	2.425E-01
7	3.153E+00	1.828E-01	1.940E-05	1.619E-04	1.773E-05	4.891E-01
14	3.310E+00	5.631E-01	9.421E-05	1.533E-04	1.327E-05	8.875E-01
28	2.182E+00	1.203E+00	2.045E-04	7.341E-05	3.707E-04	1.448E+00

Normalised Leach Rate (g·m^{-2}·day^{-1})

Day	Na	Si	Ti	Zr	Nb	Cs
3	8.863E-01	6.141E-02	0.000E+00	ND	ND	8.082E-02
7	4.504E-01	2.611E-02	2.772E-06	2.312E-05	2.533E-06	6.986E-02
14	2.365E-01	4.022E-02	6.729E-06	1.095E-05	9.476E-07	6.340E-02
28	7.793E-02	4.298E-02	7.304E-06	2.622E-06	1.324E-05	5.170E-02

ND: not detectable.

Figure 6.4 Plot of normalised mass losses (g·m^{-2}) of HIPed 12 wt.% Cs-IONSIV$^{®}$

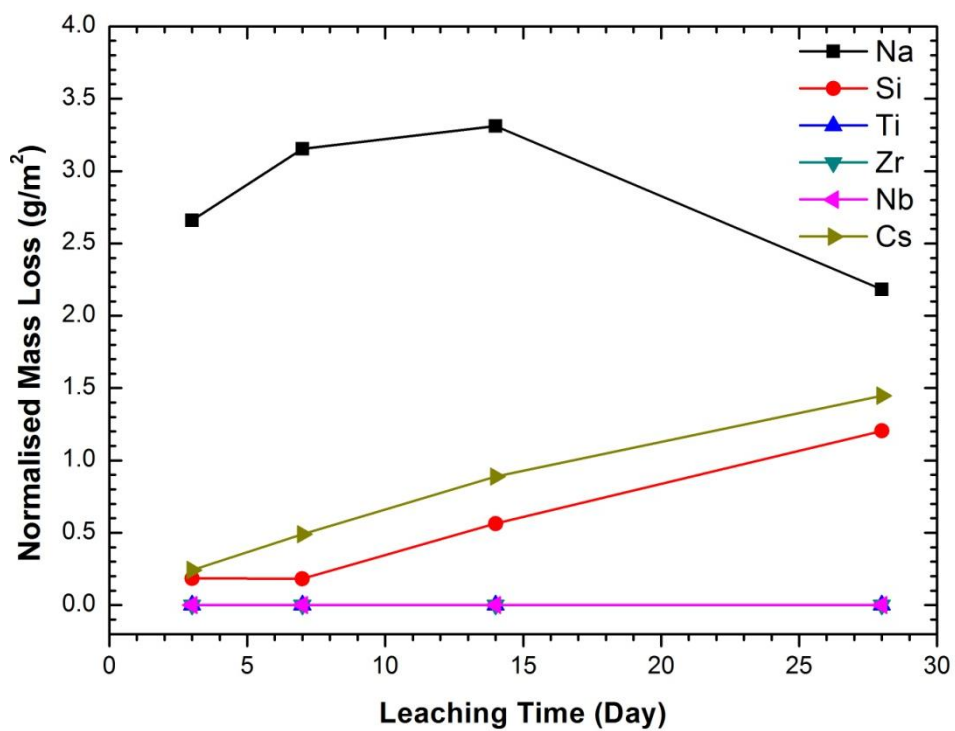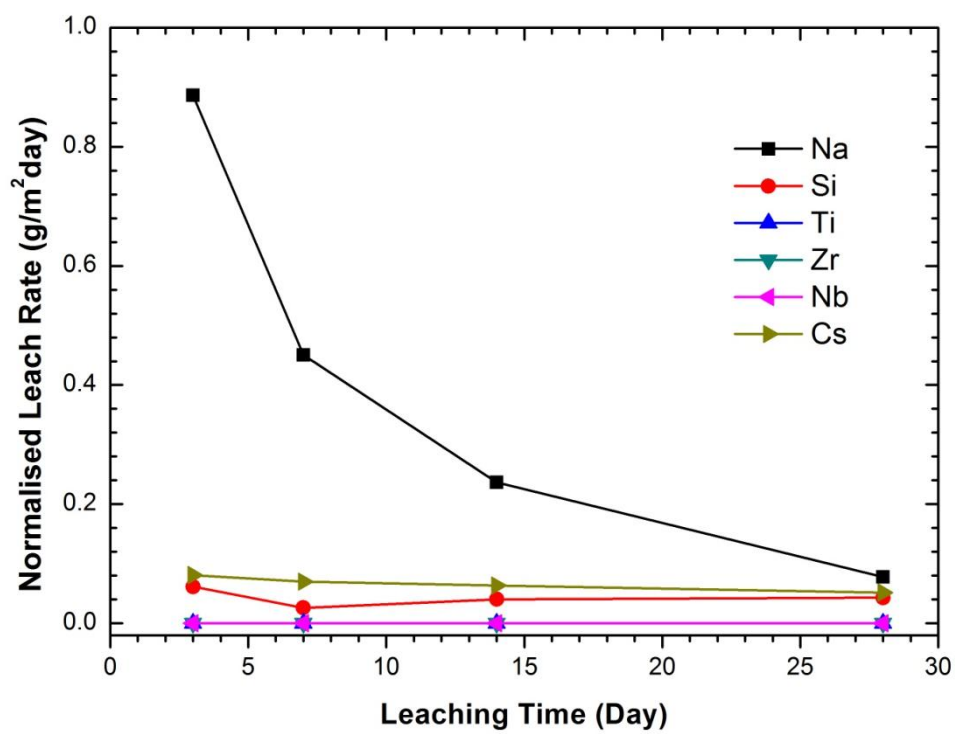Figure 6.5 Plot of normalised leach rates (g·m^{-2}·day^{-1}) of HIPed 12 wt.% Cs-IONSIV$^{®}$

(3) HIPed Cs$_2$TiNb$_6$O$_{18}$

The normalised mass losses of HIPed Cs$_2$TiNb$_6$O$_{18}$ shown in Table 6-4 and Figure 6.6 reveal that extremely low concentrations of Ti and Nb were detected in the leachant, and Cs exhibits a relatively higher mass loss than those of Ti and Nb. From the normalised leach rates, shown in Table 6-4 and Figure 6.7, Ti and Nb present almost no leachability. The leach rates for all of the three elements generally decreased as MCC-1 progressed.

Table 6-4 Normalised mass losses and leach rates (g·m^{-2}·day^{-1}) from MCC-1 results of HIPed Cs$_2$TiNb$_6$O$_{18}$

Normalised Mass Loss (g·m^{-2})

Day	Ti	Nb	Cs
3	4.266E-04	2.565E-05	7.030E-02
7	4.301E-05	5.581E-06	9.229E-02
14	0.000E+00	3.391E-06	6.137E-02
28	6.332E-04	3.043E-04	1.050E-01

Normalised Leach Rate (g·m^{-2}·day^{-1})

Day	Ti	Nb	Cs
3	1.422E-04	8.551E-06	2.343E-02
7	6.144E-06	7.973E-07	1.318E-02
14	0.000E+00	2.422E-07	4.383E-03
28	2.262E-05	1.087E-05	3.751E-03
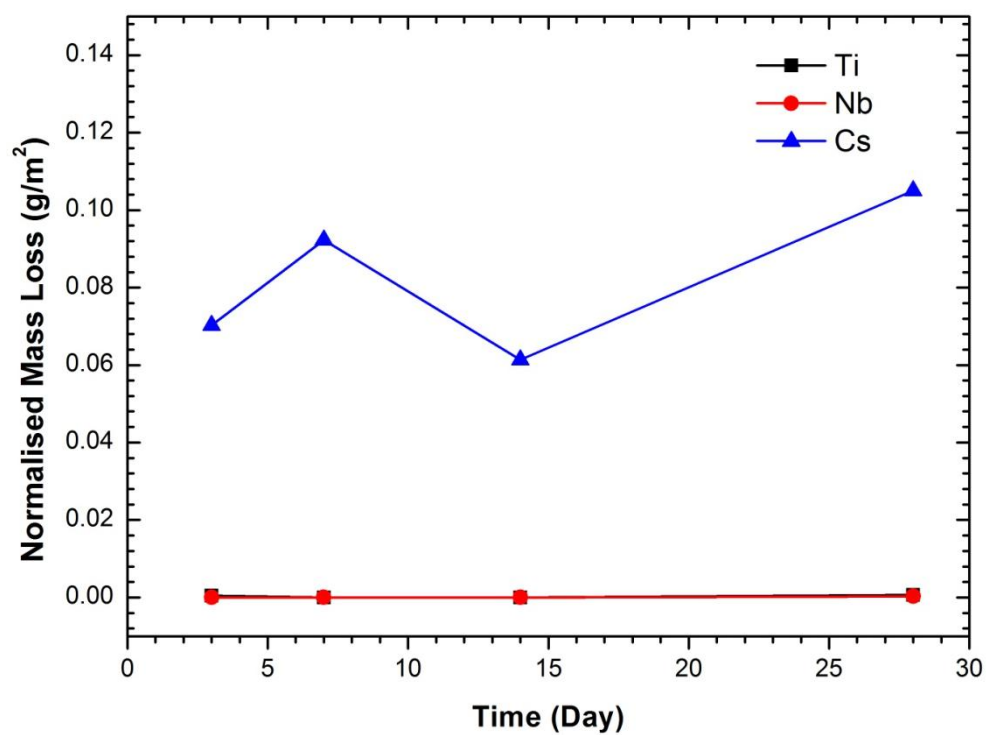
Figure 6.6 Normalised mass losses (g·m^{-2}) of HIPed Cs$_2$TiNb$_6$O$_{18}$
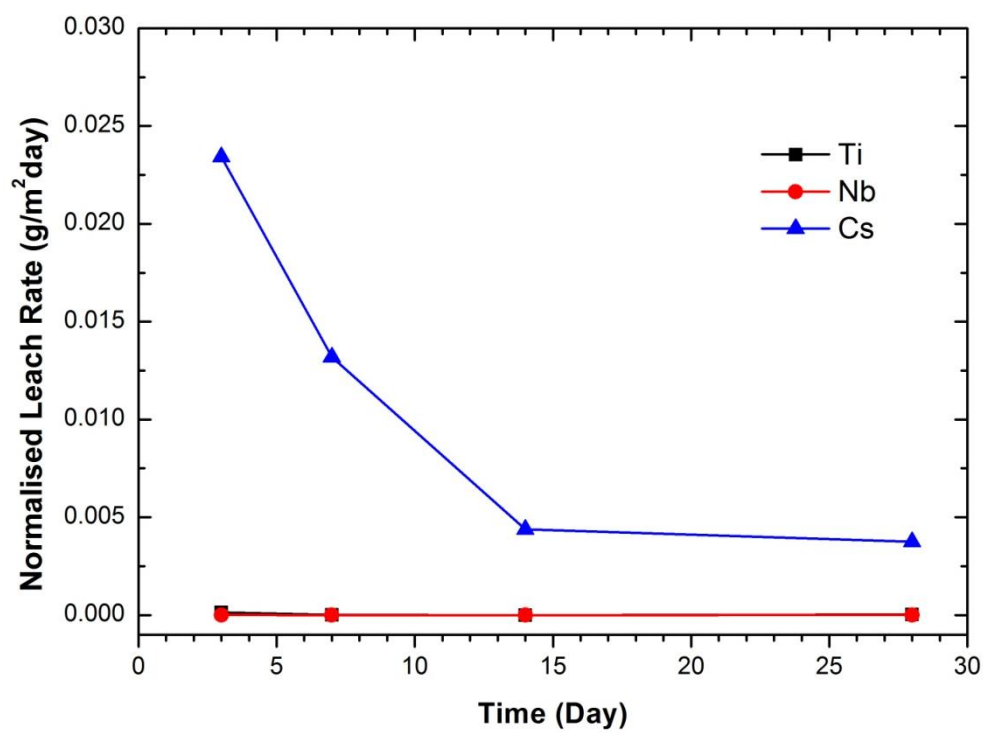
Figure 6.7 Normalised leach rates (g·m^{-2}·day^{-1}) of HIPed Cs$_2$TiNb$_6$O$_{18}$

(4) HIPed Cs₂ZrSi₆O₁₅

The normalised mass losses of HIPed $Cs_2ZrSi_6O_{15}$ shown in Table 6-5 and Figure 6.8 were found to follow the order: Si > Cs >> Zr. For their normalised leach rates, as shown in Table 6-5 and Figure 6.9, the leach rates for all of the three elements exhibited a non-linear decrease as MCC-1 progressed.

Table 6-5 Normalised mass losses and leach rates $(g \cdot m^{-2} \cdot day^{-1})$ from MCC-1results of HIPed $Cs_2ZrSi_6O_{15}$

Normalised Mass Loss $(g \cdot m^{-2})$

Day	Si	Zr	Cs
3	6.037E+00	0.000E+00	1.448E+00
7	6.343E+00	2.151E-04	1.678E+00
14	9.037E+00	1.373E-03	2.112E+00
28	1.374E+01	6.981E-03	3.514E+00

Normalised Leach Rate $(g \cdot m^{-2} \cdot day^{-1})$

Day	Si	Zr	Cs
3	2.012E+00	0.000E+00	4.827E-01
7	9.062E-01	3.073E-05	2.398E-01
14	6.455E-01	9.807E-05	1.508E-01
28	4.907E-01	2.493E-04	1.255E-01
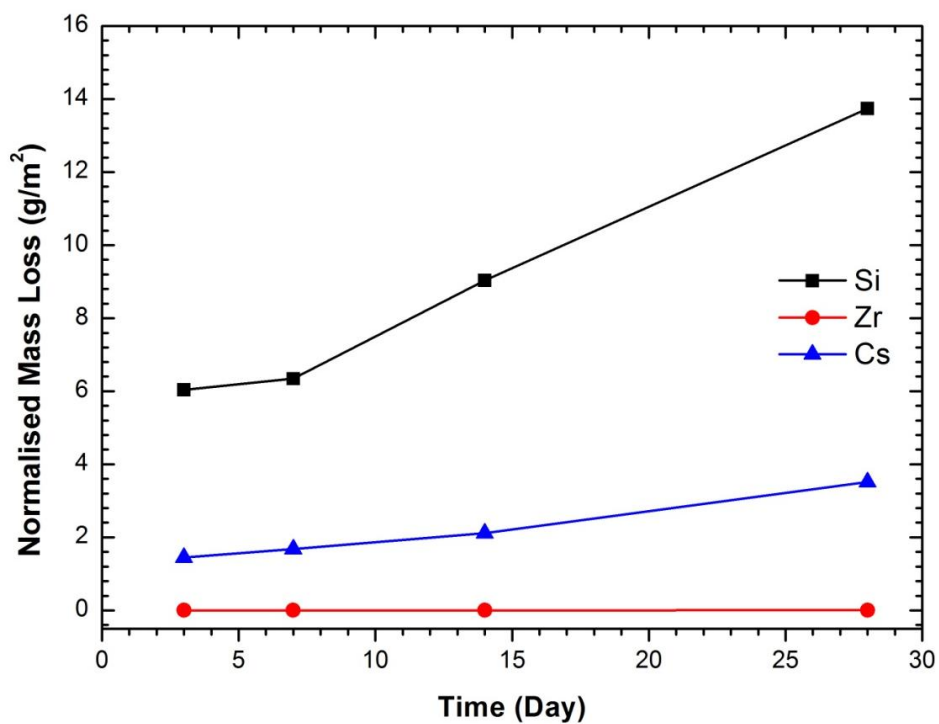
Figure 6.8 Plot of normalised mass losses ($g \cdot m^{-2}$) of HIPed $Cs_2ZrSi_6O_{15}$
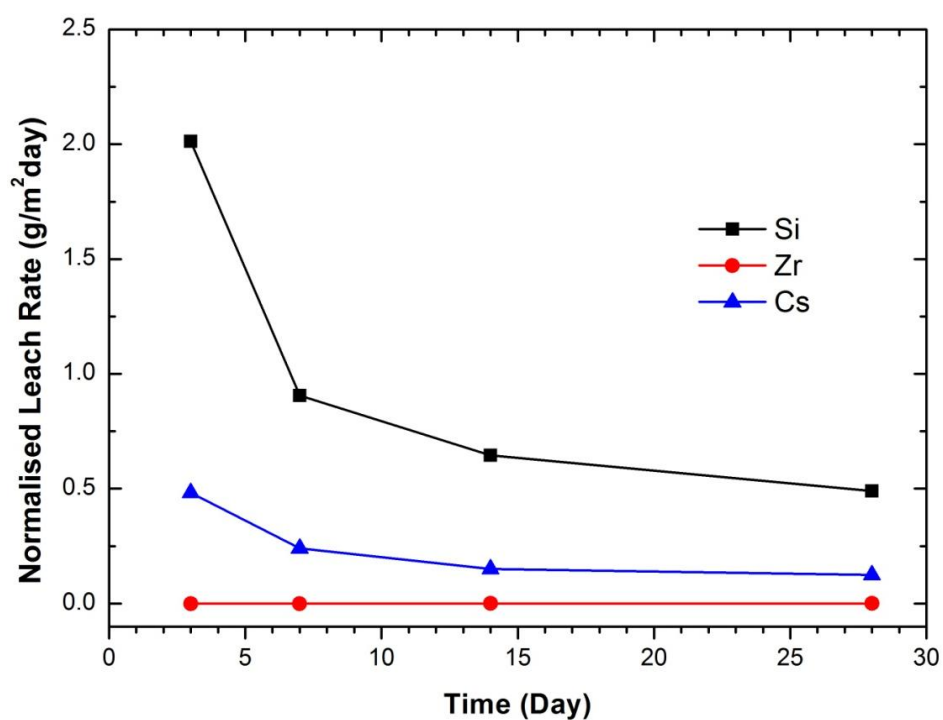
Figure 6.9 Plot of normalised leach rates ($g \cdot m^{-2} \cdot day^{-1}$) of HIPed $Cs_2ZrSi_6O_{15}$

(5) HIPed Cs₂ZrSi₃O₉

The normalised mass losses of HIPed $Cs_2ZrSi_3O_9$ shown in Table 6-6 and Figure 6.10 reveal that a particularly large amount of Si and a trace amount of Zr are released into the leachant. A relatively high amount of Cs was also detected in the leachant. For their normalised leach rates, as shown in Table 6-6 and Figure 6.11, it is seen that for all of the three elements they generally decreased as MCC-1 progressed.

Table 6-6 Normalised mass losses and leach rates ($g \cdot m^{-2} \cdot day^{-1}$) from MCC-1results of HIPed $Cs_2ZrSi_3O_9$

Normalised Mass Loss ($g \cdot m^{-2}$)

Day	Si	Zr	Cs
3	3.112E+01	5.614E-02	3.337E+00
7	4.045E+01	9.524E-02	9.190E+00
14	6.062E+00	4.309E-03	6.834E+00
28	7.726E+00	7.894E-03	8.319E+00

Normalised Leach Rate ($g \cdot m^{-2} \cdot day^{-1}$)

Day	Si	Zr	Cs
3	1.037E+01	1.871E-02	1.112E+00
7	5.779E+00	1.361E-02	1.313E+00
14	4.330E-01	3.078E-04	4.881E-01
28	2.759E-01	2.819E-04	2.971E-01
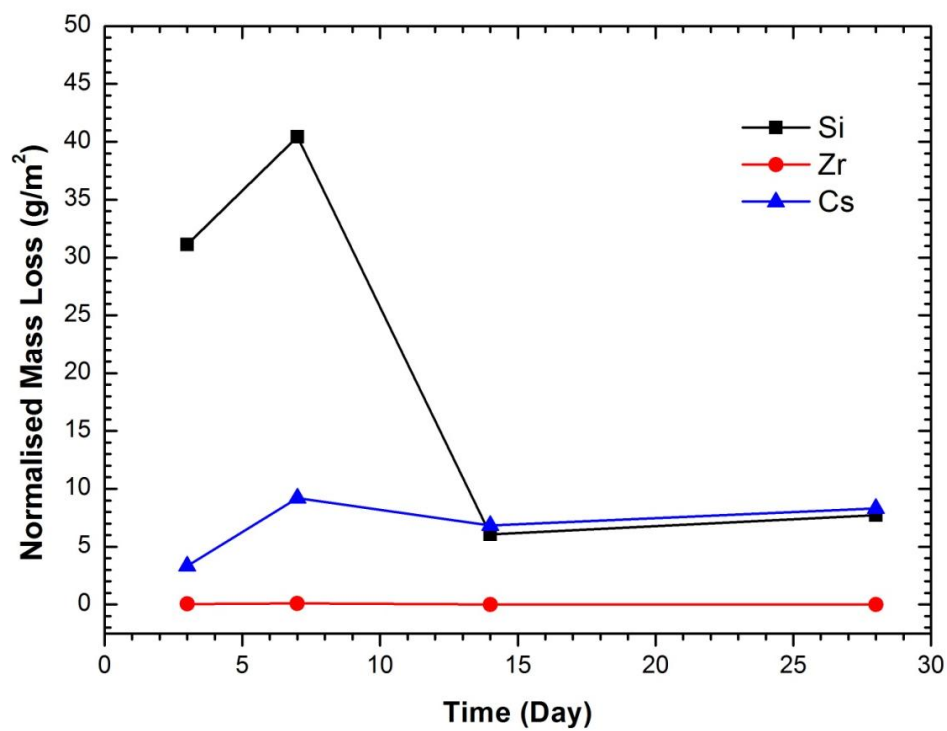
Figure 6.10 Plot of normalised mass losses (g·m^{-2}) of HIPed Cs$_2$ZrSi$_3$O$_9$
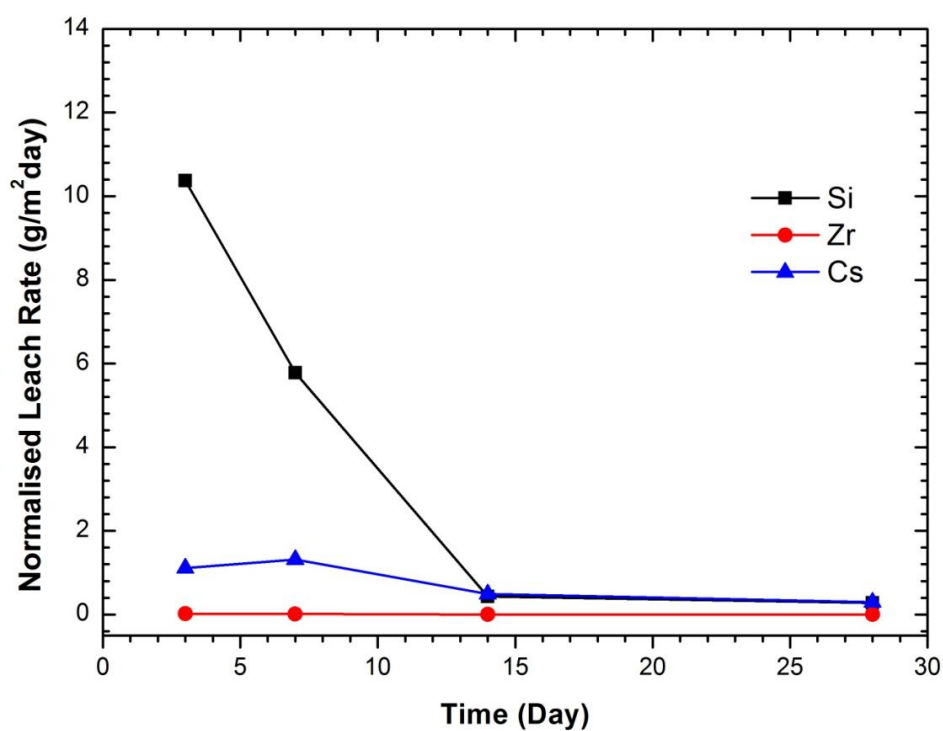
Figure 6.11 Plot of normalised leach rates (g·m^{-2}·day^{-1}) of HIPed Cs$_2$ZrSi$_3$O$_9$

6.3.2 PCT-B Results

Triplicate experiments were conducted for each sample in the PCT-B tests and the averages and standard deviations of the leach rates are shown in Table 6-7. All the HIPed samples show good consistency from the triplicate results. For both HIPed 6 wt.% and 12 wt.% Cs-IONSIV® samples, normalised elemental leach rates follow the order Na> Cs ~ Si >>Zr ~ Nb ~ Ti. This trend was the same with that in the MCC-1 tests using monolithic samples. The low concentrations of Zr, Nb and Ti in all cases are expected from the low water-solubility of these elements.

It is noted that the 7-day PCT results agree well with the MCC-1 results even though the SA/V ratios in the two forms of leach test differ by a factor of ~ 100 to 250. The normalised Cs leach rates in PCT-B tests were roughly the same order of magnitude with those in MCC-1 tests for the same duration performed, except for HIPed $Cs_2ZrSi_6O_{15}$ and $Cs_2ZrSi_3O_9$.

Table 6-7 Average values and standard deviations for normalised leach rates ($g \cdot m^{-2} \cdot day^{-1}$) from PCT-B tests of HIPed samples (N=3)

IONSIV 6 wt.%

	Average	Esd
Na	1.176E-01	1.663E-02
Si	4.243E-02	3.573E-03
Ti	1.462E-04	7.373E-05
Zr	5.036E-04	1.226E-04
Nb	5.273E-04	1.220E-04
Cs	3.230E-02	1.921E-03

IONSIV 12 wt.%

	Average	Esd
Na	1.110E-01	4.347E-03
Si	4.081E-02	5.487E-04
Ti	8.112E-05	6.694E-05
Zr	1.791E-04	1.439E-04
Nb	1.332E-04	1.077E-04
Cs	3.779E-02	1.477E-03

$Cs_2TiNb_6O_{18}$

	Average	Esd
Ti	1.408E-04	1.083E-04
Nb	6.662E-05	4.405E-05
Cs	2.063E-03	3.589E-05

$Cs_2ZrSi_6O_{15}$

	Average	Esd
Si	2.478E-02	4.371E-04
Zr	4.100E-04	6.842E-05
Cs	3.002E-03	1.804E-05

$Cs_2ZrSi_3O_9$

	Average	Esd
Si	8.195E-02	1.546E-03
Zr	3.522E-03	4.898E-04
Cs	3.174E-02	9.510E-04

6.4 Discussions

6.4.1 MCC-1

The Zr, Nb and Ti concentrations of all leachates were extremely low, barely detected using ICP. This is because Zr, Nb and Ti are much less water-soluble elements than highly soluble ones such as Cs, Na and Si. In general, the normalised mass losses of all elements in

the HIPed samples increased as the MCC-1 test progressed. However, some fluctuations in the trend were observed in some of the samples. For example, Cs and Si in HIPed 6 wt.% Cs-IONSIV®, Na in HIPed 12 wt.% Cs-IONSIV®, Cs in HIPed $Cs_2TiNb_6O_{18}$ and Si in HIPed $Cs_2ZrSi_3O_9$. These mainly arise from the surface roughness of the monolithic samples. Specimen preparations in MCC-1 test should involve a polishing procedure to a smooth 600 grit finish. Nonetheless, some of the HIPed samples were irregular monoliths rather than whole pieces with regular geometries, therefore the small scale of the samples made it difficult to achieve uniformly smooth surfaces.

Taking phase fractions into account, HIPed 6 wt.% and 12 wt.% Cs-IONSIV® sample have similar values of $Cs_2TiNb_6O_{18}$, however HIPed 12 wt.% Cs-IONSIV® shows a slightly better chemical durability than HIPed 6wt.%, which is attributed to a greater weight percentage of durable $Cs_2ZrSi_6O_{15}$ phase (Discussed in Chapter 4, section 4.5.3). The higher leach rate in HIPed 6 wt.% Cs-IONSIV® could be due to a possible Cs-containing phase formed during the HIP process.

To prove this hypothesis, SEM/EDX observation on a polished HIPed 6 wt.% Cs-IONSIV® specimen was carried out. As shown as Figure 6.12, a bright grain of size 15 μm in diameter was found and it consists of Cs, Nb and O, suggesting possible phases such as $CsNbO_3$, $Cs_2Nb_4O_{11}$ or $Cs_4Nb_{11}O_{30}$ based on a search in ICSD database. Considering the atomic fractions of each elements from EDX analyses (also see Table 6-8), this phase is most likely $Cs_4Nb_{11}O_{30}$. Although the phase is not fully characterised and confirmed, the existence of some Cs/Nb phase(s) supports the hypothesis that some leachable Cs-rich grains are formed during the HIP process and resulted in the random fluctuations in Cs release rates.
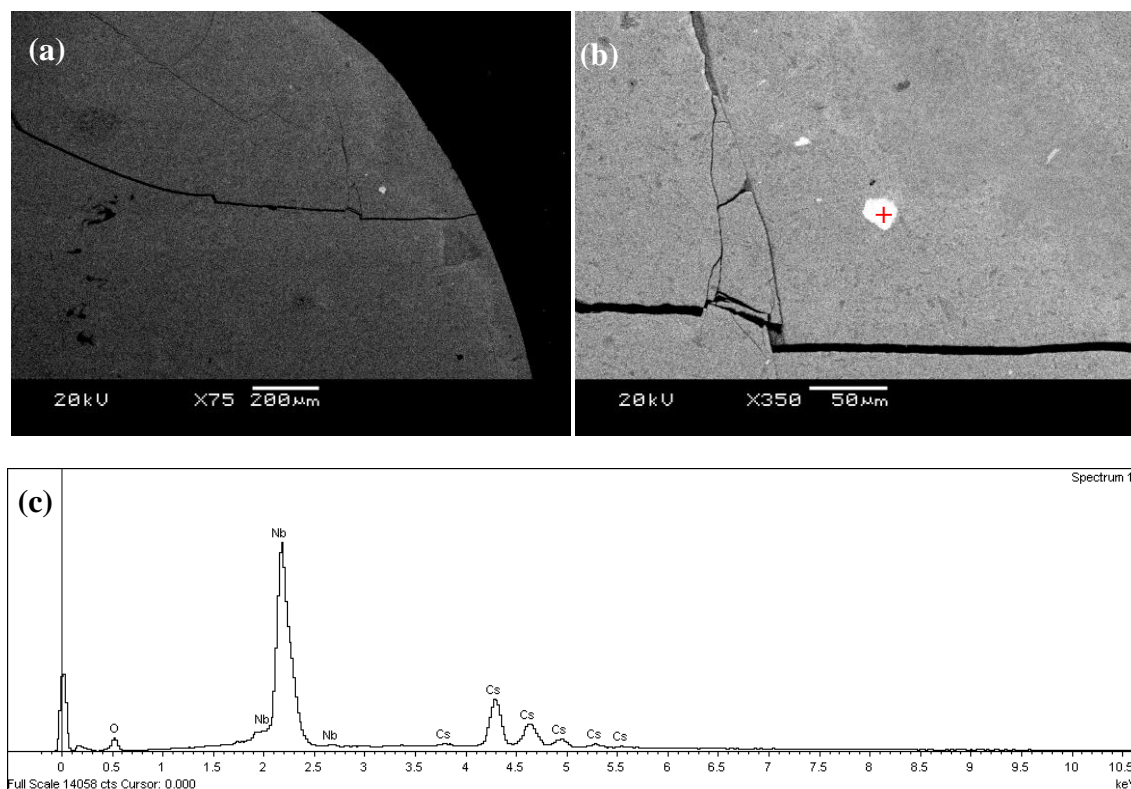
Figure 6.12 SEM/BSE micrograph of HIPed 6 wt.% Cs-IONSIV$^{\circledR}$ (a) magnification×75 (b) magnification ×350 (c) EDX analyse from the spot (+) marked in (b).

Table 6-8 EDX analyses of the bright grain in Figure 6.12 (b). Average and standard deviation in atomic % are shown in the table (N=4).

Element	Average	Esd
O K	37.60	0.95
Nb L	44.89	0.81
Cs L	17.51	0.22

In comparison, HIPed $Cs_2TiNb_6O_{18}$ demonstrated the best durability for Cs retention among these samples, followed by 12 wt.% Cs-IONSIV®, 6 wt.% Cs-IONSIV®, $Cs_2ZrSi_6O_{15}$, and then $Cs_2ZrSi_3O_9$, as shown in Figure 6.13. The reason for the superior immobilisation of Cs in $Cs_2TiNb_6O_{18}$ is because of its excellent structure leading to no diffusion pathways where Cs can migrate (as discussed in Chapter 5)[150] and a very low bulk solubility. Similarly, no infinite tunnels for Cs to travel can be found in the structures of $Cs_2ZrSi_6O_{15}$ and $Cs_2ZrSi_3O_9$, therefore a low Cs leach rate is also expected.[90, 151, 157, 179] Although $Cs_2ZrSi_3O_9$ is the least durable phase in this study, its normalised Cs leach rate value is still comparable to those reported in the literatures (see Table 6-9).
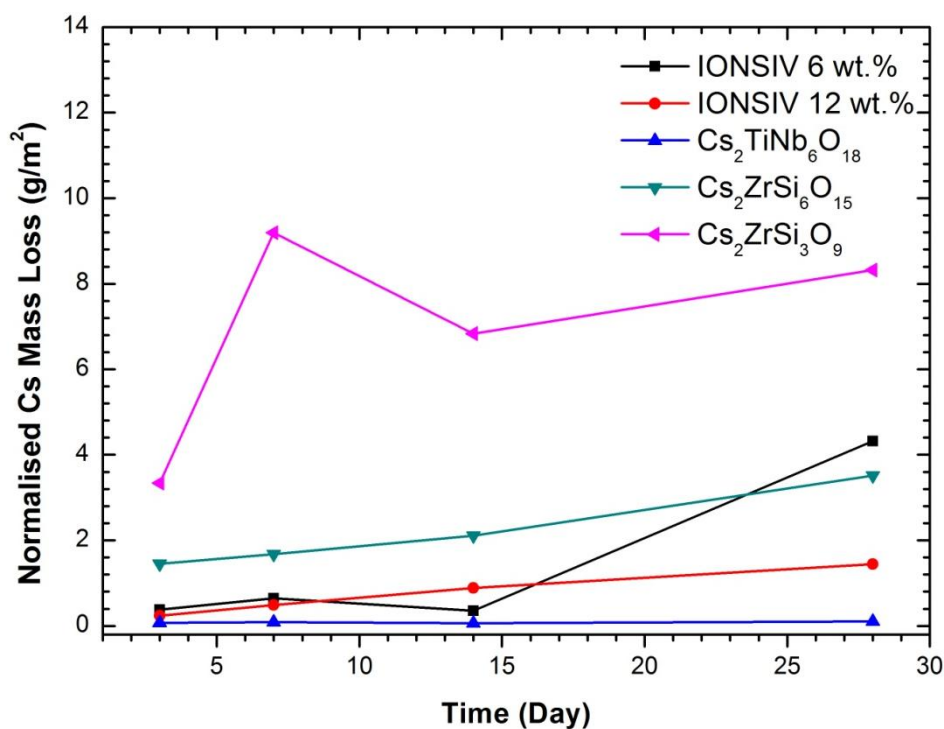
Figure 6.13 Plot of normalised Cs mass loss (g·m^{-2}) for 5 HIPed samples

Table 6-9 Comparison of normalised Cs leach rate of various waste forms (monolithic samples) for Cs immobilisation

Wasteforms		Test method /conditions	Normalised Cs Leach Rate ($g \cdot m^{-2} \cdot day^{-1}$)	Reference
Thermally converted Silicotitanate	5% Cs-TAM-5	MCC-1, 14d, 90 °C	0.62 (700 °C) [+] 0.08 (900 °C) 0.10 (1000 °C)	Balmer et al. (1998) [154]
	20% Cs-TAM-5		1.14 (700 °C) [+] 0.22 (900 °C)	
	5% Cs-IONSIV®		0.80 (700 °C) 0.08 (800 °C) 0.09 (900 °C) 0.08 (1000 °C)	
	12% Cs-IONSIV®		3.35 (700 °C) 1.48 (800 °C) 0.10 (900 °C)	
Synroc	polyphase titanate ceramic	MCC-2, 337d, 150 °C	0.028	Smith et al. (1992) [187]
Hollandite	Rb-doped Ba-hollandite	MCC-1, 128d, 90 °C	~ 0.8 initially, ~0.007 after 128 d	Carter et al. (2001) [188]
Hollandite-rich waste forms	Al-18	MCC-1, 0-1, 1-7, 7-28 day, 90 °C	0.36, 0.069, 0.025	Carter et al. (2009) [141]
	Al-12		0.35, 0.099, 0.022	
	Mg-18		18, 3.8, 1	
	Mg-12		17, 7.7, 2	
Tungsten bronze-based nuclear waste form ceramics	Cs-MoW–HTB-900°C [*]	MCC-1, 1d, 90°C	< 0.000001	Luca et al. (2006) [189]
	Cs-W–HTB-1300 °C [*]	MCC-1, 7d, 90°C	0.000057	
	Cs-MoW–HTB-	MCC-1, 7d,	0.0039	

	1300 °C[*]	90 °C		
	Cs-MoW–PYR-1300 °C[*]	MCC-1, 7d, 90 °C	< 0.000001	
Glass-ceramic	Containing MgO-SiO$_2$ 1.18-22.42 wt.%	MCC-1, 14d, 90 °C	0.8	Raman (1998) [138]
	Containing MgO-SiO$_2$ 6.9-16.7 wt.%		8.37	
Glass composite material (GCM) + clinoptilolite	GCM containing up to 73 mass% of spent clinoptilolite	MCC-1, 7d, 40 °C	< 0.0635	Juoi et al. (2008) [13]
	GCM containing 80 mass% of spent clinoptilolite		9.06	

[+] : Temperature of heat treatment.

* : HTB: hexagonal tungsten oxide bronze. W-HTB: undoped-HTB. MoW: Mo-doped HTB.

PYR: Pyrochlore material. 900 °C / 1300 °C: Calcination temperature.

As shown in Figure 6.14, Cs was leached from HIPed samples in a relatively short period, indicating that only surface adsorbed Cs is released upon initial exposure to water. The leach rates of Cs reached values between 2.971E-01 (HIPed $Cs_2ZrSi_3O_9$) and 3.751E-03 (HIPed $Cs_2TiNb_6O_{18}$) $g \cdot m^{-2} \cdot day^{-1}$ after 28 days. These results show that in all cases HIPed samples are able to retain Cs well. These materials are more leach resistant than other materials reported for Cs immobilisations, e.g. glass or even Synroc-C (see Table 6-9).
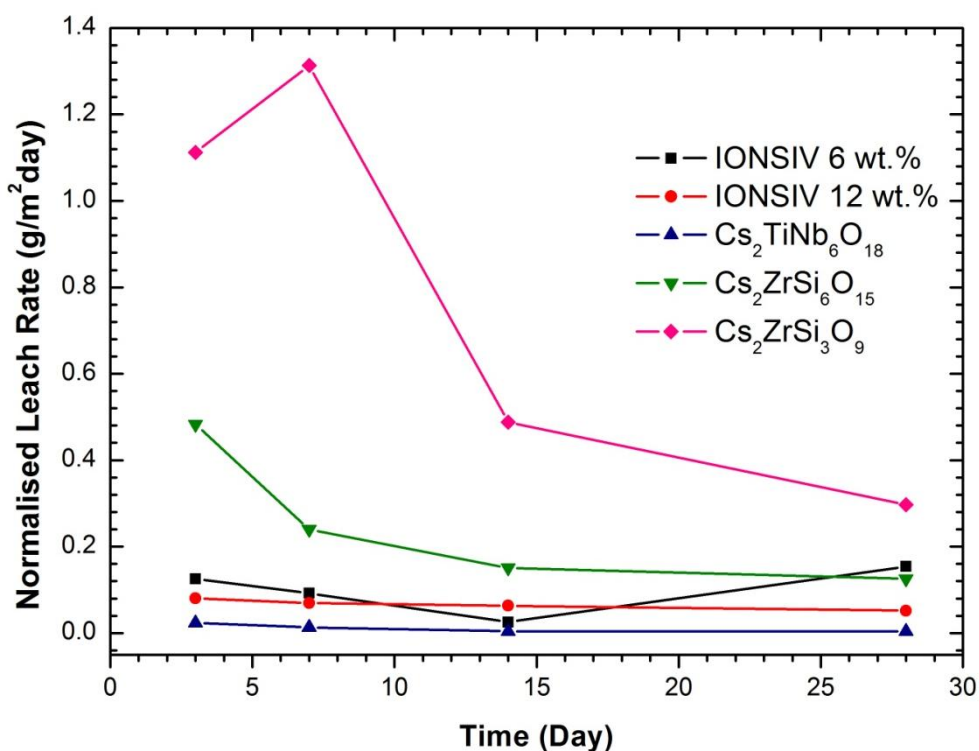
Figure 6.14 Plot of normalised Cs leach rates ($g \cdot m^{-2} \cdot day^{-1}$) for 5 HIPed samples

6.4.2 PCT-B

The PCT test results shown in Table 6-7 and Figure 6.15 demonstrate that Cs leach rates were low, ranging from 3.779E-02 to 2.063E-03 g·m^{-2}·day^{-1}. HIPed Cs$_2$TiNb$_6$O$_{18}$ exhibits the best chemical durability in this study. Compared to MCC-1 results, Cs$_2$ZrSi$_6$O$_{15}$ and Cs$_2$ZrSi$_3$O$_9$ are both much more durable based on the PCT-B test. This is possibly because of the high-solution concentrations of leached elements in the PCT-B test using powder samples, which reduce dissolution rates and yield unrealistically high durabilities. In addition, the PCT-B test cannot provide information about the effect of morphology on the leach-resistance, therefore a relatively better durability is sometimes observed.

The HIPed samples all show the potential as alternative wasteforms for Cs. Considering even the most conservative result in this work, HIPed 12 wt.% Cs-IONSIV® is one or two orders of magnitudes more durable than borosilicate glass. Based on the PCT-B test results, it is proved that Cs in the HIPed IONSIV® products is located in very stable crystalline phases such as Cs$_2$TiNb$_6$O$_{18}$ and Cs$_2$ZrSi$_6$O$_{15}$.
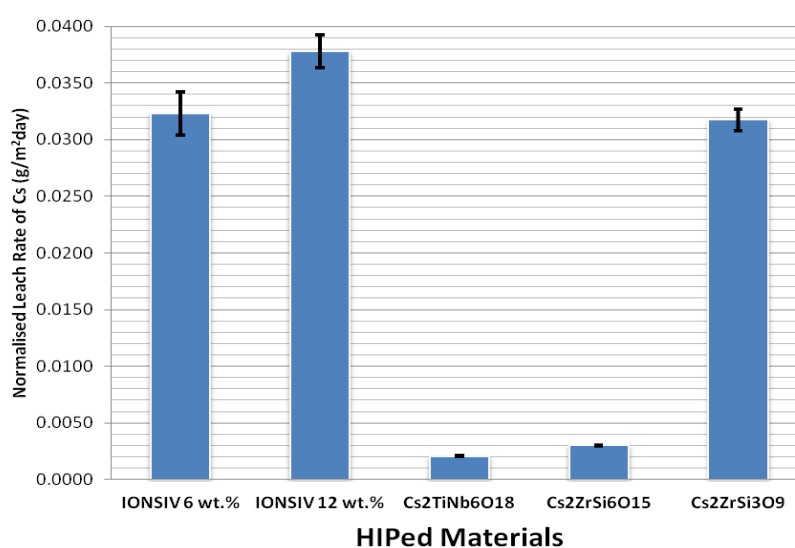
Figure 6.15 Normalised Cs leach rates of HIPed samples from the PCT-B results

Table 6-10 Comparison of normalised Cs leach rate of various waste forms (powder samples)

for Cs immobilisation

Wasteforms		Test methods /conditions	Normalised Cs Leach Rate $(g \cdot m^{-2} \cdot day^{-1})$	References	
Thermal converted Silicotitanate	12% Cs-IONSIV®	PCT-B, 7d, 90 °C	~ 10^{-3}-10^{-8}	Balmer et al. (1998)	[154]
Borosilicate glass	containing CaO	PCT-B, 7d, 90 °C	~ 0.1 - 1	Banerjee et al. (2011)	[190]
Hollandite-rich waste forms	Al-18	PCT-B, 7 d, 90 °C	0.62	Carter et al. (2009)	[141]
	Al-12		0.52		
	Mg-18		1.3		
	Mg-12		2.8		
SAP (SiO_2-Al_2O_3-P_2O_5)	25-42 wt.% glass	PCT-A, 7-56d, 90 °C	~ 0.001	Park et al. (2011)	[191]

6.5 Conclusions

The chemical durability or Cs mobility is highly related to the crystal structure of the crystalline compounds in the wasteform. Two standard leach tests, MCC-1 and PCT-B, were carried out to measure the leach resistance of IONSIV® samples after HIPing, as well as three Cs-containing phases, $Cs_2TiNb_6O_{18}$, $Cs_2ZrSi_6O_{15}$ and $Cs_2ZrSi_3O_9$, found as thermally converted phases in IONSIV®.

$Cs_2TiNb_6O_{18}$ was superior in Cs retention above all the other HIPed samples in this study, and even more leach resistant than hollandite - the material targeted for Cs sequestration in Synroc. $Cs_2ZrSi_3O_9$, the Cs-rich phase found only in HIPed IONSIV® with metal additives, was the least durable phase in this study. However, its Cs leachability was still considered moderately good compared to the values reported for other materials in the literature.

To sum up, both MCC-1 and PCT-B tests show that a highly chemically durable wasteform can be achieved by HIPing IONSIV®. This product consists of a mixture of crystalline Cs-rich phases which all have low leachability. The normalised Cs leach rates of HIPed samples were very low and better than those of all reported materials previously suggested as Cs wasteforms, proving the potential of these materials for long-term storage.

Chapter 7   Summary

The work in this thesis has focused on the potential utility in creating a stable ceramic wasteform by HIPing Cs-exchanged CSTs for nuclear waste clean-up. Na-CST and Na-Nb/CST were hydrothermally synthesised, various characterisations made and the Cs exchange properties studied and compared with the commercial CST product, IONSIV[®] (presented in Chapter 3). A methodology of HIPing for densifying the used CSTs was described in Chapter 4. By investigating the phase formation of Cs-exchanged CSTs after HIPing, the Cs behaviour within the wasteform can be furthered assessed aiming for long-term storage. $Cs_2TiNb_6O_{18}$ and $Cs_2ZrSi_6O_{15}$ are the main Cs-containing phases found in the HIPed IONSIV[®] samples, the chemical and structural properties of these two phases, as well as $Cs_2ZrSi_3O_9$, which was found in the HIPed Cs-exchanged IONSIV[®] sample with metal additives, were examined and discussed in Chapter 5. Cs leach resistances of HIPed Cs-exchanged IONSIV[®] samples and HIPed Cs-containing phases were then studied by carrying out MCC-1 and PCT-B standard leach tests, as presented in Chapter 6. Major achievements in this work are summarised in the following.

7.1 Conclusions

7.1.1 Crystalline Silicotitanates

Pure crystalline silicotitanate (Na-CST) and 25% Nb substituted CST (Na-Nb/CST) have been successfully synthesised using the hydrothermal method. Natisite (Na_2TiSiO_5) and

unreacted Nb_2O_5 are sometimes found as impurities in Na-CST and Na-Nb/CST synthesis, respectively. Natisite can be significantly washed out by applying a 2-step treatment, but Nb_2O_5 cannot be removed from the main Na-Nb/CST product. Although the crystallinity of CST declined after the purification, the 2-step treatment is still considered a more efficient way of obtaining a pure CST sample rather than optimising the hydrothermal synthesis conditions. In Na-Nb/CST synthesis, a much better purity was achieved using niobium ethoxide as the Nb source due to a more homogeneous starting material prepared for the hydrothermal synthesis.

Both Na-CST and Na-Nb/CST exhibit poor thermal stability at temperatures higher than 400 °C. A phase transition of CST to an amorphous material indicates a potential risk of Cs leaching due to the destruction of the structure. The thermal stability of IONSIV® at high temperature is also of concern. Therefore, a stable wasteform is required to accommodate the spent CST and IONSIV®.

Although it was reported that acid pretreatment was not necessary, Na-CST and Na-Nb/CST without acid activation showed almost no Cs exchange ability. IONSIV® possesses a far better Cs exchange capacity than the Na-CST and Na-Nb/CST synthesised in this work due to the small particle size which has more active area and is beneficial for the ion exchange process.

7.1.2 Cs Immobilisation into a Ceramic Wasteform by HIPing

It is important to understand the phases formed from Cs-exchanged CSTs after HIPing. It was confirmed from XRD patterns and TEM/EDX analysis that Cs-exchanged IONSIV® was thermally converted to $Cs_2TiNb_6O_{18}$ and $Cs_2ZrSi_6O_{15}$ and a series of oxides under the chosen

HIP conditions. In addition, attempts to produce a hollandite-like phase, a well-known Cs host, were made by HIPing the Cs-exchanged IONSIV® with added Ti, Fe and Al metal. From the further studies of HIPing Cs-IONSIV® with these added metals, the redox state created by the metal plays a key role and has affected the phase assemblage. It is indicated that Cs was gently locked in the crystalline phases regardless of the variety of metal addition. Although ultimately hollandite was never found in any of the HIPed samples, the main Cs-containing phases, $Cs_2TiNb_6O_{18}$, $Cs_2ZrSi_6O_{15}$ and $Cs_2ZrSi_3O_9$, were considered potential Cs wasteforms based on the structural features reported in the literature.[90, 150, 151] It also means that these Cs-containing phases can be alternative options as wasteforms for Cs immobilisation rather than hollandite.

7.1.3 $Cs_2TiNb_6O_{18}$, $Cs_2ZrSi_6O_{15}$ and $Cs_2ZrSi_3O_9$

$Cs_2TiNb_6O_{18}$, $Cs_2ZrSi_6O_{15}$ and $Cs_2ZrSi_3O_9$ were obtained via a number of synthesis methods. In this work, a sol-gel method for synthesising $Cs_2TiNb_6O_{18}$ was proposed and has been proved an easier and more efficient approach than solid state reactions to gain highly pure and crystalline samples. $Cs_2ZrSi_6O_{15}$ was also synthesised using a modified sol-gel method, which is of a better-controlled manner, and sol-gel synthesis has shown its advantages over the reported hydrothermal synthesis.

From the structural studies, these three Cs-containing phases possesses great ability for hosting the Cs atoms inside the lattice, suggesting the reason for an excellent Cs leach resistance. Rietveld refinements of these three Cs- containing phases supported that Cs atoms are located in the cavities with high coordination numbers, indicating that Cs atoms have a stable bonding environment.

7.1.4 Chemical Durability

HIPing CST is considered a promising route for densification and stabilisation of nuclear waste. Both MCC-1 and PCT-B tests showed that a highly chemically durable wasteform can be achieved by HIPing IONSIV®.

It was shown in this work that $Cs_2TiNb_6O_{18}$ was superior in Cs retention above all the other Cs-containing phases produced in this study, and even more leach resistant than hollandite.[141] Although $Cs_2ZrSi_3O_9$ was the least durable phase compared to $Cs_2TiNb_6O_{18}$ and $Cs_2ZrSi_6O_{15}$, its Cs leachability was still moderate compared to the values reported in the literature (see Chapter 6). Those low normalised Cs leach rates of HIPed samples and HIPed Cs-containing phases show that in practice these materials are promising candidates immobilising Cs in a long-term scale.

7.2 Further Work

7.2.1 Ba Solubility in $Cs_2TiNb_6O_{18}$, $Cs_2ZrSi_6O_{15}$ and $Cs_2ZrSi_3O_9$

^{137}Cs has a half-life of 30.17 years and decays to Ba by emitting one to two high-energy beta particles. Thus, it is very important to understand if the decay product of Cs, Ba, is also well contained in the structures of these three Cs-containing phases. In $Cs_2TiNb_6O_{18}$, the charge difference caused by Ba solubility can be compensated by changing Nb^{5+}/Nb^{4+} and Ti^{4+}/Ti^{3+} ratios, or by varying the Ti or Nb content. Whilst in $Cs_2ZrSi_6O_{15}$ and $Cs_2ZrSi_3O_9$, it is more difficult to accommodate Ba because Zr^{4+}/Zr^{2+} only occurs in extremely reducing

environments. It is required to examine the possibility of Ba insertion into the lattices of Cs-containing phases.

However, due to the challenges found in characterisation of these materials (as discussed in session 5.6), neutron diffraction seems to be the best method for investigating the presence of Ba inside the lattice. Therefore, further work includes the sol-gel syntheses and characterisation of Ba inserted Cs-rich phases using neutron diffraction and Rietveld refinements for structural studies as well as the evaluation of chemical and thermal durabilities of these Ba inserted Cs-rich phases.

7.2.2 Irradiation Stability of the Wasteforms and Modelling

One of the requirements of a good wasteform is the stability to irradiation. The chief sources of radiation in high-level nuclear wasteforms are the β-decay of fission products (e.g. ^{137}Cs and ^{90}Sr) and the α-decay of actinide elements (e.g. U, Np, Pu, Am and Cm). β-decay is the primary source of radiation during the first 500 year of storage, and the effects on the wasteform should be investigated.[71] Other effects, such as γ-irradiation or electrons, in the wasteform can be also studied by carrying out experiments involving exposure to an external ^{60}Co source,[69] or subjecting the specimen to a high resolution electron microscopy for high energy electron irradiation (e.g. 400 kV).[137, 192, 193]

Furthermore, the wasteforms created by HIPing are anticipated to be stored in the repositories, therefore the computational modelling of wasteform behaviour in the geological environment in a long time scale is indeed important. This study will be more complete with such supplemental data from irradiation stability and modelling.

7.2.3 Immobilisation of Sr from IONISV® by HIPing

CSTs also shows good selectivity and capacity for Sr,[119, 126, 194-198] however, an efficient way to deal with the spent Sr-exchanged CSTs is still being sought. With the successful experience of HIPing Cs-exchanged CSTs, it is interesting to understand the possibility of immobilisation of Sr from CSTs by HIPing. Phase assembly of Sr-exchanged IONSIV® after HIPing and the Sr leaching resistance of the ceramic wasteform are of much interest.

7.2.4 Development of New Ion Exchangers and Wasteforms

7.2.4.1 Crystalline Zirconosilicates and Zircononiobates

Microporous crystalline materials with heteropolyhedral frameworks have attracted considerable attention as potential ion exchangers, sorbents and catalysts. The majority of the inorganic materials as ion exchangers synthesised and characterised were titanosilicates, however, porous alkali zirconosilicates have functional properties and crystal-chemical diversity[199] and have received more attention. Therefore, the development of novel microporous zirconium silicates, for example, $K_2ZrSi_3O_9 \cdot 2H_2O$,[169] $Na_2ZrSi_6O_{15} \cdot 3H_2O$,[199, 200] and $Na_2ZrSi_3O_9 \cdot 3H_2O$,[201] as inorganic ion exchangers and the structure studies of exchanged materials will be useful for nuclear waste clear-up.

In addition, it has been well-studied that Nb-substituted silicotitanates have enhanced cation exchange properties. Therefore, synthesis of Nb-substitution in zirconosilicates and their ion exchange properties, chemical/thermal stabilities as well as the phase formation after HIPing will be an interesting topic to study.

241

7.2.4.2 Potential Wasteforms Produced using HIPing

The presence of Nb with a variable ratio of Nb^{5+}/Nb^{4+} provides a means for valence change to balance the charge when Cs radioactively decays to Ba, and the great chemical durability of $Cs_2TiNb_6O_{18}$ observed in the Cs leach tests indicates the potential of titanoniobates as wasteforms for Cs immobilisation. An interesting topic of development of alkali zircononiobates (e.g. $Na_2ZrNb_6O_{18}$ or $K_2ZrNb_6O_{18}$) as a novel wasteform for Cs stabilisation has arisen for further investigation. The chemical/thermal/irradiation stabilities and leach behaviours required for a stable wasteform will be of interest.

It was also found that the wadeite structure is very tolerant of ionic substitutions, not only in its framework sites but also over the interstitial positions. This property can be utilised to develop a system of stable wasteforms. The wadeite-type phases reported so far can be summarised as $A_2BSi_3O_9$ (A = K, Rb, Cs, and B = Ti, Zr, Sn, Ge, Si) and $A_2BGe_3O_9$ (A = K, Rb, Cs, Tl, and B = Ti, Sn, Ge).[167] The findings that Cs atoms were locked well inside $Cs_2ZrSi_3O_9$ due to the structure indicate that those wadeite-type phases are considered potential wasteform candidates.

HIPing has been proved an efficient route for densifying the materials and also provides an encapsulation of secondary shielding from environment (the metal can) preventing Cs from leaching. In this work, a systematic study of immobilisation of Cs into crystalline silicates by HIPing was conducted. The results have promisingly demonstrated that HIPing can be further developed and utilised in the nuclear industry for producing stable wasteforms.

References

[1]   N. Chapman and A. Hooper, The disposal of radioactive wastes underground, in *Proceedings of the Geologists' Association*, **123**, 46-63, 2012.

[2]   M. M. Abu-Khader, *Progress in Nuclear Energy*, 2009, **51**, 225-235.

[3]   S. V. Stefanovsky, S. V. Yudintsev, R. Gieré and G. R. Lumpkin, Nuclear Waste Forms, in *Energy, Waste and the Environment a Geochemical Perspective*, eds. R. Gieré and P. Stille, Geological Society, London, 2004.

[4]   I. Donald, B. Metcalfe and R. Taylor, *Journal of Materials Science*, 1997, **32**, 5851-5887.

[5]   S. Gaur, *Journal of Chromatography A*, 1996, **733**, 57-71.

[6]   A. Dyer, A. Chimedtsogzol, L. Campbell and C. Williams, *Microporous and Mesoporous Materials*, 2006, **95**, 172-175.

[7]   N. V. Elizondo, E. Ballesteros and B. I. Kharisov, *Applied Radiation and Isotopes*, 2000, **52**, 27-30.

[8]   M. Kuronen, R. Harjula, J. Jernstrom, M. Vestenius and J. Lehto, *Physical Chemistry Chemical Physics*, 2000, **2**, 2655-2659.

[9]   A. Malekpour, M. R. Millani and M. Kheirkhah, *Desalination*, 2008, **225**, 199-208.

[10]   P. Yang and T. Armbruster, *Journal of Solid State Chemistry*, 1996, **123**, 140-149.

[11]   A. Abusafa and H. Yucel, *Separation and Purification Technology*, 2002, **28**, 103-116.

[12]   M. E. Gunter and J. L. Palmer, *Geochimica Et Cosmochimica Acta*, 2002, **66**, A297-A297.

[13]   J. M. Juoi, M. I. Ojovan and W. E. Lee, *Journal of Nuclear Materials*, 2008, **372**, 358-366.

[14]   A. Kilincarslan and S. Akyil, *Journal of Radioanalytical and Nuclear Chemistry*, 2005, **264**, 541-548.

[15]   P. Rajec and K. Domianovia, *Journal of Radioanalytical and Nuclear Chemistry*, 2008, **275**, 503-508.

[16] T. Shahwan, D. Akar and A. E. Eroglu, *Journal of Colloid and Interface Science*, 2005, **285**, 9-17.

[17] I. Smiciklas, S. Dimovic and I. Plecas, *Applied Clay Science*, 2007, **35**, 139-144.

[18] H. Mimura, M. Kimura, K. Akiba and Y. Onodera, *Separation Science and Technology*, 1999, **34**, 17-28.

[19] H. Mimura, T. Kobayashi and K. Akiba, *Journal of Nuclear Science and Technology*, 1995, **32**, 60-67.

[20] B. de Gennaro, A. Colella, P. Aprea and C. Colella, *Microporous and Mesoporous Materials*, 2003, **61**, 159-165.

[21] R. Harjula, J. Lehto, J. H. Pothuis, A. Dyer and R. P. Townsend, *Journal of the Chemical Society-Faraday Transactions*, 1993, **89**, 1877-1882.

[22] E. Valcke, B. Engels and A. Cremers, *Zeolites*, 1997, **18**, 205-211.

[23] E. H. Borai, R. Harjula, L. Malinen and A. Paajanen, *Journal of Hazardous Materials*, 2009, **172**, 416-422.

[24] G. S. Murthy, M. V. Sivaiah, S. S. Kumar, V. N. Reddy, R. M. Krishna and S. Lakshminarayana, *Journal of Radioanalytical and Nuclear Chemistry*, 2004, **260**, 109-114.

[25] A. I. Bortun, L. N. Bortun, A. A. Stepin and N. P. Pekhamkina, *Journal of Radioanalytical and Nuclear Chemistry-Articles*, 1993, **174**, 279-289.

[26] M. V. Maslova, L. G. Gerasimova and N. V. Motina, *Russian Journal of Applied Chemistry*, 2008, **81**, 771-775.

[27] K. L. Narasimharao, K. S. Sarma, C. Mathew, A. V. Jadhav, J. P. Shukla, V. Natarajan, T. K. Seshagiri, S. K. Sali, V. I. Dhiwar, B. Pande and B. Venkataramani, *Journal of the Chemical Society-Faraday Transactions*, 1998, **94**, 1641-1647.

[28] A. Nilchi, H. Atashi, A. H. Javid and R. Saberi, *Applied Radiation and Isotopes*, 2007, **65**, 482-487.

[29] H. Kazemian, H. Zakeri and M. S. Rabbani, *Journal of Radioanalytical and Nuclear Chemistry*, 2006, **268**, 231-236.

[30] S. Taj, D. Muhammad, M. A. Chaudhry and M. Mazhar, *Journal of Radioanalytical and Nuclear Chemistry*, 2011, **288**, 79-88.

[31] J. V. Smit, W. Robb and J. J. Jacobs, *Journal of Inorganic & Nuclear Chemistry*, 1959, **12**, 104-112.

[32] J. V. R. Smit, *Nature*, 1958, **181**, 1530-1531.

[33] R. Koivula, R. Harjula and J. Lehto, Selective Removal of radionuclides from Nuclear Waste Effluents using Inorganic Ion Exchangers, in *Combined and Hybrid Adsorbents: Fundamentals and Applications*, eds. J. M. Loureiro, M. T. Kartel and D. North Atlantic Treaty Organization. Public Diplomacy, 2006, 37-47.

[34] E. H. Tusa, A. Paavola, R. Harjula and J. Lehto, *Nuclear Technology*, 1994, **107**, 279-284.

[35] R. Harjula, J. Lehto, A. Paajanen, L. Brodkin and E. Tusa, *Nuclear Science and Engineering*, 2001, **137**, 206-214.

[36] R. G. Anthony, R. G. Dosch, D. Gu and C. V. Philip, *Industrial & Engineering Chemistry Research*, 1994, **33**, 2702-2705.

[37] A. J. Celestian, D. G. Medvedev, A. Tripathi, J. B. Parise and A. Clearfield, *Nuclear Instruments & Methods in Physics Research Section B-Beam Interactions with Materials and Atoms*, 2005, **238**, 61-69.

[38] R. G. Anthony, R. G. Dosch and C. V. Philip, USA, US6110378,1994.

[39] D. M. Poojary, R. A. Cahill and A. Clearfield, *Chemistry of Materials*, 1994, **6**, 2364-2368.

[40] E. V. Sokolova, R. K. Rastsvetaeva, V. I. Andrianov, Y. K. Egorov-Tismenko and Y. P. Men'shikov, *Soviet Physics Doklady*, 1989, **34**, 583.

[41] J.-S. Kim, S.-K. Kwon, M. Sanchez and G.-C. Cho, *Ksce Journal of Civil Engineering*, 2010, **15**, 721-737.

[42] Q.-H. Hu, J.-Q. Weng and J.-S. Wang, *Journal of Environmental Radioactivity*, 2010, **101**, 426-437.

[43] I. G. McKinley, *Energy Policy*, 1992, **20**, 683-692.

[44] B. D. Solomon, *Journal of Risk Research*, 2009, **12**, 1009-1024.

[45] F. M. Ezz-Eldin, *Nuclear Instruments & Methods in Physics Research Section B-Beam Interactions with Materials and Atoms*, 2001, **183**, 285-300.

[46] Committee on Waste Forms Technology and Performance; National Research Council, Waste Forms, in *Waste Forms Technology and Performance: Final Report*, National Research Council. Committee on Waste Forms, Technology Performance, The National Academies Press, Washington, DC, 2011, 29-86.

[47] V. K. Michaelis and S. Kroeker, *Physics and Chemistry of Glasses-European Journal of Glass Science and Technology Part B*, 2009, **50**, 249-252.

[48]   J. M. Roderick, D. Holland and C. R. Scales, Characterization and radiation resistance of a mixed-alkali borosilicate glass for high-level waste vitrification, in *MRS Proceedings*, **608**, 721-726, 2000.

[49]   W. Lutze, *Radioactive Waste Forms for the Future*, North-Holland, Amsterdam, 1988.

[50]   W. E. Lee, M. I. Ojovan, M. C. Stennett and N. C. Hyatt, *Advances in Applied Ceramics*, 2006, **105**, 3-12.

[51]   M. I. Ojovan and W. E. Lee, *New Developments in Glassy Nuclear Wasteforms*, Nova Science Publishers, New York, 2007.

[52]   Y. Abe and H. Hosono, Phosphate Glasses and Glass-ceramics, in *Inorganic Phosphate Materials*, ed. T. Kanazawa, KODANSHA; Elsevier, Tokyo; Amsterdam, 1989.

[53]   I. W. Donald, B. L. Metcalfe, S. K. Fong and L. A. Gerrard, *Journal of Non-Crystalline Solids*, 2006, **352**, 2993-3001.

[54]   M. Karabulut, B. Yuce, O. Bozdogan, H. Ertap and G. M. Mammadov, *Journal of Non-Crystalline Solids*, 2011, **357**, 1455-1462.

[55]   B. Kumar and S. Lin, *Journal of the American Ceramic Society*, 1991, **74**, 226-228.

[56]   G. G. Wicks, J. M. McKibben, M. J. Plodinec and W. G. Ramsey, SRS Vitrification Studies in Support of the U.S. Program for Disposition of Excess Plutonium, in *Disposal of Weapon Plutonium - Approaches and Prospects*, eds. E. R. Merz and C. E. Walter, Springer-Verlag, New York, LLC, 1995, 352.

[57]   A. E. Ringwood, S. E. Kesson, N. G. Ware, W. Hibberson and A. Major, *Nature*, 1979, **278**, 219-223.

[58]   A. E. Ringwood, S. E. Kesson, N. G. Ware, W. O. Hibberson and A. Major, *Geochemical Journal*, 1979, **13**, 141-165.

[59]   A. E. Ringwood, V. M. Oversby, S. E. Kesson, W. Sinclair, N. Ware, W. Hibberson and A. Major, *Nuclear and Chemical Waste Management*, 1981, **2**, 287-305.

[60]   A. E. Ringwood, *Mineralogical Magazine*, 1985, **49**, 159-176.

[61]   B. C. Chakoumakos, *Journal of Solid State Chemistry*, 1984, **53**, 120-129.

[62]   R. C. Ewing, W. J. Weber and J. Lian, *Journal of Applied Physics*, 2004, **95**, 5949 - 5971

[63]   R. C. Ewing, *Comptes Rendus Geoscience*, 2011, **343**, 219-229.

[64]   C. Fillet, T. Advocat, F. Bart, G. Leturcq and H. Rabiller, *Comptes Rendus Chimie*, 2004, **7**, 1165-1172.

[65]   G. R. Lumpkin, *Elements*, 2006, **2**, 365-372.

[66]   Y. Zhang, M. W. A. Stewart, H. Li, M. L. Carter, E. R. Vance and S. Moricca, *Journal of Nuclear Materials*, 2009, **395**, 69-74.

[67]   R. Remya, K. Murali, S. Potty, V. Priyadarshini and R. Ratheesh, *Journal of Electronic Materials*, 2005, **34**, 1076-1080.

[68]   W. J. Buykx, *Journal of Nuclear Materials*, 1982, **107**, 78-82.

[69]   T. Suzuki-Muresan, J. Vandenborre, A. Abdelouas, B. Grambow and S. Utsunomiya, *Journal of Nuclear Materials*, 2011, **419**, 281-290.

[70]   W. J. Weber, Effects of alpha irradiation on barium hollandite and nickel-iron spinel, in *MRS Proceedings*, **44**, 671-678, 1984.

[71]   R. C. Ewing, W. J. Weber and F. W. Clinard, *Progress in Nuclear Energy*, 1995, **29**, 63-127.

[72]   W. J. Weber, J. W. Wald and H. Matzke, Self-radiation damage in actinide host phases of nuclear waste forms, in *MRS Proceedings*, **44**, 679-686, 1984.

[73]   I. W. Donald, B. L. Metcalfe, D. J. Bradley, M. J. C. Hill, J. L. McGrath and A. D. Bye, *Journal of Materials Science*, 1994, **29**, 6379-6396.

[74]   D. A. Knecht, T. J. Tranter, J. Macheret, A. Meyer, D. Yesso, T. Daniels, A. S. Aloy, N. V. Sapozhnikova, A. G. Anshits, O. M. Sharonova and A. A. Tretyakov, in *WM'02 Conference*, Tucson, 2002.

[75]   T. J. Tranter, A. S. Aloy, N. V. Sapozhnikova, D. A. Knecht and T. A. Todd, Porous crystalline silica (Gubka) as a inorganic support matrix for novel sorbents, in *MRS Proceedings*, 713-719, 2002.

[76]   M. I. Ojovan, N. V. Ojovan, I. V. Stratceva and A. S. Barinov, in *WM'02 Conference*, Tucson, 2002.

[77]   I. Walczak, M.-F. Libert, S. Camaro and J.-M. Blanchard, *Agronomie*, 2001, **21**, 247-257.

[78]   Committee on Waste Forms Technology and Performance; National Research Council, Waste Processing and Waste Form Production, in *Waste Forms Technology and Performance: Final Report*, Washington, DC, 2011, 87-118.

[79]   R. F. Taylor, *Chemical Engineering Science*, 1985, **40**, 541-569.

[80] M. I. Ojovan and W. E. Lee, *An Introduction to Nuclear Waste Immobilisation*, Elsevier, Oxford, 2005.

[81] I. W. Donald, Glass and Ceramic Based Systems and General Processing Methods, in *Waste Immobilization in Glass and Ceramic Based Hosts*, John Wiley & Sons, Ltd, 2010, 57-74.

[82] H. V. Atkinson and B. A. Rickinson, eds., *Hot Isostatic Processing*, Adam Hilger, Bristol, 1991.

[83] A. B. Harker, P. E. D. Morgan and J. F. Flintoff, *Journal of the American Ceramic Society*, 1984, **67**, C26-C28.

[84] Y. Zhang, H. Li and S. Moricca, *Journal of Nuclear Materials*, 2008, **377**, 470-475.

[85] H. Li, Y. Zhang, P. J. McGlinn, S. Moricca, B. D. Begg and E. R. Vance, *Journal of Nuclear Materials*, 2006, **355**, 136-141.

[86] I. W. Donald, B. L. Metcalfe, S. K. Fong, L. A. Gerrard, D. M. Strachan and R. D. Scheele, *Journal of Nuclear Materials*, 2007, **361**, 78-93.

[87] K. Byrappa and M. Yoshimura, William Andrew Publishing/Noyes, 2001.

[88] W. L. Suchanek, M. M. Lencka and R. E. Riman, Chapter 18 - Hydrothermal synthesis of ceramic materials, in *Aqueous Systems at Elevated Temperatures and Pressures*, eds. D. A. Palmer, R. Fernández-Prini and A. H. Harvey, Academic Press, London, 2004, 717-744.

[89] C. J. Brinker and G. W. Scherer, *Sol-gel Science: the Physics and Chemistry of Sol-gel Processing*, Academic Press, Boston, 1993.

[90] M. L. Balmer, Y. L. Su, H. W. Xu, E. Bitten, D. McCready and A. Navrotsky, *Journal of the American Ceramic Society*, 2001, **84**, 153-160.

[91] C. Hammond, *The basics of Crystallography and Diffraction*, Oxford University Press, Oxford, 2009.

[92] L. Brügemann and E. K. E. Gerndt, *Nuclear Instruments and Methods in Physics Research Section A: Accelerators, Spectrometers, Detectors and Associated Equipment*, 2004, **531**, 292-301.

[93] R. Rinaldi, *European Journal of Mineralogy*, 2002, **14**, 195-202.

[94] W. Kockelmann, L. C. Chapon and P. G. Radaelli, *Physica B: Condensed Matter*, 2006, **385-386 Part 1**, 639-643.

[95] GEM, General Materials Diffractometer, ISIS, http://wwwisis2.isis.rl.ac.uk/disordered/gem/gem_home.htm.

[96] NIST Center for Neutron Research, Neutron scattering lengths and cross sections http://www.ncnr.nist.gov/resources/n-lengths/.

[97] H. Rietveld, *Journal of Applied Crystallography*, 1969, **2**, 65-71.

[98] L. B. McCusker, R. B. Von Dreele, D. E. Cox, D. Louer and P. Scardi, *Journal of Applied Crystallography*, 1999, **32**, 36-50.

[99] R. Von, *Journal of Applied Crystallography*, 1997, **30**, 517-525.

[100] A. C. Larson and R. B. von Dreele, GSAS program, Los Alamos National Lab. 523, Rep. No. LA-UR-8674, 1994.

[101] I. D. Brown, *The Chemical Bond in Inorganic Chemistry: the Bond Valence Model*, Oxford University Press, 2006.

[102] I. D. Brown and D. Altermatt, *Acta Crystallographica Section B*, 1985, **41**, 244-247.

[103] I. Brown, *Journal of Applied Crystallography*, 1996, **29**, 479-480.

[104] I. D. Brown, *Chemical Reviews*, 2009, **109**, 6858-6919.

[105] I. D. Brown, Introduction to Bond Valence Analysis Using VaList, http://web.me.com/willsas/Site/Bond_valence_calculations%3A_guide.html.

[106] JEOL Ltd./JEOL DATUM Ltd., SEM_A_To_Z_light, http://www.jeolusa.com/RESOURCES/ElectronOptics/DocumentsDownloads/tabid/320/Default.aspx?EntryId=598.

[107] JEOL DATUM Ltd., SEM Q&A e, http://www.jeolusa.com/RESOURCES/ElectronOptics/DocumentsDownloads/tabid/320/Default.aspx?EntryId=597.

[108] M. H. Bocanegra-Bernal, *Journal of Materials Science*, 2004, **39**, 6399-6420.

[109] N. L. Loh and K. Y. Sia, *Journal of Materials Processing Technology*, 1992, **30**, 45-65.

[110] D. M. Poojary, A. I. Bortun, L. N. Bortun and A. Clearfield, *Inorganic Chemistry*, 1996, **35**, 6131-6139.

[111] B. R. Cherry, M. Nyman and T. M. Alam, *Journal of Solid State Chemistry*, 2004, **177**, 2079-2093.

[112] G. J. Thorogood, B. J. Kennedy, C. S. Griffith, M. M. Elcombe, M. Avdeev, J. V. Hanna, S. K. Thorogood and V. Luca, *Chemistry of Materials*, 2010, **22**, 4222-4231.

[113] Z. Zheng, C. V. Philip, R. G. Anthony, J. L. Krumhansl, D. E. Trudell and J. E. Miller, *Industrial & Engineering Chemistry Research*, 1996, **35**, 4246-4256.

[114] D. Gu, L. Nguyen, C. V. Philip, M. E. Huckman, R. G. Anthony, J. E. Miller and D. E. Trudell, *Industrial & Engineering Chemistry Research*, 1997, **36**, 5377-5383.

[115] C. V. Philip, S. H. Kim, M. Philip and R. G. Anthony, *Separation Science and Technology*, 2003, **38**, 3009-3029.

[116] A. J. Celestian, J. B. Parise, R. I. Smith, H. S. Park and A. Clearfield, *Abstracts of Papers of the American Chemical Society*, 2005, **230**, 111-GEOC.

[117] A. J. Celestian, J. D. Kubicki, J. Hanson, A. Clearfield and J. B. Parise, *Journal of the American Chemical Society*, 2008, **130**, 11689-11694.

[118] A. Dyer, J. Newton, L. O'Brien and S. Owens, *Microporous and Mesoporous Materials*, 2009, **117**, 304-308.

[119] A. Dyer, J. Newton, L. O'Brien and S. Owens, *Microporous and Mesoporous Materials*, 2009, **120**, 272-277.

[120] S. Solbra, N. Allison, S. Waite, S. V. Mikhalovsky, A. I. Bortun, L. N. Bortun and A. Clearfield, *Environmental Science & Technology*, 2001, **35**, 626-629.

[121] J. F. Walker, P. A. Taylor and D. D. Lee, *Separation Science and Technology*, 1999, **34**, 1167-1181.

[122] A. Clearfield, L. N. Bortun and A. I. Bortun, *Reactive & Functional Polymers*, 2000, **43**, 85-95.

[123] A. J. Celestian and A. Clearfield, *Journal of Materials Chemistry*, 2007, **17**, 4839-4842.

[124] A. J. Celestian, J. B. Parise, R. I. Smith, B. H. Toby and A. Clearfield, *Inorganic Chemistry*, 2007, **46**, 1081-1089.

[125] V. Luca, J. V. Hanna, M. E. Smith, M. James, D. R. G. Mitchell and J. R. Bartlett, *Microporous and Mesoporous Materials*, 2002, **55**, 1-13.

[126] A. Tripathi, D. G. Medvedev, M. Nyman and A. Clearfield, *Journal of Solid State Chemistry*, 2003, **175**, 72-83.

[127] A. Tripathi, D. G. Medvedev, J. Delgado and A. Clearfield, *Journal of Solid State Chemistry*, 2004, **177**, 2903-2915.

[128] E. A. Behrens, D. M. Poojary and A. Clearfield, *Chemistry of Materials*, 1996, **8**, 1236-1244.

[129] T. J. Tranter, R. D. Tillotson and T. A. Todd, *Separation Science and Technology*, 2005, **40**, 157-170.

[130] D. T. Bostick, S. M. DePaoli and B. Guo, *Separation Science and Technology*, 2001, **36**, 975-998.

[131] N. R. Mann and T. A. Todd, *Separation Science and Technology*, 2004, **39**, 2351-2371.

[132] F. F. Fondeur, D. D. Walker, W. R. Wilmarth and S. D. Fink, *Separation Science and Technology*, 2001, **36**, 3599-3615.

[133] F. F. Fondeur, T. Hang, D. D. Walker, W. R. Wilmarth and S. D. Fink, *Separation Science and Technology*, 2003, **38**, 3175-3188.

[134] P. A. Taylor and C. H. Mattus, *Separation Science and Technology*, 2003, **38**, 3031-3048.

[135] T. A. Todd, K. N. Brewer, D. J. Wood, P. A. Tullock, N. R. Mann and L. G. Olson, *Separation Science and Technology*, 2001, **36**, 999-1016.

[136] J. P. Larentzos, A. Clearfield, A. Tripathi and E. J. Maginn, *Journal of Physical Chemistry B*, 2004, **108**, 17560-17570.

[137] L. M. Wang, J. Chen and R. C. Ewing, *Current Opinion in Solid State & Materials Science*, 2004, **8**, 405-418.

[138] S. V. Raman, *Journal of Materials Science*, 1998, **33**, 1887-1895.

[139] M. L. Carter, E. R. Vance, D. R. G. Mitchell, J. V. Hanna, Z. Zhang and E. Loi, *Journal of Materials Research*, 2002, **17**, 2578-2589.

[140] K. R. Whittle, S. E. Ashbrook, S. A. T. Redfern, G. R. Lumpkin, J. P. Attfield, M. Dove and I. Farnan, *Scientific Basis for Nuclear Waste Management Xxvii*, 2004, **807**, 339-344.

[141] M. L. Carter, A. L. Gillen, K. Olufson and E. R. Vance, *Journal of the American Ceramic Society*, 2009, **92**, 1112-1117.

[142] M. L. Carter, H. Li, Y. Zhang, E. R. Vance and D. R. G. Mitchell, *Journal of Nuclear Materials*, 2009, **384**, 322-326.

[143] E. R. Vance, D. S. Perera, S. Moricca, Z. Aly and B. D. Begg, *Journal of Nuclear Materials*, 2005, **341**, 93-96.

[144] E. R. Vance, J. Davis, K. Olufson, I. Chironi, I. Karatchevtseva and I. Farnan, *Journal of Nuclear Materials*, 2012, **420**, 396-404.

[145] M. Okrusch, R. Hock, U. Schussler, A. Brummer, M. Baier and H. Theisinger, *American Mineralogist*, 2003, **88**, 986-995.

[146] F. J. Torres, M. A. Tena and J. Alarcon, *Journal of the European Ceramic Society*, 2002, **22**, 1991-1994.

[147] A. W. Hewat, *Ferroelectrics*, 1974, **7**, 83-85.

[148] U. Troitzsch, A. G. Christy and D. J. Ellis, *Physics and Chemistry of Minerals*, 2005, **32**, 504-514.

[149] K. Kihara, *European Journal of Mineralogy*, 1990, **2**, 63-77.

[150] G. Desgardin, C. Robert, D. Groult and B. Raveau, *Journal of Solid State Chemistry*, 1977, **22**, 101-111.

[151] G. Jolicart, M. Leblanc, B. Morel, P. Dehaudt and S. Dubois, *European Journal of Solid State and Inorganic Chemistry*, 1996, **33**, 647-657.

[152] M. P. Crosnier, C. Pagnoux, D. Guyomard, A. Verbaere, Y. Piffard and M. Tournoux, *European Journal of Solid State and Inorganic Chemistry*, 1991, **28**, 971-981.

[153] L. R. Pinckney and G. H. Beall, *Journal of the American Ceramic Society*, 2008, **91**, 773-779.

[154] M. L. Balmer, Y. Su, T. M. Nenoff, A. Navrotsky and B. C. Bunker, *Abstracts of Papers of the American Chemical Society*, 1998, **215**, U680-U680.

[155] R. J. Hill and C. J. Howard, *Journal of Applied Crystallography*, 1987, **20**, 467-474.

[156] J. E. Post and D. L. Bish, *Reviews in Mineralogy*, 1989, **20**, 277-308.

[157] G. D. Ilyushin, *Russian Journal of Inorganic Chemistry*, 2003, **48**, 1799-1811.

[158] G. Desgardin, C. Robert and B. Raveau, *Materials Research Bulletin*, 1978, **13**, 621-626.

[159] C. Robert, G. Desgardin and B. Raveau, *Journal of Inorganic and Nuclear Chemistry*, 1979, **41**, 893-894.

[160] S. G. Fleet, *Zeitschrift fiir Kristallographie*, 1965, **121**, 349-368.

[161] N. N. Neronova and N. V. Belov, *Soviet Physics-Crystallography*, 1965, **9**, 828-834.

[162] A. Grigor'eva, N. Zubkova, I. Pekov, U. Kolitsch, D. Pushcharovsky, M. Vigasina, G. Giester, T. Dordević, E. Tillmanns and N. Chukanov, *Crystallography Reports*, 2011, **56**, 832-841.

[163] P. Ferreira, A. Ferreira, J. Rocha and M. R. Soares, *Chemistry of Materials*, 2001, **13**, 355-363.

[164] C. S. Fewox and A. Clearfield, *Journal of Physical Chemistry A*, 2008, **112**, 2589-2597.

[165] D. E. Henshaw, *Mineralogical Magazine*, 1955, **30**, 585-595.

[166] R. Caruba, A. Baumer and G. H. Turco, *Chemical Geology*, 1973, **11**, 49-69.

[167] H. Xu, A. Navrotsky, M. Balmer and Y. Su, *Physics and Chemistry of Minerals*, 2005, **32**, 426-435.

[168] G. D. Ilyushin and V. A. Blatov, *Acta Crystallographica Section B*, 2002, **58**, 198-218.

[169] A. Ferreira, Z. Lin, M. R. Soares and J. Rocha, *Journal of Solid State Chemistry*, 2010, **183**, 3067-3072.

[170] N. J. Coleman, S. P. Lewis, A. P. Mendham and V. Trivedi, *Journal of Porous Materials*, 2010, **17**, 747-753.

[171] Y. Su, M. L. Balmer, L. Wang, B. C. Bunker, M. Nyman, T. Nenoff and A. Navrotsky, Evaluation of thermally converted silicotitanate waste forms, in *Scientific Basis for Nuclear Waste Management Xxii*, ed. D. J. L. J. H. Wronkiewicz, 1999, 77-84.

[172] S. M. Haile and B. J. Wuensch, *Acta Crystallographica Section B*, 2000, **56**, 349-362.

[173] S. M. Haile and B. J. Wuensch, *American Mineralogist*, 1997, **82**, 1141-1149.

[174] R. Smith, Refinement of Time-of-flight Profile Parameters in GSAS, Crystallography Group, ISIS facility, Rutherford Appleton Laboratory, Refinement of Time-of-flight Profile Parameters in GSAS.

[175] Oxford Instruments, Periodic Table of Elements with Principal lines in Energy, http://www.oxford-instruments.com/products/xrf-analysers/PublishingImages/A4_size-OI_Periodic_table_of_elements-hires.jpg.

[176] R. D. Shannon, *Acta Crystallographica Section A*, 1976, **32**, 751-767.

[177] D. Altermatt and I. D. Brown, *Acta Crystallographica Section B-Structural Science*, 1985, **41**, 240-244.

[178] G. Ilyushin, *Journal of Materials Science*, 2006, **41**, 1563-1569.

[179] H. W. Xu, A. Navrotsky, M. Nyman and T. M. Nenoff, *Journal of the American Ceramic Society*, 2005, **88**, 1819-1825.

[180] Y. Su, T. M. Nenoff, A. Navrotsky, L. Li, M. Nyman and H. Xu, New Metal Niobate and Silicotitanate Ion Exchangers: Development and Characterization, The Pacific Northwest National Laboratory, New Metal Niobate and Silicotitanate Ion Exchangers: Development and Characterization, 2002.

[181] Committee on Waste Forms Technology and Performance; National Research Council, Waste Form Testing, in *Waste Forms Technology and Performance: Final Report*, Washington, DC, 2011, 119-152.

[182] D. M. Wellman, J. P. Icenhower and W. J. Weber, *Journal of Nuclear Materials*, 2005, **340**, 149-162.

[183] H. Matzke and E. Vernaz, *Journal of Nuclear Materials*, 1993, **201**, 295-309.

[184] ASTM International, Standard Test Method for Static Leaching of Monolithic Waste Forms for Disposal of Radioactive Waste, 1998.

[185] ASTM International, Standard Test Methods for Determining Chemical Durability of Nuclear, Hazardous, and Mixed Waste Glasses and Multiphase Glass Ceramics: The Product Consistency Test (PCT), 2002.

[186] EPA Test Method 1311—TCLP, Toxicity Characteristic Leaching Procedure, http://www.ehso.com, 2012.

[187] K. L. Smith, G. R. Lumpkin, M. G. Blackford, R. A. Day and K. P. Hart, *Journal of Nuclear Materials*, 1992, **190**, 287-294.

[188] M. L. Carter, E. R. Vance, G. R. Lumpkin and E. Loi, Aqueous dissolution of Rb-bearing hollandite and Synroc-C at 90 °C, in *MRS Proceedings*, **663**, 381-388, 2000.

[189] V. Luca, C. S. Griffith, E. Drabarek and H. Chronis, *Journal of Nuclear Materials*, 2006, **358**, 139-150.

[190] D. Banerjee, V. Sudarsan, A. Joseph, I. J. Singh, J. Nuwad, C. G. S. Pillai, P. K. Wattal and D. Das, *Journal of Nuclear Materials*, 2011, **413**, 177-182.

[191] H.-S. Park, I.-H. Cho, H. C. Eun, I.-T. Kim, Y. Z. Cho and H.-S. Lee, *Environmental Science & Technology*, 2011, **45**, 1932–1939.

[192] L. A. Bursill and D. J. Smith, *Journal of Solid State Chemistry*, 1987, **69**, 343-354.

[193] R. Devanathan, *Nuclear Instruments and Methods in Physics Research Section B: Beam Interactions with Materials and Atoms*, 2009, **267**, 3017-3021.

[194] A. Clearfield, *Solid State Sciences*, 2001, **3**, 103-112.

[195] T. Moller, R. Harjula and J. Lehto, *Separation and Purification Technology*, 2002, **28**, 13-23.

[196] A. Tripathi, D. G. Medvedev and A. Clearfield, *Journal of Solid State Chemistry*, 2005, **178**, 253-261.

[197] Y. Park, W. S. Shin, G. S. Reddy, S.-J. Shin and S.-J. Choi, *Journal of Nanoelectronics and Optoelectronics*, 2010, **5**, 238-242.

[198] S. Chitra, R. Sudha, S. Kalavathi, A. Mani, S. Rao and P. Sinha, *Journal of Radioanalytical and Nuclear Chemistry*, 2012, 1-7.

[199] V. Nedel'ko, N. Chukanov and I. Pekov, *Inorganic Materials*, 2011, **47**, 502-505.

[200] N. Zubkova, D. Ksenofontov, Y. Kabalov, N. Chukanov, V. Nedel'ko, I. Pekov and D. Pushcharovsky, *Inorganic Materials*, 2011, **47**, 506-512.

[201] N. Chukanov, A. Kazakov, I. Pekov and A. Grigor'eva, *Russian Journal of Physical Chemistry A, Focus on Chemistry*, 2010, **84**, 2154-2159.

Appendices

(Appendices CD attached here)

Appendix 1 Refinement parameters, unit cell parameters, refined atom positions, multiplicities, occupancies and isotropic displacement parameters from the refinement of synchrotron X-ray diffraction for Na-CST

Refinement parameters		*Lattice parameters*	
R_{wp}	6.65%	$a/Å$	7.8040(1)
R_p	4.52%	$c/Å$	11.9729(1)
χ^2	5.502	$Volume/Å^3$	729.17(3)

Refined atom positions, multiplicities, occupancies and isotropic displacement parameters

|	x	y	z	Mult	Occup	U_{iso}
Ti1	0.13857(16)	0.13857(16)	0.15394(14)	8	1	0.0105(4)
Si2	0	0.5	0.25	4	1	0.0105(4)
O3	0.1223(5)	0.3922(5)	0.16759(25)	16	1	0.0105(4)
O4	0.1176(5)	0.1176(5)	0.3354(4)	8	1	0.0105(4)
O5	0.1395(7)	0.1395(7)	0	4	1	0.0105(4)
Na6	0	0.5	0.25	4	0.872(7)	0.0105(4)
O7	0.2767(6)	0.2767(6)	0.5	4	1	0.0105(4)
O8	0.4592(16)	0.4592(16)	0.1767(11)	8	0.301(6)	0.0105(4)
Na9	0.4413(10)	0.4413(10)	0.0758(10)	8	0.267(4)	0.0105(4)

Appendix 2 Refinement parameters, unit cell parameters, refined atom positions, multiplicities, occupancies and isotropic displacement parameters from the refinement of synchrotron X-ray diffraction for Na-Nb/CST

Refinement parameters		*Lattice parameters*	
R_{wp}	9.74%	$a/Å$	7.8251(1)
R_p	6.66%	$c/Å$	12.0001(2)
χ^2	9.599	$Volume/Å^3$	734.78(3)

Refined atom positions, multiplicities, occupancies and isotropic displacement parameters

	x	*y*	*z*	*Mult*	*Occp*	U_{iso}
Ti1	0.13893(21)	0.13893(21)	0.15493(19)	8	0.909(8)	0.0158(3)
Nb2	0.13893(21)	0.13893(21)	0.15493(19)	8	0.091(8)	0.0158(3)
Si3	0	0.5	0.25	4	1	0.0158(3)
O4	0.1152(6)	0.3908(6)	0.1678(4)	16	1	0.0158(3)
O5	0.1192(6)	0.1192(6)	0.3368(6)	8	1	0.0158(3)
O6	0.1378(10)	0.1378(10)	0	4	1	0.0158(3)
Na7	0	0.5	0.5	4	1	0.0158(3)
O8	0.2755(9)	0.2755(9)	0.5	4	1	0.0158(3)
O9	0.4706(23)	0.4706(23)	0.1871(11)	8	0.379(9)	0.0158(3)
Na10	0.4380(10)	0.4380(10)	0.0704(9)	8	0.371(5)	0.0158(3)

Appendix 3 Selected Rietveld refinement data for $Cs_2TiNb_6O_{18}$ (solid state reaction)

(U_{iso} of Cs is fixed at 0.004 $Å^2$)
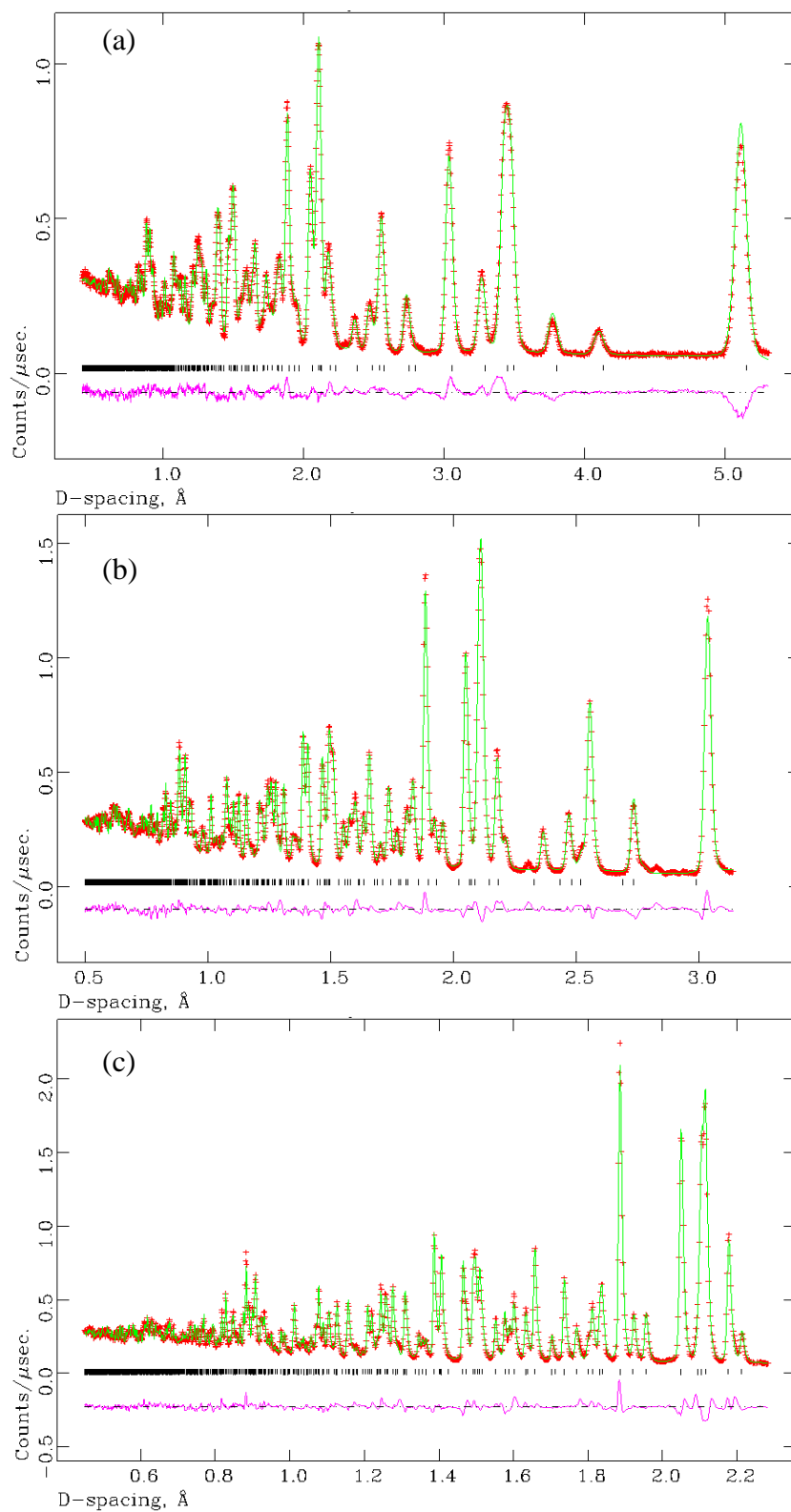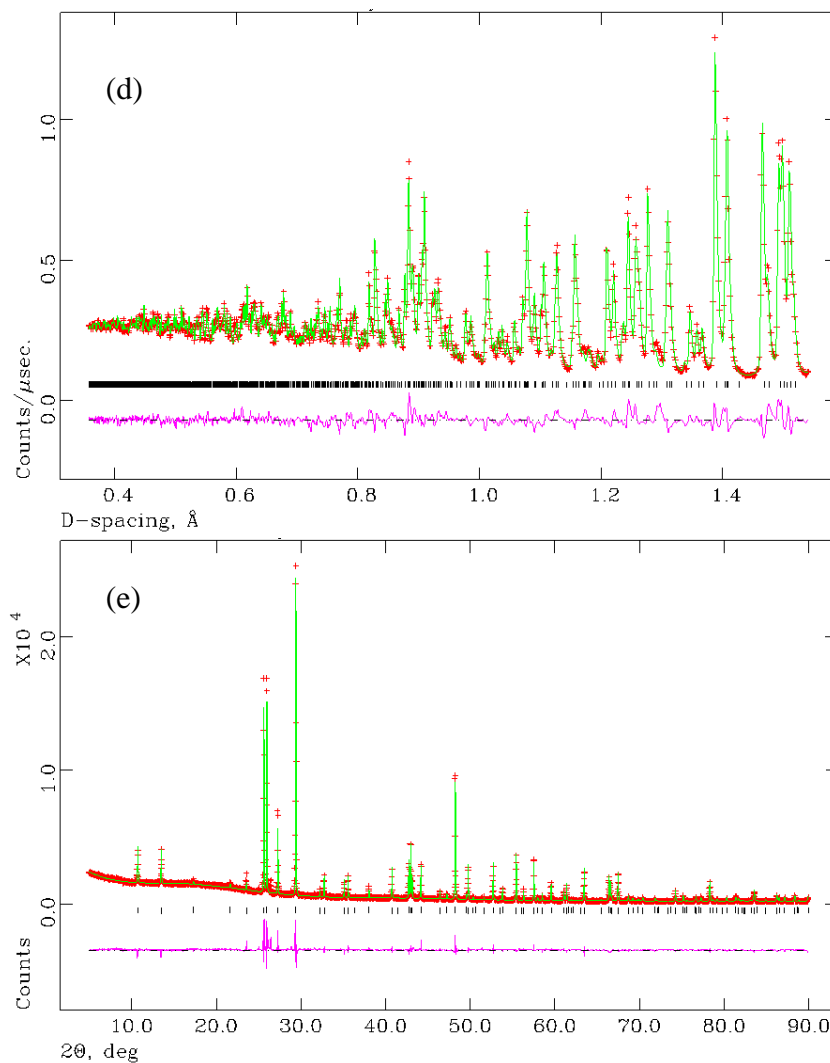
Simulated (green line) and experimental diffraction patterns (red dots) as well as difference pattern (purple) for $Cs_2TiNb_6O_{18}$ (solid state reaction) using neutron diffraction data from GEM (a) Bank 3, $2\theta = 34.96°$ (b) Bank 4, $2\theta = 63.62°$ (c) Bank 5, $2\theta = 91.30°$ (d) Bank 6, $2\theta = 154.40°$, and (e) using laboratory XRD data.

Appendix 4 Relationship between sample mass and surface area

Examination of particles produced by the planetary mill suggests them to be tetrahedral. Consider a tetrahedron inscribed within a cube of edge length *a*. The surface area of such a tetrahedron is given by $2\sqrt{3}a^2$ and the volume $a^3/3$. Given that the particles have been sieved between 150 μm and 75 μm it is reasonable to take these two values as the upper and lower limits for the above cube.

Assuming the population of particles is independent of size then the total area and volume are given by:

$A_{TOTAL} = g \int 2\sqrt{3}a^2 \, \mathrm{d}a$ between a = 0.015 cm and 0.0075 cm.

$V_{TOTAL} = g \int a^3/3 \, \mathrm{d}a$ which multiplied by the density ρ of the waste form gives the total mass.

The constant *g* is effectively the population distribution function.

Integrating and eliminating g, then substituting in for the above values of *a* gives:

$$\mathbf{A_{TOTAL} = M_{TOTAL}\ 862.2/\rho}$$

[This equation is valid in CGS units, i.e. g and cm]